Solid-State NMR Investigations of ^{67}Zn and ^{27}Al Nuclei in Zinc-Amino Acid Complexes, Zinc-Insulin Hexamers, and Aluminum-Centered Dyes

by

Kamal Mroue

A thesis
presented to the University of Waterloo
in fulfillment of the
thesis requirement for the degree of
Doctor of Philosophy
in
Chemistry

Waterloo, Ontario, Canada, 2010

I hereby declare that I am the sole author of this thesis. This is a true copy of the thesis, including any required final revisions, as accepted by my examiners.

I understand that my thesis may be made electronically available to the public.

Abstract

Modern solid-state nuclear magnetic resonance (NMR) methodologies are applied to investigate two spin-$\frac{5}{2}$ nuclei, ^{67}Zn and ^{27}Al, in different coordination environments in order to characterize the magnitudes and orientations of their electric field gradient (EFG) and nuclear magnetic shielding tensors. The advantages of using high (21.1 T) applied magnetic fields for detecting ^{67}Zn directly at ambient temperatures, using the quadrupolar Carr-Purcell Meiboom-Gill (QCPMG) pulse sequence and the stepped-frequency technique, are demonstrated by the successful investigation of the different zinc sites in several zinc-amino acid coordination compounds, and in the more complex polymorphs of the zinc-insulin hexamers. In all systems, the high-field ^{67}Zn NMR spectra are dominated only by the quadrupolar interaction. The first two ^{67}Zn NMR spectra of pentacoordinated zinc sites are reported and analyzed. The experimental results are corroborated by *ab initio* and density functional theory (DFT) calculations of the ^{67}Zn NMR parameters in order to gain better understanding of the zinc local electronic environments.

Solid-state ^{27}Al NMR is applied to study three commercial aluminum-phthalocyanine dyes. Solid-state ^{27}Al NMR experiments, including multiple-quantum magic-angle-spinning (MQMAS) and quadrupolar Carr-Purcell Meiboom-Gill (QCPMG), are employed at multiple high magnetic field strengths (11.7, 14.1 and 21.1 T) to determine the composition and number of aluminum distinct sites in these dyes. The quadrupolar parameters for each ^{27}Al site are determined from spectral simulations, with quadrupolar coupling constants (C_{Q}) ranging from 5.40 to 10.0 MHz and asymmetry parameters (η_{Q}) ranging from 0.10 to 0.50, and compare well with the results of quantum chemical calculations of these tensors. The largest ^{27}Al chemical shielding anisotropy (CSA), with a span of 120 ± 10 ppm, observed directly in a solid material is also reported. The combination of MQMAS and

computational chemistry are used to interpret the presence of multiple aluminum sites in two of the three samples.

Acknowledgements

In his most famous book *The Alchemist*, the Brazilian author Paulo Coelho reveals the central theme through a phrase said by the old man, King Melchizedek, to the young shepherd Santiago:"When you want something, all the universe conspires in helping you to achieve it." I believe this with all my heart!

There are lots of people in *my universe*, who have helped me reach this point of my life, to whom I owe my deepest thanks and gratitude for a huge variety of reasons.

I begin by saying that I could not have imagined having a better supervisor and advisor for my graduate studies than Dr. Bill Power; without Bill's knowledge, perceptiveness, enthusiasm, and encouragement this thesis would never have seen the light. I specially thank Bill for his incredible patience with my imperfections and with my continuous delays in completing many jobs, for always keeping the door to his office open for questions, and for his generous support that allowed me to reach this point. ***Thank You*** for everything Bill.

Next, my thanks are due to my PhD committee members, Dr. Glenn Penner, Dr. Marcel Nooijen, Dr. Pavle Radovanovic, and Dr. Raymond Laflamme (internal-external) for managing to read the whole thesis so thoroughly. I would also like to thank all the rest of the academic and support staff of the Department of Chemistry at the University of Waterloo (UW). My special thanks go to Cathy van Esch, the administrative coordinator for graduate studies in Chemistry, for her help with the administrative work.

I am grateful to Mike Ditty, a former member of the Power Lab, for his help with setting up the QCPMG experiment on our spectrometers. Mike's prompt and quick showing up whenever I asked for his assistance with complicated hardware or software problems on the NMR spectrometers, as well as his unstinting willingness to share with me his NMR

knowledge and expertise, are unforgettable. Jan Venne, the outstanding NMR Facility Manager at UW, is also thanked for giving me technical support over these years. Dr. Jalil Assoud, an excellent X-ray crystallographer and a supportive friend of mine, is thanked for solving and analyzing crystal structures. Much respect to present and former members of the Power Lab: Jun Gu, Abdul-Hamid Emwas, Fernando Amador, Sam Andrey, and Mike Chan. Sam and Mike are particularly thanked for their assistance with the syntheses of the samples for the zinc-insulin project.

Most of the NMR spectra contained in this thesis were acquired at the *National Ultrahigh-Field NMR Facility for Solids* at the NRC in Ottawa, Ontario. Having access to the state-of-the-art 900 MHz spectrometer there was a turning point in my PhD studies. I am very grateful to Dr. Victor Terskikh, the Facility Manager, for introducing me to the spectrometer and for his significant assistance with the acquisition of the zinc and aluminum spectra. Dr. Eric Ye is also thanked for his technical help.

My warm thanks go to Firas Mansour, my best friend in Waterloo, for always dragging me out of the lab for a coffee break, and for the great times we have spent together around his dining table enjoying one of his "most delicious" Lebanese meals. I must also thank my friends Mustapha Makkook, Adel Fakih, and Mohamad Awad from Electrical and Computer Engineering. Mustapha is particulary thanked for introducing me to LaTeX and helping me into its basic concepts. Adel is thanked for showing real interest in my research, and for being patient with me talking about it. Special thanks are extended to my friends Waseem El-Huneidi and Ahmed Magdy for their helpful suggestions on the syntheses of my samples and for the wonderful times we had together.

I wish to express my special love and gratitude to my brother Ali and his wife Ann for their continuous love and help, especially during the first years of my life in Canada. Without their support, those times would have been unbearable. I am grateful to my

other siblings Nahla, Mahmoud, Kamel, Ikmal, and Mohammad, and their families, for rendering me the sense and the value of brotherhood. I am glad to be one of them.

I feel a deep sense of gratitude to my late father, Hussein Mroué, and my mother, Mahassen, who early in my life formed a part of my educational path and taught me the good things that really matter in life. I am wholeheartedly indebted to my father who never had the chance to gain formal education, but with his visionary thinking and persistent will, knew the real value and importance of education. He worked very hard to provide us with the best education, despite all the difficult and dangerous circumstances we lived through during the Civil War in Lebanon (1975–1990). My hard work and efforts put forth in this thesis are merely a result of all that he instilled in me over the years.

Last but surely not least, I am eternally grateful to my wife, Nesrine, for always providing me with her endless love, support, and patience during these years. Words cannot express my gratitude and love; I could not have done this without Nesrine by my side. One of the best life experiences that we have been living through together in the past three years was the birth of our son Ali Daniel and our daughter Juliana, both of whom have provided a new dimension full of joy and pleasure to our joint life.

Dedication

To the memory of my father, Hussein Mroué (1937 - 2003)

To my wife, Nesrine, and my children, Ali & Juliana

Table of Contents

List of Tables

List of Figures

List of Symbols and Abbreviations

α, β, γ	Euler angles defining the relative orientation of two tensors
$\boldsymbol{\mu}$	nuclear magnetic moment
ΔE	energy difference
$\Delta\nu_{CT}$	breadth of the central transition
δ_{aniso}	anisotropy of the chemical shift tensor
δ_{iso}	isotropic chemical shift
δ_{11}, δ_{22}, δ_{33}	principal components of the chemical shift tensor
δ_{qis}	isotropic second-order quadrupole induced shift
ΔJ	anisotropy of the indirect spin-spin coupling tensor
m	magnetic quantum number
η_{cs}	asymmetry parameter of the chemical shift tensor
η_{Q}	asymmetry parameter of the electric field gradient tensor
η_J	asymmetry parameter of the indirect spin-spin coupling tensor
γ	gyromagnetic ratio
$\hat{\mathbf{I}}$	nuclear spin angular momentum operator
$\hat{\mathbf{I}}_{\text{z}}$	operator of the z-component of the nuclear spin angular momentum
$\hat{\mathbf{I}}_+$, $\hat{\mathbf{S}}_+$	nuclear spin raising operator
$\hat{\mathbf{I}}_-$, $\hat{\mathbf{S}}_-$	nuclear spin lowering operator

$\hat{\mathcal{H}}_Z$	Zeeman Hamiltonian
$\hat{\mathcal{H}}_{\text{tot}}$	total NMR Hamiltonian
$\hat{\mathcal{H}}_J$	indirect spin-spin Hamiltonian
$\hat{\mathcal{H}}_{SR}$	spin-rotation Hamiltonian
$\hat{\mathcal{H}}_Q$	quadrupolar Hamiltonian
$\hat{\mathcal{H}}_{CS}$	chemical shielding Hamiltonian
$\hat{\mathcal{H}}_{DD}$	direct dipolar Hamiltonian
$\hat{\mathcal{H}}_{rf}$	radiofrequency Hamiltonian
$\hbar$	$\frac{h}{2\pi}$, h is Planck's constant
κ	skew of the chemical shift tensor
$\mathbf{B}_{\text{o}}$	external applied magnetic field
$\mathbf{B_{rf}}(\mathbf{t})$	time-dependent radiofrequency field
$\mathbf{P}$	nuclear spin angular momentum
μ_0	permeability of free space
ν_{o}	Larmor frequency
ν_{Q}	quadrupolar frequency
ν_{rot}	sample spinning rate
Ω	span of the chemical shift tensor
ω_{rf}	nutation angular frequency
$\rho(\mathbf{r})$	nuclear charge density
σ_{iso}	isotropic magnetic shielding
σ_{11}, σ_{22}, σ_{33}	principal components of the magnetic shielding tensor
τ_p	duration of radiofrequency pulse
θ, ϕ	polar angles orienting the principal axis system of a tensor in the direction of the external applied magnetic field

$\underline{\underline{\sigma}}$	nuclear mgnetic shielding tensor
$\underline{\underline{\mathbf{V}}}$	electric field gradient tensor
$\underline{\underline{\mathcal{D}}}$	direct dipolar coupling tensor
$\underline{\underline{\mathcal{J}}}$	indirect spin-spin coupling tensor
$\underline{\underline{\sigma}}^T$	transpose of the shielding tensor
$\underline{\underline{\sigma}}^a$	antisymmetric component of the shielding tensor
$\underline{\underline{\sigma}}^s$	symmetric component of the shielding tensor
B_1	amplitude of the *rf* field
C_Q	nuclear quadrupolar coupling constant
I	nuclear spin quantum number
J_iso	isotropic indirect spin-spin coupling constant
$J_\perp$, $J_\parallel$	components of the indirect spin-spin coupling tensor perpendicular and along the internuclear vector
P_Q	second-order quadrupole effect (SOQE)
r_ij	distance between nuclei i and j
R_{DD}	direct dipolar coupling constant
R_{eff}	effective dipolar coupling constant
$V(\mathbf{r})$	electrostatic potential
V_{11},V_{22}, V_{33}	principal components of the EFG tensor
x, y, z	Cartesian coordinates
A	mass number of the nucleus
e	elementary charge
J	indirect spin-spin coupling constant
Q	nuclear quadrupole moment

rf	radiofrequency
Z	atomic number of the nucleus
σ^d	diamagnetic term of the magnetic shielding tensor
σ^p	paramagnetic term of the magnetic shielding tensor
$\underline{\underline{\mathcal{C}}}$	spin-rotation coupling tensor
CP	cross-polarization
CS	chemical shift (shielding)
CSA	chemical shift anisotropy
CT	central transition: $m = \frac{1}{2} \leftrightarrow m = \frac{-1}{2}$
DAS	dynamic-angle spinning
DFS	double-frequency sweep
DFT	density functional theory
DOR	double rotation
EFG	electric field gradient
FID	free induction decay
FT	Fourier Transform
GIAO	gauge-including (or invariant) atomic orbitals
HS	hyperbolic secant
MAS	magic-angle spinning
MCSCF	multiconfigurational self-consistent field
MQMAS	multiple-quantum magic-angle spinning
Nc	naphthalocyanine
NMR	nuclear magnetic resonance
o.d.	outer diameter

PAS	principal axis system
Pc	phthalocyanine
PXRD	powder X-ray diffraction
QCPMG	quadrupolar Carr-Purcell Meiboom-Gill
QE	quadrupolar echo
RAPT	rotor-assisted population transfer
RHF	restricted Hartree-Fock
S/N	signal-to-noise ratio
SE	solid echo
SHARCNET	Shared Hierarchical Academic Research Computing Network
SIMPSON	simulation program for solid-state NMR
SSNMR	solid-state nuclear magnetic resonance
TMS	tetramethylsilane
TPPM	two-pulse phase modulation
WURST	Wideband Uniform Rate Smooth Truncation

Chapter 1

A General Introduction

1.1 Preamble

The history of magnetic resonance begins in the early 1920s when M. H. Belz reported unsuccessful attempts to search for a dependence of magnetic susceptibility on frequency using different solutions of paramagnetic salts.[1] No frequency dependence was observed at that time. There were, however, subsequent molecular–beam magnetic resonance experiments over the next several years. Magnetic resonance was first demonstrated in 1938 by I. I. Rabi and his colleagues.[2] They constructed a molecular–beam magnetic resonance apparatus and detected the ^{7}Li signal in the LiCl molecule; this work resulted in the award to Rabi of a Nobel Prize in Physics in 1944. This led to the discovery of the phenomenon of *nuclear magnetic resonance* (NMR) spectroscopy by two independent groups in 1946. E. Purcell and his co-workers at Harvard University detected NMR signals of protons in solid paraffin wax,[3] while F. Bloch and his group at Stanford University observed NMR signals from the protons in liquid water.[4] These achievements were promptly recognized when the Nobel Prize in Physics was awarded to Purcell and Bloch in 1952. In the years since

then, NMR has evolved as an indispensable tool for elucidating molecular structure and dynamics, and has expanded as a powerful technique in all fields of science and technology.[5]

The observation of the chemical shift[6] and the indirect spin-spin (or J-coupling)[7] interactions in the early 1950s enabled researchers to recognize liquid-state NMR as a characterization tool for molecular structure, thus initiating a new era in structural elucidation of unknown systems via NMR. While NMR of solids and liquids were first implemented almost simultaneously, the applications of NMR to solid systems have lagged behind those to liquids since, due to many difficulties encountered with solid samples. These difficulties arise mainly from low sensitivity and poor resolution, which in turn are due to the broad and featureless line shapes exhibited in solid-state NMR spectra. These spectra are broadened because of the anisotropy (*i.e.*, orientation dependence) of the various nuclear spin interactions associated with the given sample, which may include: the nuclear magnetic shielding, dipolar coupling, and the nuclear quadrupole interaction (valid only for quadrupolar nuclei, those with spin quantum number, I, greater than $\frac{1}{2}$). In isotropic fluids, the anisotropies of these interactions are averaged to their isotropic values due to rapid molecular tumbling, which is not the case in solids. Nevertheless, it is the wealth of information that can be obtained from the magnitude and orientations of these anisotropic interactions that makes NMR of solids more informative than that of liquids. There are other practical benefits to solid-state NMR as well. First, solid-state NMR is the only method available if the sample is insoluble. Second, when dissolved in a solvent, some materials may become unstable and may lose or alter their solid-state structure; in this case, the desired structural information cannot be obtained from solution NMR.

In the periodic table of elements and their associated nuclear isotopes, the vast majority of the NMR-active nuclei are quadrupolar (and of these, the vast majority have half-integer spins) such as ^{23}Na, ^{17}O, ^{27}Al, $^{35/37}$Cl, and ^{67}Zn. While solution-state NMR of

quadrupolar nuclei is often uninformative due to extremely rapid nuclear spin relaxation, the solid-state NMR spectra of quadrupolar nuclei are dominated mainly by the quadrupolar interaction, which is often much stronger than other nuclear spin interactions, yielding very broad, featureless, and anisotropic line shapes. Fortunately, much progress has been made during the past several decades with regard to overcoming the difficulties presented by solid-state NMR. Several important line-narrowing and sensitivity-enhancement techniques have been developed for the NMR spectra of solids, especially those containing quadrupolar nuclei. The most important of these include: *spin-echo* experiments,[8] *magic-angle spinning* (MAS),[9] *cross-polarization* (CP),[10] *double rotation* (DOR),[11,12] *dynamic-angle spinning* (DAS),[12,13] *multiple-quantum magic-angle spinning* (MQMAS),[14] as well as other techniques based on the quadrupolar Carr-Purcell Meiboom-Gill (QCPMG)[15–18] experiment. The QCPMG experiment is used extensively in this thesis to acquire static spectra of the unreceptive ^{67}Zn quadrupolar nucleus.

Another very important technical development of the past decade is the increasing availability of high-field NMR instruments, such as the 900 MHz NMR spectrometer ($B_o = 21.1$ T) at the *National Ultrahigh-Field NMR Facility for Solids* in Ottawa, Canada (www.nmr900.ca). Access to such high-field instruments has enabled the study of more challenging and difficult quadrupolar nuclei as, in addition to the gain in intrinsic sensitivity due to the high-field strength, the total width (in Hz) of the central-transition line shape in a quadrupolar-dominated NMR spectrum is significantly narrowed due to its inverse scaling with the applied magnetic field.

By virtue of the increasing advancement in computational hardware and the development of commercial quantum chemistry computing softwares, theoretical calculation of NMR properties from first principles has emerged as an indispensable tool for structure elucidation as a corroboratory technique to experimental solid-state NMR spectroscopy. The

accurate reproduction of experimental NMR parameters serves as a good test of the theory employed in computing such anisotropic NMR properties as the nuclear magnetic shielding and the electric field gradient tensors. Because these calculations are always carried on known structural models, which are often obtained either from available crystal structures or by computational geometry optimization, the calculated NMR parameters correspond to well-known structural sites and can successfully be assigned to specific resonance peaks in the experimental spectrum. Moreover, the orientation of the calculated interaction tensor within the molecule-fixed axis system is important information that can only obtained from calculations, and often cannot be directly extracted from the experimental NMR spectra of polycrystalline powders.

In light of these developments and advances, the realm of solid-state NMR spectroscopy has been constantly evolving over the past decades, and nowadays it is well established as one of the most powerful and flexible techniques for chemical analysis, structure determination, and the study of molecular dynamics in a wide variety of solid systems, with diverse applications to almost all areas of modern science: chemistry, physics, biology, biochemistry, chemical engineering, material science, medicine, and other areas of technology as well.

1.2 Research Objectives and Thesis Outline

The main objective of the research presented in this thesis is to provide a detailed characterization of the NMR properties, particularly nuclear magnetic shieldings and electric field gradients, for the two spin-$\frac{5}{2}$ quadrupolar nuclei ^{67}Zn and ^{27}Al using a combined experimental - computational approach. The first nucleus, ^{67}Zn, belongs to a group of nuclei that are not commonly examined by NMR because of the experimental challenges they present

due to their unfavorable nuclear and magnetic properties: their low natural abundances, low resonance frequencies, and their quite large nuclear quadrupole moments. The second nucleus, ^{27}Al, has comparatively favorable NMR properties, and the aluminum-centered phthalocyanine dyes investigated in this work by solid-state ^{27}Al NMR are of considerable significance in technology and industry, in addition to their distinctive insolubility and amorphous nature.

This thesis is laid out as follows: the basic principles of NMR are discussed in Chapter 2 in order to provide a theoretical background for the research results presented thereafter. The theory describing the relevant nuclear spin interactions is covered from the solid-state NMR perspective, as well as the influence of these interactions on NMR line shapes of polycrystalline powder solids. Also presented in Chapter 2 are general concepts pertaining to the NMR methods that are of great importance in solid-state NMR studies of half-integer-spin quadrupolar nuclei. Chapter 3 discusses the application at room temperature of high-field ^{67}Zn solid-state NMR spectroscopy to a series of four zinc-amino acid coordination complexes, as well as a related zinc-imidazole coordination complex. Zinc adopts a variety of coordination geometries in these complexes, which serve as good representatives of the the zinc-binding sites in systems of biological relevance. Static ^{67}Zn QCPMG NMR spectra as wide as *ca.* 750 kHz are recorded at 21.1 T and used to extract the NMR tensor parameters at the zinc sites. Complementary techniques, such as ^{13}C solid-state CP/MAS NMR spectroscopy, X-ray diffraction, and quantum chemical calculations, are also employed to correlate the experimental ^{67}Zn NMR parameters with the molecular and electronic structures.

The promising high-field ^{67}Zn NMR results obtained in Chapter 3 have encouraged us to expand our investigation into the zinc-binding sites to more complex and challenging zinc-containing bioinorganic systems, in order to gain more insights about the changes

in ^{67}Zn NMR spectral features as a function of ligand type and geometry. The three polymorphs of the zinc-insulin hexamer (T_6, R_6, and T_3R_3) are an ideal test case for the feasibility of solid-state ^{67}Zn NMR spectroscopy to observe such changes, since the three zinc-insulin hexamers and their respective conformational transformations have been well characterized by X-ray crystallography and other spectroscopic methods. Preliminary ^{67}Zn solid-state NMR spectra of ^{67}Zn-enriched (94.2 %) powdered samples of the three polymorphs, acquired at 21.1 T, are presented and analyzed in Chapter 4.

In Chapter 5, the ability of solid-state NMR to characterize solid materials, for which no sufficient information about the solid-state structure is available, is demonstrated. Solid-state ^{27}Al NMR spectra, including MAS, MQMAS, and static QCPMG spectra, have been acquired at multiple high magnetic field strengths (11.75, 14.1 and 21.1 T) to determine the composition and number of aluminum sites in three aluminum-centered phthalocyanine dyes. The resulting line shapes are analyzed in order to extract detailed information concerning the aluminum electric field gradient (EFG) and nuclear magnetic shielding tensors. The combination of MQMAS and quantum chemical calculations are used to interpret the presence of multiple aluminum sites in two of the three studied dyes.

The conclusions presented in this thesis are highlighted and summarized in the final chapter, Chapter 6, as well as the limitations of the projects conducted. In addition, some directions for future research are briefly suggested. Following these concluding remarks, the thesis ends with supplementary material included in three appendices. Appendix A contains supplementary data concerning the results of Chapter 3. These data include detailed information about the X-ray single-crystal structures of three zinc-amino acid coordination complexes, as well as several *Gaussian* input files that were used in computing the ^{67}Zn NMR parameters of the studied systems. Appendix B consists of four *Gaussian* input files that were used to compute the ^{67}Zn NMR parameters for the molecular cluster models of the

zinc-insulin hexamers, the subject of the NMR studies in Chapter 4. Appendix C contains Cartesian atomic coordinates employed in the calculations of the ^{27}Al NMR parameters of the aluminum-phthalocyanine dyes studied in Chapter 5, as well as sample input files used for numerical simulations of ^{27}Al static and spinning one-dimensional NMR line shapes.

Chapter 2

NMR: Basics, Theory, and Techniques

This chapter will review the fundamentals of NMR spectroscopy from the solid-state point of view. In order to adequately interpret and analyze the NMR spectra of solid systems, and consequently to extract quantitative information related to molecular structure and symmetry, a thorough discussion of the NMR spin interactions is essential. Therefore, the next section reviews the frequency response of the various NMR interactions, with a particular emphasis on those interactions most relevant to the research presented in this thesis, namely the nuclear magnetic shielding (or chemical shift) interaction and the nuclear quadrupole interaction. The theory of NMR interactions has been discussed comprehensively in several excellent books written by: Abragam,[19] Slichter,[20] Haeberlen,[21] Mehring,[22] Ernst *et al.*,[23] Harris,[24] Levitt,[25] Schmidt-Rohr and Spiess,[26] and Duer,[27] as well as a variety of reviews like those written by: Cohen and Reif,[28] Taylor *et al.*,[29] Vaughan,[30] Man,[31] and Vega.[32] The interested reader is referred to these works for a more extensive and detailed treatment of the principles of nuclear magnetic resonance.

2.1 NMR Spin Interactions

NMR is based on the interaction between a nucleus having non-zero spin quantum number (I) and an external magnetic field; I is often called the *nuclear spin* for simplicity. The atomic nucleus is made up of Z positively charged protons and (A - Z) uncharged neutrons, where Z and A are, respectively, the atomic number and mass number of the nucleus. Each proton and neutron possesses an intrinsic spin of $\frac{1}{2}$ in the same way as electrons do. In nuclei with even numbers of both protons and neutrons, all spins are paired and the nuclear spin quantum number I is zero. Such nuclei are NMR inactive *i.e.*, they cannot be observed by NMR. Important examples are the major isotopes ^{12}C and ^{16}O, a fact that results in a considerable simplification of the NMR spectra of organic molecules. If there are an odd number of either or of both of protons and neutrons, then the nuclear spin is a non-zero multiple of $\frac{1}{2}$ ($I = \frac{n}{2}$, n being an integer from 1 to 9), as shown in Table 2.1.

	Protons	
Neutrons	Even	Odd
Even	$I = 0$	half-integer I
Odd	half-integer I	integer I

Table 2.1: Nuclear spin (I) value as a function of the numbers of protons and neutrons.

Nuclei with spin $I = \frac{1}{2}$ are the easiest, hence also the most commonly observed by NMR. They are characterized by a uniform spherical charge distribution. The commonly observed spin-$\frac{1}{2}$ nuclei are ^{1}H, ^{13}C, ^{15}N, ^{19}F, and ^{31}P. Nuclei with spin $I > \frac{1}{2}$ are called *quadrupolar nuclei*. They comprise the vast majority of elemental isotopes in the periodic table, with about 75% of the known elements having at least one quadrupolar nuclear isotope. Unlike spin-$\frac{1}{2}$ nuclei, quadrupolar nuclei possess a non-spherical charge distribution. Examples are ^{2}H and ^{14}N ($I = 1$), ^{11}B and ^{23}Na ($I = \frac{3}{2}$), ^{27}Al and ^{67}Zn ($I = \frac{5}{2}$), ^{59}Co ($I = \frac{7}{2}$), and

^{87}Sr ($I = \frac{9}{2}$). Quadrupolar nuclei will be discussed in detail in Section 2.1.7.

For an ensemble of nuclei of spin $I > 0$ in an external magnetic field, the total Hamiltonian, $\hat{\mathcal{H}}_{\text{tot}}$, is given by:

$$\hat{\mathcal{H}}_{\text{tot}} = (\hat{\mathcal{H}}_Z + \hat{\mathcal{H}}_{rf}) + (\hat{\mathcal{H}}_{CS} + \hat{\mathcal{H}}_{DD} + \hat{\mathcal{H}}_J + \hat{\mathcal{H}}_{SR} + \hat{\mathcal{H}}_Q) \tag{2.1}$$

The subscripts on the right-hand side of equation (2.1) denote the various interactions experienced by the spin system under study: Z stands for Zeeman; rf for radiofrequency; CS for chemical shielding (nuclear magnetic shielding); DD for direct dipolar; J for indirect spin-spin; SR for spin-rotation; and Q for quadrupolar. The first two terms are known as external Hamiltonians because they represent the interactions of the spin system with: external static magnetic field as in the case of the Zeeman Hamiltonian, or with the external time-dependent radiofrequency (rf) fields generated by the probe coil in the case of the rf Hamiltonian. The last five terms are known as internal spin Hamiltonians because they represent various interactions within the sample itself.

2.1.1 The Zeeman Interaction

All nuclei with a non-zero spin possess a corresponding magnetic moment, $\boldsymbol{\mu}$, collinear with the vector describing the nuclear spin angular momentum, $\mathbf{P}$. The value of $\boldsymbol{\mu}$ is given by:

$$\vec{\boldsymbol{\mu}} = \gamma \vec{\mathbf{P}} \tag{2.2}$$

The constant of proportionality γ is called the magnetogyric (or gyromagnetic) ratio, a characteristic constant for each nucleus. It can be either positive or negative, corresponding to a $\vec{\boldsymbol{\mu}}$ that is either parallel or antiparallel to $\vec{\mathbf{P}}$. Moreover, the numerical value of γ gives

a crude idea of how sensitive a nucleus is in an NMR experiment. A large value of γ means that the nucleus is highly sensitive, and often can be readily observed in NMR.

Like all forms of angular momentum, the nuclear spin angular momentum is quantized in quantum mechanics. It is a vector quantity having both magnitude and direction. Its magnitude is given by:

$$|\vec{\mathbf{P}}| = \hbar\sqrt{I(I+1)} \tag{2.3}$$

where $\hbar = \frac{h}{2\pi}$, h being Planck's constant, and I is the nuclear spin quantum number (or simply the nuclear spin). In the absence of a magnetic field, all orientations are of equal energy. However, the presence of a magnetic field causes loss of this degeneracy. This splitting of spin energy levels by a magnetic field is known as the *Zeeman effect*.

Equation (2.2) can be expressed quantum-mechanically by replacing each vector with its corresponding operator:

$$\hat{\boldsymbol{\mu}} = \gamma\hbar\hat{\mathbf{I}} \tag{2.4}$$

where $\hat{\boldsymbol{\mu}}$ is the operator describing the magnetic moment, and $\hat{\mathbf{I}}$ is the operator describing the nuclear spin angular momentum $\vec{\mathbf{P}}$. The application of a static magnetic field, $\mathbf{B}_\mathrm{o}$, produces an interaction between the magnetic moment $\boldsymbol{\mu}$ of the nucleus and $\mathbf{B}_\mathrm{o}$. This interaction is called the *Zeeman interaction*. We have, therefore, a very simple Hamiltonian, called the *Zeeman Hamiltonian*:

$$\hat{\mathcal{H}}_Z = -\hat{\boldsymbol{\mu}} \cdot \hat{\mathbf{B}}_\mathrm{o} = -\gamma\hbar\hat{\mathbf{I}} \cdot \hat{\mathbf{B}}_\mathrm{o} \tag{2.5}$$

Here, $\hat{\boldsymbol{\mu}}$ is the nuclear magnetic moment operator, $\hat{\mathbf{B}}_\mathrm{o}$ is the magnetic field operator, and $\hat{\mathbf{I}}$ is the nuclear spin angular momentum operator. The applied static magnetic field is chosen, by convention, to lie along the z-axis of the laboratory frame [$\mathbf{B}_\mathrm{o} = (0, 0, B_\mathrm{o})$]. We

thus have:

$$\hat{\mathcal{H}}_Z = -\gamma\hbar B_{\mathrm{o}} \cdot \hat{\mathbf{I}}_{\mathrm{z}} \tag{2.6}$$

The eigenvalues of this Hamiltonian are simple, being only multiples ($-\gamma\hbar B_{\mathrm{o}}$) of the eigenvalues of $\hat{\mathbf{I}}_{\mathrm{z}}$, the operator of the z-component of the nuclear spin angular momentum. The eigenvalues of $\hat{\mathbf{I}}_{\mathrm{z}}$ can be determined by the following equation:

$$\hat{\mathbf{I}}_z \psi_{I,m} = m\psi_{I,m} \tag{2.7}$$

Using the bra-ket notation, this equation can be written as:

$$\hat{\mathbf{I}}_z |I, m\rangle = m|I, m\rangle \tag{2.8}$$

where m is the magnetic quantum number, having $(2I+1)$ values ranging from -I to +I :

$$m = \text{-}I \ , \ \text{-}I + 1 \ , \ \text{-}I + 2 \ , \ \ldots \ , \ I \ \text{-} \ 1 \ , \ I$$

The eigenvalues of the Zeeman Hamiltonian will be:

$$E_m = \langle I, m| - \gamma\hbar B_{\mathrm{o}} \hat{\mathbf{I}}_{\mathrm{z}} |I, m\rangle = -\gamma\hbar B_{\mathrm{o}} m \tag{2.9}$$

The $(2I+1)$ values of m thus correspond to different nuclear magnetic energy levels separated by the *Zeeman* splitting ($\gamma\hbar B_{\mathrm{o}}$). Hence, there is a constant separation, $\Delta E = \gamma\hbar B_{\mathrm{o}}$, between adjacent energy levels. The selection rule governing magnetic dipole transitions is $\Delta m = \pm 1$. Thus NMR transitions occur when we induce transitions between these nuclear spin energy levels by the use of electromagnetic radiation, and monitor the absorption. The magnitudes of the magnetogyric ratio and the static field $\mathbf{B}_{\mathrm{o}}$ are such as to require

radiofrequency (rf) radiation, with frequency ν_o satisfying the resonance condition

$$\Delta E = h\nu_o = \gamma\hbar B_o \tag{2.10}$$

Hence

$$\nu_o = \frac{\gamma B_o}{2\pi} \tag{2.11}$$

The above equation (2.11) gives the frequency ν_o in Hz of a pure Zeeman single-quantum transition. This frequency is called the *Larmor frequency*. It corresponds to the frequency needed to induce a Zeeman transition for a bare nucleus in a static field $\mathbf{B}_o$.

2.1.2 The Radiofrequency Interaction

In modern Fourier Transform (FT) NMR spectroscopy, radiofrequency (rf) pulses with a frequency ν_{rf} are usually used to create an oscillating time-dependent magnetic field, $\mathbf{B_{rf}(t)}$, in order to induce excitations of the spins in the studied system. This field is applied in a direction perpendicular to that of the z-direction of the laboratory frame, which is the direction of $\mathbf{B}_o$. When $\mathbf{B_{rf}(t)}$ is applied along the x-direction in the laboratory frame, for example, it will have the expression:[24]

$$\mathbf{B_{rf}} = 2B_1 \cos(\omega t + \phi)\mathbf{i} \tag{2.12}$$

where B_1 and ϕ are the amplitude and phase of the rf field respectively, and $\omega/2\pi$ is the carrier frequency. $\mathbf{i}$ is the x-axis unit vector in the laboratory frame. The interaction of the nuclear spin with this rf field is expressed by a Hamiltonian similar to that of the Zeeman interaction:

$$\hat{\mathcal{H}}_{rf} = -\gamma\hbar\hat{\mathbf{I}} \cdot \hat{\mathbf{B}}_{rf} \tag{2.13}$$

The oscillating *rf* field $\mathbf{B_{rf}(t)}$ can be viewed as a summation of two counter-rotating fields about $\mathbf{B}_o$: one at ω, and the other at $-\omega$:[20]

$$\mathbf{B_{rf}} = B_1[\cos(\omega t + \phi)\mathbf{i} + \sin(\omega t + \phi)\mathbf{j}] + B_1[\cos(\omega t + \phi)\mathbf{i} - \sin(\omega t + \phi)\mathbf{j}] \tag{2.14}$$

The *rf* Hamiltonian in the laboratory frame becomes:

$$\hat{\mathcal{H}}_{rf} = -\gamma\hbar B_1[\cos(\omega t + \phi)\hat{\mathbf{I}}_x + \sin(\omega t + \phi)\hat{\mathbf{I}}_y] - \gamma\hbar B_1[\cos(\omega t + \phi)\hat{\mathbf{I}}_x - \sin(\omega t + \phi)\hat{\mathbf{I}}_y] \tag{2.15}$$

The time evolution of this Hamiltonian is more easily observed by transforming the whole problem into a *rotating frame of reference*, which is rotating around $\mathbf{B}_o$ with a frequency ω. In such a frame, one of the two rotating components will be *on resonance* oscillating at $\omega - \omega_o \approx 0$ if $\omega \approx \omega_o$ (the first term in equation 2.15), and the other will be *off resonance* oscillating at $-\omega - \omega_o \approx -2\omega$ if $\omega \approx \omega_o$ (the second term). Thus, the *on-resonance* component will appear static (time-independent), and the *off-resonance* one will be time-dependent, which can be assumed to have a first-order time-average of zero, and therefore neglected.[27]

According to the preceding classical arguments, the *rf* Hamiltonian in the *rotating frame* during an on-resonance ($\omega \approx \omega_o$) pulse is then:

$$\begin{aligned} \hat{\mathcal{H}}_{rf} &= -\gamma\hbar B_1(\cos\phi\hat{\mathbf{I}}_x + \sin\phi\hat{\mathbf{I}}_y) \\ &= \hbar\omega_{rf}(\cos\phi\hat{\mathbf{I}}_x + \sin\phi\hat{\mathbf{I}}_y) \end{aligned} \tag{2.16}$$

where $\omega_{rf} = -\gamma B_1 = 2\pi\nu_{rf}$ is the *nutation angular frequency* (sometimes referred to as the *rf* amplitude).

Under the influence of $\mathbf{B_{rf}(t)}$, the net magnetization resulting from the nuclear magnetic

moments is flipped away from its equilibrium position by an angle $\theta_p = \omega_{rf}\tau_p = 2\pi\nu_{rf}\tau_p$. Hence, a 90° pulse is one that has a "flip" angle of $\theta_p = \pi/2$ radians, with a corresponding pulse duration of τ_p, which is normally of the order of microseconds.

These oscillating *rf* fields are used in FT-NMR experiments to allow the observation, and sometimes the suppression, of the effects of the following internal nuclear spin interactions.

2.1.3 The Nuclear Magnetic Shielding Interaction

The resonance condition, expressed by the Larmor frequency in equation (2.11), is not of great interest to NMR spectroscopists, in that it implies that all nuclei with the same value of γ are expected to produce a single peak in the NMR spectrum. That this need not be the case was demonstrated in 1950 when two well-separated ^{14}N NMR signals were observed for the two nitrogen nuclei in NH_4NO_3,[6] thus indicating that the precise signal frequency depends upon the chemical environment of the nucleus. In seeking a molecular interpretation of this phenomenon, it is necessary to realize that an external static magnetic field, $\mathbf{B}_o$, induces the electrons surrounding a nucleus to circulate, giving rise to a secondary field, $\mathbf{B_{ind}}$, at that nucleus, which may oppose $\mathbf{B}_o$, and hence shields (or screens) the nucleus from the influence of the field $\mathbf{B}_o$. $\mathbf{B}_o$ and $\mathbf{B_{ind}}$ need not be precisely antiparallel to each other, but are related by the second-rank tensor $\underline{\underline{\sigma}}$:

$$\mathbf{B_{ind}} = -\underline{\underline{\sigma}}\mathbf{B}_o \tag{2.17}$$

where $\underline{\underline{\sigma}}$ is the *nuclear magnetic shielding tensor* (or the *chemical shielding tensor*) particular to the chemical environment of the nucleus. The nucleus then experiences an *effective*

field given by:

$$\mathbf{B_{eff}} = \mathbf{B}_{\mathrm{o}} - \underline{\underline{\sigma}}\mathbf{B}_{\mathrm{o}} = \mathbf{B}_{\mathrm{o}}(\underline{\underline{1}} - \underline{\underline{\sigma}}) \tag{2.18}$$

and the resonance condition of equation (2.11) becomes:

$$\nu = \frac{\gamma B_{\mathrm{o}}(1-\sigma)}{2\pi} \tag{2.19}$$

where ν is the observed frequency of the nuclear Zeeman transition, and σ represents the absolute chemical shielding constant of this nucleus. The Hamiltonian of the chemical shielding interaction is written as :

$$\hat{\mathcal{H}}_{CS} = -\gamma\hbar\hat{\mathbf{I}} \cdot \underline{\underline{\sigma}} \cdot \hat{\mathbf{B}}_{\mathbf{o}} \tag{2.20}$$

and in terms of the Cartesian basis tensors, it has the following form in the laboratory frame:

$$\hat{\mathcal{H}}_{CS} = -\gamma\hbar \begin{pmatrix} \hat{\mathbf{I}}_x & \hat{\mathbf{I}}_y & \hat{\mathbf{I}}_z \end{pmatrix} \begin{pmatrix} \sigma_{xx} & \sigma_{xy} & \sigma_{xz} \\ \sigma_{yx} & \sigma_{yy} & \sigma_{yz} \\ \sigma_{zx} & \sigma_{zy} & \sigma_{zz} \end{pmatrix} \begin{pmatrix} B_x \\ B_y \\ B_z \end{pmatrix} \tag{2.21}$$

Now, since the applied field $\mathbf{B}_{\mathrm{o}}$ is along z-axis, this means that $\mathbf{B}_{\mathrm{o}} = (0, 0, B_o)$. The shielding Hamiltonian is simplified to:

$$\hat{\mathcal{H}}_{CS} = -\gamma\hbar B_{\mathrm{o}}(\sigma_{xz}\hat{\mathbf{I}}_x + \sigma_{yz}\hat{\mathbf{I}}_y + \sigma_{zz}\hat{\mathbf{I}}_z) \tag{2.22}$$

Moreover, the magnitude of chemical shielding is usually very small relative to that of the Zeeman interaction ($\hat{\mathcal{H}}_Z >> \hat{\mathcal{H}}_{CS}$), so it is considered a small perturbation of the spin system. According to the perturbation theory, the only terms of $\hat{\mathcal{H}}_{CS}$ which affect the energy levels of the spin system to first order are those terms which commute with $\hat{\mathcal{H}}_Z$.

Higher order effects may in principle occur, but they are not important in determining the NMR spectrum in this case of "high-field" approximation. This case is also called the "secular" approximation. Thus, since $\hat{\mathbf{I}}_x$ and $\hat{\mathbf{I}}_y$ do not commute with the $\hat{\mathcal{H}}_Z$, then the only non-vanishing term in equation (2.22) is the one containing $\hat{\mathbf{I}}_z$, and the shielding Hamiltonian will finally have the secular form in the laboratory frame:

$$\hat{\mathcal{H}}_{CS} = -\gamma\hbar B_{\mathrm{o}}\sigma_{zz}\hat{\mathbf{I}}_z \tag{2.23}$$

For comparison with experimental results, the chemical shielding tensor $\underline{\underline{\sigma}}$ is usually split into its symmetric ($\underline{\underline{\sigma}}^s$) and antisymmetric ($\underline{\underline{\sigma}}^a$) components:

$$\underline{\underline{\sigma}} = \underline{\underline{\sigma}}^s + \underline{\underline{\sigma}}^a \tag{2.24}$$

The elements of each component are derived from those of the main tensor $\underline{\underline{\sigma}}$:[33,34]

$$\begin{aligned}
\underline{\underline{\sigma}}^s &= \frac{1}{2}\left(\underline{\underline{\sigma}} + \underline{\underline{\sigma}}^T\right) \\
&= \begin{pmatrix} \sigma_{xx} & \frac{1}{2}(\sigma_{xy}+\sigma_{yx}) & \frac{1}{2}(\sigma_{xz}+\sigma_{zx}) \\ \frac{1}{2}(\sigma_{yx}+\sigma_{xy}) & \sigma_{yy} & \frac{1}{2}(\sigma_{yz}+\sigma_{zy}) \\ \frac{1}{2}(\sigma_{zx}+\sigma_{xz}) & \frac{1}{2}(\sigma_{zy}+\sigma_{yz}) & \sigma_{zz} \end{pmatrix}
\end{aligned} \tag{2.25}$$

, and

$$\begin{aligned}
\underline{\underline{\sigma}}^a &= \frac{1}{2}\left(\underline{\underline{\sigma}} - \underline{\underline{\sigma}}^T\right) \\
&= \begin{pmatrix} 0 & \frac{1}{2}(\sigma_{xy}-\sigma_{yx}) & \frac{1}{2}(\sigma_{xz}-\sigma_{zx}) \\ -\frac{1}{2}(\sigma_{xy}-\sigma_{yx}) & 0 & \frac{1}{2}(\sigma_{yz}-\sigma_{zy}) \\ -\frac{1}{2}(\sigma_{xz}-\sigma_{zx}) & -\frac{1}{2}(\sigma_{yz}-\sigma_{zy}) & 0 \end{pmatrix}
\end{aligned} \tag{2.26}$$

where $\underline{\underline{\sigma}}^T$ is the transpose of $\underline{\underline{\sigma}}$. Practically, the antisymmetric components ($\underline{\underline{\sigma}}^a$) do not affect NMR spectra to first order.[21] This is because it enters the Zeeman Hamiltonian only in terms that are second order in the magnetic field, and thus it is not normally observed in NMR. So, NMR spectra are only affected by the symmetric component ($\underline{\underline{\sigma}}^s$) of the shielding tensor. Henceforth, the symbol "σ" will be considered to refer exclusively to the symmetric component, which has only 6 independent elements. It is always possible to find an axis system, called the *principal axis system* (PAS), in which the symmetric part of the shielding tensor is diagonal, and its orientation with respect to the molecular axis system can be defined by three Euler angles. In the PAS, all the off-diagonal elements are zero. Thus, one can describe $\underline{\underline{\sigma}}$ in terms of its three principal components σ_{11}, σ_{22}, and σ_{33}:

$$\underline{\underline{\sigma}}^{LAB} = \begin{pmatrix} \sigma_{xx} & \sigma_{xy} & \sigma_{xz} \\ \sigma_{xy} & \sigma_{yy} & \sigma_{yz} \\ \sigma_{xz} & \sigma_{yz} & \sigma_{zz} \end{pmatrix} \longmapsto \underline{\underline{\sigma}}^{PAS} = \begin{pmatrix} \sigma_{11} & 0 & 0 \\ 0 & \sigma_{22} & 0 \\ 0 & 0 & \sigma_{33} \end{pmatrix} \tag{2.27}$$

where σ_{11} is the least shielded component, and σ_{33} is the most shielded one *i.e.*, $\sigma_{11} \leq \sigma_{22} \leq \sigma_{33}$. The average value is called the isotropic chemical shielding, σ_{iso}, and it is equivalent to one-third of the trace of the shielding tensor:

$$\sigma_{\text{iso}} = \frac{\sigma_{11} + \sigma_{22} + \sigma_{33}}{3} \tag{2.28}$$

The remarkable property of the magnetic shielding tensor is that the sum of its diagonal elements, and therefore its trace, does not, in principle, vanish. This is why the fast molecular tumbling in solution does not average out the chemical shielding to zero, but rather to its isotropic value (σ_{iso}). Several conventions are used in the literature to describe the principal values of the chemical shielding anisotropy. These conventions will

be discussed later in this section along with the chemical shift tensor.

The theoretical basis for chemical shielding were established by N. F. Ramsey in the early 1950s,[35] when he decomposed the shielding tensor into a diamagnetic term, σ^d, and a paramagnetic term, σ^p:

$$\boldsymbol{\sigma} = \boldsymbol{\sigma^d} + \boldsymbol{\sigma^p} \tag{2.29}$$

Perturbation theory was used to produce an expression for these two terms:

$$\sigma^d = \frac{\mu_0}{4\pi}\frac{e^2}{2m}\left\langle 0 \mid \sum_k \frac{\mathbf{r}_k \cdot \mathbf{r}_{kN}\hat{\mathbf{1}} \; - \; \mathbf{r}_k \cdot \mathbf{r}_{kN}}{r_{kN}^3} \mid 0 \right\rangle \tag{2.30}$$

$$\begin{aligned}\sigma^p = -\frac{\mu_0}{4\pi}\frac{e^2}{2m^2}\sum_{n\neq 0}({}^1E_n - E_0)^{-1}\Bigg[&\langle 0|\sum_k r_{kN}^{-3}\,\hat{l}_{kN}|n\rangle\langle n|\sum_k \hat{l}_k|0\rangle \\ &+ \langle 0|\sum_k \hat{l}_k|n\rangle\langle n|\sum_k r_{kN}^{-3}\,\hat{l}_{kN}|0\rangle\Bigg]\end{aligned} \tag{2.31}$$

Here, μ_0 is the permeability of free space, e is the electron charge, m is the electron mass, the sum over n indicates a sum over excited singlet states, the sum over k indicates a sum over all electrons, 0 and n indicate the ground and excited states electronic wave functions respectively, $\mathbf{r}_k$ is the position vector for electron k, $\hat{l}_k$ is the orbital angular momentum operator with respect to the origin of the vector potential of the external applied magnetic field (the so-called gauge origin), $\mathbf{r}_{kN}$ and $\hat{l}_{kN}$ are those same parameters but with respect to the observed nucleus N, E_0 and E_n are the respective ground and excited states energies.

Equation (2.30) shows that the diamagnetic term depends only on the ground electronic state of the molecule, and therefore can be easily calculated. Moreover, its dependence on r_{kN}^{-3} means that it is very local, resulting mainly from the core electrons surrounding the nucleus. On the other hand, the paramagnetic term is more difficult to calculate because it arises from the mixing of the ground state with singlet excited electronic states in the

presence of a magnetic field, as shown in equation (2.31). Also, the r_{kN}^{-3} in equation (2.31) indicates that only those electrons in the vicinity of the observed nucleus contribute the most in the calculation of σ^p. Two important remarks can be concluded from Ramsey's equations:

1. Both σ^d and σ^p depend on the origin of coordinates, and their calculated values will change with the relative position of the nucleus with respect to the chosen origin of coordinates. However, the total chemical shielding (σ) is invariant under such a change of the origin of coordinates. This is because, for exact and variational wave functions in a complete Hilbert space, the origin-dependent terms in σ^d and σ^p cancel each other. Unfortunately, this is not always feasible, because certain approximations used in calculating the excited state wave functions needed to evaluate σ^p will cause practical complications. This will result in imperfect cancellation of the origin-dependent terms in σ^d and σ^p.

2. For free atoms and ions, the electronic charge distribution around the nucleus is spherically symmetrical. This means that $\hat{l}_k$ is diagonal in its eigenstates. Moreover, it is natural to chose the gauge origin to be at the observed nucleus itself. In this case, σ^p becomes equal to zero, and the shielding is totally diamagnetic. Calculations of diamagnetic absolute shielding constants have been reported in the literature for many neutral free gaseous atoms using their ground-state wave functions.[36,37]

The Chemical Shift:

Quantum mechanical calculations of the NMR absolute chemical shielding components are performed on a scale relative to the corresponding bare nucleus (no electrons surrounding it), which is not a practical reference. In practice, NMR experiments do not measure the

chemical shielding directly; instead, the common practice is to measure the chemical shift as the difference between the resonance frequency of the sample and that of a standard reference, usually a compound containing the observed nucleus that gives a sharp NMR signal independent of temperature, concentration, *etc.* The chemical shift, δ, given in field-independent units of parts per million (*ppm*), is defined as:[34]

$$\delta_{\text{sample}} = \frac{\nu_{\text{sample}} - \nu_{\text{ref}}}{\nu_{\text{ref}}} \times 10^6 \tag{2.32}$$

where ν_{sample} is the resonance frequency of the sample of interest, and ν_{ref} is that of the reference compound. The absolute shielding, σ, also in *ppm*, is defined as:[34]

$$\sigma_{\text{sample}} = \frac{\nu_{\text{nucl}} - \nu_{\text{sample}}}{\nu_{\text{nucl}}} \times 10^6 \tag{2.33}$$

where ν_{nucl} is the resonance frequency of the bare nucleus. Combining these two equations, it is straightforward to verify that:

$$\begin{aligned} \delta_{\text{sample}} &= \frac{\sigma_{\text{ref}} - \sigma_{\text{sample}}}{1 - \sigma_{\text{ref}}} \\ &\approx \sigma_{\text{ref}} - \sigma_{\text{sample}} \end{aligned} \tag{2.34}$$

The approximation $|\sigma_{\text{ref}}| << 1$ is usually justified because shielding constants for light atoms are very small compared to unity (they are on the order of 10^{-6}). Moreover, the shift scale is reversed compared to the shielding scale. This means that nuclei more shielded than the reference have lower chemical shifts, and those less shielded have larger chemical shifts. Similar to chemical shielding, the chemical shift is a second-rank tensor, represented by a 3×3 matrix, whose principal components in its (PAS) system are arranged as $\delta_{11} \geq \delta_{22} \geq \delta_{33}$ following automatically the order of the chemical shielding components. Thus

δ_{11} corresponds to the least shielded (highest-frequency) component, while δ_{33} corresponds to the most shielded (lowest-frequency) component.

In the literature, several different conventions are used to describe completely the magnitude of the chemical shift tensors extracted from experimental spectra. This discrepancy has created much confusion, especially whenever comparison between reported results of the same spin system is needed. Also, another problem arises concerning whether the reported parameters are those of the chemical shift or of the chemical shielding tensors, in addition to the imperfect conversion between the two according to equation (2.34), especially for heavy atoms where there is a large difference between the frequency of the spectrometer and that of the reference compound. The three most common conventions are defined below:

1. The standard convention in which the three principal components δ_{11}, δ_{22}, and δ_{33} are reported, after being defined such that: $\delta_{11} \geq \delta_{22} \geq \delta_{33}$.

2. The Haeberlen-Mehring-Duncan convention,[21,22,38] in which different combinations of the principal components are used: the average (isotropic) value (δ_{iso}), the chemical shift anisotropy (δ_{aniso}) describing the largest separation from the centre of gravity, and the asymmetry parameter (η_{cs}) describing the deviation from axial symmetry, with $0 \leq \eta_{\text{cs}} \leq 1$:

$$\delta_{\text{iso}} = \frac{1}{3}(\delta_{11} + \delta_{22} + \delta_{33})$$

if $|\delta_{11} - \delta_{\text{iso}}| \geq |\delta_{33} - \delta_{\text{iso}}|$, then

$$\begin{aligned} \delta_{\text{aniso}} &= \delta_{11} - \frac{\delta_{22} + \delta_{33}}{2} = \frac{3}{2}(\, \delta_{11} - \delta_{\text{iso}} \,) \\ \eta_{\text{cs}} &= \frac{\delta_{22} - \delta_{33}}{\delta_{11} - \delta_{\text{iso}}} \end{aligned}$$

if $|\delta_{11} - \delta_{\text{iso}}| \leq |\delta_{33} - \delta_{\text{iso}}|$, then

$$\begin{aligned} \delta_{\text{aniso}} &= \frac{\delta_{11} + \delta_{22}}{2} - \delta_{33} = \frac{3}{2}(\, \delta_{\text{iso}} - \delta_{33}\,) \\ \eta_{\text{cs}} &= \frac{\delta_{22} - \delta_{11}}{\delta_{33} - \delta_{\text{iso}}} \end{aligned} \tag{2.35}$$

3. The Herzfeld-Berger convention,[39] also referred to as the "Maryland convention". This convention was proposed by the participants in the NATO Advanced Research Workshop (ARW) on NMR shielding that was held in July 1992 at the University of Maryland, College Park. According to this convention, the the chemical shift or shielding tensor can be described by three parameters:[34]

   - The isotropic value which is the average value of the principal components, and corresponds to the centre of gravity of the line shape:

     $$\sigma_{\text{iso}} = \frac{\sigma_{11} + \sigma_{22} + \sigma_{33}}{3}$$

     and

     $$\delta_{\text{iso}} = \frac{\delta_{11} + \delta_{22} + \delta_{33}}{3}$$

   - The span (Ω) which is a measure of the breadth of the powder pattern resulting due to the presence of chemical shift anisotropy, and is always positive:

     $$\Omega = \sigma_{33} - \sigma_{11} \approx \delta_{11} - \delta_{33} > 0 \tag{2.36}$$

   - The skew (κ), which is a measure of the symmetry of the shielding and shift tensors, and $-1 \leq \kappa \leq +1$. If $\kappa = +1$ or -1, the chemical shift tensor is axially

symmetric, with δ_{33} and δ_{11} as the unique component respectively.

$$\begin{aligned} \kappa &= \frac{3(\sigma_{\rm iso} - \sigma_{22})}{\sigma_{33} - \sigma_{11}} = \frac{3(\sigma_{\rm iso} - \sigma_{22})}{\Omega} \\ &= \frac{3(\delta_{22} - \delta_{\rm iso})}{(\delta_{11} - \delta_{33})} = \frac{3(\delta_{22} - \delta_{\rm iso})}{\Omega} \end{aligned} \tag{2.37}$$

The span and the skew are defined such that they are the same for the chemical shielding and the chemical shift tensors. This convention will therefore be adopted in this thesis, as well as for other reasons including its lower ambiguity compared to other conventions, and for the wide acceptance it has gained within the solid-state NMR community over the past two decades.

Effect of Magnetic Chemical Shift Anisotropy on Spectra of Powder Solids:

Due to rapid and random tumbling of the molecules in solution, only the isotropic value of the chemical shift, $\delta_{\rm iso}$, is observed. In solids, however, the molecules are generally not free to rotate isotropically. In a single crystal, the shielding of a certain nucleus will depend on the particular orientation of the crystal with respect to the external magnetic field. In a polycrystalline powder sample, the presence of a vast number of randomly oriented crystallites ensures that all of the possible molecular orientations with respect to the applied field $\mathbf{B}_{\rm o}$ are sampled. The corresponding frequency of each molecular orientation contributes to the observed signal. This leads to a characteristically broad static spectrum, which is referred to as *powder pattern* line shape. The frequency observed for a nucleus in a static solid-state NMR experiment of a powder sample dominated by Zeeman and

chemical shielding interactions is given by:[40]

$$\begin{aligned} \nu(\theta,\phi) &= \nu_{\mathrm{z}} + \nu_{\mathrm{cs}} \\ &= \nu_{\mathrm{o}}[1 - (\sigma_{11}\sin^2\theta\cos^2\phi + \sigma_{22}\sin^2\theta\sin^2\phi + \sigma_{33}\cos^2\theta)] \end{aligned} \tag{2.38}$$

where θ and ϕ are the polar and azimuthal angles orienting the applied magnetic field direction in the PAS of chemical shielding tensor, as shown in Figure 2.1. In accordance with experiments, it is more convenient to express equation (2.38) in terms of the experimentally measured parameter, the chemical shift, rather than shielding. Since chemical shielding decreases and chemical shift increases with increasing frequency, then equation (2.38) becomes, in terms of the principal components of the chemical shift tensor:

$$\nu(\theta,\phi) = \nu_{\mathrm{o}}(\delta_{11}\sin^2\theta\cos^2\phi + \delta_{22}\sin^2\theta\sin^2\phi + \delta_{33}\cos^2\theta) \tag{2.39}$$

The spectra of powder samples, under the sole influence of chemical shift anisotropy, show characteristic line shapes, with limits marked by inflection points at δ_{11} and δ_{33}, and a discontinuity at δ_{22}. These patterns are illustrated collectively in Figures 2.2 and 2.3. Figure 2.2 shows 3 characteristic powder pattern line shapes, each depicting a different symmetry level at the nuclear site. Figure 2.3 shows the change of the powder pattern line shape as a function of the skew (κ).

Despite the impression that chemical shift anisotropy complicates the spectra of powder solids due to line broadening, its presence is very helpful in yielding more detailed information about the electronic structure around the nucleus of interest. This information can be used to study the geometry of bonds around that nucleus, and helps in determining molecular geometry, either through correlations between experimental chemical shift parameters and known bond lengths and angles, or through quantum mechanical calcu-

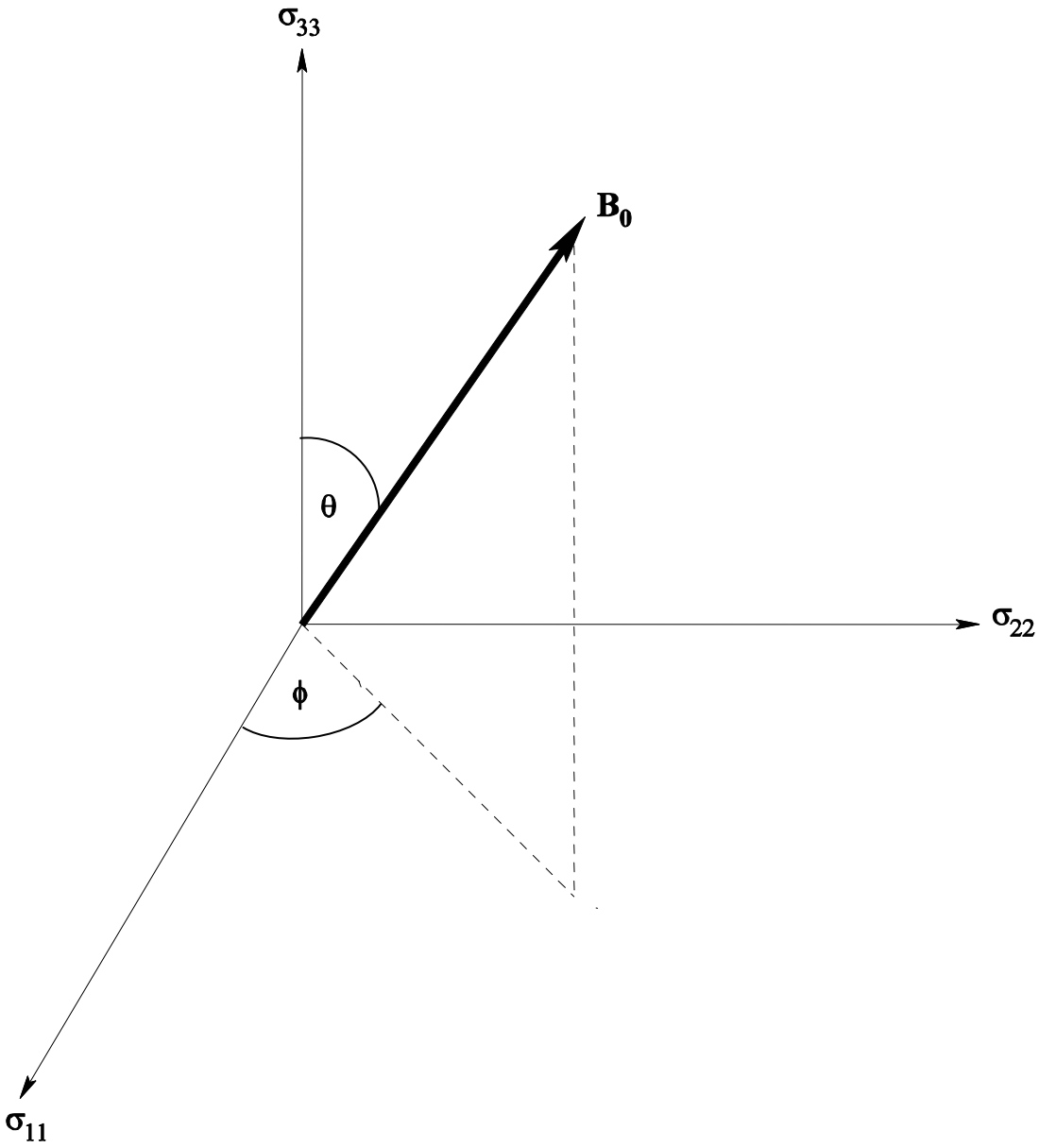

Figure 2.1: The orientation of $\mathbf{B}_o$ in the PAS of the chemical shielding tensor.

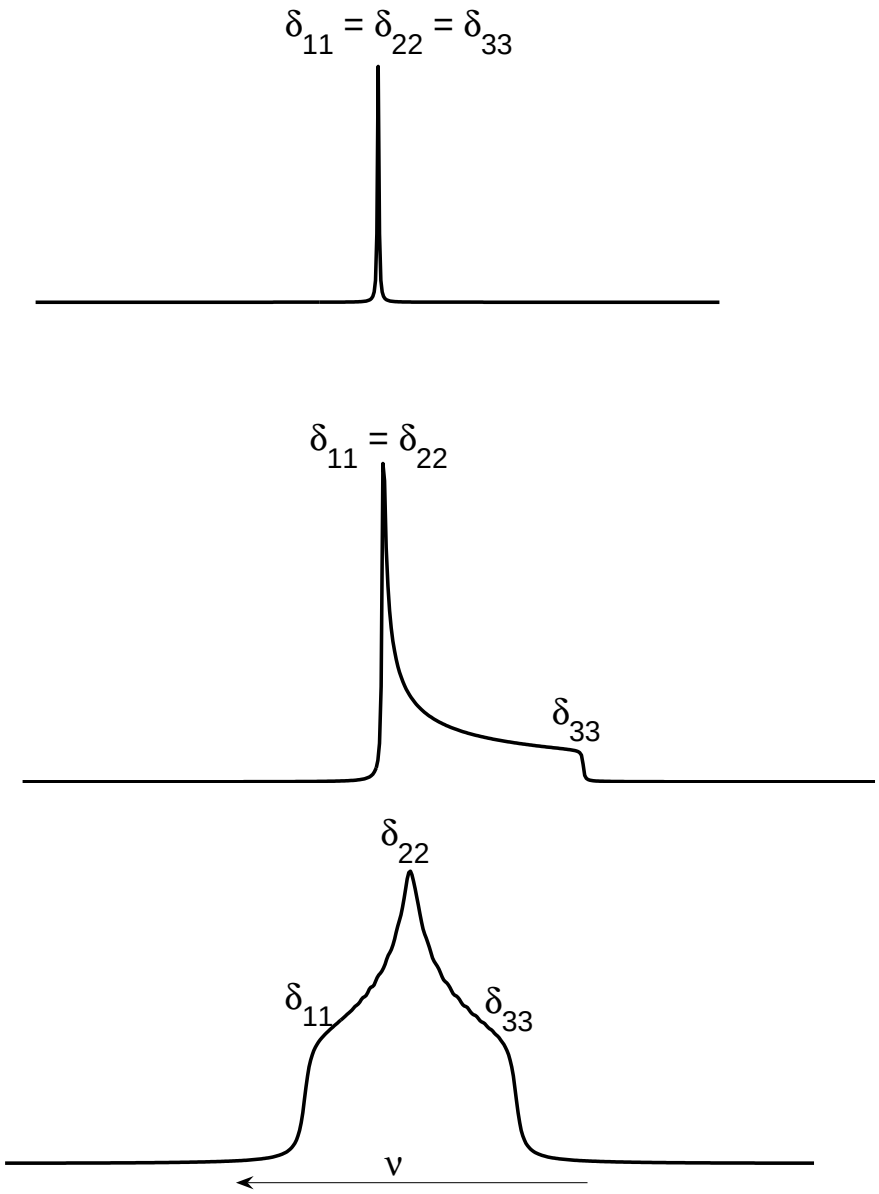

Figure 2.2: Calculated powder pattern line shapes due to chemical shift anisotropy: cubic symmetry (top), axial symmetry (middle), and non-axial symmetry(bottom).

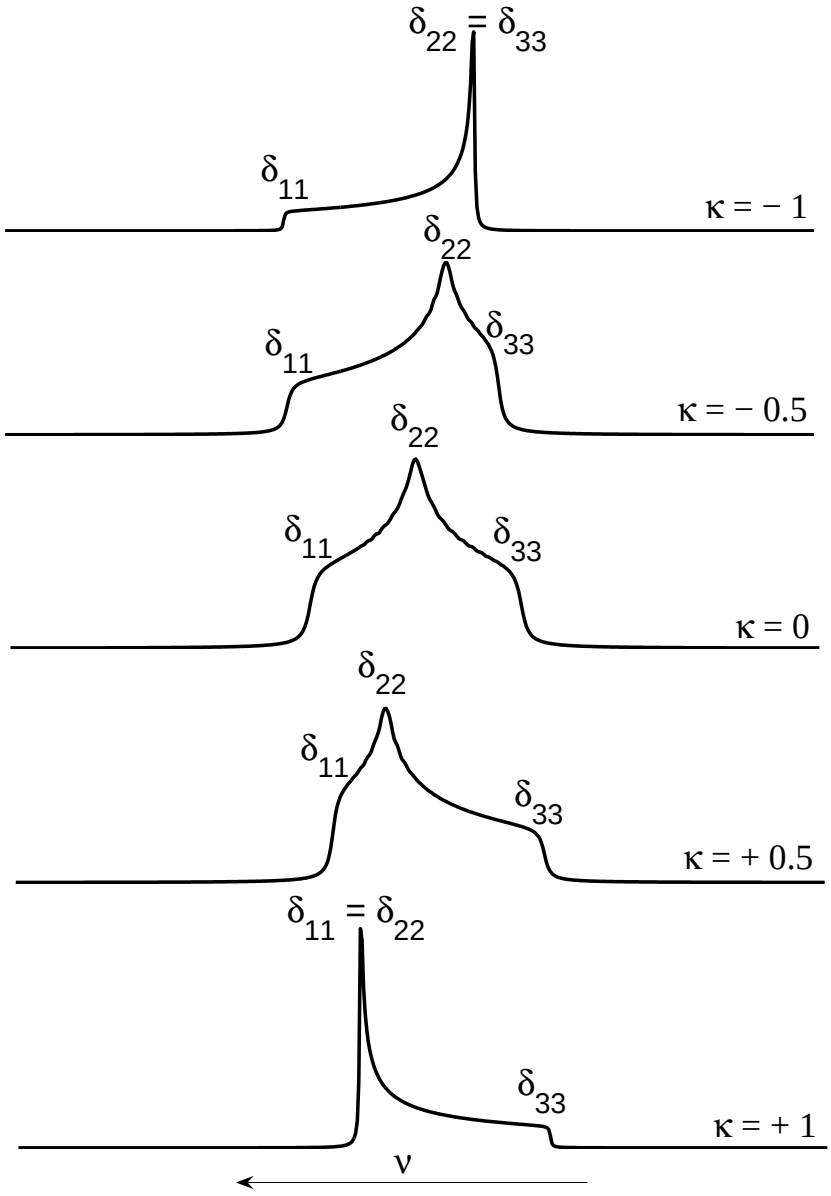

Figure 2.3: Dependence of powder pattern line shapes, due to chemical shift anisotropy, on the skew (κ). The top and bottom spectra correspond to axially-symmetric chemical shift tensors. The remaining spectra arise from non-axial symmetric tensors.

lations of the shielding tensor and then comparing these with the experimental chemical shift parameters.

2.1.4 The Direct Dipolar Interaction

A nucleus with non-zero spin quantum number possesses a magnetic dipole moment. This dipole acts as a bar magnet, generating a magnetic field in its vicinity. Two nuclear spins, therefore, can interact similar to two bar magnets; each spin experiences the local magnetic field of the other spin. This through-space coupling between two magnetic dipoles (nuclear spins) is known as the *direct dipolar* coupling, and it is sometimes referred to as a *dipole-dipole* or simply *dipolar* coupling. This dipolar interaction depends inversely on the distance between the two nuclear spins, and also on the molecular orientation. Classically, the interaction energy between two point magnetic dipoles $\boldsymbol{\mu_1}$ and $\boldsymbol{\mu_2}$ separated by a distance r is:[20]

$$E = \frac{\mu_0}{4\pi r^3}\left[(\vec{\boldsymbol{\mu}}_{\mathbf{1}} \cdot\ \vec{\boldsymbol{\mu}}_{\mathbf{2}}) - \frac{3(\vec{\boldsymbol{\mu}}_{\mathbf{1}} \cdot\ \vec{\mathbf{r}})(\vec{\boldsymbol{\mu}}_{\mathbf{2}} \cdot\ \vec{\mathbf{r}})}{r^2}\right] \tag{2.40}$$

Quantum mechanically, replacing each of the vectors by its corresponding "vector operator" gives the Hamiltonian for the direct dipolar interaction between two spins I and S separated by a distance r:[19,20,24]

$$\hat{\mathcal{H}}_{DD} = \frac{\mu_0}{4\pi}\frac{\gamma_I\gamma_S\hbar^2}{r^3}\left[\hat{\mathbf{I}}\cdot\hat{\mathbf{S}} - 3\frac{(\hat{\mathbf{I}}\cdot\hat{\mathbf{r}})(\hat{\mathbf{S}}\cdot\hat{\mathbf{r}})}{r^2}\right] \tag{2.41}$$

I and S can be like or unlike spins. $\hat{\mathbf{r}}$ is the operator of the I–S internuclear vector. The above dipolar Hamiltonian may be expressed in the Cartesian tensor form:

$$\hat{\mathcal{H}}_{DD} = \hat{\mathbf{I}} \cdot \underline{\underline{\mathcal{D}}} \cdot \hat{\mathbf{S}} = hR_{DD} \begin{pmatrix} \hat{\mathbf{I}}_x & \hat{\mathbf{I}}_y & \hat{\mathbf{I}}_z \end{pmatrix} \begin{pmatrix} 1 - \frac{3x^2}{r^2} & \frac{-3xy}{r^2} & \frac{-3xz}{r^2} \\ \frac{-3xy}{r^2} & 1 - \frac{3y^2}{r^2} & \frac{-3yz}{r^2} \\ \frac{-3xz}{r^2} & \frac{-3yz}{r^2} & 1 - \frac{3z^2}{r^2} \end{pmatrix} \begin{pmatrix} \hat{\mathbf{S}}_x \\ \hat{\mathbf{S}}_y \\ \hat{\mathbf{S}}_z \end{pmatrix} \quad (2.42)$$

where h is Planck's constant. R_{DD} is the *dipolar coupling constant*, expressed in Hz as

$$R_{DD} = \frac{\mu_0}{4\pi} \frac{\gamma_I \gamma_S}{r^3} \frac{\hbar}{2\pi} \quad (2.43)$$

A "short-cut" numerical expression for R_{DD} can be derived if the numerical values of the fundamental physical constants are substituted in the above equation ($\mu_0 = 4\pi \times 10^{-7}\, N \cdot A^{-2}$; $\hbar = 1.054571628 \times 10^{-34}\, J \cdot s \cdot rad^{-1}$).[41] When γ_I and γ_S are expressed in units of $10^7\, rad \cdot T^{-1} \cdot s^{-1}$, and r in Å, then the following numerical expression is obtained for R_{DD}, in units of Hertz (Hz):

$$R_{DD} = \frac{167.84030\, \gamma_I \gamma_S}{r^3} \quad (2.44)$$

where $167.84\,030\, T^2 \cdot s \cdot \text{Å}^3 \cdot rad^{-2}$ is the conversion factor.

$\underline{\underline{\mathcal{D}}}$ is the *direct dipolar coupling tensor*:

$$\underline{\underline{\mathcal{D}}} = R_{DD} \begin{pmatrix} 1 - \frac{3x^2}{r^2} & \frac{-3xy}{r^2} & \frac{-3xz}{r^2} \\ \frac{-3xy}{r^2} & 1 - \frac{3y^2}{r^2} & \frac{-3yz}{r^2} \\ \frac{-3xz}{r^2} & \frac{-3yz}{r^2} & 1 - \frac{3z^2}{r^2} \end{pmatrix} \quad (2.45)$$

$\underline{\underline{\mathcal{D}}}$ is a symmetric and traceless tensor, where in its PAS it is given by:

$$\underline{\underline{\mathcal{D}}} = R_{DD} \begin{pmatrix} 1 & 0 & 0 \\ 0 & 1 & 0 \\ 0 & 0 & -2 \end{pmatrix} \tag{2.46}$$

Therefore, dipolar coupling has no directly observable effect in solution NMR because it is averaged to zero due to rapid molecular tumbling. Unlike the chemical shielding interaction, where more than one parameter is needed for complete description of the shielding tensor, the value of the dipolar coupling constant R_{DD} is sufficient to describe the dipolar coupling completely, since it is both traceless and axially symmetric.

The Hamiltonian for the dipolar interaction (equation 2.41) can be also expressed in spherical polar coordinates, and the result is a sum of six terms called the "dipolar alphabet":[19,20]

$$\hat{\mathcal{H}}_{DD} = hR_{DD}\left[A + B + C + D + E + F\right] \tag{2.47}$$

where:

$$\begin{aligned} A &= -\hat{\mathbf{I}}_z\hat{\mathbf{S}}_z(3\cos^2\theta - 1) \\ B &= \frac{1}{4}[\hat{\mathbf{I}}_+\hat{\mathbf{S}}_- + \hat{\mathbf{I}}_-\hat{\mathbf{S}}_+](3\cos^2\theta - 1) \\ C &= -\frac{3}{2}[\hat{\mathbf{I}}_z\hat{\mathbf{S}}_+ + \hat{\mathbf{I}}_+\hat{\mathbf{S}}_z]\sin\theta\cos\theta\, e^{-i\phi} \\ D &= -\frac{3}{2}[\hat{\mathbf{I}}_z\hat{\mathbf{S}}_- + \hat{\mathbf{I}}_-\hat{\mathbf{S}}_z]\sin\theta\cos\theta\, e^{i\phi} \\ E &= -\frac{3}{4}\hat{\mathbf{I}}_+\hat{\mathbf{S}}_+\sin^2\theta\, e^{-2i\phi} \\ F &= -\frac{3}{4}\hat{\mathbf{I}}_-\hat{\mathbf{S}}_-\sin^2\theta\, e^{2i\phi} \end{aligned} \tag{2.48}$$

$\hat{\mathbf{I}}_+$, $\hat{\mathbf{S}}_+$, $\hat{\mathbf{I}}_-$, and $\hat{\mathbf{S}}_-$ are the ladder operators, each acting on its corresponding spin:

$$\begin{aligned} \hat{\mathbf{I}}_\pm &= \hat{\mathbf{I}}_x \pm i\hat{\mathbf{I}}_y \\ \hat{\mathbf{S}}_\pm &= \hat{\mathbf{S}}_x \pm i\hat{\mathbf{S}}_y \end{aligned} \tag{2.49}$$

θ and ϕ are the polar angles orienting the I–S internuclear vector along the applied magnetic field direction, which is the laboratory z-axis (shown in Figure 2.4).

As in the case of chemical shielding, in the high-field approximation, where $\hat{\mathcal{H}}_{DD}$ is considered as a small perturbation to $\hat{\mathcal{H}}_Z$ ($\hat{\mathcal{H}}_Z >> \hat{\mathcal{H}}_{DD}$), only terms A and B of equation (2.47) survive because they both commute with $\hat{\mathcal{H}}_Z$. In this case, $\hat{\mathcal{H}}_{DD}$ becomes

$$\hat{\mathcal{H}}_{DD} = -R_{DD}(3\cos^2\theta - 1)\left[\hat{\mathbf{I}}_z\hat{\mathbf{S}}_z - \frac{1}{4}(\hat{\mathbf{I}}_+\hat{\mathbf{S}}_- + \hat{\mathbf{I}}_-\hat{\mathbf{S}}_+)\right] \tag{2.50}$$

At this point, one should distinguish the extent of dipolar coupling between homonuclear spin pairs (spins I and S are the same species, which is conventionally named A_2 spin system) and its extent between heteronuclear spin pairs (I and S are different, an AX spin system). In the case of heteronuclear dipolar coupling, term B also vanishes. This is because term B contains the so-called "flip-flop" operator ($\hat{\mathbf{I}}_+\hat{\mathbf{S}}_- + \hat{\mathbf{I}}_-\hat{\mathbf{S}}_+$). This operator corresponds to an exchange of magnetization between the two spins. It is not energy-conserving for unlike spins, and therefore it must be dropped from the Hamiltonian as it does not commute with $\hat{\mathcal{H}}_Z$. In homonuclear dipolar coupling, both terms A and B remain, and contribute to the NMR spectrum. This situation gives rise to two different equations concerning the resonance frequencies of dipolar-coupled spins. For two isolated spin-1/2

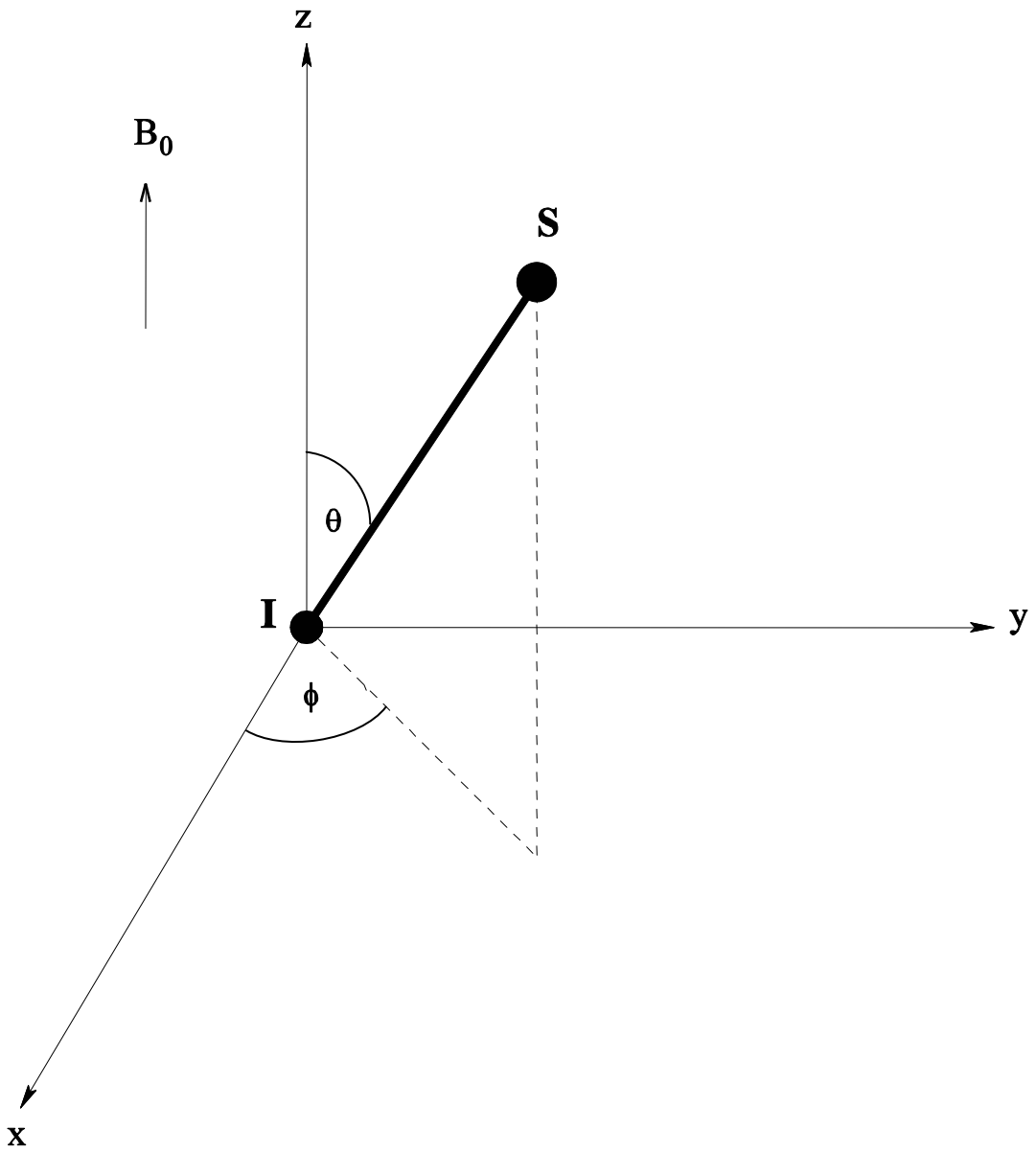

Figure 2.4: Orientation of the I-S internuclear vector with respect to the applied magnetic field $\mathbf{B}_o$, which is along z-axis in the laboratory frame.

nuclei, the resonance frequency of one nuclear spin in presence of dipolar coupling is:[42]

$$\nu = \nu_o \pm \frac{1}{2} R_{DD}(3\cos^2\theta - 1) \quad \text{in heteronuclear dipolar coupling} \tag{2.51}$$

$$\nu = \nu_o \pm \frac{3}{4} R_{DD}(3\cos^2\theta - 1) \quad \text{in homonuclear dipolar coupling} \tag{2.52}$$

In a powder sample in which the crystallites are present in all possible orientations, and in the absence of other anisotropic interactions, dipolar coupling produces a spectrum such as that shown in Figure 2.5. This distinct spectrum is termed the "Pake doublet".[43] The intensity of the pattern at a certain frequency depends on the number of crystallites that resonate at that frequency. As shown in both parts of Figure 2.5 for a powdered solid, the singularities of the Pake pattern correspond to crystallites for which the I–S internuclear vector is perpendicular to the external magnetic field ($\theta = 90°$). The two outer shoulders correspond to the relatively few crystallites for which the I–S internuclear vector lies parallel to the external field ($\theta = 0°$). For an AX spin system, the splitting between the singularities is R_{DD}, and between the outer shoulders is $2R_{DD}$. For an A_2 spin system, the splitting between the singularities is $3R_{DD}/2$ and between the outer shoulders is $3R_{DD}$.

As mentioned earlier in this section, knowledge of the value of the dipolar coupling constant R_{DD} is sufficient to describe completely the direct dipolar interaction. The r^{-3} dependence in the expression of R_{DD} (equation 2.43) makes this dipolar coupling a sensitive measure of the internuclear distances, and hence the structural geometry of the molecule. Direct structural determination of molecules which do not form single crystals but exist only as amorphous solids is not possible with the usual diffraction techniques. A number of NMR techniques have been developed, however, which deal with such situations. All these techniques rely on measurement of the direct dipolar interaction between two nuclei.

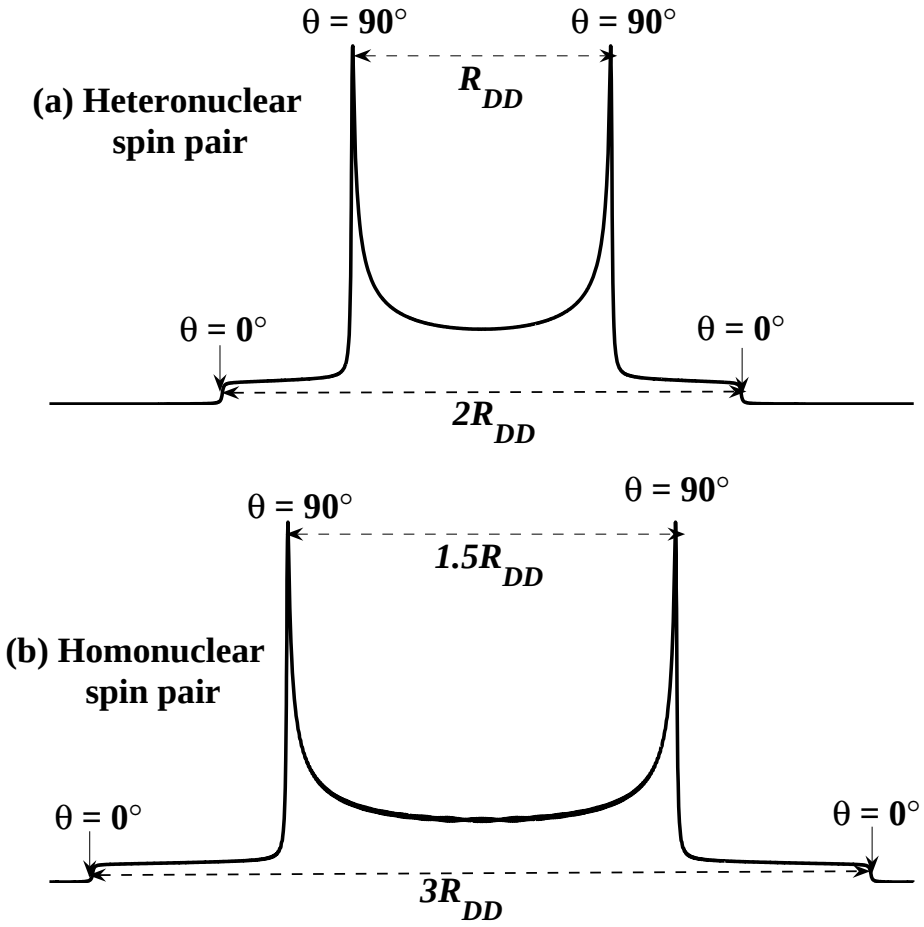

Figure 2.5: "Pake doublet" resulting from two dipolar-coupled spin-$\frac{1}{2}$ nuclei: **(a)** For a heteronuclear spin pair, the splitting between the singularities is R_{DD} and between the outer shoulders is $2R_{DD}$.**(b)** For a magnetically equivalent homonuclear spin pair, the splitting between the singularities is $3R_{DD}/2$ and between the outer shoulders is $3R_{DD}$. Both spectra were simulated using $R_{DD} = 4.0$ kHz.

2.1.5 The Indirect Spin-Spin Interaction

In addition to the direct dipolar interaction between nuclei described above, which is averaged to zero in liquids, there exists another mechanism by which magnetic nuclei can interact together, the spin-spin coupling commonly observed in solution NMR. Unlike the through-space interaction between two nuclear spins, this coupling between the two spins angular momenta is transmitted indirectly via the intervening electrons. It is called *indirect*, to indicate the role of the bonding electrons in the coupling mechanism. This coupling is sometimes termed as *indirect spin-spin coupling*, *J-coupling*, or *scalar coupling*. In a molecule, the mechanism of this through-bond coupling, as opposed to the through-space coupling, is as follows: the spin angular momentum of a magnetic nucleus is coupled to the spin angular momentum of one of the core electrons. This electron spin then couples to other electron spins in the molecule which, in turn, can couple to other magnetic nuclei in the molecule. The Hamiltonian that describes the indirect spin-spin coupling is given by:[23,25]

$$\hat{\mathcal{H}}_J = h\hat{\mathbf{I}} \cdot \underline{\underline{\mathcal{J}}} \cdot \hat{\mathbf{S}} \tag{2.53}$$

where $\hat{\mathbf{I}}$ and $\hat{\mathbf{S}}$ are the nuclear spin angular momentum operators of spins I and S respectively, and $\underline{\underline{\mathcal{J}}}$ is the indirect spin-spin coupling tensor. This tensor describes the change of the indirect spin-spin coupling with the orientation of the molecule in the magnetic field. It is represented by a 3 x 3 real matrix which, in general, has 9 independent elements:

$$\underline{\underline{\mathcal{J}}} = \begin{pmatrix} J_{xx} & J_{xy} & J_{xz} \\ J_{yx} & J_{yy} & J_{yz} \\ J_{zx} & J_{zy} & J_{zz} \end{pmatrix} \tag{2.54}$$

Analogous to the chemical shielding tensor, $\underline{\underline{\mathcal{J}}}$ can de decomposed into symmetric and antisymmetric parts. However, the antisymmetric part does not affect the NMR line shape to first order, and therefore is often ignored. The symmetric part is given, in its PAS, by:

$$\underline{\underline{\mathcal{J}}} = \begin{pmatrix} J_{11} & 0 & 0 \\ 0 & J_{22} & 0 \\ 0 & 0 & J_{33} \end{pmatrix} \tag{2.55}$$

The J-coupling tensor is described by it isotropic value J_{iso}, its anisotropy ΔJ, and its asymmetry parameter η_J:[44]

$$\begin{aligned} J_{\text{iso}} &= \frac{1}{3}(J_{11} + J_{22} + J_{33}) \\ \Delta J &= J_{33} - \frac{J_{11} + J_{22}}{2} \\ \eta_J &= |\frac{J_{22} - J_{11}}{J_{33} - J_{\text{iso}}}| \end{aligned} \tag{2.56}$$

with the 3 principal components defined and ordered as: $|J_{33} - J_{\text{iso}}| \geq |J_{11} - J_{\text{iso}}| \geq |J_{22} - J_{\text{iso}}|$. In liquids, only the isotropic value (J_{iso}) is observed due to motional averaging, and is denoted simply by J, the *indirect spin-spin coupling constant* or the *scalar coupling constant*. This coupling constant is usually written as ${}^{n}J_{XY}$, where n is the number of covalent bonds that separate nuclei X and Y.

As mentioned above, it has generally been assumed that the J-coupling tensor is axially symmetric. However, this assumption has been shown recently not to be perfectly valid when high level multiconfigurational self-consistent field (MCSCF) calculations have indicated that the magnitudes of the components of the antisymmetric part of the J-coupling tensor are comparable to those of its symmetric portion.[45] However, based on the absence of any observed experimental influence of the antisymmetric part,[44] this assumption can

still hold to a certain extent. In the case of axially symmetric $\underline{\underline{\mathcal{J}}}$, we can separate the isotropic and anisotropic terms as follows:[44,46]

$$\begin{aligned} \underline{\underline{\mathcal{J}}} &= \begin{pmatrix} J_\perp & 0 & 0 \\ 0 & J_\perp & 0 \\ 0 & 0 & J_\parallel \end{pmatrix} \\ &= J_{\text{iso}}\underline{\underline{\mathbf{1}}} - \frac{\Delta J}{3}\begin{pmatrix} 1 & 0 & 0 \\ 0 & 1 & 0 \\ 0 & 0 & -2 \end{pmatrix} \end{aligned} \tag{2.57}$$

where $J_\perp$ is the component perpendicular to the internuclear vector and $J_\parallel$ is the one parallel to it; $\underline{\underline{\mathbf{1}}}$ is the unit tensor; $\Delta J = J_\parallel - J_\perp$.

Comparing equations (2.46) and (2.57), one can easily conclude that the anisotropic term of $\underline{\underline{\mathcal{J}}}$ has an identical mathematical form to the direct dipolar coupling. Consequently, it is practically impossible to distinguish experimentally between the direct dipolar interaction and the anisotropy of the indirect spin-spin interaction. Therefore, what one observes via experiment is an *effective dipolar coupling constant* (if ΔJ is not zero), R_{eff}:[47]

$$R_{eff} = R_{DD} - \frac{\Delta J}{3} = R_{DD} - \frac{J_\parallel - J_\perp}{3} \tag{2.58}$$

2.1.6 The Spin-Rotation Interaction

As a molecule rotates, the circulating electrons and nuclei generate a small electric current, which in turn induces a local magnetic field at the nucleus, which may couple with the magnetic moment of the nucleus. This coupling of the nuclear spin angular momentum with the molecule's rotational angular momentum is called the spin-rotation interaction,

and is given by the following Hamiltonian:[22]

$$\hat{\mathcal{H}}_{SR} = h\hat{\mathbf{I}} \cdot \underline{\underline{\mathcal{C}}} \cdot \hat{\mathbf{J}} \tag{2.59}$$

where $\hat{\mathbf{I}}$ is the spin angular momentum operator of the nucleus, $\hat{\mathbf{J}}$ is the rotational angular momentum of the molecule, and $\underline{\underline{\mathcal{C}}}$ is the spin-rotation tensor relating the two angular momenta.

The spin-rotation interaction has no significance in solid-state NMR due to the restricted molecular rotation in solids. In liquids, it averages to zero but contributes to the spin-lattice relaxation mechanism. It is generally important in the microwave spectroscopy of gases.[25]

2.1.7 The Quadrupolar Interaction

This interaction is important for those nuclei that have a spin quantum number $I \geq 1$. Such nuclei comprise about 75% of the NMR active nuclear isotopes in the periodic table, and they are called *quadrupolar nuclei*. Moreover, the vast majority of quadrupolar nuclei possess half-integer spins ($I = \frac{3}{2}, \frac{5}{2}, \frac{7}{2}, \frac{9}{2}$), and therefore are more of interest to solid-state NMR spectroscopists than the integer quadrupolar spins. In fact, ^2H ($I = 1$) is the only integer quadrupolar nucleus that has been studied extensively, especially in molecular dynamics. In addition to the magnetic dipole moment possessed by spin-$\frac{1}{2}$ nuclei, quadrupolar nuclei possess an electric quadrupole moment, Q, due to the non-spherical charge distribution within the nucleus. The quadrupole moment is usually expressed as eQ, where e is the elementary charge. When the charge distribution of the nucleus has the shape of a prolate spheroid, eQ is positive; if it has the shape of an oblate spheroid, eQ is negative (Figure 2.6). Q is an intrinsic property of the nucleus, and it is always the same

regardless of the nuclear environment. It is measured in units of *barn* ($10^{-28}\,m^2$).

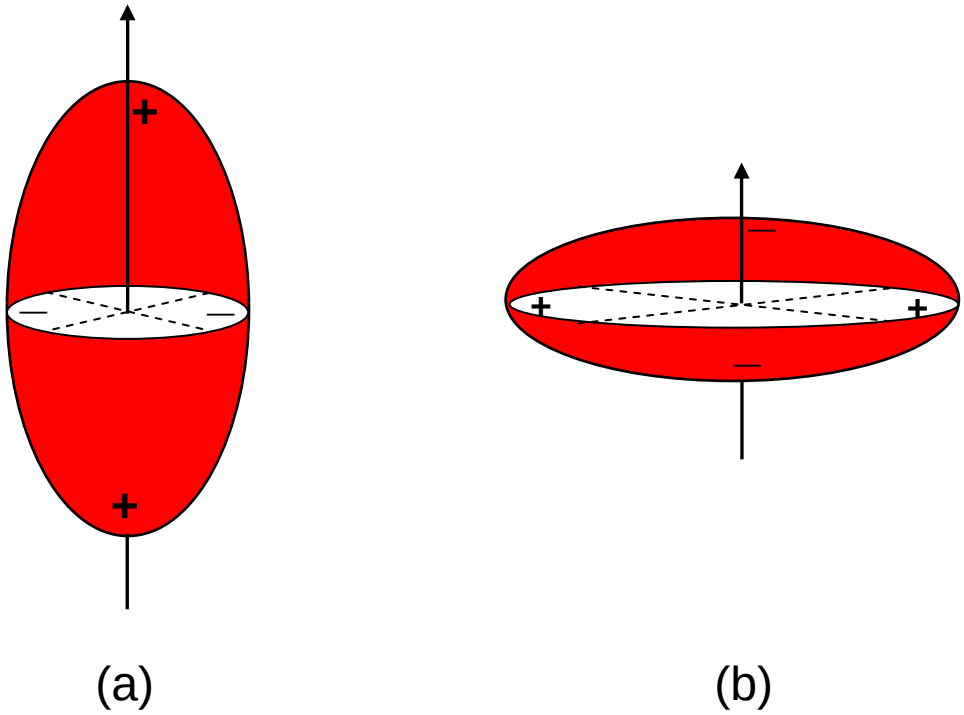

Figure 2.6: Charge distribution for a quadrupolar nucleus with respect to the nuclear spin axis: **(a)** prolate, $eQ > 0$. **(b)** oblate, $eQ < 0$.

The electric quadrupole moment of a nucleus, eQ, interacts with any gradients of the electric field at the nucleus. Such gradients are generated naturally by other charges (electrons and nuclei) in the vicinity of the nucleus of interest. The best way to understand this interaction is to study the classical physical description of the interaction between the charge density of a nucleus, $\rho(\mathbf{r})$, and the electrostatic potential, $V(\mathbf{r})$, generated by surrounding charges at the point $\mathbf{r}$ inside that nucleus. The classical discussion of the quadrupolar interaction presented herein is based mainly on the monographs of Slichter,[20]

and Cohen and Reif.[28] The interaction energy E_Q is[20]

$$E_Q = \int \rho(\mathbf{r}) V(\mathbf{r})\, d\tau \tag{2.60}$$

The potential $V(\mathbf{r})$ is then expanded in a power series about the centre of mass of the nucleus:

$$V(r) = V(0) + \sum_j j \left(\frac{\partial V}{\partial j}\right)\Big|_{\mathbf{r}=0} + \frac{1}{2!}\sum_{j,k} jk \left(\frac{\partial^2 V}{\partial j \partial k}\right)\Big|_{\mathbf{r}=0} + \cdots \tag{2.61}$$

where $\{j,k\} \subset \{x,y,z\}$ are the Cartesian components of $\mathbf{r}$ relative to the specified origin. Thus, equation (2.60) becomes

$$\begin{aligned} E_Q = V(0) \int \rho(\mathbf{r})\, d\tau + \sum_j \frac{\partial V}{\partial j}\Big|_{\mathbf{r}=0} \int j\rho(\mathbf{r})\, d\tau \\ + \frac{1}{2!}\sum_{j,k} \frac{\partial^2 V}{\partial j \partial k}\Big|_{\mathbf{r}=0} \int jk\, \rho(\mathbf{r})\, d\tau + \cdots \end{aligned} \tag{2.62}$$

The first term in this equation is simply the electrostatic energy of the nucleus taken as point charge (an electric monopole); it is of no direct significance in NMR. The second term involves the electric dipole moment of the nucleus, the $\int j\rho(\mathbf{r})\, d\tau$ term; it vanishes by virtue of its odd parity.[20,28] The third term is the only term of interest as far as NMR is concerned. It is called the electric quadrupole term. It shows the electrostatic energy of a non-spherical nuclear charge distribution varying with its orientation relative to the orientation of the field gradient. By making use of these simplifications and ignoring higher-order terms in the potential expansion, the interaction energy E_Q will be expressed as

$$E_Q = \frac{1}{2}\sum_{j,k} Q'_{jk} V_{jk} \tag{2.63}$$

Here $Q'_{jk} = \int jk\, \rho(\mathbf{r})\, d\tau$ are the elements of the electric quadrupole moment tensor of the

nucleus, a symmetric second-rank tensor; $V_{jk} = \frac{\partial^2 V}{\partial j \partial k}\big|_{\mathbf{r}=0}$ are the elements of the electric field gradient (EFG) tensor, a symmetric and traceless second-rank tensor. It is always possible to find a coordinate system in which the EFG tensor, $\underline{\underline{\mathbf{V}}}$, is diagonalized. Thus, in its PAS, $\underline{\underline{\mathbf{V}}}$ is represented by three principal components V_{XX}, V_{YY} and V_{ZZ}, where $|V_{ZZ}| \geq |V_{YY}| \geq |V_{XX}|$ with $V_{XX} + V_{YY} + V_{ZZ} = 0$ due to the Laplace equation. This tensor is fully described by two parameters:[20,23,27]

$$\begin{aligned} eq &= V_{ZZ} \\ \eta_{\mathrm{Q}} &= \frac{V_{XX} - V_{YY}}{V_{ZZ}} \end{aligned} \tag{2.64}$$

where eq indicates the size of the EFG tensor, and η_{Q} is its *asymmetry parameter*, a measure of the deviation of the EFG from axial symmetry. η_{Q} can have any value between 0 and 1, with $\eta_{\mathrm{Q}} = 0$ corresponding to an axially symmetric EFG tensor. The orientation of the EFG tensor with respect to the molecular or crystalline axes is defined by three Euler angles (α, β, and γ). Equation (2.63) can be simplified further by defining a simpler quadrupole moment tensor which renders it not only symmetric, but also traceless. This can be done by simply defining[28]

$$Q_{jk} = 3Q'_{jk} - \delta_{jk} \sum_{i=x,y,z} Q'_{ii} \tag{2.65}$$

where δ_{jk} is the Kronecker delta ($\delta_{jk} = 1$ if $j = k$, and 0 if $j \neq k$). Substituting equation (2.65) into equation (2.63) gives

$$E_Q = \frac{1}{6} \sum_{j,k} \left(Q_{jk} V_{jk} + \delta_{jk} V_{jk} \sum_{i=x,y,z} Q'_{ii} \right) \tag{2.66}$$

The second term to the right is zero due to Laplace equation applied to $\underline{\underline{\mathbf{V}}}$. This will leave

us with

$$E_Q = \frac{1}{6}\sum_{j,k} Q_{jk}V_{jk} \tag{2.67}$$

To obtain the Hamiltonian operator we have to find a quantum mechanical expression for the quadrupole moment operator. It is, therefore, necessary to express the quadrupole operator, $\hat{Q}_{jk}$, in terms of spin angular momentum operators. According to the Wigner-Eckart theorem, the corresponding matrix elements of all irreducible, traceless, symmetric tensors are proportional to each other.[48] Applying this to equation (2.65), we can construct the matrix elements of the $\hat{Q}_{jk}$ operator from the components of the spin angular momentum operator $\hat{\mathbf{I}}$, which are well-known:[28]

$$\langle Im'|\hat{Q}_{jk}|Im\rangle = C\langle Im'|\frac{3}{2}\big(\hat{\mathbf{I}}_j\hat{\mathbf{I}}_k + \hat{\mathbf{I}}_k\hat{\mathbf{I}}_j\big) - \delta_{jk}\hat{\mathbf{I}}^2|Im\rangle \tag{2.68}$$

where C is a constant independent of m, m', j, and k. It can be obtained by the evaluation of the matrix element $\langle Im'|\hat{Q}_{jk}|Im\rangle$ with $j = k = z$ and $m = m' = I$:

$$\begin{aligned} C &= \frac{\langle II|\hat{Q}_{zz}|II\rangle}{\langle II|3\hat{\mathbf{I}}_z^2 - \hat{\mathbf{I}}^2|II\rangle} \\ &= \frac{eQ}{I(2I-1)} \end{aligned} \tag{2.69}$$

with $eQ = \langle II|\hat{Q}_{zz}|II\rangle$ being the nuclear electric quadrupole moment. According to this equality, Q is defined as the expectation value of $\hat{Q}_{zz}$ in the state where the z-component of $\mathbf{I}$ is a maximum, in units of the charge e.[28] The quadrupolar electrostatic energy in equation (2.67) thus becomes the NMR spin Hamiltonian, $\hat{\mathcal{H}}_Q$, given by

$$\hat{\mathcal{H}}_Q = \frac{eQ}{6I(2I-1)}\sum_{j,k} V_{jk}\left[\frac{3}{2}\big(\hat{\mathbf{I}}_j\hat{\mathbf{I}}_k + \hat{\mathbf{I}}_k\hat{\mathbf{I}}_j\big) - \delta_{jk}\hat{\mathbf{I}}^2\right] \tag{2.70}$$

where $\{j,k\} \subset \{x,y,z\}$ represents any arbitrary reference frame. The fact that the EFG tensor, $\underline{\underline{\mathbf{V}}}$, is symmetric and traceless in any reference frame leads to a more compact form of the quadrupolar Hamiltonian if one expands the above equation in terms of the Cartesian elements of $\underline{\underline{\mathbf{V}}}$ and $\hat{\mathbf{I}}$:[22,23,26,27]

$$\hat{\mathcal{H}}_Q = \frac{eQ}{2I(2I-1)} \hat{\mathbf{I}} \cdot \underline{\underline{\mathbf{V}}} \cdot \hat{\mathbf{I}} \tag{2.71}$$

Moreover, transforming the whole problem into the PAS of the EFG tensor and using the fact that the EFG tensor is traceless ($V_{XX} + V_{YY} + V_{ZZ} = 0$), the quadrupolar Hamiltonian becomes:[19]

$$\hat{\mathcal{H}}_Q = \frac{e^2qQ}{4I(2I-1)} \left[3\hat{\mathbf{I}}_Z^2 - \hat{\mathbf{I}}^2 + \frac{1}{2}\eta_{\mathrm{Q}}(\hat{\mathbf{I}}_+^2 + \hat{\mathbf{I}}_-^2) \right] \tag{2.72}$$

It is important to note that many authors use the order $|V_{ZZ}| \geq |V_{XX}| \geq |V_{YY}|$ instead of $|V_{ZZ}| \geq |V_{YY}| \geq |V_{XX}|$. In such case, η_{Q} will be defined as:[21,44]

$$\eta_{\mathrm{Q}} = \frac{V_{YY} - V_{XX}}{V_{ZZ}} \tag{2.73}$$

As a result, the sign of the term containing η_{Q} in equation (2.72) will be reversed. This change in the sign of the η_{Q}-containing terms also applies to the formulae of equations (2.78)–(2.81) that are derived from the quadrupolar Hamiltonian of equation (2.72), as discussed below.

As mentioned earlier, the EFG tensor is traceless. This means that the quadrupolar interaction vanishes in solution due to the rapid tumbling of molecules. In solids, the strength of the quadrupolar interaction experienced by a nucleus in a molecule is given by the *quadrupolar coupling constant* (QCC), which is the product of the nuclear quadrupole

moment, eQ, and the largest component of the EFG tensor, $eq = V_{ZZ}$. In the literature, QCC is often denoted by C_{Q} (sometimes the symbol χ is used instead), and is given (in Hz) by:

$$C_{\mathrm{Q}} = \chi = \frac{e^2qQ}{h} = \frac{eQ \cdot V_{ZZ}}{h} \tag{2.74}$$

where eQ is the quadrupole moment, eq is the magnitude of the EFG, e is the elementary charge, and h is Planck's constant. Alternatively, some authors use the quadrupolar frequency ν_{Q} (in Hz) to describe the actual strength of the quadrupolar interaction. Unfortunately, several different definitions for ν_{Q} are found in the literature, which makes the discussions related to ν_{Q} quite confusing. Herein, the definition given by Abragam is adapted:[19]

$$\nu_{\mathrm{Q}} = \frac{3C_{\mathrm{Q}}}{2I(2I-1)} \tag{2.75}$$

In NMR experiments of quadrupolar nuclei in solids, the measurable quadrupolar parameters are the quadrupolar coupling constant (C_{Q}) and the quadrupolar asymmetry parameter (η_{Q}). Also, the orientation of the quadrupolar interaction is reported as three Euler angles with respect to the molecular frame or with respect to another tensorial quantity of the system, often the chemical shielding tensor.

In accordance with the trend followed recently in the literature, the three principal components of the EFG tensor will be labeled and ordered as follows in the remaining parts of this thesis: $|V_{33}| \geq |V_{22}| \geq |V_{11}|$, with $V_{11} + V_{22} + V_{33} = 0$. Hence, the quadrupolar parameters C_{Q} and η_{Q} will be defined as:

$$C_{\mathrm{Q}} = \frac{e^2qQ}{h} = \frac{eQ \cdot V_{33}}{h} \tag{2.76}$$

$$\eta_{\mathrm{Q}} = \frac{V_{11} - V_{22}}{V_{33}} \tag{2.77}$$

The quadrupolar interaction in solids is often much stronger than either the chemical shielding or dipolar interactions in low symmetry sites, and consequently dominates the spectra of quadrupolar nuclei in solids. Most often, the quadrupolar frequency (ν_{Q}) is on the order of MHz. This gives rise to very broad and featureless line shapes, whose widths may reach to hundreds of kHz. To explain the qudrupolar effects on the NMR spectra of solids, it is not sufficient to refer to first-order perturbation theory as in the case of the shielding and dipolar interactions, whose magnitudes are very small compared to that of the quadrupolar interaction. This is because first-order quadrupolar corrections are only considered when the quadrupolar frequency, ν_{Q}, is much smaller than the Larmor frequency, ν_{o}. But, when ν_{Q} becomes in the range of one-tenth of ν_{o}, second-order, or even higher-order, quadrupolar corrections must be considered.[49] According to the perturbation theory, the first-order energy corrections to the pure Zeeman states due to quadrupolar coupling are:[19,27]

$$E_m^{(1)} = \frac{hC_{\mathrm{Q}}}{8I(2I-1)}[3m^2 - I(I+1)][3\cos^2\theta - 1 + \eta_{\mathrm{Q}}\sin^2\theta\cos 2\phi] \tag{2.78}$$

Hence, the corresponding frequencies of the allowed transitions $m \leftrightarrow m-1$ for the first-order quadrupolar interaction are given by:

$$\nu_{m\leftrightarrow m-1}^{(1)} = -\frac{\nu_{\mathrm{Q}}}{2}\left(m - \frac{1}{2}\right)\left[3\cos^2\theta - 1 + \eta_{\mathrm{Q}}\sin^2\theta\cos 2\phi\right] \tag{2.79}$$

The angles θ and ϕ are the polar angles orienting the applied magnetic field, $\mathbf{B}_{\mathrm{o}}$, in the PAS of the EFG tensor, in a way similar to the chemical shielding tensor (Figure 2.1). Several points can be deduced from the above equation to explain the effect of first-order quadrupolar interaction on the spectra of quadrupolar nuclei:

- The spectrum of a quadrupolar nucleus splits, to first order, into $2I$ lines that are equally spaced by $\frac{1}{2}\nu_{\mathrm{Q}}(3\cos^2\theta - 1 + \eta_{\mathrm{Q}}\sin^2\theta\cos 2\phi)$.

- For half-integer-spin quadrupolar nuclei, equation (2.79) indicates that the central transition (CT: $m = \frac{1}{2} \leftrightarrow m = \frac{-1}{2}$) is not perturbed by the quadrupolar interaction to first order, whereas the satellite transitions ($m \leftrightarrow m-1, m \neq \frac{1}{2}$) are affected.

- The first-order quadrupolar effect is totally anisotropic *i.e.*, it is totally orientation-dependent, and it has no isotropic contribution. This means that this orientation-dependence will only cause broadenings of the individual transitions, while the centre of gravity of each transition will not be shifted from the isotropic chemical shift, to first order.

The broadenings of the satellite transitions due to first-order quadrupolar interaction are usually too large to be detected in standard NMR experiments of powder samples. Thus, only the central transition of quadrupolar nuclei is usually observed in solid state NMR of powder samples. Its line shape is totally dominated by second-order quadrupolar interaction, as outlined below. The second-order quadrupolar corrections to the Zeeman energy states are:[27]

$$E_m^{(2)} = -h\left[\frac{C_{\mathrm{Q}}}{4I(2I-1)}\right]^2\left(\frac{m}{\nu_{\mathrm{o}}}\right)\Big(A + B + C\Big) \tag{2.80}$$

where:

$$
\begin{aligned}
A &= -\frac{1}{5}\left[I(I+1)-3m^2\right](3+\eta_{\mathrm{Q}}^2) \\
B &= \frac{1}{28}\left[8I(I+1)-12m^2-3\right]\left[(\eta_{\mathrm{Q}}^2-3)(3\cos^2\theta-1)+6\eta_{\mathrm{Q}}\sin^2\theta\cos 2\phi\right] \\
C &= \frac{1}{8}\left[18I(I+1)-34m^2-5\right]\left[\frac{1}{140}(18+\eta_{\mathrm{Q}}^2)(35\cos^4\theta-30\cos^2\theta+3)\right. \\
&\quad \left.+\frac{3}{7}\eta_{\mathrm{Q}}\sin^2\theta(7\cos^2\theta-1)\cos 2\phi+\frac{1}{4}\eta_{\mathrm{Q}}^2\sin^4\theta\cos 4\phi\right]
\end{aligned}
$$

and the corresponding second-order broadening of the central transition (CT: $m=\frac{1}{2}\leftrightarrow m=\frac{-1}{2}$) for half-integer-spin quadrupolar nuclei will be:[31]

$$
\nu_{1/2\leftrightarrow -1/2}^{(2)} = -\frac{\nu_{\mathrm{Q}}^2}{6\nu_{\mathrm{o}}}\left[I(I+1)-\frac{3}{4}\right]\left[E(\phi)\cos^4\theta+F(\phi)\cos^2\theta+G(\phi)\right] \tag{2.81}
$$

where:

$$
\begin{aligned}
E(\phi) &= -\frac{27}{8}+\frac{9}{4}\eta_{\mathrm{Q}}\cos 2\phi-\frac{3}{8}\eta_{\mathrm{Q}}^2\cos^2 2\phi \\
F(\phi) &= \frac{30}{8}-\frac{1}{2}\eta_{\mathrm{Q}}^2-2\eta_{\mathrm{Q}}\cos 2\phi+\frac{3}{4}\eta_{\mathrm{Q}}^2\cos^2 2\phi \\
G(\phi) &= -\frac{3}{8}+\frac{1}{3}\eta_{\mathrm{Q}}^2-\frac{1}{4}\eta_{\mathrm{Q}}\cos 2\phi-\frac{3}{8}\eta_{\mathrm{Q}}^2\cos^2 2\phi
\end{aligned}
$$

Obviously, equations (2.80) and (2.81) are simplified greatly in the case of axially symmetric EFG tensor ($\eta_{\mathrm{Q}}=0$). Abragam[19] gives elegant expressions for the second-order energy correction and the second-order CT frequency shift in such case:

$$
E_m^{(2)} = -h\left(\frac{\nu_{\mathrm{Q}}^2}{12\nu_{\mathrm{o}}}\right)m\left[\frac{3}{2}\mu^2(1-\mu^2)(8m^2-4a+1)+\frac{3}{8}(1-\mu^2)^2(-2m^2+2a-1)\right] \tag{2.82}
$$

and

$$\nu^{(2)}_{1/2\leftrightarrow -1/2} = -\frac{\nu_{\mathrm{Q}}^2}{16\nu_{\mathrm{o}}}\left(a-\frac{3}{4}\right)(1-\mu^2)(9\mu^2-1) \tag{2.83}$$

where $a = I(I+1)$ and $\mu = \cos\theta$

It is clear from equation (2.80) that second-order quadrupolar interaction depends directly on C_{Q}^2, and inversely on the Larmor frequency (the $1/\nu_{\mathrm{o}}$ term), which means that this interaction is only important for large quadrupolar coupling constants and/or low magnetic fields. As the strength of the magnetic field increases, the effect of the second-order quadrupolar interaction becomes less and less visible in the spectrum, which results in a high resolution spectrum. Another close examination of this equation reveals that the first term (A) has no orientation dependence, thus it is an isotropic term. This is very important as it means that in addition to the second-order quadrupolar broadening, there is an isotropic second-order quadrupolar shift, which shifts the centre of gravity of an allowed transition, $\nu^{CG}_{m\leftrightarrow m-1}$, relative to the isotropic chemical shift by:[50,51]

$$\begin{aligned}\nu^{CG}_{m\leftrightarrow m-1} - \nu_{\mathrm{iso}} &= -\frac{3C_{\mathrm{Q}}^2}{40\nu_{\mathrm{o}}}\left[\frac{I(I+1)-9m(m-1)-3}{I^2(2I-1)^2}\right]\left(1+\frac{1}{3}\eta_{\mathrm{Q}}^2\right)\\ &= -\frac{\nu_{\mathrm{Q}}^2}{30\nu_{\mathrm{o}}}\left[I(I+1)-9m(m-1)-3\right]\left(1+\frac{1}{3}\eta_{\mathrm{Q}}^2\right)\end{aligned} \tag{2.84}$$

For the central transition, the isotropic second-order quadrupolar shift will be :

$$\begin{aligned}\nu^{CG}_{1/2\leftrightarrow -1/2} - \nu_{\mathrm{iso}} &= -\frac{3}{40\nu_{\mathrm{o}}}\left[\frac{C_{\mathrm{Q}}}{I(2I-1)}\right]^2\left[I(I+1)-\frac{3}{4}\right]\left(1+\frac{1}{3}\eta_{\mathrm{Q}}^2\right)\\ &= -\frac{\nu_{\mathrm{Q}}^2}{30\nu_{\mathrm{o}}}\left[I(I+1)-\frac{3}{4}\right]\left(1+\frac{1}{3}\eta_{\mathrm{Q}}^2\right)\end{aligned} \tag{2.85}$$

This means that the experimental (observed) chemical shift for the centre of gravity of the central transition, and even any satellite transition, of a powdered sample is the isotropic

chemical shift *plus* the isotropic second-order quadrupolar shift.

Using equations (2.78) and (2.82) for the first- and second-order energy corrections, one can sketch an energy level diagram for a quadrupolar spin in a magnetic field, as shown schematically in Figure 2.7 for a spin-$\frac{5}{2}$ nucleus. The case of axial symmetry ($\eta_{\mathrm{Q}} = 0$) is considered for simplicity, and the units of the first- and second-order broadenings are chosen for convenience.

Second-order quadrupolar effects are clearly manifested in the central-transition line shape of half-integer-spin quadrupolar nuclei in powder solids. They produce, not only a frequency shift of the line, but also a large broadening. The breadth of the central transition (CT) line shape for a stationary powder solid due to second-order quadrupolar interaction is given by:[51]

$$\begin{aligned} \Delta\nu_{CT} &= \left[\frac{3C_{\mathrm{Q}}}{2I(2I-1)}\right]^2 \left[\frac{I(I+1)-\frac{3}{4}}{144}\right] \frac{\left(25+22\eta_{\mathrm{Q}}+\eta_{\mathrm{Q}}^2\right)}{\nu_{\mathrm{o}}} \\ &= \frac{\nu_{\mathrm{Q}}^2}{\nu_{\mathrm{o}}} \left[\frac{I(I+1)-\frac{3}{4}}{144}\right] \left(25+22\eta_{\mathrm{Q}}+\eta_{\mathrm{Q}}^2\right) \end{aligned} \tag{2.86}$$

In fact, it is the second-order quadrupolar interaction that gives rise to some characteristic and useful CT line shapes in solid-state NMR of half-integer-spin quadrupolar nuclei. Typical NMR line shapes of static powder samples are presented in Figure 2.8. In principle, these line shapes are very useful as they contain information about the dominant interactions, namely the quadrupolar and the chemical shift interactions in most cases. The parameters that define the magnitudes of both interactions can be extracted from these line shapes, as well as the relative orientations of the the chemical shielding (CS) and the EFG tensors. These include eight parameters: δ_{iso}, Ω, κ for the chemical shift tensor; C_{Q} and η_{Q} for the EFG tensor; and three Euler angles (α, β, γ) for their relative orientation(*vide*

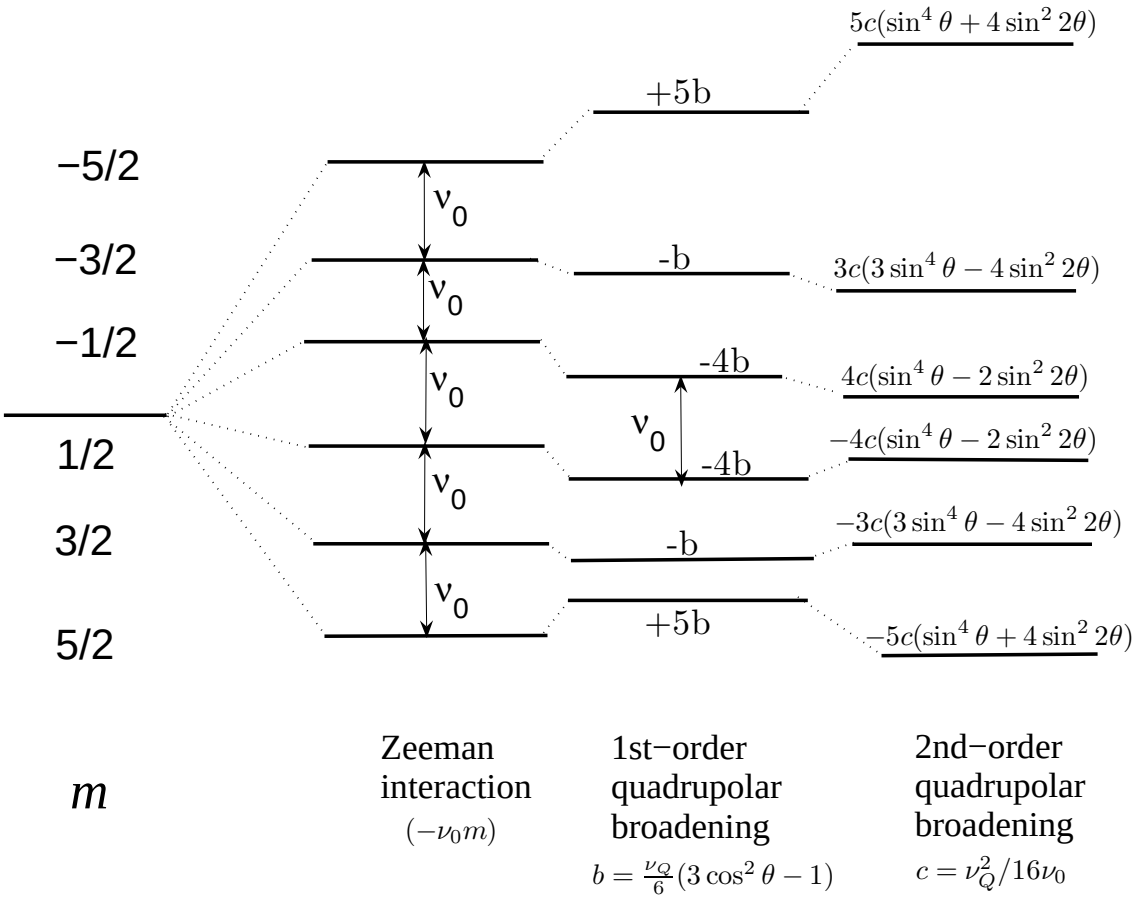

Figure 2.7: Energy level diagram, in frequency units, of a spin-$\frac{5}{2}$ nucleus in a magnetic field, showing the effects of first- and second-order quadrupolar broadenings on the Zeeman levels. For simplicity, $\eta_{\mathrm{Q}} = 0$ is considered. The first- and second-order broadenings are calculated *via* equations (2.78) and (2.82), respectively. The central transition ($\frac{1}{2} \leftrightarrow -\frac{1}{2}$), though not perturbed to first order, is significantly broadened by second-order quadrupolar interaction. Satellite transitions are perturbed to both orders. The scheme is adapted from Reference 52.

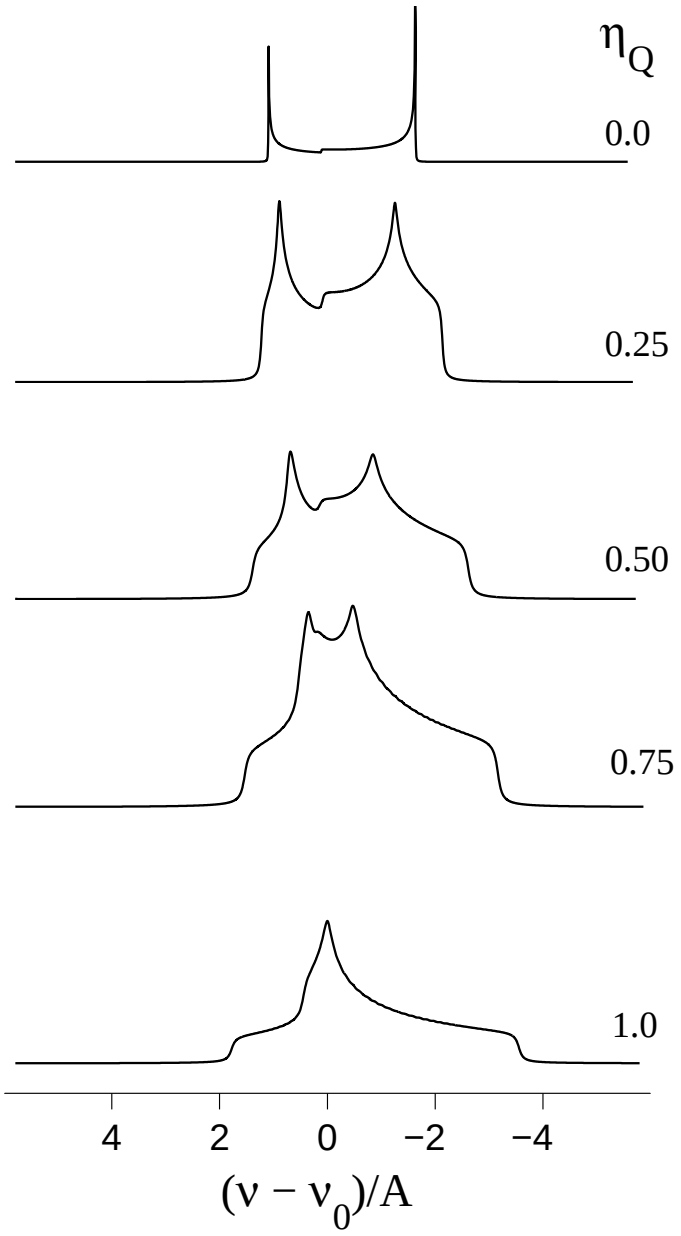

Figure 2.8: Second-order stationary powder line shape as a function of asymmetry parameter, η_{Q}, for the central transition of a half-integer-spin quadrupolar nucleus. The frequency scale is in units of $A = \frac{\nu_{\mathrm{Q}}^2}{16\nu_{\mathrm{o}}}\left[I(I+1) - \frac{3}{4}\right]$.

infra: Section 2.1.8). The only method available to extract reliable values of these parameters from the experimental spectra is computer simulation.[53] Two commonly used software packages in spectral simulation of several solid-state NMR experiments are WSOLIDS1[54] and SIMPSON.[55] However, the determination of a *best-fit* simulated spectrum, by manual iteration of eight different parameters, is a very tedious job. To simplify this job, a magic-angle spinning (MAS) spectrum of the same sample is usually acquired, allowing the determination of δ_{iso}, C_{Q} and η_{Q}, as rapid spinning of the sample at the magic angle (54.74°) would ideally eliminate the chemical shielding anisotropy and the heteronuclear dipolar interaction (*vide infra*: Section 2.2.1). These three parameters, already determined by simulation of the MAS spectrum, would be held constant while simulating the spectrum of a stationary sample for the determination of the remaining five parameters. To ensure that the eight best-fit parameters are the unique solution, it is always recommended to collect experimental spectra at more than one magnetic field, whenever possible. All the experimental spectra would then be simulated, and a unique set of the eight parameters would be confirmed.

2.1.8 Euler Angles

For a quadrupolar nucleus, the main contribution to its solid-sate NMR spectrum comes from the Zeeman, chemical shielding, and the quadrupolar interactions.[56] The last two interactions are orientation-dependent. Thus, in addition to their magnitudes, the orientations relative to the molecular frame of the tensors describing the chemical shielding (CS) and the quadrupolar interaction (the EFG tensor) must be determined. However, it is only possible to obtain the orientations of these tensors with respect to the molecule using single-crystal NMR, a dipolar interaction, or in systems where there is high crystal symmetry.[57] Moreover, the CS and EFG tensors usually have different orientations in the

molecular frame of reference unless restricted by crystal symmetry. Hence, it is very important to describe the relative orientation of these two tensors. In general, the relative orientation of two coordinate systems, with a common origin, is performed by a series of rotations, described by three Euler angles (α, β, γ). Unfortunately, like few other concepts in NMR, several different definitions exist for the Euler angles in NMR textbooks and literature. The most common definition, the so-called "z-y-z" convention of Rose,[58] termed as *passive rotations* by Schmidt-Rohr and Spiess,[26] is used in this work. The progression of the successive rotations is schematically shown in Figure 2.9a, where all rotations are performed in the counter-clockwise (mathematically positive) direction. The original coordinate system (X,Y,Z) is rotated by angle α about its Z-axis to give a new coordinate system (x′, y′, z′). (x′, y′, z′) is then rotated by angle β about its y′-axis to give a new coordinate system (x″, y″,z″). (x″, y″,z″) is finally rotated by angle γ about its z″-axis to give the required coordinate system (x, y, z). Applying this definition to the EFG and CS tensors, the rotations required to bring the EFG PAS into coincidence with the CS PAS are shown in Figure 2.9b. Mathematically, the combined effect of these rotations can be expressed by an Euler rotation matrix $\underline{\underline{R}}(\alpha, \beta, \gamma)$:

$$\begin{aligned} \underline{\underline{R}}(\alpha,\beta,\gamma) &= \underline{\underline{R_z}}(\gamma)\underline{\underline{R_y}}(\beta)\underline{\underline{R_z}}(\alpha) \\ &= \begin{pmatrix} \cos\gamma & \sin\gamma & 0 \\ -\sin\gamma & \cos\gamma & 0 \\ 0 & 0 & 1 \end{pmatrix} \begin{pmatrix} \cos\beta & 0 & -\sin\beta \\ 0 & 1 & 0 \\ \sin\beta & 0 & \cos\beta \end{pmatrix} \begin{pmatrix} \cos\alpha & \sin\alpha & 0 \\ -\sin\alpha & \cos\alpha & 0 \\ 0 & 0 & 1 \end{pmatrix} \end{aligned} \tag{2.87}$$

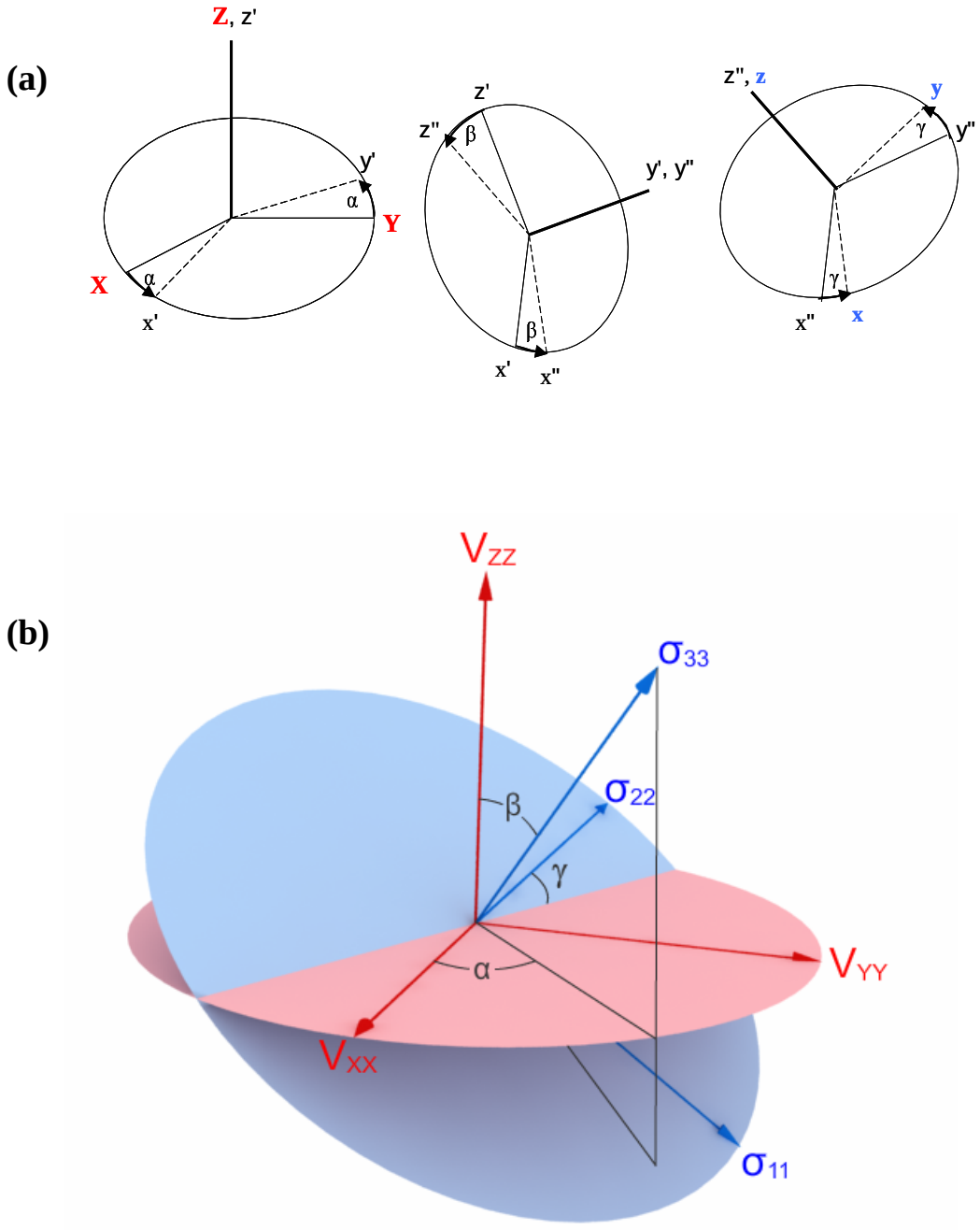

Figure 2.9: **(a)** Successive rotational operations via the Euler angles (α, β, γ) relating two coordinate systems (XYZ) and (xyz) according to the Rose convention.**(b)** Euler angles (α, β, γ) defining the orientation of the chemical shielding (CS) tensor in the reference frame of the EFG tensor.

which gives:

$$\underline{\underline{R}}(\alpha,\beta,\gamma) = \begin{pmatrix} c\alpha.c\beta.c\gamma - s\alpha.s\gamma & s\alpha.c\beta.c\gamma + c\alpha.s\gamma & -s\beta.c\gamma \\ -c\alpha.c\beta.s\gamma - s\alpha.c\gamma & -s\alpha.c\beta.s\gamma + c\alpha.c\gamma & s\beta.s\gamma \\ c\alpha.s\beta & s\alpha.s\beta & c\beta \end{pmatrix} \tag{2.88}$$

where: $cj = \cos j$ and $sj = \sin j$, $j = \alpha, \beta, \gamma$. The 3 angles α, β, and γ are restricted to the following ranges: $0 \leq \alpha \leq 2\pi$; $0 \leq \beta \leq \pi$; $0 \leq \gamma \leq 2\pi$.

2.2 Typical NMR Techniques

In this section, solid-state NMR techniques employed in this thesis are discussed in brief. In experiments performed on half-integer quadrupolar spins exhibiting strong quadrupolar interactions, only the central transition (CT: $m = \frac{1}{2} \leftrightarrow m = -\frac{1}{2}$) is usually observed, as the satellite transitions are difficult to observe due to their wide extension beyond the spectral window. To do so, the durations of the applied *rf* pulses must be selected such that these pulses exclusively excite the central transition. This concept has been outlined by Abragam,[19] who differentiates between *non-selective* and *selective rf* pulses depending on whether all (*non-selective*) or one (*selective*) of the allowed transitions are being excited. In the case where the strength of quadrupolar interaction is much smaller than that of the *rf* field, all transitions can be excited and the corresponding pulse is *non-selective* or *hard*. In the opposite case, which is most encountered in NMR of quadrupolar nuclei, the *rf* pulse is called *selective* or *soft*. The *rf* pulse that gives the maximum signal intensity is the $\pi/2$ pulse. Experimentally, the non-selective $\pi/2$ pulse is usually calibrated using a solution or a solid with cubic symmetry containing the probed nucleus (for example, $Zn(NO_3)_2$(aq) for ^{67}Zn). For selective excitation of the central transition of a half-integer-spin quadrupolar

nucleus, the non-selective $\pi/2$ pulse must be reduced by a factor of $(I + 1/2)$.[32,59]

2.2.1 Magic-Angle Spinning (MAS)

Since its inception in 1958–59 by Andrew and Lowe,[9] *magic-angle spinning* (MAS) has been the most widely used line narrowing technique in solid-state NMR. The technique is performed by rapidly spinning the sample in a rotor oriented at the so-called *magic angle* $\beta = \arccos(1/\sqrt{3}) = 54.7356°$ relative to the external applied magnetic field. Its popularity stems from its success in producing high-resolution spectra by the complete elimination of the first-order anisotropic interactions (chemical shielding anisotropy, heteronuclear dipolar, and the first-order quadrupolar interactions), because of the angular-dependent term, $(3\cos^2\theta - 1)$, contained in the theory of these interactions, as described in previous sections. Therefore, spinning the sample at exactly this angle will eliminate completely this angular term, and will average each of these anisotropic interactions to its isotropic value, provided the spinning speed is significantly greater than the magnitude of the interaction. In the case of second-order quadrupolar interaction, the discussion is rather complicated. Without digging into tedious mathematical details, the second-order frequency shift of the central transition under spinning conditions can be time-averaged to give the following expression:[14]

$$\nu^{(2)}_{1/2\leftrightarrow -1/2} = \frac{\nu_{\mathrm{Q}}^2}{\nu_{\mathrm{o}}}\left[I(I+1) - \frac{3}{4}\right]\left[A_0 + 8A_2(\theta,\phi)P_2(\cos\beta) + 18A_4(\theta,\phi)P_4(\cos\beta)\right] \qquad (2.89)$$

where A_0 is a constant proportional to the isotropic quadrupolar shift; $A_2(\theta,\phi)$ and $A_4(\theta,\phi)$ are angular-dependent functions responsible for the line broadening observed even under MAS conditions; $P_2(\cos\beta)$ and $P_4(\cos\beta)$ are the second- and fourth-order Legèndre poly-

nomials of $\cos\beta$, respectively:

$$P_2(\cos\beta) = \frac{1}{2}(3\cos^2\beta - 1) \tag{2.90}$$

$$P_4(\cos\beta) = \frac{1}{8}(35\cos^4\beta - 30\cos^2\beta + 3) \tag{2.91}$$

where β is the angle between the spinning axis and the external applied magnetic field. Mathematically, it can be shown that $P_2(\cos\beta)$ and $P_4(\cos\beta)$ do not share a common root, as shown graphically in Figure 2.10. Hence, no single spinning angle β can simultaneously cancel out the effects of the second- and fourth-rank quadrupolar broadenings. At the magic angle (54.74°), $P_2(\cos\beta)$ vanishes, while $P_4(\cos\beta)$ is scaled to a value of -0.389. This means that that second-order quadrupolar broadening, albeit reduced, is not removed completely by MAS, thus producing spectra that are about 2 to 3 times narrower than static spectra (depending on the value of η_{Q}).[60,61] The corresponding breadth of the central transition (CT) for a powder solid under MAS due to quadrupolar interactions will be:[51]

$$\begin{aligned}\Delta\nu_{CT}^{MAS} &= \left[\frac{3C_{\mathrm{Q}}}{2I(2I-1)}\right]^2\left[\frac{I(I+1)-\frac{3}{4}}{504}\right]\frac{(6+\eta_{\mathrm{Q}})^2}{\nu_{\mathrm{o}}} \\ &= \frac{\nu_{\mathrm{Q}}^2}{\nu_{\mathrm{o}}}\left[\frac{I(I+1)-\frac{3}{4}}{504}\right](6+\eta_{\mathrm{Q}})^2 \end{aligned} \tag{2.92}$$

To illustrate the significant reduction in line widths produced by MAS, Figure 2.11 shows typical central transition powder line shapes for static and MAS spectra of half-integer-spin quadrupolar nuclei. Clearly, the MAS line widths are inversely proportional to the Larmor frequency, ν_{o}. This means that high magnetic fields are favored for MAS to produce narrow solid-state NMR line shapes. Moreover, the dependence of second-order line widths on C_{Q}^2 indicates that when C_{Q} is sufficiently large, perfectly high-resolved spectra cannot

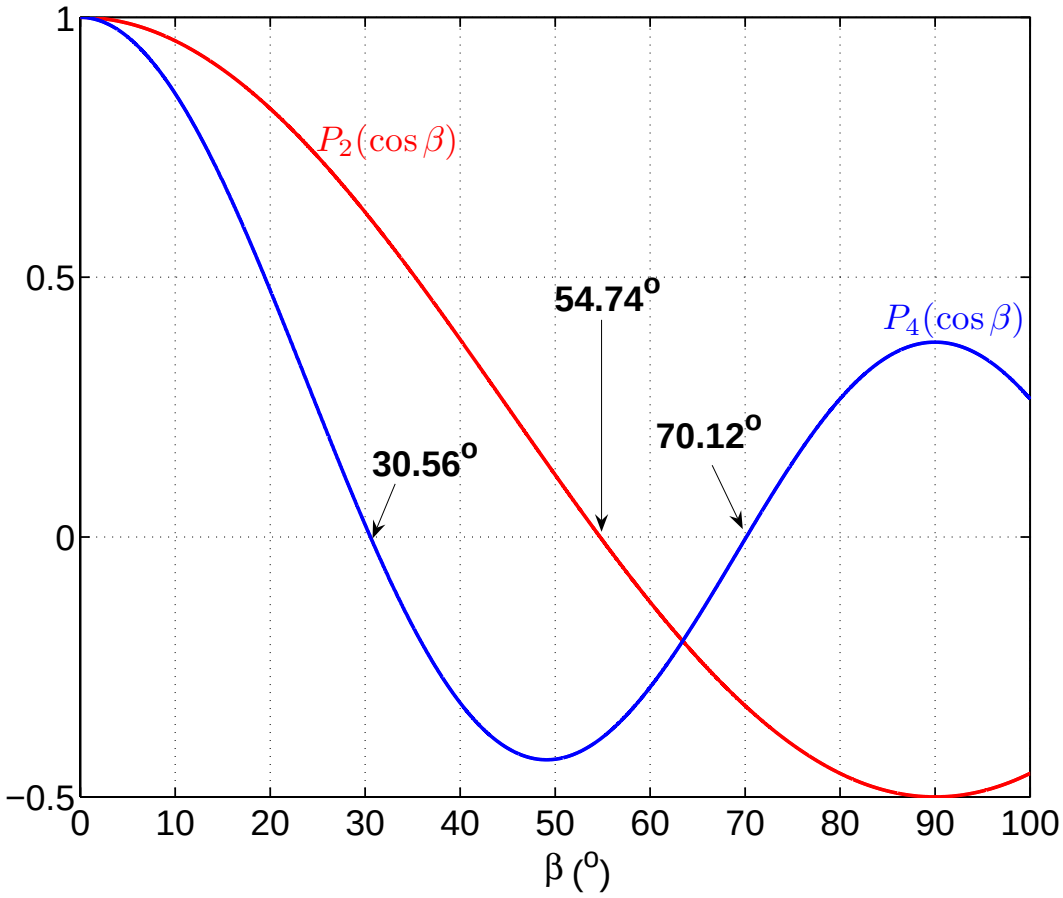

Figure 2.10: The second- and fourth-order Legèndre polynomials of $\cos\beta$, where β is the angle between the spinning axis and the external magnetic field. As there is no single value of β for which $P_2(\cos\beta)$ and $P_4(\cos\beta)$ are simultaneously zero, spinning around a single axis can not average the second-order quadrupolar broadening. Spinning at the magic angle (54.74°) cancels out $P_2(\cos\beta)$, and scales $P_4(\cos\beta)$ to a value of -0.389.

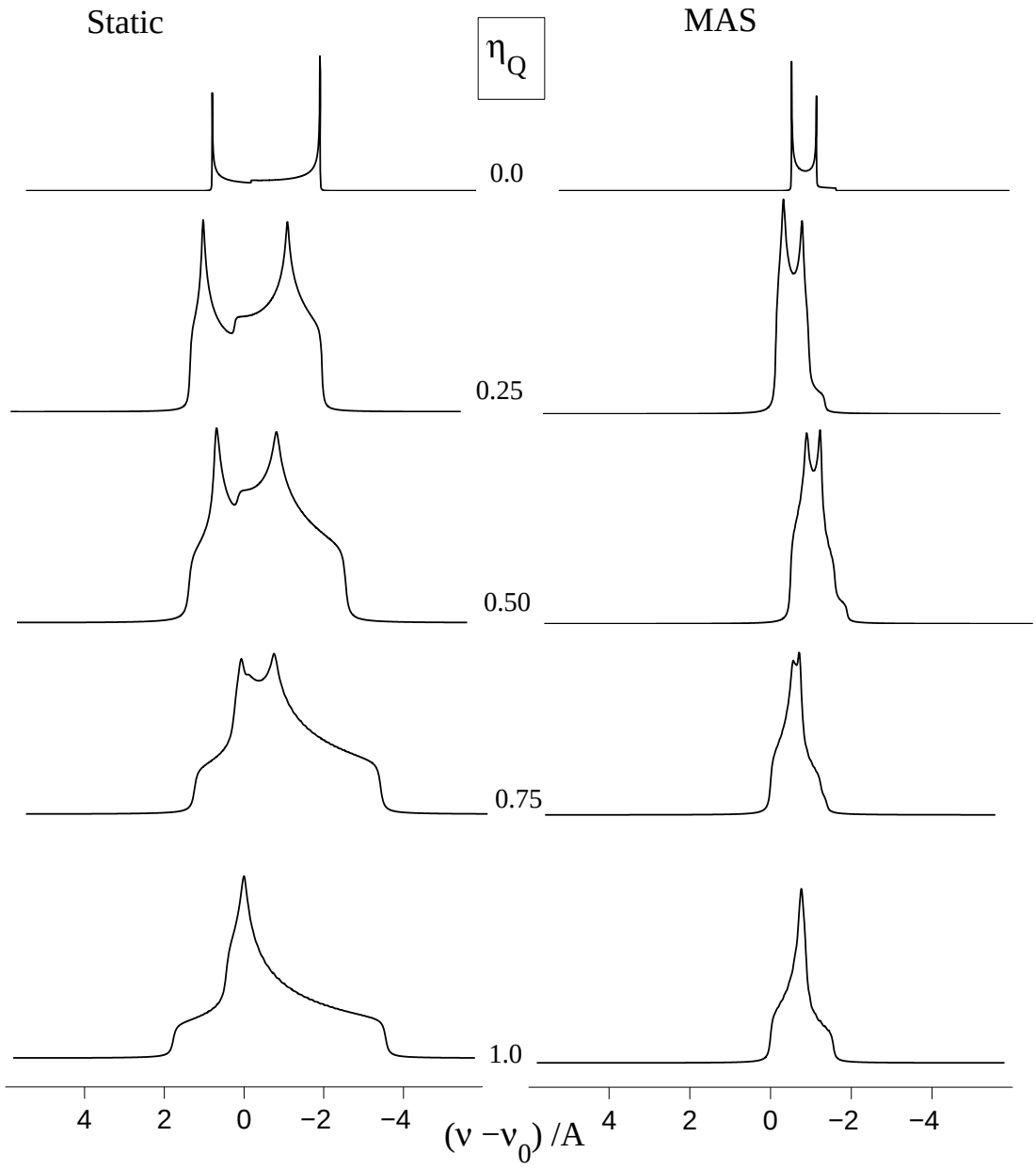

Figure 2.11: Effect of MAS on the second-order powder line shape of the central transition (CT) for a half-integer quadrupolar nucleus, as a function of asymmetry parameter η_{Q}. *Left*: static CT line shape . *Right*: the same transition under MAS. The sample is assumed to be spinning rapidly with an infinite speed. The frequency scale is in units of $A = \frac{\nu_{\mathrm{Q}}^2}{16\nu_{\mathrm{o}}}\left[I(I+1) - \frac{3}{4}\right]$.

be produced by MAS alone, due to the more complex orientation of the second-order broadening. Only partial narrowing is achieved by MAS, and an anisotropic residual line broadening remains in the spectrum, as in Figure 2.11, with a characteristic line shape determined primarily by η_{Q}.

Finally, one practical issue must be addressed here. For efficient line narrowing to occur, the spinning speed (ν_{rot}) of a particular sample must be considerably greater than (in Hz) the breadth of the spectrum of the stationary sample. For a half-integer-spin quadrupolar nucleus, the breadth of the central transition (CT) line shape for a stationary powder was given in Section 2.1.7 by equation (2.86):[51]

$$\Delta\nu_{CT} = \left[\frac{3C_{\mathrm{Q}}}{2I(2I-1)}\right]^2 \left[\frac{I(I+1)-\frac{3}{4}}{144}\right] \frac{\left(25+22\eta_{\mathrm{Q}}+\eta_{\mathrm{Q}}^2\right)}{\nu_{\mathrm{o}}}$$

This means that ν_{rot} depends on I, C_{Q}, η_{Q}, and ν_{o}. For $I = 5/2$, the minimum spinning speed must exceed $C_{\mathrm{Q}}^2/32\nu_{\mathrm{o}}$ when $\eta_{\mathrm{Q}} = 0$ and $3C_{\mathrm{Q}}^2/50\nu_{\mathrm{o}}$ when $\eta_{\mathrm{Q}} = 1$ in order to obtain distinctive CT line shapes. For example, consider an ^{27}Al atom in a powder sample at an axially symmetric site ($\eta_{\mathrm{Q}} = 0$) with $C_{\mathrm{Q}} = 7.0$ MHz. The overall width of its stationary CT spectrum will be approximately 12.0 kHz at 11.75 T [$\nu_{\mathrm{o}}(^{27}\mathrm{Al})$=130.3 MHz]. The spinning speed must significantly exceed this value in order to obtain efficient line narrowing. The effect of spinning speed on the spectrum of this ^{27}Al nucleus is shown schematically in Figure 2.12. At $\nu_{\mathrm{rot}} < \Delta\nu_{CT}$, spinning sidebands of non-uniform shapes will appear, and may overlap with the centreband giving a complex line shape, as depicted in Figure 2.12b. Even when ν_{rot} is equal or slightly greater than $\Delta\nu_{CT}$, spinning sidebands will appear to both sides of the centreband, which will now have a distinctive line shape [Figure 2.12(c, d, e)]. In order to completely eliminate these spinning sidebands, the spinning speed must largely exceed the breadth of the CT static spectrum, sometimes 2-3 times greater, as

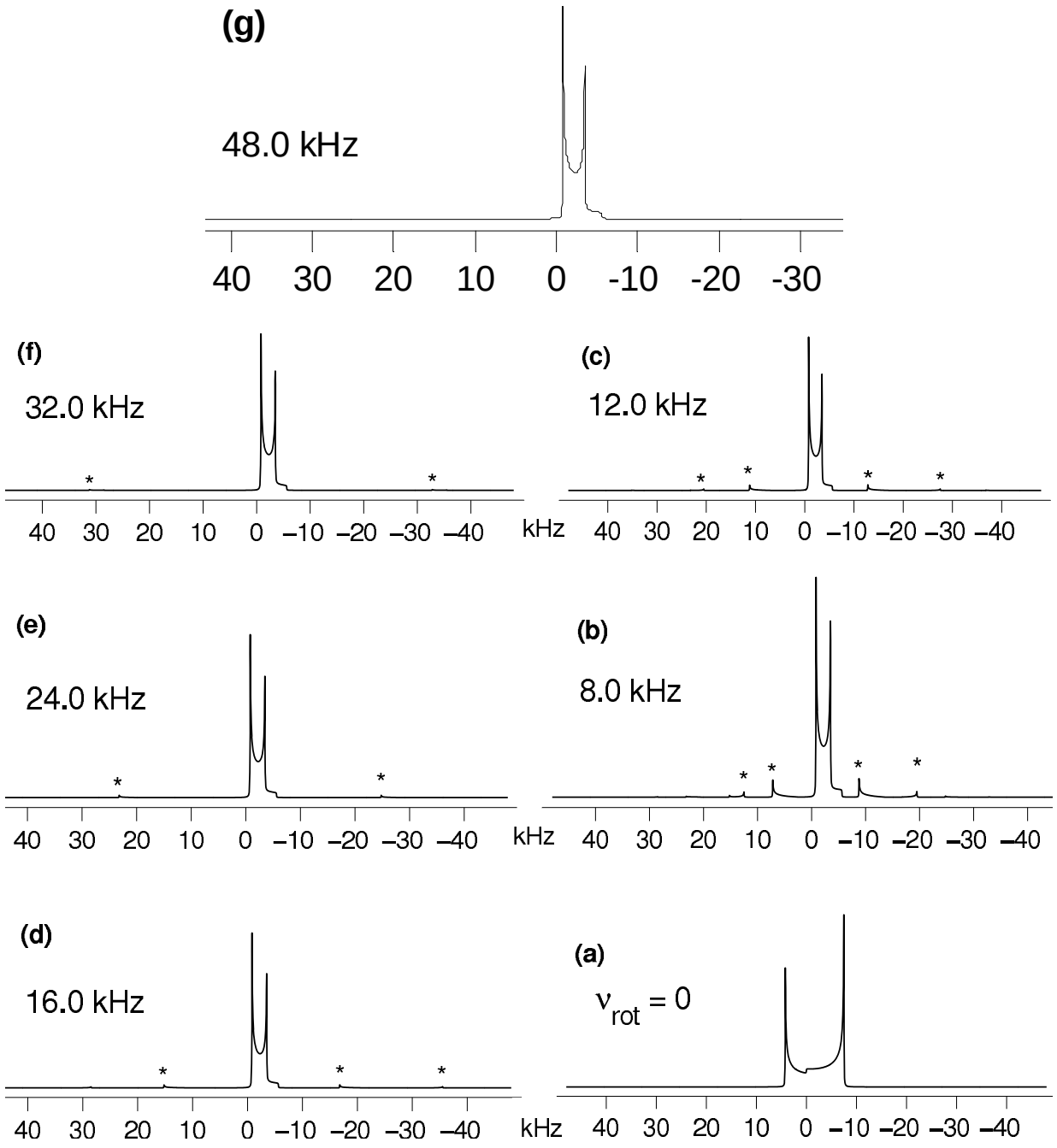

Figure 2.12: The effect of spinning speed on the solid-state ^{27}Al MAS spectra. The spectra were simulated in SIMPSON[55] using the following parameters: $\delta_{iso} = 0$; $C_{\mathrm{Q}} = 7.0$ MHz; $\eta_{\mathrm{Q}} = 0$; $B_{\mathrm{o}} = 11.75\,\mathrm{T}$. The spinning speed is given with each spectrum. The asterisks denote spinning sidebands.

shown in Figure 2.12(f, g). With the current advances in technology, spinning speeds up to 35 kHz are very common in most solid-state NMR Laboratories, using sample holders (rotors) as tiny as 2.5 mm outer diameters. With 1.0 mm outer-diameter rotors, one can reach even higher spinning rates.

As a practical illustration for the potential of MAS to render solid-state NMR spectra better resolved and more informative, Figure 2.13 shows the experimental ^{27}Al static and MAS spectra of the mineral andalusite, one of the naturally occurring polymorphs of aluminum silicate, Al_2SiO_5. The crystal structure of this mineral, which is named after Andalusia (Spain) where it has been found, shows two crystallographically distinct aluminum sites: a pentacoordinated site (site 1), and a hexacoordinated site (site 2) in a 1:1 population ratio.[62] The ^{27}Al spectrum of a stationary powder sample of andalusite at $B_o = 14.1$ T exhibits a complex and broad line shape, as shown in the bottom spectrum in Figure 2.13. However, upon spinning the same sample at 20.0 kHz, the spectrum will be well-resolved, and the two Al sites now exhibit distinctive second-order quadrupolar line shapes (middle spectrum). The simulation of the MAS spectrum (top) gives the following chemical shift and quadrupolar parameters for each of the two sites: $\delta_{iso} = 34.0 \pm 3$ ppm, $C_Q = 5.87 \pm 0.04$ MHz, and $\eta_Q = 0.70 \pm 0.02$ for the 5-coordinated site; $\delta_{iso} = 15.0 \pm 2$ ppm, $C_Q = 15.4 \pm 0.2$ MHz, and $\eta_Q = 0.09 \pm 0.01$ for the 6-coordinated site. These results agree well with other ^{27}Al NMR studies performed on this compound.[63,64]

2.2.2 Spin-Echo Techniques

As mentioned in previous sections, solid-state NMR of quadrupolar nuclei is hindered by broad and featureless lines that result in spectra suffering from poor sensitivity and low resolution. These broad lines have a short time-domain signal [free induction decay(FID)]

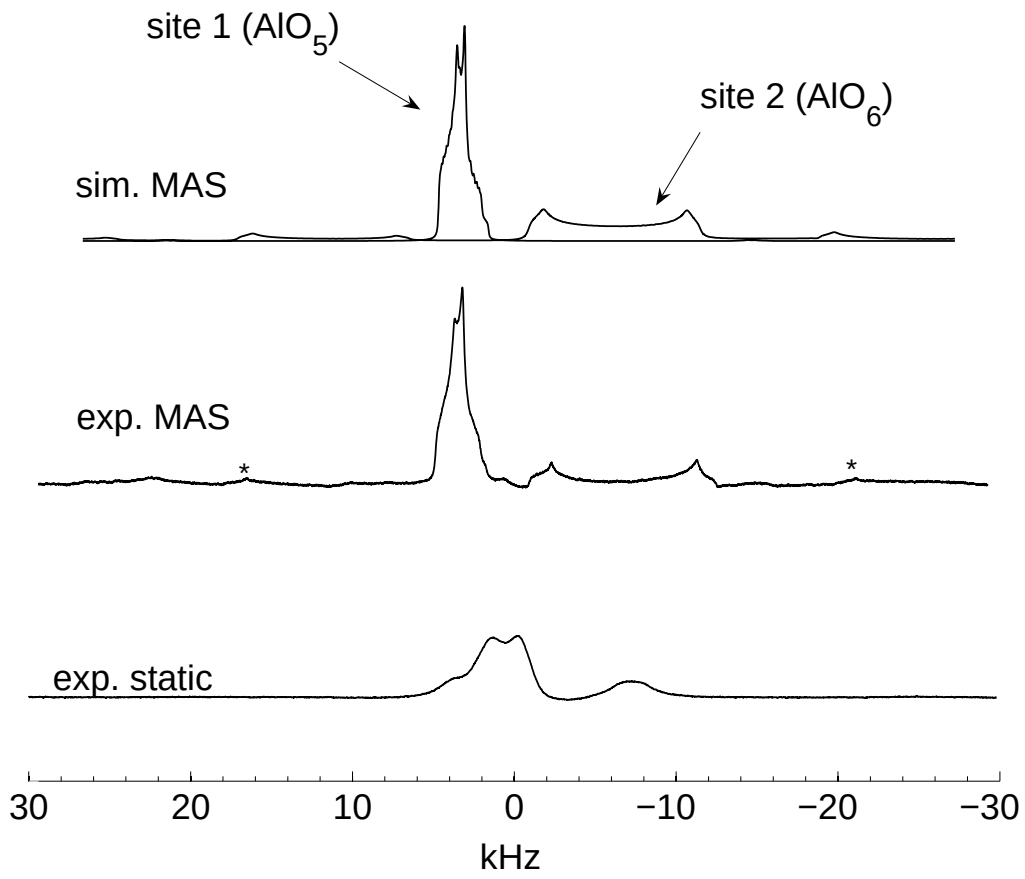

Figure 2.13: Experimental ^{27}Al static (bottom) and MAS (middle) NMR spectra of andalusite at 14.1 T. The standard single-pulse experiment was used to collect both spectra. Spinning rate was 20.0 kHz in the MAS spectrum. Spinning sidebands arising from the CT of site 2 are marked with asterisks. The simulated MAS spectrum (top) was calculated using the following "best-fit" parameters: $\delta_{\mathrm{iso}} = 34.0 \pm 3$ ppm, $C_{\mathrm{Q}} = 5.87 \pm 0.04$ MHz, and $\eta_{\mathrm{Q}} = 0.70 \pm 0.02$ for site 1; $\delta_{\mathrm{iso}} = 15.0 \pm 2$ ppm, $C_{\mathrm{Q}} = 15.4 \pm 0.2$ MHz, and $\eta_{\mathrm{Q}} = 0.09 \pm 0.01$ for site 2.

when acquired using the standard single-pulse NMR experiment. This means that most of the information pertaining to the line shape will be contained in the initial part of the FID. However, the problem arises because of the spectrometer *dead time* and probe "ringing" artifacts.[52,65] The dead time is the time after a pulse, during which the electronics and the probe circuit recover from the effects of the *rf* pulses. As a result of the dead time, which is on the order of μs, the beginning of the rapidly-decaying FID will be corrupted. This leads to loss of intensity and distortions of the line shape. Probe or acoustic ringing can cause similar problems, especially for low-frequency quadrupolar nuclei such as ^{67}Zn, ^{39}K, and ^{25}Mg. It is the result of the probe response to the *rf* field generated by the transmitter coil. It is manifested in the spectrum as a rolling baseline. To avoid these problems, the *spin-echo* experiments have been successfully used. The spin-echo experiments were introduced in 1950 by E. L. Hahn,[8] as a technique for measuring the spin-spin (transverse) relaxation time T_2 in solutions. The general form of a *spin-echo pulse sequence* is:

$$\theta_1 - \tau_1 - \theta_2 - \tau_2 - acquire$$

where θ_1 and θ_2 are pulse lengths of the *rf* pulses; τ_1 and τ_2 are short time delays ($10 - 100\mu$s). In the traditional *spin-echo* experiment, θ_1 is chosen to be a $\pi/2$ pulse, while θ_2 is a π refocusing pulse. This pulse sequence works well in liquids, and in solids where the line shape is effectively broadened by first-order interactions, like chemical shielding or dipolar interactions. For quadrupolar nuclei in solids, however, a *solid-echo* is used instead, in which θ_2 is chosen to be a $\pi/2$ refocusing pulse. The general form of a *solid-echo pulse sequence* will then be:

$$(\frac{\pi}{2})_x - \tau_1 - (\frac{\pi}{2})_y - \tau_2 - acquire$$

The *solid-echo* has been proven both theoretically and experimentally to be more successful for quadrupolar nuclei in solids than the traditional spin-echo in that although the latter gives the maximum signal, it induces some spectral distortions. The *solid-echo* is a reasonable compromise between intensity and spectral distortions.[66] The delays τ_1 and τ_2 are generally equal, but τ_2 is usually set to be several microseconds shorter than τ_1, so that the data acquisition can begin exactly at or before the echo maximum. Moreover, if the echo experiment is being performed with MAS, then the rotor-synchronization condition must be fulfilled, which means that the time delays should be an integer multiple of the rotor period.

2.2.3 Quadrupolar Carr-Purcell Meiboom-Gill (QCPMG) Experiment

Many important sensitivity enhancement techniques in use today are based on the Carr–Purcell Meiboom–Gill (CPMG) pulse sequence. This sequence was first introduced in 1954 by Carr and Purcell as a modification of the Hahn's spin-echo experiment by employing a train of π pulses following the initial $\pi/2$ pulse in order to circumvent the effects of molecular diffusion on the measurements of the transverse relaxation time T_2 in solutions.[15] Four years later, Meiboom and Gill introduced a phase cycling scheme into the Carr-Purcell experiment to compensate for inaccurate settings of the pulse widths.[16] The CPMG experiment was first applied to half-integer-spin quadrupolar nuclei in the solid state by Cheng and Ellis to study the motion of Rb^+ ions present in rubidium salts adsorbed to γ-alumina using ^{87}Rb ($I = \frac{3}{2}$) NMR.[17] In 1997, Larsen and co-workers utilized the CPMG experiment for the purpose of enhancing the sensitivity for half-integer-spin quadrupolar nuclei.[18] The authors also used the spectra obtained from the quadrupolar CPMG (QCPMG) experi-

ment to determine the magnitudes and relative orientation of quadrupolar coupling and anisotropic chemical shielding tensors for half-integer-spin quadrupolar nuclei (^{87}Rb and ^{59}Co) exhibiting very large quadrupolar coupling constants.

As depicted in Figure 2.14, the QCPMG pulse sequence consists of three parts. Part A is a standard spin-echo sequence which starts with a selective $\pi/2$ pulse along the x-axis in the rotating frame. After a short delay τ_1, typically 10–100 μs, optimized to avoid acoustic probe ringing, a selective π pulse is applied along the y-axis. Following this pulse, a spin echo will appear with maximum intensity at time τ_2; the receiver is turned on and the FID is acquired for a time $\tau_a/2$. Part B of the sequence is repeated N times, and each repeating unit consists of a refocusing π_y pulse bracketed by receiver-off periods of τ_3 and τ_4, and an acquisition time of τ_a. The receiver-off periods τ_3 and τ_4 protect the receiver from the effects of the π_y pulses. Finally, part C extends the sampling period to ensure the full decay of the free induction decay (FID) to avoid undesired baseline problems upon Fourier transformation. It is noted that the delays τ_1, τ_2, τ_3, and τ_4 are generally equal, and they are much less than the total acquisition time ($N\tau_a + \tau_a/2$). In the time domain, the train of π_y pulses results in echo-maxima at τ_a, $2\tau_a$, $3\tau_a$, $4\tau_a$, etc. The decay in intensity of these echo-maxima is governed by the transverse relaxation time T_2 of the nuclei in the sample. Upon Fourier transformation of the obtained FID, a series of "spikelets" uniformly separated by τ_a^{-1} (denoted by ν_{qcpmg}) is observed in the frequency domain. The overall spikelet envelope mimics the static powder line shape obtained from the single spin-echo experiment, as shown in Figure 2.15.

There are numerous advantages to employing the QCPMG experiment. The most important one lies in the substantial gain in the signal-to-noise ratio (S/N) compared to standard single-pulse or spin-echo experiment, resulting in a considerable reduction in the experimental time of the NMR spectra. The S/N gain achieved in the QCPMG exper-

iment has enabled the study of important, yet challenging, half-integer-spin quadrupolar nuclei such as ^{25}Mg,[67–69] ^{33}S,[70,71] $^{35/37}$Cl,[72–74] ^{39}K,[67] ^{53}Cr,[75] ^{67}Zn,[67,76–84] ^{87}Sr,[67,85] ^{91}Zr,[69,86] ^{95}Mo,[87,88] and ^{131}Xe.[89] When combined with other signal enhancement techniques such as cross polarization (CP),[10] rotor-assisted population transfer (RAPT),[90,91] double-frequency sweep (DFS),[91,92] hyperbolic secant pulses (HS),[93–95] or wideband uniform rate smooth truncation (WURST) adiabatic pulses,[96,97] the QCPMG experiment is capable of increasing the the sensitivity by an order of magnitude or greater in comparison to classical spin-echo experiments. Other practical advantages of this experiment include its straightforward implementation and efficacy to study stationary as well as spinning samples. The spikelet envelope obtained from the QCPMG NMR experiment can be readily analyzed in order to characterize the magnitudes of quadrupolar and chemical shielding interactions, as well as the relative orientation of their tensors.

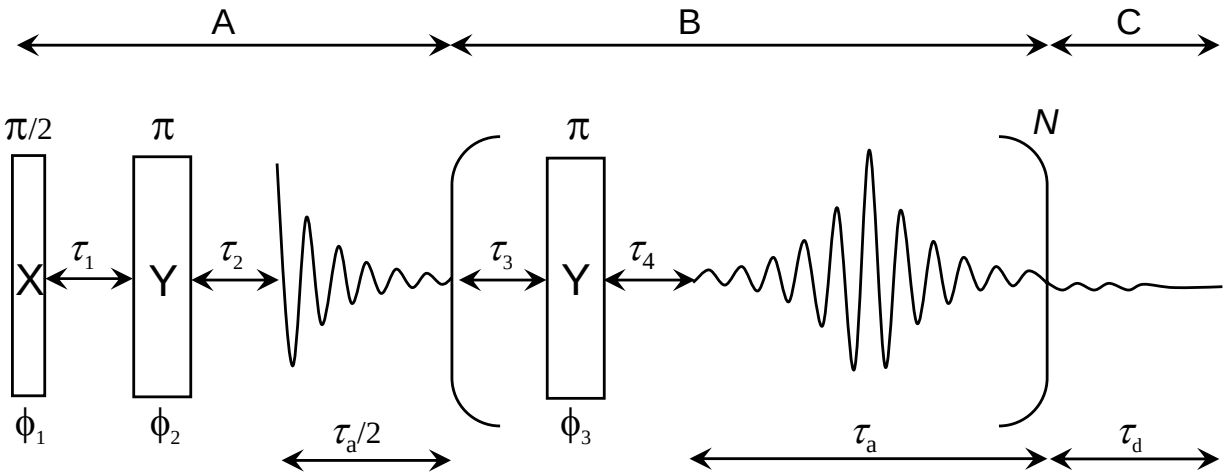

Figure 2.14: Timing scheme of the quadrupolar Carr-Purcell Meiboom-Gill (QCPMG) pulse sequence. The scheme is adapted from Reference 18.

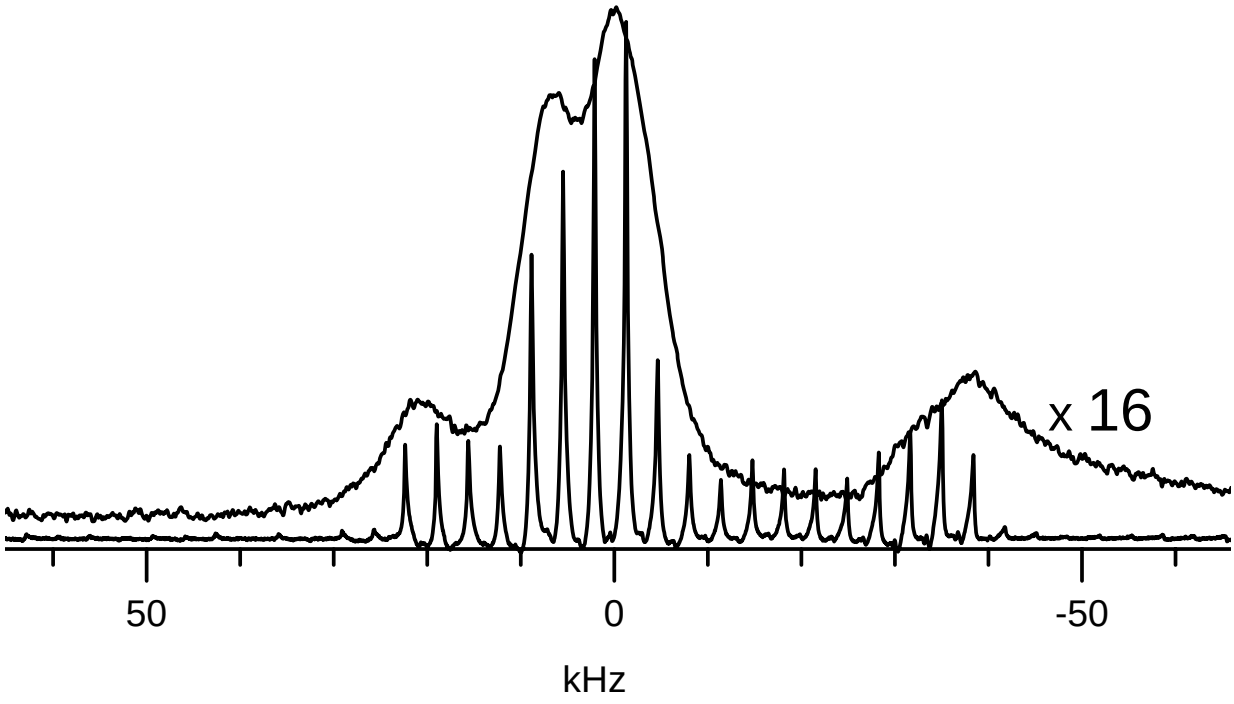

Figure 2.15: Solid-state ^{27}Al QCPMG NMR spectrum at 11.75 T of a stationary sample of andalusite acquired with $\tau_1 = \tau_2 = \tau_3 = \tau_4 = 40.0\,\mu s$ and $\tau_a = 300\,\mu s$ ($\nu_{\mathrm{qcpmg}} = 3.3$ kHz), $N = 54$. Also shown for comparison a spin-echo ^{27}Al NMR spectrum (multiplied by a factor of 16).

2.2.4 WURST–QCPMG Experiment

The WURST–QCPMG experiment was introduced very recently by O'Dell and Schurko[96] as a means to compensate for the limited excitation bandwidth of *rf* pulses during the acquisition of ultrawide solid-state NMR spectra. Their adiabatic Wideband Uniform Rate Smooth Truncation (WURST)–QCPMG pulse sequence is an extension of Bhattacharyya and Frydman's WURST–echo experiment,[97] which can achieve uniform and quantitative excitation of quadrupolar nuclei across a wide bandwidth, to a QCPMG–like sequence that combines the uniform broadband excitation of adiabatic pulses with the signal enhancement advantage of QCPMG. The WURST–QCPMG pulse sequence is shown in Figure 2.16. The sequence starts with an adiabatic pulse (WURST A) whose frequency is swept for a period P_1 between positive and negative offset frequencies (not necessarily equal) at a constant rate, R_{exc}, followed by a delay τ_1. Similar to the standard QCPMG experiment, this is followed by a train of refocusing π pulses. In this case each repeating unit consists of a WURST B adiabatic pulse, also swept at a constant rate, R_{ref}, between positive and negative offsets for a period P_2. This refocusing pulse, bracketed by delays τ_2 and τ_3, is followed by an echo acquisition time τ_4. The utility of this experiment has been tested on several half-integer-spin quadrupolar nuclei (^{87}Rb, ^{71}Ga, ^{91}Zr, ^{59}Co, ^{35}Cl, ^{65}Cu)[96,98] experiencing strong quadrupolar and chemical shielding interactions. The results have shown that this technique is very useful for the acquisition of very broad NMR spectra with good S/N, and has enabled recording NMR spectra as wide as 0.5 MHz in one step without the need for any frequency or field adjustment.

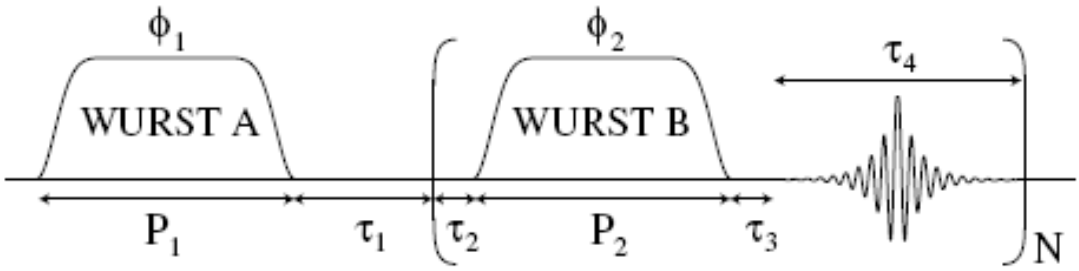

Figure 2.16: Timing scheme of the WURST-QCPMG pulse sequence. The scheme is taken from Reference 96.

2.2.5 Stepped-Frequency Technique

In many instances, the quadrupolar interaction is strong enough to broaden the central transition of a quadrupolar nucleus to the extent where it cannot be be uniformly excited, even with very short *rf* pulses. In such cases, the line width of the central transition is much larger than the bandwidth excitation profile, τ_p^{-1}, where τ_p is the duration of the *rf* pulse. The stepped-frequency piecewise acquisition technique[77,99] is thus employed to collect the full SSNMR spectrum. This approach is very simple and involves stepping the *rf* transmitter frequency systematically across the entire breadth of the spectrum at a constant field strength, with a spectrum being acquired in each step; the probe head must also be retuned at each step. The series of spectra obtained are then combined together using either the skyline projection process (simply overlapping) or the co-addition process (summing up the individual spectra) to produce the entire SSNMR spectrum. The step size for the transmitter frequency offset must be chosen such that it is less than τ_p^{-1}. The total number of subspectra required to construct the whole line shape depends on the breadth of the full spectrum. In cases where the QCPMG method is used, the transmitter frequency offset must be chosen to be an integer multiple of the spikelet spacing, ν_{qcpmg},

otherwise the spikelet spacing will not be uniform throughout the final spectrum. The only drawback of the frequency-stepped technique is that it necessitates the presence of the experimenter in order to retune the probe before each acquisition.

2.2.6 Quantum Chemical Computation of NMR Parameters

Extensive quantum chemical calculations of the anisotropic NMR interactions, namely the nuclear magnetic shielding and the electric field gradient tensors, are performed in this thesis in order to gain better insights into the relationship between NMR parameters and the metal-binding local environments, and in some cases to aid in spectral assignments. All calculations have been carried out using the *Gaussian 03* software package,[100] employing both the *ab initio* restricted Hartree-Fock (RHF) and the density functional theory (DFT) levels of theory. Full descriptions underlying these theories are beyond the scope of this thesis and have been thoroughly discussed elsewhere.[101–104] Only the concepts that are necessary to implement and evaluate *ab initio* and DFT calculations of NMR parameters are discussed briefly below.

Modern computational chemistry softwares such as *Gaussian 03* do not apply Ramsey's equations (2.30) and (2.31) to the calculation of the nuclear magnetic shielding tensor. Alternatively, the components of the shielding tensor are calculated by evaluating the second derivative of the total energy, E, with respect to the magnetic moment of the nucleus, $\boldsymbol{\mu}$, and with respect to the external applied magnetic field, $\boldsymbol{B}$:[103–106]

$$\boldsymbol{\sigma}_{\alpha\beta} = \left.\frac{\partial^2 E}{\partial \boldsymbol{\mu}_\alpha \, \partial \boldsymbol{B}_\beta}\right|_{\boldsymbol{\mu}=0, \boldsymbol{B}=0} \quad \text{where } \alpha, \beta = x, y, z \tag{2.93}$$

One of the problems related to the computation of the shielding tensor is the gauge origin problem, where the calculated values of the shielding tensor will differ depending on the

position of the origin of the vector potential of the external applied magnetic field. This is a direct consequence of using finite basis sets, commonly used in theoretical calculations, in the expansion of the wave function or electron density. Nonetheless, being a molecular property, the nuclear magnetic shielding must be invariant to the choice of gauge origin. The use of complete (infinite) basis sets is an obvious solution to this problem; however, this is often impractical with finite computer resources. A number of different methodologies are available to mitigate the gauge problem, among which the London atomic orbitals or "gauge-including (or invariant) atomic orbitals" (GIAO) method is the most effective and widespread.[107,108] In this method, a field-dependent phase factor is explicitly attached to the atomic basis functions in a way that makes the calculated shielding tensor origin-independent even when using a finite basis set. One of the reasons for the popularity of the GIAO method is that it allows faster convergence of the calculated shielding tensors with respect to basis-set size.[109] The GIAO method is used in this thesis for the calculations of the nuclear magnetic shielding tensors.

Compared to the nuclear magnetic shielding, the electric field gradient (EFG) tensor is considered to be less computationally demanding to calculate. The EFG at a nucleus, $\mathbf{V}$, is calculated using the second-derivative of the electrostatic potential, V, with respect to the position $\boldsymbol{r}$:

$$\mathbf{V}_{\alpha\beta} = \left.\frac{\partial^2 V}{\partial\alpha\,\partial\beta}\right|_{\boldsymbol{r}=0} \text{where } \alpha,\beta = x,y,z \tag{2.94}$$

Unlike the magnetic shielding interaction which is a second-order property that depends on excited electronic states, the EFG is a first-order property that depends only on the ground electronic state of the molecule. Calculations of EFG tensors are often performed on a single molecular species, with far charges being ignored because inclusion of higher coordination spheres is not important. Indeed, the magnitude of the EFG at a nucleus can be estimated using the point-charge approximation method. This involves a simple

electrostatic modeling of atoms surrounding the nucleus, where a point charge is assigned to each atom. The three principal components of the EFG tensor can then be calculated based on the coordinates and the charge of each surrounding atom.

Chapter 3

High-Field Solid-State ^{67}Zn NMR Spectroscopy of Several Zinc–Amino Acid Complexes

A modified version of this chapter has been published as an article in *The Journal of Physical Chemistry A*:
Kamal H. Mroué and William P. Power. High-Field Solid-State ^{67}Zn NMR Spectroscopy of Several Zinc–Amino Acid Complexes. *J. Phys. Chem. A* **2010**, *114*, 324–335. DOI: 10.1021/jp908325n.

3.1 Introduction

Zinc, the second-most abundant trace metal in the human body after iron, is indispensable for all forms of animal and plant life with an average adult human body containing 2.3 g of zinc compared to 4 g of iron.[110–113] Moreover, zinc plays significant roles in a number of fundamental biological processes, as it is found in more than 300 enzymes covering all six classes of enzymes.[114–116] This high occurrence of zinc in enzyme catalysis is due to the distinctive electronic and metallic properties displayed by this metal. First, the zinc ion exists in only one oxidation state, the +2 oxidation state, and does not undergo redox activities, but rather functions as a strong Lewis acid to accept a pair of electrons. Second, zinc is

an element of moderate polarizability (hard–soft character) reflected by its high affinity to nitrogen, oxygen and sulfur ligands. In zinc enzymes, the common ligands are histidine, cysteine, aspartic acid, glutamic acid, and water/hydroxide, which provide nitrogen, oxygen, and sulfur donor atoms. Finally, the closed d^{10} electronic configuration of Zn^{2+} indicates that the coordination number and geometry of its complexes are only controlled by the ligand size and charge. This flexibility in coordination geometry enhances ligand exchange and facilitates the ability of zinc to regulate catalytic processes. In catalytic sites, the zinc ion is usually tetrahedrally bound to three amino acid residues, with a solvent molecule (water or hydroxide) completing the tetrahedral coordination sphere.[110,117–119] However, five-coordinate distorted trigonal bipyramidal and square pyramidal geometries have been observed in some catalytic zinc-binding sites.[120–122]

In addition to its catalytic role, zinc plays a structural role in proteins that may involve lowering the folding enthalpy of a protein to induce an active conformation or to stabilize a particular quaternary structure.[111,112,123] In structural sites, the zinc ion is usually coordinated to four amino acid residues, in a tetrahedral geometry, so that the solvent is excluded as a first-coordination sphere ligand.[116,124] The most important class of proteins in which zinc plays mainly a structural role is the zinc-finger family, which are involved in DNA binding and gene regulation. In zinc-finger proteins, zinc is tetrahedrally coordinated to cysteines and/or histidines that form various types of zinc-coordination environments, the most common of which are the Cys_2His_2Zn, Cys_3His_1Zn, and Cys_4Zn polyhedra, thus providing ZnS_2N_2, ZnS_3N, and ZnS_4 coordination motifs, respectively.[123,125] Hence, another avenue toward a complete understanding of the structure and function of zinc fingers is provided by a detailed knowledge about the local structure of the zinc-binding sites in the different protein environments in which they exist. This can be achieved by the investigation of small and stable zinc-coordination complexes that mimic the structure of the

zinc-binding sites in zinc-finger domains.

Unfortunately, direct observation of the Zn^{2+} ion in biologically relevant systems by routine electronic or EPR spectroscopy is difficult, if not impossible, because the ion is colorless and diamagnetic. A potentially more powerful tool for providing new physical insights into the structure about the zinc ions in these systems is direct nuclear magnetic resonance (NMR) spectroscopy of zinc nuclei. From this perspective, zinc has only one NMR-active isotope, namely the ^{67}Zn isotope. Zinc-67 is one of the so-called low-γ nuclides (those with Larmor frequencies smaller than 10% of that of ^{1}H) that are remarkably challenging to study by NMR spectroscopy. The intrinsic difficulty of ^{67}Zn NMR spectroscopy is due to a combination of many of its unfavorable NMR properties: ^{67}Zn is a half-integer quadrupolar nucleus of spin $I = \frac{5}{2}$ with a fairly large nuclear quadrupole moment $Q = 15.0 \pm 1.5\,\mathrm{fm}^2$,[126] a small magnetic dipole moment ($\Xi = 6.256\,803\%$),[127] and a low natural abundance of 4.10%.[127] The quadrupolar nature of ^{67}Zn, combined with its quite large quadrupole moment, result in significant second-order quadrupolar broadening of the powder line shapes in solid-state NMR (SSNMR). In solution NMR, rapid quadrupolar relaxation of ^{67}Zn nuclei in isotropic solutions results in broad resonances, in addition to the intrinsic weak signals due to their low natural abundance, thus making ^{67}Zn NMR in solutions practically uninformative. The low natural abundance of ^{67}Zn translates directly into low sensitivity unless isotopic enrichment and large sample volumes are employed. These deleterious effects are drastically intensified by the small magnetic moment of ^{67}Zn (*i.e.*, a small gyromagnetic ratio) which makes ^{67}Zn an insensitive nucleus in NMR.

Despite all the aforementioned difficulties associated with ^{67}Zn NMR studies, significant developments in its application have been achieved in the past decade and have rendered ^{67}Zn NMR, as well as other low-γ nuclei (such as ^{25}Mg, ^{33}S, $^{35/37}$Cl, ^{43}Ca, ^{53}Cr, and ^{95}Mo), more accessible in the solid state. These developments involve the increasing availability

of ultrahigh magnetic field NMR spectrometers ($B_o \geq 18.8$ T) equipped with adequate hardware and software necessary for SSNMR spectroscopy, as well as the introduction of new sensitivity enhancement techniques that can improve the signal-to-noise ratio (S/N) of NMR spectra for low-γ half-integer-spin quadrupolar nuclei. In addition to the gain in intrinsic sensitivity acquired by all nuclei at high magnetic fields, performing NMR experiments of a half-integer-spin quadrupolar nucleus at the highest possible magnetic field strength is beneficial for two reasons. One is that the second-order quadrupolar broadening of the central ($+\frac{1}{2} \leftrightarrow -\frac{1}{2}$) transition is substantially reduced because it scales inversely with the applied magnetic field, B_o, meaning that narrower line shapes are obtained at higher applied magnetic fields. The other is the more precise and complete detection of chemical shift anisotropy (CSA) at higher fields due to the direct scaling of the breadth (in Hz) of the chemical shift interaction with B_o.[53,57,128] The most popular signal enhancement method utilizes the quadrupolar Carr–Purcell Meiboom–Gill (QCPMG) pulse sequence[15–18] as a robust technique for increasing S/N and reducing experimental times in SSNMR experiments on unreceptive nuclei. The QCPMG pulse sequence, which consists of a train of π refocusing pulses following an initial $\pi/2$ pulse, produces a series of spin echoes in the time domain. Fourier transformation of this echo train yields an NMR spectrum composed of equally separated spikelets that mimic the spectrum of a stationary sample in the solid state. As mentioned earlier in Section 2.2.3, the QCPMG experiment is capable of increasing the sensitivity by an order of magnitude or greater, especially when combined with other signal enhancement techniques. In the case of ^{67}Zn NMR, only the QCPMG method has been reported, either alone or in combination with CP (*vide infra*).

Although recent advances in solid-state NMR techniques and instrumentation, as well as the availability of very high magnetic fields, have provided new opportunities for NMR of low-frequency quadrupolar nuclei like ^{67}Zn in the solid state, the number of zinc systems

that have been studied so far is still limited in comparison to other nuclei. Table 3.1 summarizes all ^{67}Zn SSNMR data that have been reported to date. These data include NMR studies on metallic zinc,[129–131] numerous simple inorganic salts,[132–140] 19 small organozinc complexes,[67,76–81,135,141–144] and five zinc-containing macromolecules.[78,82–84] The data in Table 3.1 have been classified according to the zinc coordination geometry in each system. Aside from zinc metal which has a hexagonal close-packed structure, all other zinc atoms are found in sites of tetrahedral or octahedral coordination, with the former being more abundant. A quick inspection of Table 3.1 reveals two fairly-separated ranges of isotropic chemical shifts for the tetrahedral and octahedral coordinations, albeit with a few exceptions. Octahedral chemical shifts range from -27 to 112 ppm, while tetrahedral ones are less shielded and cover a wider range from 119 to 495 ppm. These two ranges are disturbed by the shift values of $ZnCl_2$ and $ZnBr_2$ in the octahedral region, and by those of ZnTe, $[Tp^{But,Me}]ZnBr$, and $Zn[S_2CN(CH_3)_2]_2$ in the tetrahedral region.

Bennett appears to have performed the first measurement of solid-state ^{67}Zn NMR in 1966, in which the ^{67}Zn NMR signal in the tetrahedral LiZn environment was observed.[132] Several years later, Hayes and Pound determined the ^{67}Zn nuclear quadrupolar coupling constant and the asymmetry parameter of hexagonal ZnO by measuring the second-order shift of the central transition line shape as a function of single crystal orientation.[138] Over the following years, there had been several reports on SSNMR studies on cubic zinc chalcogenides (ZnS, ZnSe, ZnTe),[136,139] and on zinc metal.[129,130] The first SSNMR investigation on zinc in noncubic environments was reported by Kunwar *et al.*,[141] who recorded a static ^{67}Zn quadrupolar-echo spectrum of $Zn(acetate)_2 \cdot 2\,H_2O$ in natural abundance at 11.75 T. This same compound, which has distorted ZnO_6 octahedra,[145] was studied more thoroughly in later years, either by single-crystal ^{67}Zn NMR,[142] or as a relevant test case for the successful applicability of the QCPMG method on low-γ nuclei in natural abundance.[67,146]

Sham and Wu[135] applied the magic-angle spinning (MAS) technique to record the 9.4 T ^{67}Zn spectra of ^{67}Zn-enriched powdered zinc complexes with imidazole and thiourea, in which ZnN_4 and ZnS_4 respectively exist.[147,148]

The first application of QCPMG on zinc compounds was reported by Ellis and co-workers,[76] in which the ^{67}Zn quadrupolar coupling parameters and the isotropic chemical shifts in ^{67}Zn-enriched powdered Zn(imidazole)$_2$(acetate)$_2$ and Zn(formate)$_2 \cdot 2\,H_2O$ were extracted from static QCPMG NMR spectra collected at 9.40 and 11.75 T. They have since developed a general methodology to directly observe low-γ half-integer-spin quadrupolar nuclei (such as ^{67}Zn, ^{25}Mg, and ^{43}Ca) in dilute environments such as proteins via low-temperature solid-state NMR experiments.[146,149] This method involves the utilization of cryogenic temperatures (as low as 10 K) to enhance the Boltzmann factor and reduce the ambient noise of the NMR probe, in combination with cross polarization (CP) from ^{1}H to the dilute spin (^{67}Zn for example), followed by signal averaging through a quadrupolar echo (QE) or QCPMG pulse sequence. The combination of these techniques have allowed the application of ^{67}Zn NMR spectroscopy to the zinc-binding sites in metalloproteins, such as the minimal DNA binding domain of *xeroderma pigmentosum A* (XPA-MBD),[78] human carbonic anhydrase isozyme (CAII),[82] Zn^{2+}-substituted *Pyrococcus furiosis* rubredoxin (*Pf* Zn-Rd),[83] and both the wild type and the H265A mutant of *Aquifex aeolicus* LpxC.[84] This method was also applied to small systems, as synthetic analogues of zinc-containing enzymes, with naturally abundant zinc (at 4.10% ^{67}Zn) such as the tris(pyrazolyl)hydroborato zinc complex [Tp^{But,Me}]ZnOH along with its bromide and chloride derivatives.[80]

In the present chapter, five small zinc-coordination complexes (with imidazole, L-alanine, L-histidine, L-cysteine, and glycine) previously uncharacterized by solid-state NMR, are investigated using ^{67}Zn NMR spectroscopy and complementary single-crystal X-ray diffraction, as well as quantum chemical calculations. These complexes are: (**1**)

bis(imidazole)zinc(II) chloride; (**2**) bis(L-alaninato)zinc(II); (**3**) bis(L-histidinato)zinc(II) dihydrate; (**4**) sodium bis(L-cysteinato)zincate(II) hexahydrate; (**5**) bis(glycinato)zinc(II) monohydrate (see Figure 3.1). A summary of relevant crystallographic information for the five complexes is given in Table 3.2. These complexes were chosen because they contain ligands that are representatives of the zinc-binding sites in zinc-containing biological materials. For example, **1** is implicated in the binding sites of two polymorphs of the zinc-insulin hexamers.[150–152] Histidine and cysteine are key amino acids in the binding site of the zinc-finger domains, as mentioned earlier. The alaninate (**2**) and glycinate (**5**) zinc salts, on the other hand, both represent the first report of ^{67}Zn SSNMR on pentacoordinated zinc coordination geometry. The ZnN_2O_3 coordination motifs in these two complexes are similar to the active zinc-binding site in thermolysin (*Bacillus thermoproteolyticus*).[118,153] Considering the limited number of systems studied by ^{67}Zn SSNMR and the absence of such studies on five-coordinate zinc environments, evident from Table 3.1, the results presented here add to a more general understanding of the effects of the local electronic and bonding structure on the ^{67}Zn SSNMR parameters; and demonstrate the utility of ^{67}Zn NMR to explore biologically relevant zinc-binding systems in the solid state.

This experimental NMR study is further complemented with density functional theory (DFT) and restricted Hartree-Fock (RHF) calculations of the ^{67}Zn electric field gradient (EFG) and chemical shift (CS) tensors in order to provide other insights into the relationship between NMR data and the structural properties of various zinc-binding sites. In order for the quantum chemical calculations to produce reliable results that can be correctly compared with experiment, accurate atomic coordinates from X-ray or neutron diffraction structures of the studied systems must be available. All five complexes studied herein have X-ray crystal structures reported previously.[154–158] However, the published structures required some reexamination to be useful. For example, the crystal structure of

1 is nearly 45 years old with an *R*-value 9.8%,[154] while those of **4** and **5** contain disordered sodium and water oxygen atoms (in **4**)[157] and zinc atoms (in **5**).[158] Therefore, the X-ray crystal structures of the three complexes have been redetermined with better precision.

Table 3.1: Survey of ^{67}Zn NMR parameters available in the solid state.

zinc system		zinc coord.	δ_{iso} [a] (ppm)	C_Q (MHz)	η_Q	NMR method [b]	ref.
		Octahedral systems and higher					
Zinc metal		$ZnZn_{12}$	1500	12.73	0	QE	130
			1776	11.983	0	SE	131
			1000	12.0	0	QE	129
LiZn		$ZnLi_4Zn_4$	2000	-	-	Static	132
ZnF_2		ZnF_6	-20	7.87	0.18	SE	133
$\gamma-ZnCl_2$		$ZnCl_6$	300	2.50	0	SE	133
$ZnBr_2$		$ZnBr_6$	240	1.95	0.95	SE	133
ZnI_2		ZnI_6	70	2.70	0.67	SE	133
$ZnSO_4$		ZnO_6	15	1.75	0.2	SE	133
$ZnSO_4 \cdot 7\,H_2O$		ZnO_6	13	4.50	0.23	SE	133
			10	1.7	0.2	Static	134
$ZnSO_4 \cdot xH_2O$		ZnO_6	25	4.65	0.70	SE	133
$Zn(ClO_4)_2 \cdot 6\,H_2O$		ZnO_6	-3.0	< 0.2	-	MAS	135
$Zn(acetate)_2 \cdot 2\,H_2O$		ZnO_6	0	5.3	0.87	QE	141
			-123 [c]	5.34	0.819	SC	142
			-125 [c]	5.20	0.898	SC	142
			2	5.35	0.86	QCPMG	67
$Zn(formate)_2 \cdot 2\,H_2O$	site 1	ZnO_6	-9	6.05	0.99	QCPMG	76
			-27	6.24	0.93	QE	143
			-24	6.34	0.98	SC	143
	site 2	ZnO_6	0	9.52	0.39	QCPMG	76
			-15	9.58	0.42	QE	143
			-26	9.63	0.45	SC	143

Table 3.1 – *Continued*

zinc system	zinc coord.	δ_{iso} [a] (ppm)	C_Q (MHz)	η_Q	NMR method [b]	ref.
$[Tp]_2Zn$ [d]	ZnN_6	112	4.17	0.33	CP/QCPMG	77
$[Tp^{Me_2}]_2Zn$ [d]	ZnN_6	92	4.17	0.59	CP/QCPMG	77
	Tetrahedral systems					
ZnO (wurtzite)	ZnO_4	240.1	2.407	0	SE, SC	136
		240	2.40	0	MAS, Static	134
		238	2.40	0	MAS	137
		-	2.409	< 0.007	SC	138
ZnS (wurtzite)	ZnS_4	365	< 0.5	0	SE	136
		364.5	< 0.4	0	MAS, Static	134
		360	~ 0	0	MAS	137
ZnS (cubic)	ZnS_4	380.5	0	-	SE	136
		381.9	0	-	MAS, Static	134
		378	0	-	MAS	137
		378	0	-	Static	139
ZnSe (cubic)	$ZnSe_4$	276.3	0	-	SE	136
		276	0	-	MAS	135
		273	0	-	Static	139
ZnTe (cubic)	$ZnTe_4$	87.6	0	-	SE	136
		85	0	-	Static	139
Rb_2ZnCl_4	$ZnCl_4$	350	3.45	0.60	SE	133
$K_2Zn(CN)_4$	ZnC_4	291	0	-	MAS	140
$Zn(imidazole)_4(ClO_4)_2$	ZnN_4	291	2.80	0.4	MAS	135
$Zn(thiourea)_4(NO_3)_2$	ZnS_4	359	3.15	1.0	MAS	135
		325	3.08	0.9	QE	78
		337.1	3.25	0.89	QE	79
$Zn(acetate)_2$	ZnO_4	245	2.42	0.1	MAS	135
		67	8.25	-	QE	144

Table 3.1 – *Continued*

zinc system		zinc coord.	δ_{iso} [a] (ppm)	C_Q (MHz)	η_Q	NMR method [b]	ref.
$Zn(imidazole)_2(acetate)_2$		ZnN_2O_2	155	8.20	0.62	QCPMG	76
$[Bp]_2Zn$ [d]		ZnN_4	119	13.66	0.87	CP/QCPMG	77
$[Bp^{Me_2}]_2Zn$ [d]		ZnN_4	158	15.27	0.90	CP/QCPMG	77
$Zn[S_2CN(CH_3)_2]_2$		ZnS_4	70.0	15.7	0.94	CP/QCPMG	79
$Zn[SPh]_4(Me_4N)_2$		ZnS_4	333.0	3.90	0.65	CP/QCPMG	79
$Zn[SPhMe]_4(Me_4N)_2$	site 1	ZnS_4	339.0	3.95	0.15	CP/QCPMG	79
	site 2	ZnS_4	340.0	6.80	0.11	CP/QCPMG	
$[Tp^{But,Me}]ZnOH$ [d]		ZnN_3O	166.5	30.5	0	CP/QCPMG	80
$[Tp^{But,Me}]ZnCl$ [d]		ZnN_3Cl	311.3	12.3	0	CP/QCPMG	80
$[Tp^{But,Me}]ZnBr$ [d]		ZnN_3Br	57.7	9.5	0	CP/QCPMG	80
$[Tm^{Ph}]ZnSPh$ [d]	site 1	ZnS_4	400	15.7	0.10	CP/QCPMG	79
	site 2	ZnS_4	495	16.7	0.33	CP/QCPMG	
$\{[Tp^{But,Me}]Zn(OH_2)\}[HOB(C_6F_5)_3]$ [d]		ZnN_3O	-	4.3	0.6	CP/QCPMG	81
Human CAII [e]		ZnN_3O	-	9.80	1.0	CP/QCPMG	82
XPA-MBD [f]		ZnS_4	327.6	4.9	0.84	CP/QCPMG	78
Pf Zn-Rd [g]		ZnS_4	429	4.35	0.84	CP/QCPMG	83
WT *Aa* LpxC [h], pH 6	site 1	ZnN_2O_2	133	12.9	0.90	CP/QCPMG	84
	site 2	ZnN_2O_2	170	~ 10	-	CP/QCPMG	
WT *Aa* LpxC, pH 9		ZnN_2O_2	284	14.3	0.92	CP/QCPMG	84
H265A *Aa* LpxC [i], pH 6.3 and 8.7		ZnN_2O_2	-	9.55	0.87	CP/QCPMG	84
		Unclassified systems					
$Zn(L-Alaninate)_2 \cdot H_2O$	site 1	-	110	11.9	0.70	QCPMG	67
	site 2	-	273	19.0	0.03	QCPMG	

[a] Chemical shifts are referenced relative to Zn^{2+} in dilute aqueous solutions, unless otherwise indicated.

[b] SC, single crystal; SE, solid echo ($90^\circ - 90^\circ$); QE, quadrupolar echo ($90^\circ - 180^\circ$); Static, single-pulse experiment; MAS, magic-angle spinning; CP/QCPMG, cross polarization with QCPMG.

[c] Relative to 1.0 M aqueous $ZnCl_2$.

[d] [Tp] is an abbreviation of the tris-(pyrazolyl)hydroborato ligand, with the 3- and 5-alkyl substituents listed, respectively, as superscripts (Me for methyl, But for *tert*-butyl). Similarly, [Bp] is an abbreviation of the bis(pyrazolyl)hydroborato ligand, and [Tm^{Ph}] is the tris(2-mercapto-1-phenylimidazolyl)hydroborato ligand.

[e] Human carbonic anhydrase isozyme II.

[f] Minimal DNA binding domain of xeroderma pigmentosum A.

[g] Zn^{2+}- substituted *Pyrococcus furiosis* rubredoxin.

[h] Wild type *Aquifex aeolicus* LpxC.

[i] The H265A mutant of *Aquifex aeolicus* LpxC.

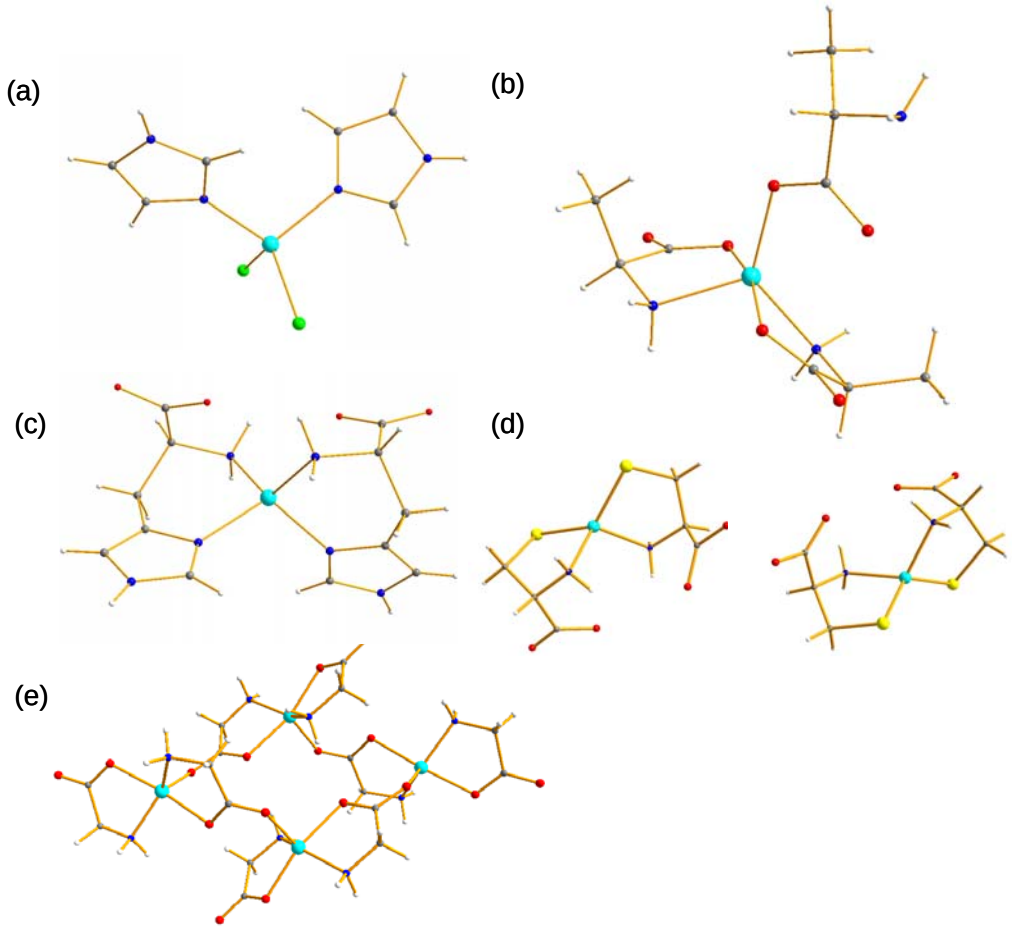

Figure 3.1: Coordination environment of the zinc ion in solid (a) $Zn(imidazole)_2Cl_2$, (b) $Zn(L\text{-}Ala)_2$, (c) $Zn(L\text{-}His)_2.2H_2O$, (d) $Na_2Zn(L\text{-}Cys)_2.6H_2O$, and (e) $Zn(Gly)_2 \cdot H_2O$. These are the models used in quantum chemical calculations of the zinc NMR interaction tensors in the present work. Zinc is shown in cyan, chlorine in green, sulfur in yellow, carbon in gray, nitrogen in blue, oxygen in red, and hydrogen in white.

Table 3.2: Selected structural data for the studied complexes.

zinc complex	crystal system	space group	number of unique zincs	symmetry at Zn	zinc coordination	reference
$Zn(imidazole)_2Cl_2$	Monoclinic	$P2_1/n$	1	1	ZnN_2Cl_2	this study, 154
$Zn(L\text{-}Ala)_2$	Monoclinic	$P2_1$	1	1	ZnN_2O_3	155
$Zn(L\text{-}His)_2.2H_2O$	Tetragonal	$P4_32_12$	1	2	ZnN_4	156
$Na_2Zn(L\text{-}Cys)_2.6H_2O$	Monoclinic	$C2$	2	2	ZnN_2S_2	this study, 157
$Zn(Gly)_2 \cdot H_2O$	Triclinic	$P\bar{1}$	2	1	ZnN_2O_3	this study, 158

3.2 Experimental Section

3.2.1 Sample Preparation and Single-Crystal X-ray Crystallography

Compounds **1**–**4** were synthesized according to published methods, whereas **5** was purchased from a commercial source. L-alanine, L-histidine, L-cysteine, and imidazole were purchased from Sigma-Aldrich and used as received. The histidinate **(3)** and the cysteinate **(4)** zinc complexes were made using 87.8% ^{67}Zn-enriched zinc metal purchased from Trace Sciences International (Ontario, Canada). An aqueous solution of $^{67}ZnSO_4$ was prepared by dissolving the enriched metal in sufficient volume of 1.5 M aqueous H_2SO_4.

(**1**) **Bis(imidazole)zinc(II) Chloride**. This compound was synthesized by slow evaporation of a hot methanol solution containing $ZnCl_2$ and imidazole in 1:2 molar ratio.[159] Colorless single crystals suitable for X-ray determination were obtained by recrystallization from methanol.

(**2**) **Bis(L-alaninato)zinc(II)**. This compound was prepared using the method of Démaret and Mercier.[160] 3.0 mmol of ZnO and 5.0 mmol of L-alanine were added to 50 ml of boiling water, and allowed to react with continuous stirring. The residual solid was then filtered off, and the clear solution was slowly evaporated to dryness. Unit cell parameters

for zinc L-alaninate were obtained at room temperature and were found to be in good agreement with those previously published.[155] However, this crystal was not of suitable quality for complete refinement, and such a crystal could not be obtained after several attempts.

(**3**) **Bis(L-histidinato)zinc(II) Dihydrate**. This complex was prepared by adapting a general method for the preparation of Mn(II)-amino acid chelates.[161] Typically, an aqueous solution containing 0.75 mmol of barium hydroxide, $Ba(OH)_2$, was added to 1.5 mmol of L-histidine dissolved in water. After one hour of continuous stirring, an aqueous solution containing 0.75 mmol of $^{67}ZnSO_4$ was added slowly at room temperature. The barium sulfate was filtered off. The volume of the collected filtrate was reduced to half by placing the flask in a temperature controlled oven at 80 °C. The solution was then evaporated slowly to dryness, and the obtained solid was recrystallized several times from hot water. Single-crystals suitable for X-ray analysis could not be obtained from this compound.

(**4**) **Sodium Bis(L-cysteinato)zincate(II) Hexahydrate**. This complex was prepared using the method reported by Shindo and Brown.[162] An aqueous solution containing 1.5 mmol of L-cysteine and 0.75 mmol of $^{67}ZnSO_4$ was mixed with a solution containing 3.0 mmol of NaOH. A white precipitate which at once appears is soon dissolved by continuous stirring. The clear solution was evaporated to dryness and the residue was recrystallized several times from a 1:1 ethanol-water solution as suggested by the crystal-structure paper.[157]

(**5**) **Bis(glycinato)zinc(II) Monohydrate**. This sample was purchased from TCI (Portland, OR) and used without further purification. Single crystals were obtained by recrystallization from a water-ethanol (1:1) mixture.

All samples were analyzed by electrospray ionization (ESI) mass spectrometry to confirm their identities. Powder X-ray diffractometry was also performed on these samples,

and the obtained X-ray powder patterns were compared to the calculated ones that are available from X-ray single-crystal structures. With the sole exception of **3**, the experimental patterns were in good agreement with the calculated ones. Suitable single crystals of **1**, **4**, and **5** were selected, mounted on a thin glass fiber using paraffin oil, and cooled to the data collection temperature of 243 K for **1**, and 200 K for **4** and **5**. Diffraction data were collected on a Bruker Smart Apex CCD diffractometer equipped with an area detector using graphite-monochromated Mo Kα radiation (λ = 0.71073 Å) operating at 50 kV and 40 mA and utilizing ω scans (0.3°, 30 s exposures). Data were corrected for Lorentz and polarization effects. Absorption corrections were based on fitting a function to the empirical transmission surface as sampled by multiple equivalent measurements of numerous reflections using the scale function of the APEX II software.[163] The space groups for the three compounds were determined on the basis of the systematic absences. Structures were solved by direct methods and refined on F^2 by full-matrix least-squares methods using the SHELXTL package,[164] with anisotropic displacement parameters for all non-hydrogen atoms. All hydrogen atoms were treated as idealized contributions. A summary of relevant crystallographic information for the five complexes investigated herein is given in Table 3.2. Details of crystal data, data collection, and structure refinement are listed in Table 3.3.

3.2.2 Solid-State ^{13}C NMR

Natural abundance ^{13}C{^{1}H} cross-polarization magic-angle spinning (CP/MAS) NMR spectra of the five zinc complexes, as well as those of their corresponding free (unbound) amino acid ligands, were acquired at 11.75 T [$\nu_o(^{13}C)$ = 125.76 MHz] on a Bruker Avance DRX-500 spectrometer with a Bruker 4 mm MAS NMR probe. A ^{1}H $\pi/2$ pulse width of 4.00 μs, contact times of 2.0-3.0 ms, recycle delays of 5.0 s (60 s recycle delay was used for

Table 3.3: Crystallographic data and structure refinement for the zinc-amino acid complexes.

	(**1**)	(**4**)	(**5**)
	$Zn(imidazole)_2Cl_2$	$Na_2Zn(L\text{-}Cys)_2.6H_2O$	$Zn(Gly)_2 \cdot H_2O$
Empirical formula	$C_6H_8N_4Cl_2Zn$	$C_6H_{22}N_2O_{10}S_2Na_2Zn$	$C_4H_{10}N_2O_5Zn$
Formula weight	272.43	457.73	231.51
Temperature (K)	243(1)	200(2)	200(2)
Wavelength (Å)	0.71073	0.71073	0.71073
Crystal size (mm^3)	0.30 x 0.26 x 0.23	0.50 x 0.10 x 0.02	0.52 x 0.12 x 0.02
Crystal system, space group	Monoclinic, $P2_1/n$	Monoclinic, $C2$	Triclinic, $P\bar{1}$
Unit cell dimensions			
a (Å)	7.9306(3)	5.1893(2)	9.090(3)
b (Å)	11.7739(4)	23.2065(8)	9.537(3)
c (Å)	11.4156(4)	15.0008(5)	10.420(5)
α (°)	90.0	90.0	106.112(7)
β (°)	105.441(1)	92.5610(10)	105.815(7)
γ (°)	90.0	90.0	106.854(5)
Volume ($Å^3$)	1027.45(6)	1804.67(11)	766.9(5)
Z	4	4	4
Calculated density ($g.cm^{-3}$)	1.761	1.685	2.005
Absorption coefficient (mm^{-1})	2.869	1.685	3.189
$F(000)$	544	944	472
θ range for data collection (°)	2.53 to 30.00	3.24 to 29.99	3.48 to 27.99
Limiting indices	$-11 \leq h \leq 10$	$-7 \leq h \leq 7$	$-11 \leq h \leq 11$
	$-16 \leq k \leq 16$	$-32 \leq k \leq 32$	$-12 \leq k \leq 12$
	$-16 \leq l \leq 15$	$-20 \leq l \leq 21$	$-13 \leq l \leq 13$
Reflections collected	8289	11986	6515
Unique reflections	2970 [$R_{int} = 0.0153$]	5220 [$R_{int} = 0.0246$]	3628 [$R_{int} = 0.0212$]
Absorption correction	Empirical	Empirical	Empirical
Max. and min. transmission	1.000 and 0.825	0.9666 and 0.4817	0.9390 and 0.2879
Refinement method	full-matrix least-squares on F^2		
Data/restraints/parameters	2970 / 0 / 119	5220 / 13 / 262	3628 / 0 / 230
Goodness-of-fit on F^2	1.968	1.377	1.302
Final R indices [$I > 2\sigma(I)$]	$R_1 = 0.0211$,	$R_1 = 0.0355$,	$R_1 = 0.0348$,
	$wR_2 = 0.0528$	$wR_2 = 0.0887$	$wR_2 = 0.0897$
R indices (all data)	$R_1 = 0.0228$,	$R_1 = 0.0379$,	$R_1 = 0.0381$,
	$wR_2 = 0.0531$	$wR_2 = 0.0898$	$wR_2 = 0.0957$
Extinction coefficient	0.0140(8)	-	-
Absolute structure parameter	-	0.007(10)	-
Largest diff. peak and	0.278 and	1.618 and	1.823 and
hole (e $Å^{-3}$)	-0.334	-0.872	-0.932

free imidazole), and high-power proton decoupling fields of *ca.* 88 kHz using the TPPM sequence,[165] were applied. A spinning speed of 6.0 kHz was used for all samples. Carbon chemical shifts were referenced with respect to TMS using the lower frequency chemical shift of solid adamantane (δ_{iso} = 29.5 ppm) as a secondary reference.

3.2.3 Solid-State ^{67}Zn NMR

Zinc-67 NMR experiments were performed at room temperature on a standard-bore 900 MHz (B_o = 21.14 T) Bruker Avance II spectrometer running TopSpin 1.3 software at the *National Ultrahigh-Field NMR Facility for Solids* in Ottawa (http://www.nmr900.ca). All ^{67}Zn NMR spectra were performed on home-built 4 mm and 7 mm H/X low-gamma NMR probes for stationary samples with a dual resonator design.[166] The probes were tuned to ^{67}Zn Larmor frequency of 56.316 MHz. Samples were ground into fine powders and packed into either 4 or 7 mm o.d. zirconia rotors. Experimental setup, pulse calibrations, and chemical shift referencing were performed using 1.0 M aqueous $Zn(NO_3)_2$ solution set to 0.0 ppm at room temperature. The central transition (CT) selective $\pi/2$ ^{67}Zn pulse width was found by dividing the non-selective $\pi/2$ pulse measured on the reference sample by $(I + 1/2) = 3$, and was typically 2.0 and 3.0 μs for the 4 and 7 mm probes, respectively. Spectra of stationary samples were collected using the QCPMG pulse sequence for complexes **1**-**4**, and the WURST-QCPMG sequence introduced recently by O'Dell and Schurko[96] for **5**. The interpulse delays in QCPMG experiments were typically 40-100 μs and were optimized on each sample in order to minimize the effects of probe ringing. The acquisition time for each echo was adjusted to attain a spikelet separation of either 2.0 or 4.0 kHz in the frequency domain, and the number of refocusing π pulses was set to acquire the complete transverse decay of the free induction decay (FID) for each sample. For the WURST-QCPMG experiment, a 50 μs WURST pulse length, swept across a range

of 1000 kHz at a rate of 20 MHz/ms, was used. The number of echoes was set to 32, and the spectral width to 1.0 MHz. Proton decoupling was applied during acquisition on the 4 mm probe (for **3** and **4**) and the 7 mm probe (for **5**) with *rf* fields of *ca.* 25 and 30 kHz, respectively. Recycle delays were 1.0 s for complex **1** and 0.5 s for the other four complexes. The stepped-frequency piecewise acquisition technique[99] was employed when the line widths of the CT ^{67}Zn NMR spectra were larger than the pulse width excitation profile. In such cases, the transmitter offset frequency was changed in even steps set as a multiple of the spikelet separation. The obtained subspectra were then co-added to construct the full CT NMR line shape. Analytical simulations of the experimental NMR spectra were performed, within the high-field approximation, using the WSOLIDS1 program.[54] Spectral stack plots were generated using SpecPlot.[167]

3.2.4 Quantum Chemical Calculations

Quantum chemical calculations were performed using *Gaussian 03*[100] running on SHARCNET clusters of high performance computing.[168] Calculations of the ^{67}Zn nuclear magnetic shielding and EFG tensors were carried out on models constructed using atomic coordinates from the X-ray structures determined in the present study for **1**, **4**, and **5**; the atomic coordinates used for **2** was obtained from the X-ray crystal structures of Dalosto *et al.*[155] For the zinc-histidinate complex (**3**), large discrepancies were observed between computational NMR results calculated using the published X-ray coordinates[156] and those determined experimentally; hence, full geometry optimization was performed on this complex using the B3LYP method and the 6-31G* basis set, and the optimized structure was subsequently used for NMR tensor calculations, whose results are reported herein. Shown in Figure 3.1 are the molecular cluster models used in calculations of the ^{67}Zn NMR parameters. Zinc-

67 electric field gradient and nuclear magnetic shielding tensors were calculated for the resulting structures using both the restricted Hartree-Fock (RHF) and density functional theory (DFT) methods. The B3LYP exchange functional was employed in the DFT calculations.[169,170] At both levels of theory, the 6-31G* and 6-311G* standard basis sets were employed on the zinc atoms, while the 6-311+G* basis set was used on atoms directly coordinated to zinc, and the 6-31G* basis was used on other atoms including hydrogens. The nuclear magnetic shielding tensors were calculated using the gauge-including atomic orbitals (GIAO) method.[107,108] Convergence criteria were unchanged and left at their default values. In order to compare between the calculated magnetic shielding constants and the experimentally measured chemical shifts, the calculated ^{67}Zn isotropic chemical shielding (σ_{iso}) values were converted into the corresponding isotropic chemical shifts (δ_{iso}) using the absolute shielding scale for ^{67}Zn,[171,172] derived from optical pumping and non-relativistic calculations:

$$\delta_{\mathrm{iso}} = 1832 - \sigma_{\mathrm{iso}}$$

where all quantities are in ppm, and 1832 ppm is the absolute shielding constant of an infinitely dilute Zn^{2+} ion in D_2O at 303 K. The computed ^{67}Zn EFG and chemical shift parameters were extracted from the *Gaussian 03* output files using the EFGShield program (version 2.3) developed in the laboratory of D.L. Bryce.[33]

3.3 Results and Discussion

3.3.1 Solid-State ^{13}C NMR

Carbon-13 CP/MAS NMR spectroscopy was performed on samples of the complexes studied herein in order to confirm their phase purity. Figures 3.2 and 3.3 show the natural

abundance ^{13}C CP/MAS spectra of these complexes, along with their corresponding free (unbound) ligands. The effect of metal-ligand interaction is manifested by the shifting of the isotropic ^{13}C resonances in the zinc-amino acid complexes, as compared to those in the free amino acid spectra. For example, an imidazole molecule has three magnetically nonequivalent carbons (labeled as C2, C4, and C5) that have respective isotropic chemical shifts of 136.7, 127.2, and 115.5 ppm (Figure 3.2a, top trace). In diimidazole zinc chloride (**1**), those peaks shift to 137.9 ppm for C2, to 126.3 ppm for C4, and to 116.7 ppm for C5. The presence of a fourth peak at 119.7 ppm in the diimidazole zinc chloride spectrum is due to the fact that the two imidazole rings in this complex are not related by symmetry, and therefore the three carbon atoms of each ring are not equivalent to their counterparts in the other imidazole ring. The isotropic chemical shifts of C_0, C_α, and C_β in L-alanine are 20.6, 50.9, and 177.7 ppm respectively. In zinc alaninate, these peaks shift to 19.3, 49.1, and 182.0 ppm, respectively, as shown in Figure 3.2b. The presence of peaks from unbound alanine in the spectrum of zinc alaninate is helpful in understanding the effect of zinc on the ^{13}C chemical shifts. In Figure 3.3, The presence of two distinct zinc sites in each of (**4**) and (**5**) is justified by the splitting of the ^{13}C peaks of C_α and C_β in (**4**), and the splitting of the peak from the carboxylate carbon in (**5**). Of note in the zinc cysteinate spectrum, Figure 3.3a, is the high degree of shift experienced by its carbons relative to those in the free cysteine molecule: the carboxyl carbon is shifted to a higher frequency by 7.2 ppm, the α-carbon is shifted to a lower frequency by 5.03 ppm, and the β-carbon is shifted to a higher frequency by 9.3 ppm.

3.3.2 Solid-State ^{67}Zn NMR

In this section, solid-state ^{67}Zn NMR spectra of the five complexes will be discussed in detail. All static solid-state NMR spectra, acquired at 21.1 T, and associated simulations are

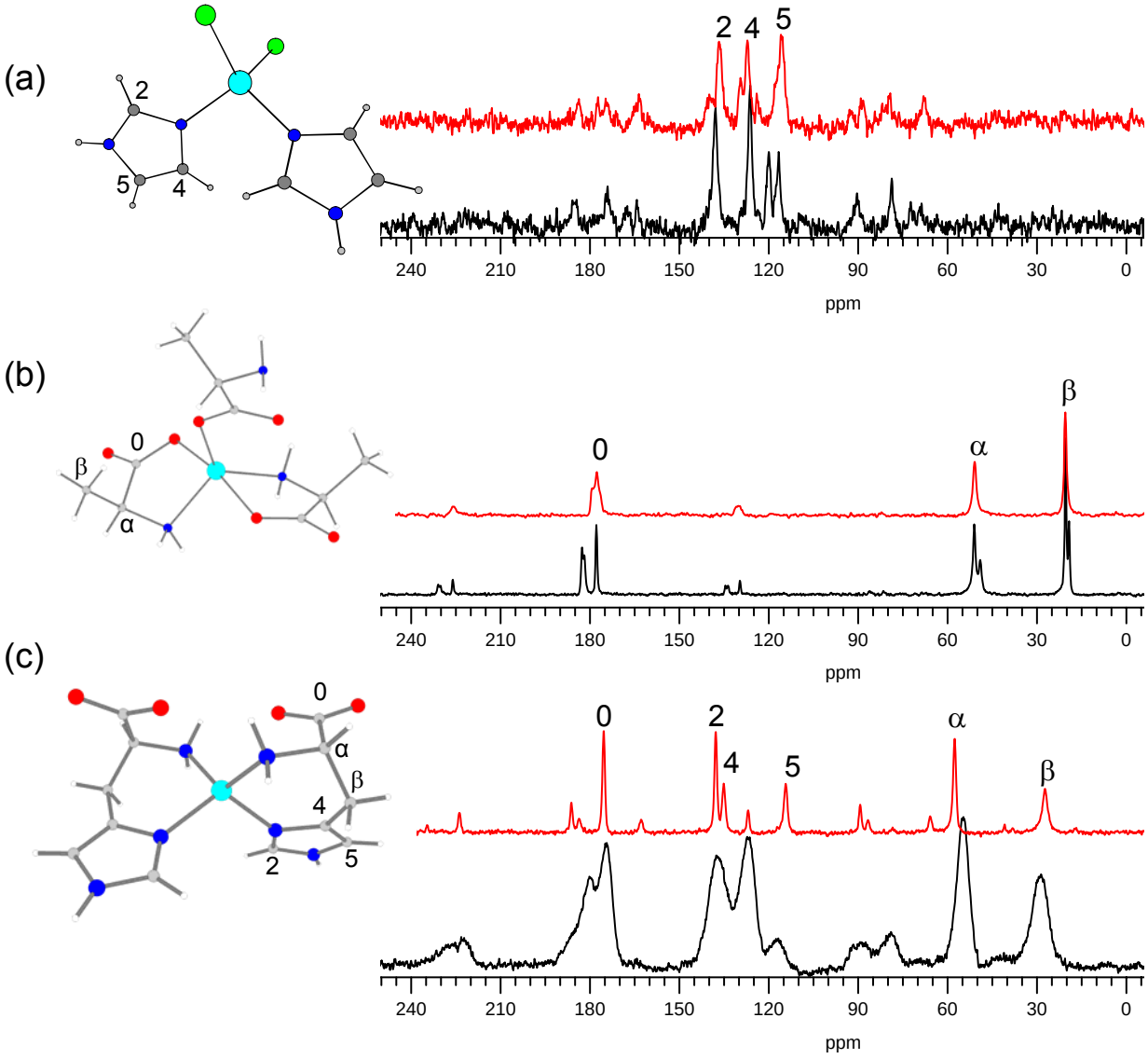

Figure 3.2: Natural abundance solid-state ^{13}C CP/MAS NMR spectra of: (a) Zn(imidazole)$_2$Cl$_2$ (bottom, black), imidazole (top, red). (b) Zn(L-Ala)$_2$ (bottom, black), L-alanine (top, red). (c) Zn(L-His)$_2$.2H$_2$O (bottom, black), L-histidine (top, red). All spectra were acquired at $B_o = 11.75$ T with a spinning rate of 6.0 kHz. Also shown for clarity the numbering scheme of the carbon atoms in each complex.

shown in Figures 3.4–3.12, and the corresponding parameters extracted from simulations are listed in Table 3.4. Experimental results will be analyzed in correlation to the crystal

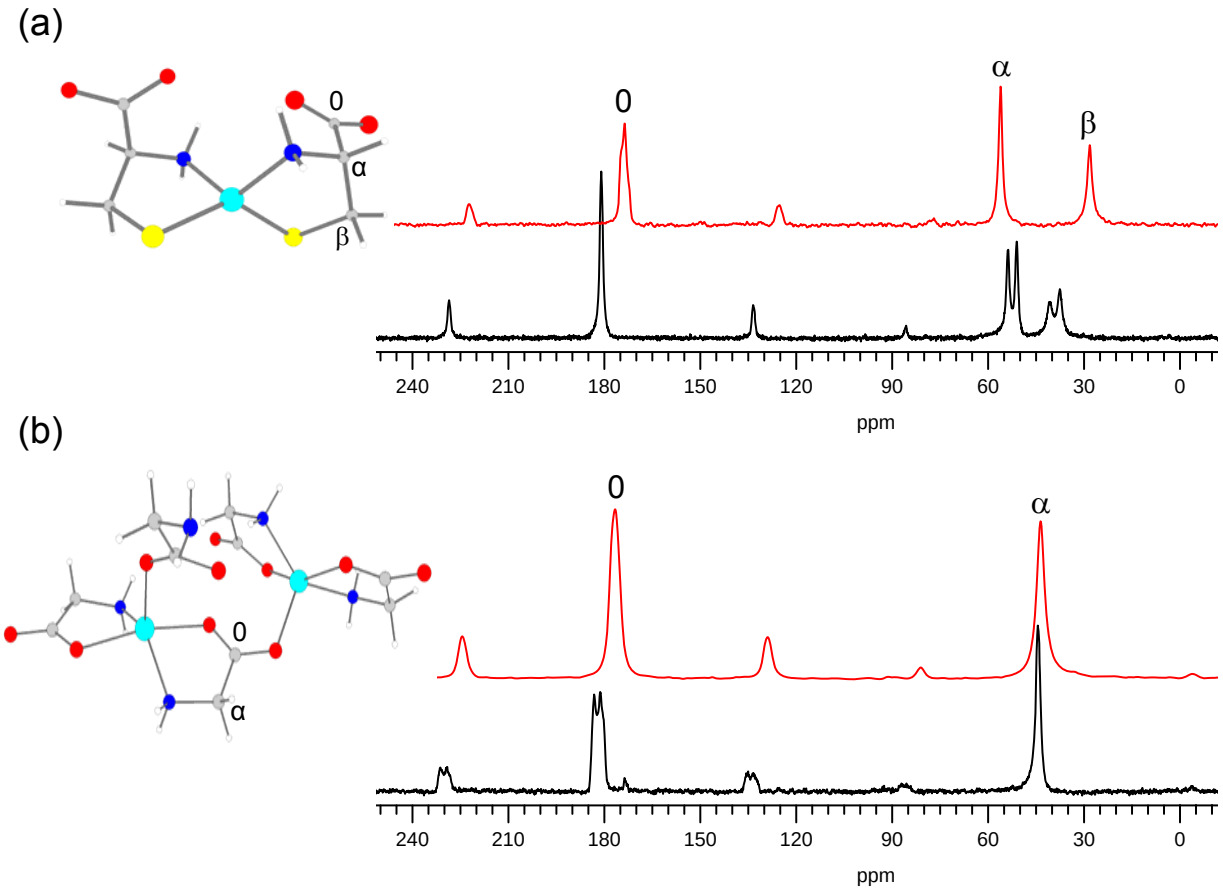

Figure 3.3: Natural abundance solid-state ^{13}C CP/MAS NMR spectra of: (a) Na_2Zn(L-Cys)$_2$.6H_2O (bottom, black), L-cysteine (top, red). (b) Zn(Gly)$_2$.H_2O (bottom, black), glycine (top, red). All spectra were acquired at $B_o = 11.75$ T with a spinning rate of 6.0 kHz. Also shown for clarity the numbering scheme of the carbon atoms in each complex.

structure of each complex, followed by a comparative analysis of the data from quantum chemical calculations.

Bis(imidazole)zinc(II) Chloride (1). The structure of Zn(imidazole)$_2$Cl$_2$, as determined by single-crystal X-ray diffraction at 243 K (monoclinic $P2_1/n$ space group), indicates that there is a single zinc ion in the asymmetric unit and that it is not located on any symmetry element (Figure 3.1a). This is consistent with an earlier report on this

Table 3.4: ^{67}Zn NMR parameters for the complexes investigated in this study as obtained from simulations of the experimental spectra.

complex			C_Q (MHz)	η_Q	δ_{iso} (ppm)
(**1**)	$Zn(imidazole)_2Cl_2$		7.0 ± 0.1	0.30 ± 0.05	265 ± 15
(**2**)	$Zn(L\text{-}Ala)_2$		9.6 ± 0.2	0.75 ± 0.05	140 ± 15
(**3**)	$Zn(L\text{-}His)_2.2H_2O$		11.2 ± 0.6	0.95 ± 0.05	185 ± 20
(**4**)	$Na_2Zn(L\text{-}Cys)_2.6H_2O$		26.4 ± 0.8	0.93 ± 0.05	180 ± 20
(**5**)	$Zn(Gly)_2 \cdot H_2O$	site 1	23.6 ± 0.6	0.2 ± 0.1	175 ± 20
		site 2	25.2 ± 0.8	0.2 ± 0.1	145 ± 20

compound.[154] The ^{67}Zn EFG and CS tensors are therefore not constrained to be axially symmetric or to have any particular orientation in the molecular frame of reference. The zinc atom lies at the centre of a distorted tetrahedron, at 2.24 and 2.26 Å from two chloride ions, and at 2.00 Å from two N(3) atoms of the imidazole rings. The bond angles in this tetrahedral arrangement range from 105.6 to 114.4°, in slight departure from the perfect tetrahedral angle. A small to moderate quadrupolar interaction is therefore expected at the zinc nucleus due to the slight lack of spherical symmetry in the local electronic environment. The ^{67}Zn QCPMG NMR spectrum of a stationary powdered sample acquired at 21.1 T indeed exhibits a second-order central-transition quadrupolar line shape corresponding to an EFG tensor with asymmetry parameter η_Q of 0.30 ± 0.05, consistent with the diffraction data which do not place the zinc ion on any symmetry element (Figure 3.4). The value of the quadrupolar coupling constant, 7.0 ± 0.1 MHz, is the smallest relative to the other complexes studied herein, but comparable to the values reported by Larsen *et al.* for $Zn(imidazole)_2(acetate)_2$.[76] The isotropic chemical shift value of 265 ± 15 ppm observed for this complex falls within the range of the values reported for other tetrahedrally coordinated zinc environments (Table 3.1). Of note in the iterative simulations was that this experimental NMR spectrum could also be reasonably simulated with a slightly different set of ^{67}Zn NMR parameters including a CS tensor with a span of 105 ± 15 ppm,

as shown in Figure 3.5. However, the lack of a second field-strength spectrum for this complex does not allow us to definitely demonstrate the presence of any ^{67}Zn shielding anisotropy.

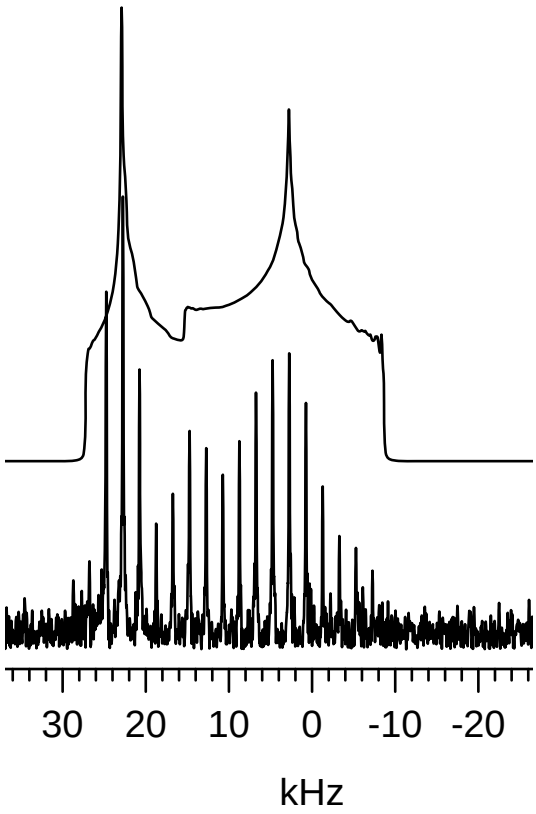

Figure 3.4: ^{67}Zn solid-state NMR spectrum of Zn(imidazole)$_2$Cl$_2$ in natural abundance at 21.1 T. Experimental (bottom) QCPMG spectrum was acquired under static conditions at room temperature with a recycle time of 1.0 s for 4096 transients and a 2 kHz spikelet separation. The best-fit simulation of the spikelet envelope is shown on top of the experimental spectrum. Parameters used in simulations are listed in Table 3.4.

Bis(L-alaninato)zinc(II) (2). This complex crystallizes in the low-symmetry $P2_1$ monoclinic space group, and it has a single zinc site in its asymmetric unit located on a general position.[155] The ^{67}Zn EFG and shielding tensors do not therefore exhibit any particular orientation in the molecular framework enforced by the crystallographic sym-

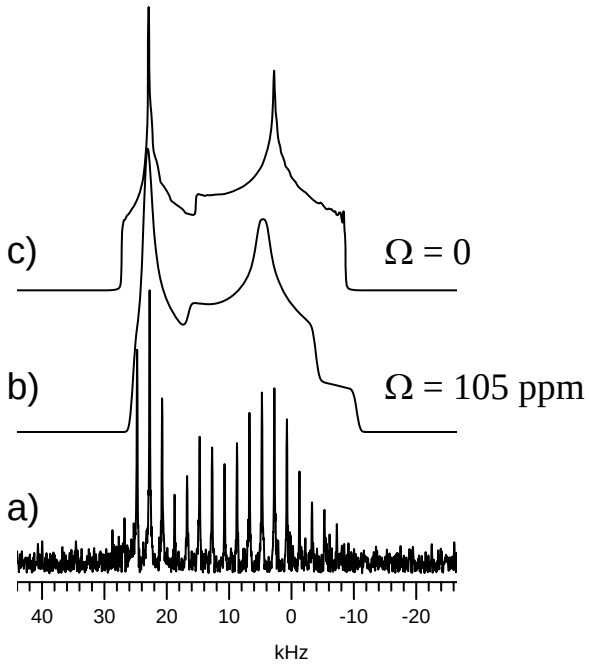

Figure 3.5: (a) Experimental static QCPMG spectrum of Zn(imidazole)$_2$Cl$_2$. (b) Best-fit simulation using the following parameters: $C_{\mathrm{Q}} = 6.85$ MHz, $\eta_{\mathrm{Q}} = 0.38$, $\delta_{\mathrm{iso}} = 270$ ppm, $\Omega = 105$ ppm, $\kappa = -0.2$, $\alpha = 60°$, $\beta = 45°$, $\gamma = 17°$. (c) Best-fit simulation using the parameters listed in Table 3.4: $C_{\mathrm{Q}} = 7.0$ MHz, $\eta_{\mathrm{Q}} = 0.30$, $\delta_{\mathrm{iso}} = 265$ ppm.

metry. The Zn^{2+} ion is five-fold coordinated, chelated by two alaninate ions acting as bidentate ligands (average Zn–N and Zn–O distances of 2.048 and 2.12 Å, respectively), and forming a fifth bond with a carboxylate oxygen of another symmetry-related alanine molecule at a Zn–O distance of 1.992 Å. The zinc-centered bond angles in this coordination geometry vary from 79.5 to 166.8°, giving rise to a nearly square pyramidal coordination. Shown in Figure 3.6 is the QCPMG ^{67}Zn NMR spectrum of a stationary sample of this complex, along with its best-fit simulations. The experimental spectrum was obtained by the co-addition of three frequency-stepped subspectra each with an experimental time of 4.5 h (Figure 3.7). The total breadth of the CT ^{67}Zn NMR spectrum is *ca.* 85 kHz. The C_Q value determined via simulation is 9.6 ± 0.2 MHz with $\eta_Q = 0.75 \pm 0.05$. Slightly improved simulations could be obtained by including a small ^{67}Zn CSA of 145 ppm, however the inability to obtain spectra at a different magnetic field precludes any definitive estimate of its influence.

Bis(L-histidinato)zinc(II) Dihydrate (3). A single-crystal X-ray diffraction structure of this zinc histidinate complex reveals that it has a tetragonal crystal structure (space group $P4_32_12$, Z = 4) with the Zn^{2+} ions located on two-fold rotation axes.[156] The four Zn^{2+} ions in the unit cell are related by rotation and translation, and thus only one resonance in the ^{67}Zn NMR spectrum is expected. Because of the local two-fold symmetry at the Zn^{2+} ions, the ^{67}Zn EFG and shielding tensors must each have one principal axis parallel to the C_2 rotation axis.[173] Each zinc atom is tetracoordinated by two bidentate histidinate anions, through their amino nitrogens and the π-nitrogens of the imidazole rings (the imidazole nitrogens that are close to the histidine side chain), in a highly distorted tetrahedral ZnN_4 geometry (see Figure 3.1c). There are two pairs of Zn–N bonds, one pair at 2.026 Å and the other slightly longer at 2.035 Å. These bonds are slightly longer than the average Zn–N bonds found in other tetrahedral ZnN_4 complexes listed

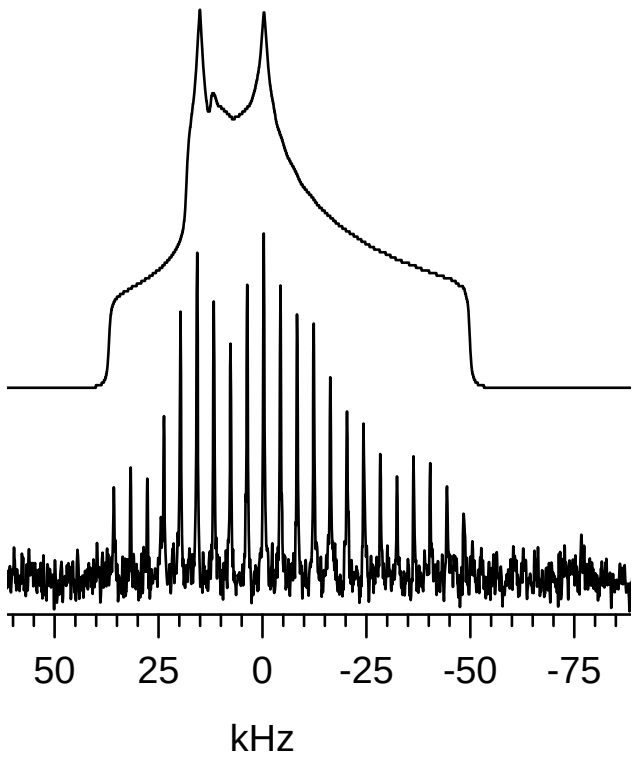

Figure 3.6: ^{67}Zn solid-state NMR spectrum of Zn(L-Ala)$_2$ at 21.1 T. Experimental (bottom) QCPMG spectrum of a stationary powdered sample was obtained by the co-addition of three QCPMG pieces. The best-fit simulation of the spikelet envelope is shown on top of the experimental spectrum. Parameters used in simulations are listed in Table 3.4.

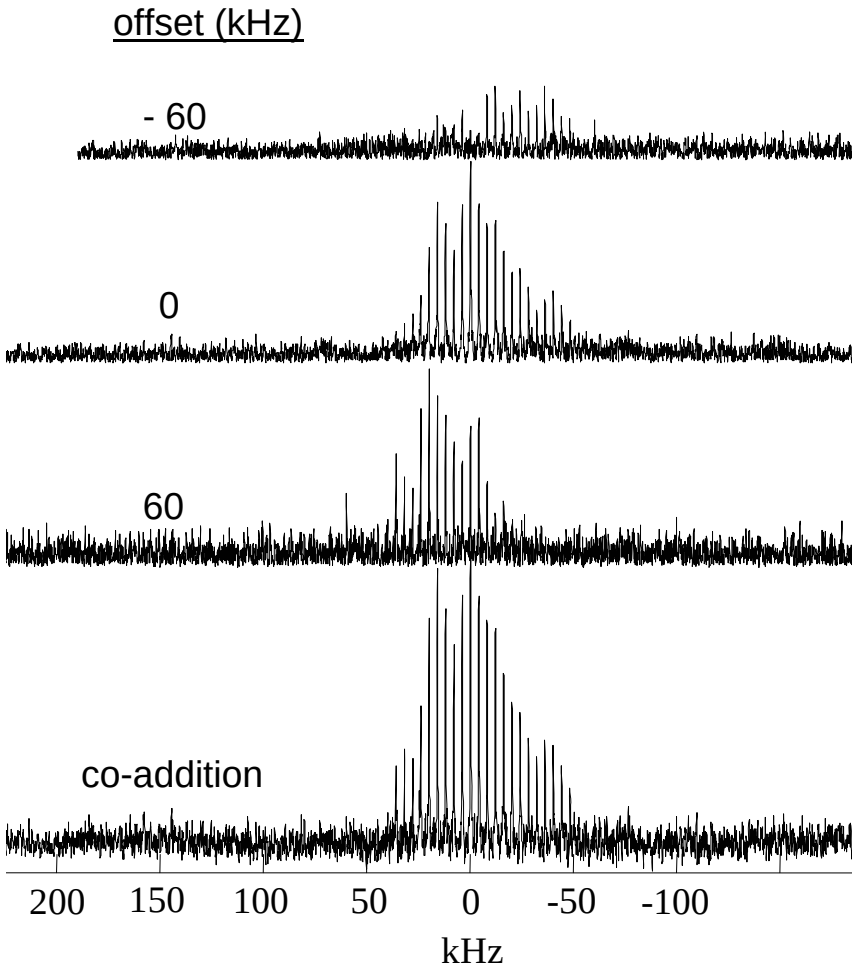

Figure 3.7: ^{67}Zn QCPMG frequency-stepped NMR subspectra of Zn(L-Ala)$_2$ at 21.1 T. Each QCPMG subspectrum was acquired with a recycle time of 0.5 s for 32768 transients and a 4 kHz spikelet separation. The bottom spectrum represents the co-addition of the three QCPMG pieces.

in Table 3.1, such as in $Zn(imidazole)_4(ClO_4)_2$ whose two Zn–N distances are 1.997 and 2.001 Å, and in $[Bp]_2Zn$ whose four Zn–N bonds range from 1.986 to 2.009 Å. The high distortion of the tetrahedral arrangement in the zinc histidinate complex is better reflected in the deviation of its N–Zn–N angles from their ideal tetrahedral values of 109.47° (they range from 96.5° to 121.6°). Based on these observations, a large ^{67}Zn EFG tensor, and hence a strong quadrupolar interaction, is expected for this complex. Figure 3.8 shows the ^{67}Zn QCPMG NMR spectrum of a stationary powdered sample at 21.1 T obtained with proton decoupling. This static QCPMG spectrum, having broad, featureless and almost Gaussian line shape, lacks the specific spectral features (shoulders and steps) that characterize NMR spectra dominated by second-order quadrupolar and/or chemical shielding interactions. The featureless line shape observed is likely due to the presence of disordered and/or amorphous electronic environment around the Zn^{2+} ions. It is well-known that such a disorder in the bonding around a certain nucleus causes a distribution in the NMR parameters of that nucleus, that results in Gaussian-like NMR line shapes.[70,83,174,175] The powder X-ray diffraction experiment performed on a sample of this complex provides another evidence of its highly disordered nature. It is quite difficult to extract NMR parameters accurately from such a featureless peak, especially those parameters related to the ^{67}Zn chemical shielding tensor. Simulation of the spikelet envelope in the experimental QCPMG spectrum gives the best-fit values of 11.2 MHz, 0.95, and 185 ppm for C_Q, η_Q, and δ_{iso}, respectively. The inclusion of CSA in the simulations did not provide any noticeable improvement for the calculated line shape. The observed C_Q value of 11.2 MHz for this complex is comparable to that of $[Bp]_2Zn$ (C_Q = 13.66 MHz), but much larger than that of $Zn(imidazole)_4(ClO_4)_2$ (C_Q = 2.80 MHz). This observation can be easily understood by inspecting the coordination bond lengths and angles of the zinc atom in the three species. The Zn–N bonds in zinc histidinate are on average 0.03 Å longer than those observed in the

other two complexes. From the perspective of coordination angles, the maximum deviation from perfect tetrahedral geometry for the N–Zn–N angles in Zn-histidinate (ranging from -13.0 to 12.2°) is very similar to that in $[Bp]_2Zn$ (from -13.3 to 12.4°), whereas this deviation is more modest in the perchlorate complex (ranging from -4.2 to 3.8°). This causes the ZnN_4 motif in $Zn(imidazole)_4(ClO_4)_2$ to be the least distorted tetrahedron, hence it has the smallest EFG, and accordingly the smallest C_Q value among the three systems. Furthermore, the smaller C_Q value of Zn-histidinate relative to that of $[Bp]_2Zn$ is because it has slightly longer Zn–N bonds and slightly smaller tetrahedral angular distortion, as the EFG magnitude varies inversely with r^3 according to a simple point charge model.

One comment should be made on the effect of proton decoupling on the experimental ^{67}Zn NMR spectrum of this complex. Figure 3.9 shows the ^{67}Zn QCPMG NMR spectrum of this complex obtained by the co-addition of three frequency-offset pieces, where each individual subspectrum was acquired without proton decoupling. The co-added spectrum is essentially identical to that in Figure 3.8 that was obtained in one step with proton decoupling. This demonstrates the significance of proton decoupling in increasing the signal-to-noise ratio of the NMR spectrum by removing the cumulative broadening caused by zinc-proton direct dipolar coupling, which is due to the presence of several protons at different distances from the zinc nucleus. The X-ray structure of this compound indicates that the shortest zinc-hydrogen distance is 2.494 Å, giving a direct dipolar coupling constant $R_{DD}(^{67}Zn, ^{1}H)$ of 485 Hz, using equation (2.44).

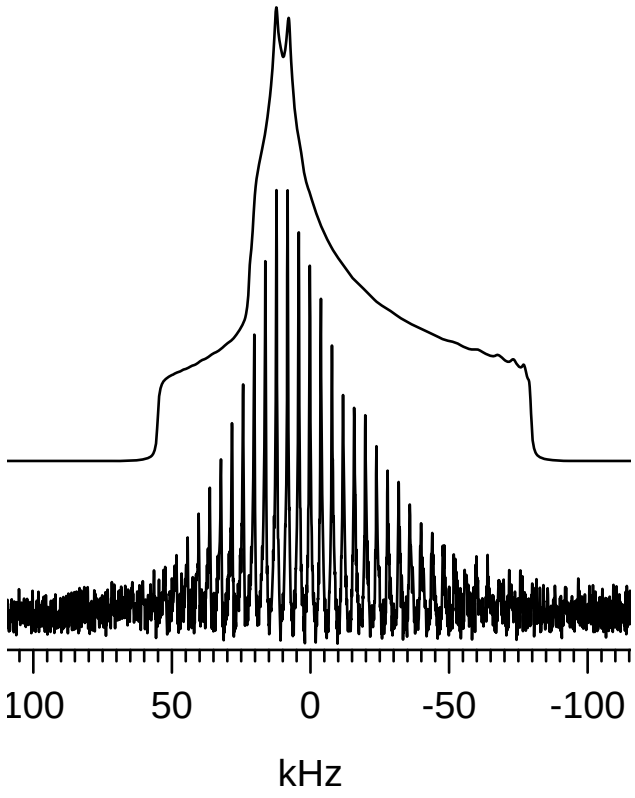

Figure 3.8: ^{67}Zn solid-state NMR spectrum of a stationary powdered sample of ^{67}Zn-enriched (87.8%) Zn(L-His)$_2$.2H$_2$O at 21.1 T. Experimental (bottom) QCPMG spectrum was acquired at room temperature with proton decoupling using a recycle time of 0.5 s for 8192 transients and a 4 kHz spikelet separation. The best-fit simulation is shown above the experimental spectrum. Parameters used in simulations are listed in Table 3.4.

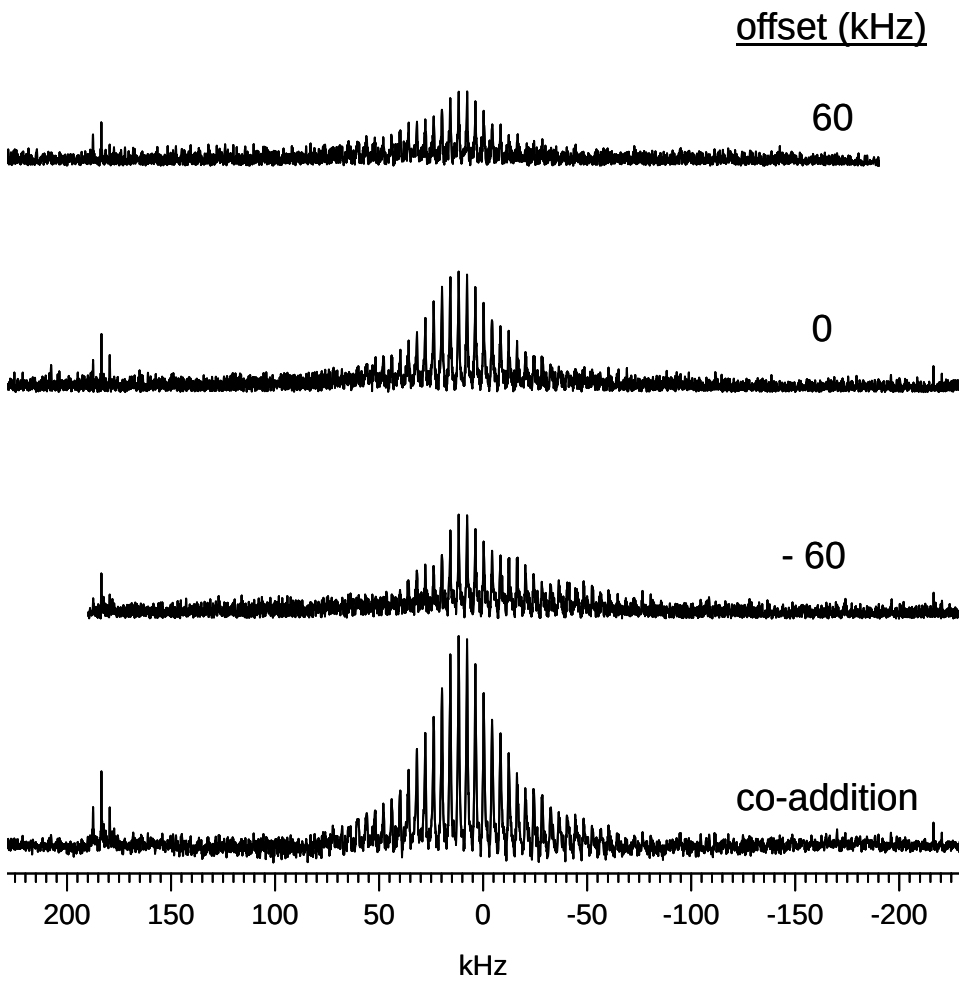

Figure 3.9: Solid-state ^{67}Zn QCPMG frequency-stepped NMR subspectra of ^{67}Zn-enriched powdered sample of Zn(L-His)$_2$.2H$_2$O at 21.1 T. Each piece was acquired without proton decoupling using a recycle time of 0.5 s for 8192 transients and a 4 kHz spikelet separation. The bottom spectrum represents the co-addition of the three QCPMG pieces.

Sodium Bis(L-cysteinato)zincate(II) Hexahydrate (4). According to our single-crystal X-ray structure of $Na_2Zn(L\text{-}Cys)_2.6H_2O$ (monoclinic C2, Z = 4), the asymmetric unit contains two independent $[Zn(L\text{-}Cys)_2]^{2-}$ anions. The four zinc atoms in the unit cell are related in pairs by symmetry, thereby forming two crystallographically and magnetically distinct sites in the repeating unit. The Zn atom in each anion is located on a C_2 rotation axis, and is tetracoordinated by two bidentate cysteine residues through their sulfur atom and the α-amino nitrogen. The bond lengths are similar in the two anions: Zn–S distances are 2.300 and 2.285 Å; Zn–N distances are 2.048 and 2.072 Å, respectively . The coordination angles are also similar, as they range from 91.3 to 133.1° in one anion , and from 91.5 to 132.2° in the other. These observations place the zinc atoms of both anions in similar tetrahedral ZnN_2S_2 environments, with both geometries being highly distorted. The static co-added ^{67}Zn QCPMG NMR spectrum of this complex is shown in Figure 3.10. The total breadth of the CT powder pattern is *ca.* 740 kHz, requiring the collection of 15 piecewise frequency-stepped subspectra each with an experimental time of 1.2 h (Figure 3.11). Despite the presence of two magnetically distinct zinc sites in this complex, the extremely large breadth of the powder line shape and their very similar chemical environments precluded their resolution, hence a single set of average parameters representative of both sites is reported. The extracted C_Q and η_Q values are 26.4 MHz and 0.93 respectively. Given the strong quadrupolar interactions experienced by both sites, reflected by the large magnitude of the observed ^{67}Zn C_Q, effects from the anisotropic zinc chemical shielding interaction are relatively too small to be detected, even at the very high magnetic field applied here.

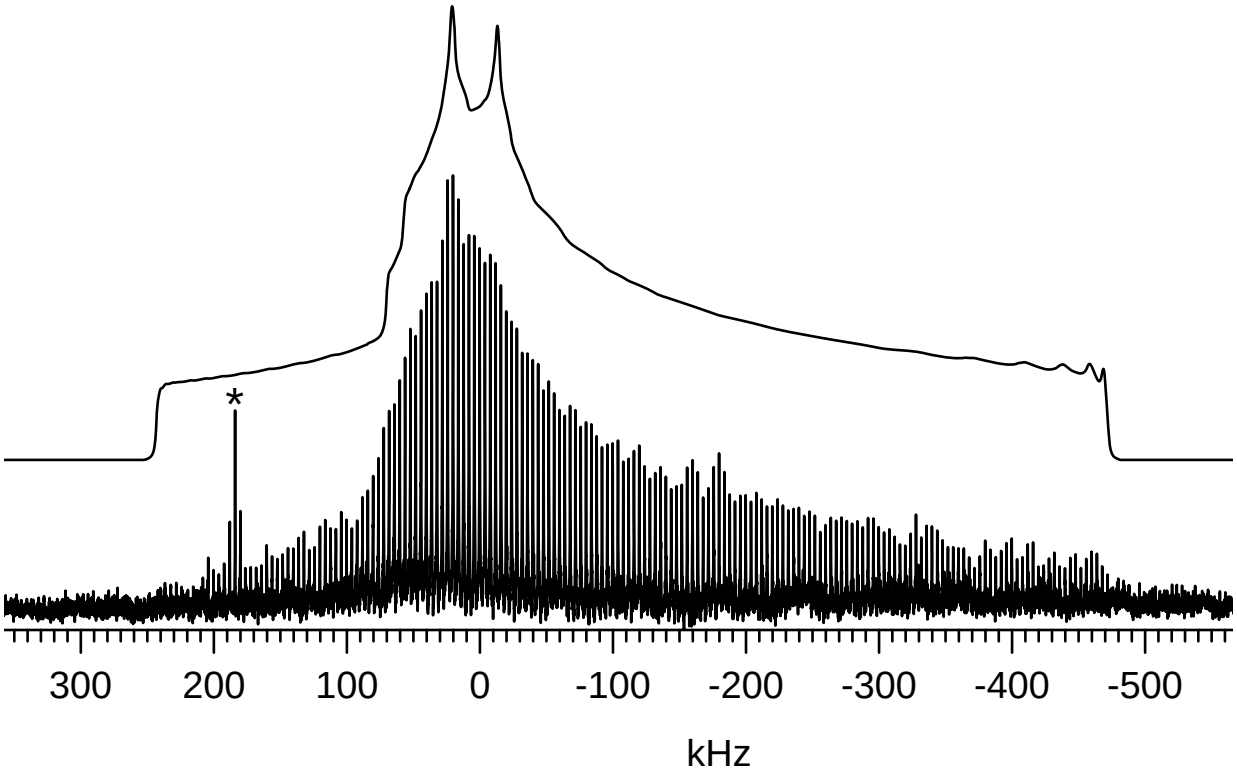

Figure 3.10: ^{67}Zn solid-state NMR spectrum of a stationary powdered sample of ^{67}Zn-enriched (87.8%) $Na_2Zn(\text{L-Cys})_2.6H_2O$ at 21.1 T. Experimental QCPMG spectrum is the co-addition of 15 pieces collected with 60 kHz steps in transmitter offset. The best-fit simulation is shown above the experimental spectrum. Parameters used in simulations are listed in Table 3.4. The asterisk denotes radio signal interference.

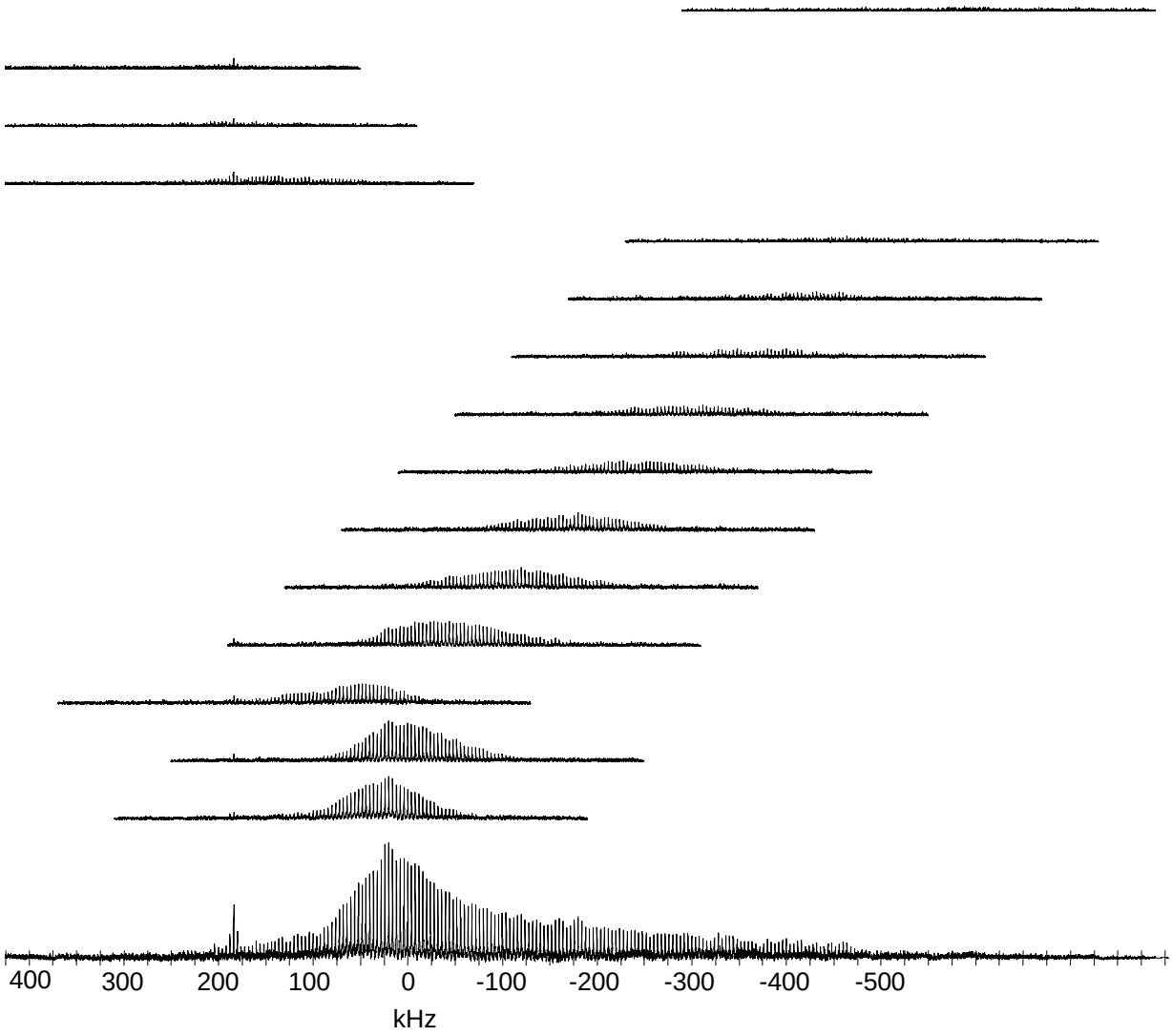

Figure 3.11: Solid-state ^{67}Zn QCPMG frequency-stepped NMR subspectra of a ^{67}Zn-enriched $Na_2Zn(L\text{-}Cys)_2.6H_2O$ at 21.1 T. Each piece was acquired with proton decoupling using a recycle time of 0.5 s for 8192 transients and a 4.0 kHz spikelet separation. The bottom spectrum represents the co-addition of the 15 QCPMG pieces collected with 60 kHz steps in transmitter offset.

Bis(glycinato)zinc(II) Monohydrate (5). A summary of the X-ray crystallographic data for the structure of $Zn(Gly)_2 \cdot H_2O$ is given in Table 3.3. This salt crystallizes in the triclinic space group $P\bar{1}$ and features four asymmetric units per unit cell. There are two crystallographically nonequivalent zinc ions in the unit cell. However, the coordination geometry of both ions are very similar; each site possesses approximate square-pyramidal five-coordinate ZnN_2O_3 geometry, where the zinc atom is chelated by two bidentate glycinate ions and forms the fifth apical bond with a carboxyl oxygen of a neighboring glycinate. Such linking gives rise to polymeric sheets, with water molecules lying between these sheets connected by hydrogen bonds. From an experimental perspective, the hygroscopic and polymeric nature of this complex made its ^{67}Zn NMR study the most troublesome among the complexes investigated in this work. Presented in Figure 3.12 is the ^{67}Zn co-added WURST-QCPMG NMR spectrum of a stationary powdered sample of zinc glycinate monohydrate, acquired in natural abundance at 21.1 T. For this complex, the WURST-QCPMG sequence was more successful in providing a spectrum with better S/N in a much shorter time than the standard QCPMG pulse sequence (see Figures 3.13 and 3.14). Twelve frequency-stepped standard QCPMG subspectra were required to construct the whole CT line shape, whereas the WURST-QCPMG sequence required only 3 subspectra (40 960 transients and 0.5 s recycle delay for each), thus reducing the total experimental time by a factor of 4, as well as reducing the spectral distortions. The quality of the co-added spectrum is not optimal, as it suffers from a low signal-to-noise (S/N) that can be attributed to the significantly short ^{67}Zn effective transverse relaxation time T_2^*. This limited the number of refocusing π-pulses that could be applied in the QCPMG experiment. Nonetheless, useful information can still be extracted from this spectrum. For instance, its total breadth is approximately 450 kHz. It is quite difficult to extract the relevant ^{67}Zn NMR parameters accurately for each of the two zinc sites from such a featureless spectrum.

Nevertheless, approximate values for δ_{iso}, C_Q, and η_Q could be estimated via simulation by using the calculated NMR parameters for these two sites as an initial guess. It must be noted that relatively large errors are reported for the observed ^{67}Zn NMR parameters of this complex.

Interpretation of observed ^{67}Zn NMR data. The ^{67}Zn isotropic chemical shifts observed in this study cover a range between 140 and 265 ppm, and the quadrupolar coupling constants are between 7.0 and 26.4 MHz. This variation in the zinc NMR parameters among the five complexes is not surprising given the differences in the local environments about the zinc atoms in these complexes. Many correlations can be made from the observed data. First, the isotropic chemical shifts of the tetrahedrally coordinated zinc atoms in **1**, **3**, and **4** fall very well within the range of chemical shifts for this coordination number determined from the data in Table 3.1. The trend followed by the quadrupolar coupling constants of the three complexes reflects the relative distortions that exist within the tetrahedral framework in each. In **2** and **5**, the three pentacoordinated zinc atoms are more shielded than the tetracoordinated ones, and lie roughly between the octahedral and the tetrahedral shift ranges. The striking observation is the large difference between the quadrupolar coupling constants of both complexes. The two zinc sites in **5** have very large quadrupolar coupling constants (23.6 and 25.2 MHz), whereas the ^{67}Zn C_Q value is only 9.65 MHz in **2**. This large difference is mainly due to long-range effects of the polymeric network on the EFG in **5**, as noted in the next section.

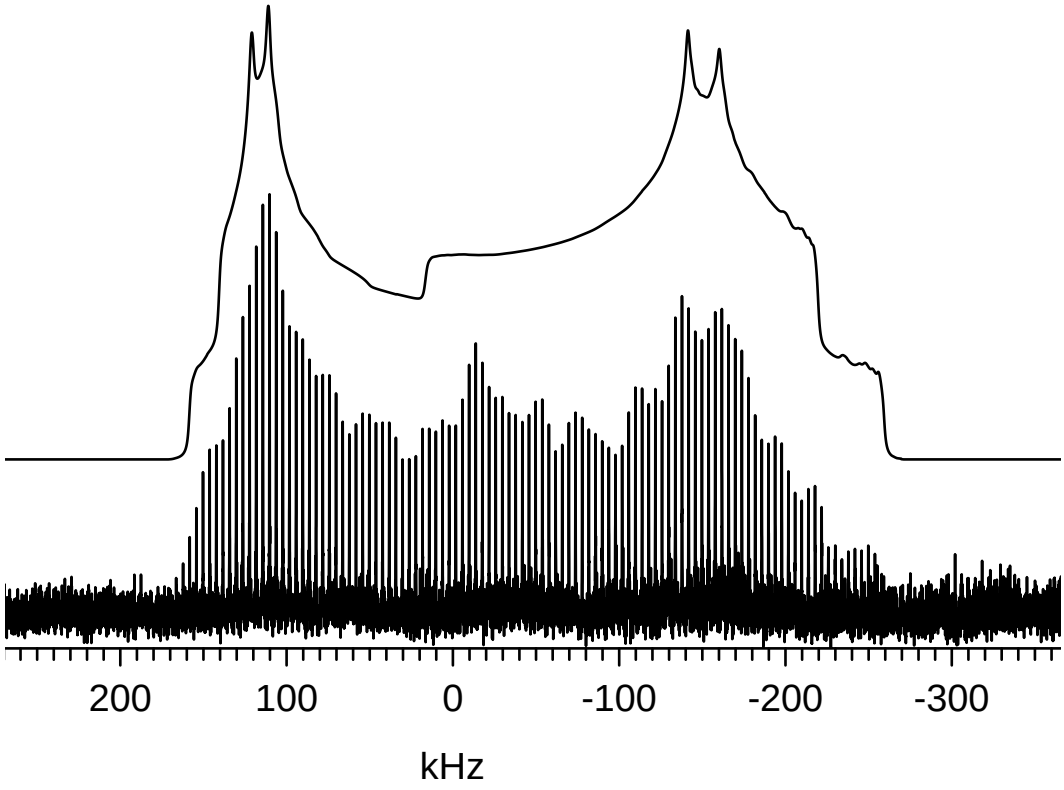

Figure 3.12: ^{67}Zn solid-state NMR spectrum of a stationary powdered sample of $Zn(Gly)_2 \cdot H_2O$ in natural abundance at 21.1 T. Experimental (bottom) WURST-QCPMG spectrum is the co-addition of three pieces collected with transmitter offsets of -125, 0, and 25 kHz. The simulated spectrum is shown above the experimental one. Parameters used in simulations are listed in Table 3.4.

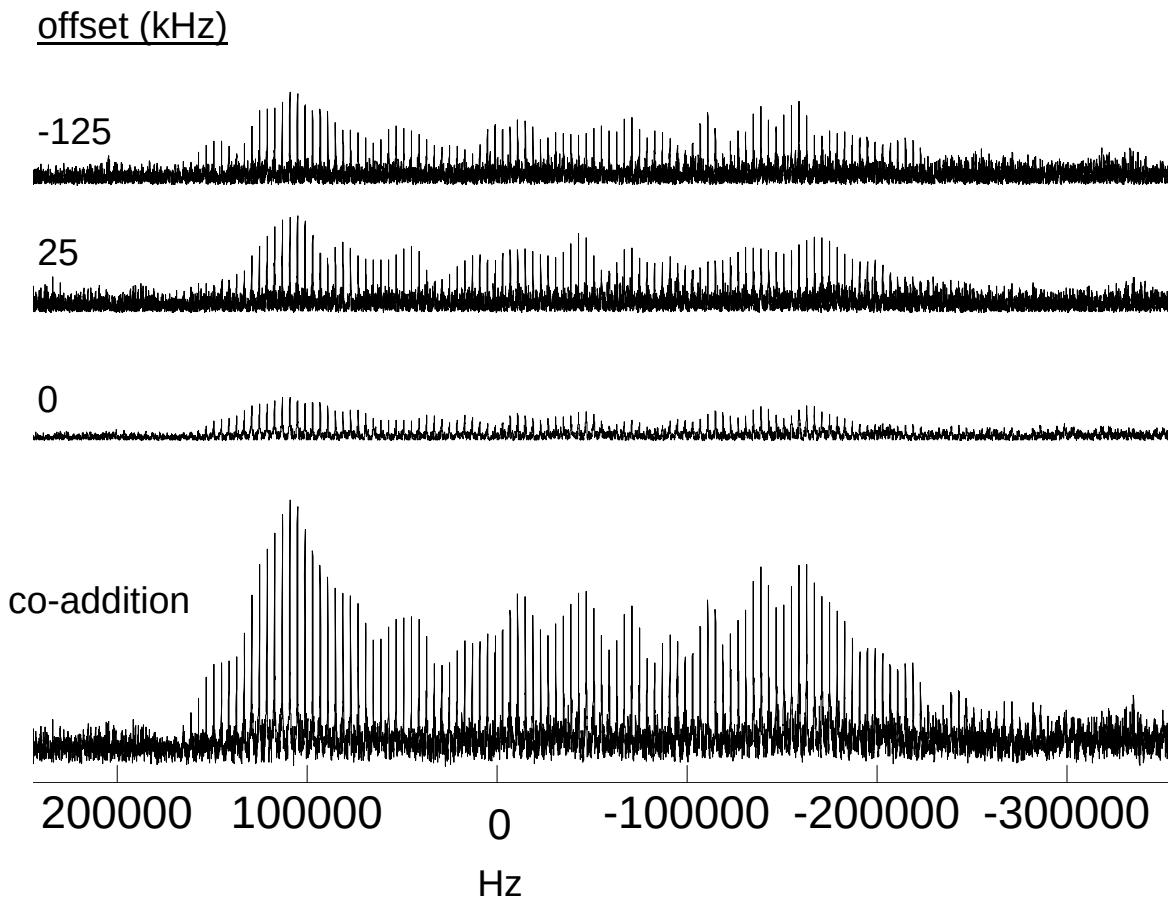

Figure 3.13: ^{67}Zn solid-state WURST-QCPMG frequency-stepped NMR subspectra of a powdered sample of $Zn(Gly)_2 \cdot H_2O$ at 21.1 T. Each subspectrum was acquired at room temperature with proton decoupling using a recycle time of 0.5 s for 40960 transients and a 4.0 kHz spikelet separation. The bottom spectrum represents the co-addition of the three subspectra.

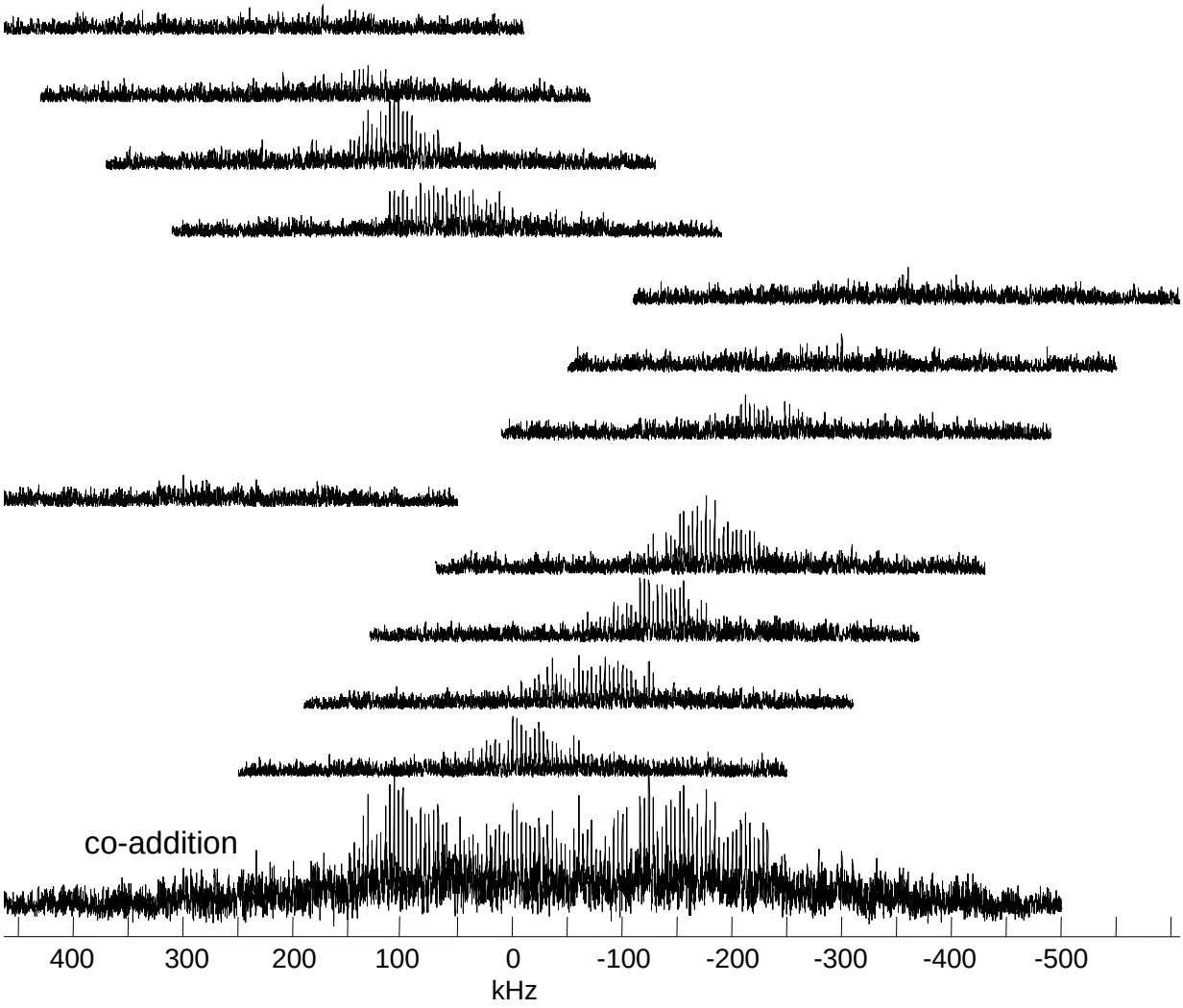

Figure 3.14: Frequency-stepped ^{67}Zn QCPMG NMR subspectra of a powdered sample of $Zn(Gly)_2 \cdot H_2O$ at 21.1 T. Each piece was acquired with 40960 scans, 0.5 s recycle delay, and 4.0 kHz spikelet separation. The bottom spectrum represents the co-addition of the 12 subspectra, collected with 60 kHz steps in transmitter offset. No proton decoupling was applied.

3.3.3 Quantum Chemical Calculations

To gain more insight into the experimentally observed results, a series of quantum chemical calculations of the ^{67}Zn EFG and CS tensors were performed on complexes **1**–**5**. The models used in quantum chemical calculations are based on the X-ray structure of each complex, and are shown in Figure 3.1. The results of these calculations are shown in Table 3.5. Also shown for direct comparison are the experimental NMR parameters measured in this study. In general, the calculations indicate that the B3LYP method employing the triple-zeta 6-311G* basis set on zinc atoms produces the closest agreement with experiment for both the ^{67}Zn EFG and CS tensor parameters. This is consistent with the results of Zhang *et al.* for their calculations of both the ^{67}Zn δ_{iso} and the C_{Q} values in a series of zinc complexes.[144] They used the B3LYP method with the same 6-311G* basis set on zinc, but with 6-311+G(2d) on ligand atoms, 6-311G* on other heavy atoms, and 6-31G* on hydrogen atoms. In our case, the smaller double-zeta 6-31G* basis set performs poorly for the calculations of the EFG and CS parameters, at both the RHF and B3LYP levels of theory. Moreover, the calculations at the RHF level with the 6-311G* basis on Zn provide a significant overestimation of the C_{Q} values, and an underestimation of δ_{iso}. At the B3LYP/6-311G* level, the computed coupling constants are in fair agreement with their corresponding experimental values, with the sole exception of the zinc cysteinate complex. Fair agreement between the calculated and experimental isotropic chemical shifts is also achieved at this level, except for the zinc glycinate salt, whose calculated values are much smaller than the observed ones. For the other complexes, the computed δ_{iso} values are all either within, or close to within, experimental error. Since the ^{67}Zn CSA could not be reliably extracted experimentally for the studied complexes, the quality of the computed spans and skews of the CS tensors can not be completely evaluated at this point. In light of the good agreement between the experimental data and the B3LYP/6-311G* calculations,

the discussion below is therefore based on the results computed from this basis set.

Table 3.5: Quantum chemical calculations of ^{67}Zn quadrupolar and chemical shift tensors for the complexes investigated in this study.

complex/method		C_Q(MHz)	η_Q	δ_{iso}(ppm)	Ω(ppm)	κ	$\alpha(^\circ)$	$\beta(^\circ)$	$\gamma(^\circ)$
Zn(imidazole)$_2$Cl$_2$	exptl	7.0 ± 0.1	0.30 ± 0.05	265 ± 15					
b3lyp/6-311G* on Zn		8.76	0.24	293	133	-0.10	46	45	156
b3lyp/6-31G* on Zn		-4.66	0.72	85	147	-0.39	79	23	0
rhf/6-311G* on Zn		9.50	0.17	102	109	-0.09	62	74	154
rhf/6-31G* on Zn		-4.37	0.81	-71	129	-0.32	292	9	157
Zn(L-Ala)$_2$	exptl	9.6 ± 0.2	0.75 ± 0.05	140 ± 15					
b3lyp/6-311G* on Zn		10.46	0.15	163	347	-0.68	112	57	41
b3lyp/6-31G* on Zn		7.97	0.25	7	232	-0.78	162	45	132
rhf/6-311G* on Zn		12.47	0.43	-12	254	-0.65	110	63	37
rhf/6-31G* on Zn		9.02	0.01	-134	191	-0.72	160	61	135
Zn(L-His)$_2$.2H$_2$O	exptl	11.2 ± 0.6	0.95 ± 0.05	185 ± 20					
b3lyp/6-311G* on Zn		-12.31	0.38	39	119	0.42	0	42	90
b3lyp/6-31G* on Zn		-9.09	0.53	-76	116	-0.18	0	35	90
rhf/6-311G* on Zn		-13.85	0.28	-107	92	0.41	0	37	90
rhf/6-31G* on Zn		-11.70	0.37	-206	97	0.12	0	22	90
Na$_2$Zn(L-Cys)$_2$.6H$_2$O	site 1	26.4 ± 0.8	0.93 ± 0.05	180 ± 20					
b3lyp/6-311G* on Zn		-15.6	0.42	362	267	0.57	0	27	90
b3lyp/6-31G* on Zn		-14.5	0.31	180	228	0.67	0	2	90
rhf/6-311G* on Zn		-20.3	0.51	160	247	0.67	0	19	90
rhf/6-31G* on Zn		-20.2	0.36	18	214	0.75	0	3	90
	site 2	26.4 ± 0.8	0.93 ± 0.05	180 ± 20					
b3lyp/6-311G* on Zn		-16.2	0.37	356	296	0.98	90	20	0
b3lyp/6-31G* on Zn		-15.3	0.24	180	271	0.93	90	3	0
rhf/6-311G* on Zn		-22.1	0.22	156	278	0.91	90	15	0
rhf/6-31G* on Zn		-21.8	0.17	17	255	0.87	90	5	0
Zn(Gly)$_2 \cdot$ H$_2$O	site 1	23.6 ± 0.6	0.2 ± 0.1	175 ± 20					
b3lyp/6-311G* on Zn		-22.0	0.27	89	346	0.38	177	4	5
b3lyp/6-31G* on Zn		11.4	0.85	11	297	0.12	100	87	89
rhf/6-311G* on Zn		-23.0	0.27	0	315	0.11	188	8	171
rhf/6-31G* on Zn		-15.2	0.60	-116	274	0.36	178	13	179
	site 2	25.2 ± 0.8	0.2 ± 0.1	145 ± 20					
b3lyp/6-311G* on Zn		-23.8	0.50	61	328	0.76	147	7	76
b3lyp/6-31G* on Zn		12.2	0.86	-1	274	0.44	78	83	107
rhf/6-311G* on Zn		-25.9	0.55	-9	283	0.28	154	10	48
rhf/6-31G* on Zn		-16.6	0.78	-125	242	0.54	22	12	140

One comment should be made on the cluster model used in the calculations performed on $Zn(Gly)_2 \cdot H_2O$. Preliminary calculations performed on small models of each of the two sites in this complex, where each model consists of one zinc atom coordinated to the three glycinate ligands of the first-coordination sphere, yielded EFG values that are much smaller than those determined by the NMR experiment. For example, the calculated quadrupolar coupling constants were -13.7 and -16.9 MHz for the two sites on the B3LYP/6-311G* method using this small cluster model. Since this compound has a polymeric structure, a larger cluster consisting of four zinc atoms and eight glycinate ligands was used, as depicted in Figure 3.1e. Each pair of zinc atoms in this model corresponds to one of the two crystallographically distinct zinc sites. For this larger cluster, the B3LYP/6-311+G* calculations predict the C_Q and η_Q values shown in Table 3.5, which lie in the proximity of the experimental parameters.

Figure 3.15 shows the orientations of the EFG tensors in the molecular frames of complexes **1**–**5**, as calculated at the B3LYP/6-311G* level. For complex **1**, the largest EFG component, V_{33}, is 31.3° off the longer Zn–Cl bond axis, while V_{22} lies at a pseudo-C_2 rotation axis at 45.6° from the slightly longer Zn–N axis, and V_{11} is at 49° off that axis. In complex **2**, V_{33} is almost perpendicular to the shortest Zn–O bond axis, while V_{22} lies at only 13.9° off that axis. The calculated EFG tensor orientations for the other three complexes, **3**–**5**, are also presented in Figure 3.15 for completeness. Since no conclusive evidence of CSA was available experimentally for all complexes, the calculated CS tensors are not shown.

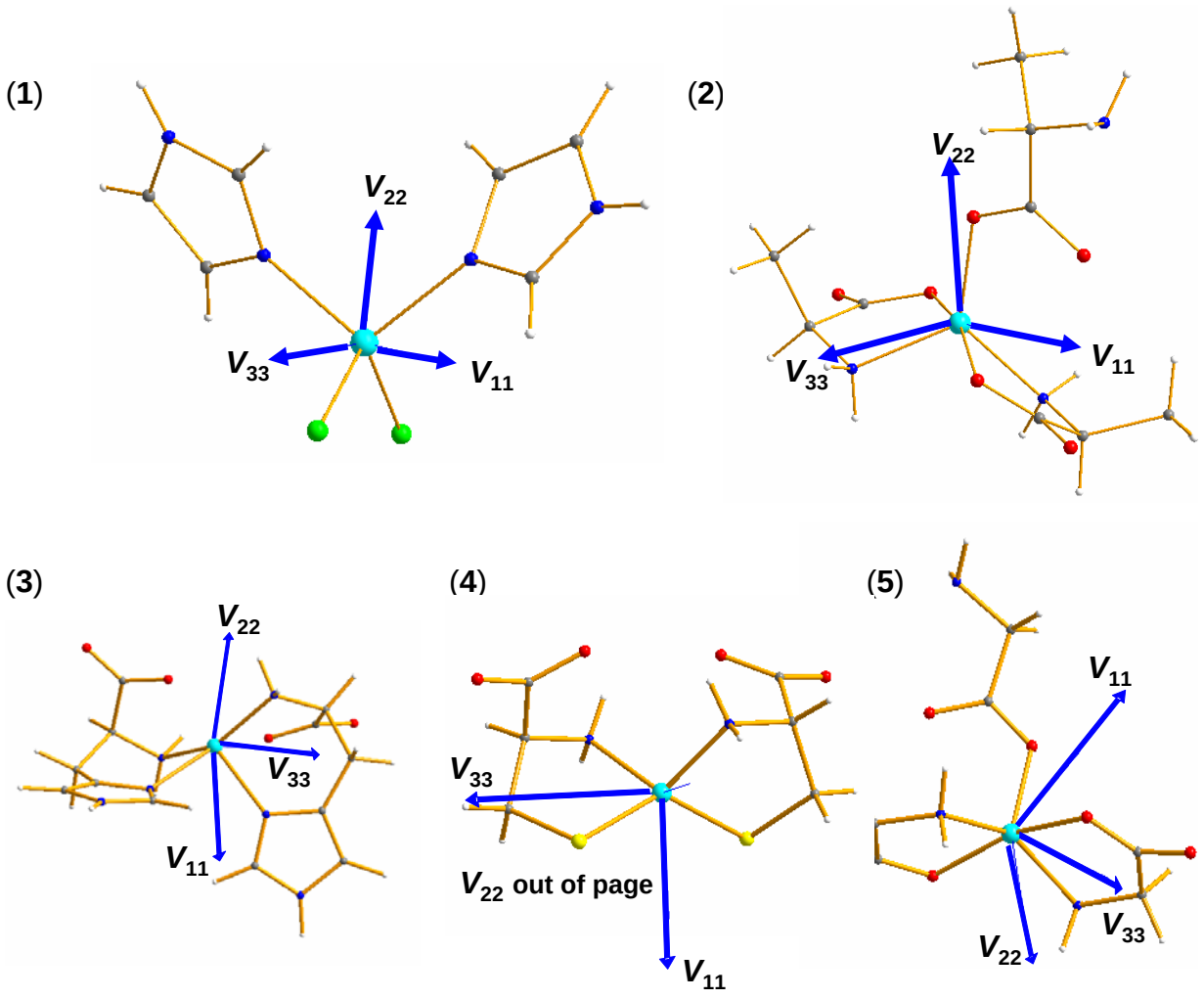

Figure 3.15: Orientations of ^{67}Zn EFG tensors for (**1**) Zn(imidazole)$_2$Cl$_2$, (**2**) Zn(L-Ala)$_2$, (**3**) Zn(L-His)$_2$.2H$_2$O, (**4**) Na$_2$Zn(L-Cys)$_2$.6H$_2$O, and (**5**) Zn(Gly)$_2\cdot$H$_2$O. All orientations are from the B3LYP/6-311G* calculations.

3.4 Conclusions

Zinc-67 SSNMR spectroscopy has been used to study the local environment of zinc in four zinc-amino acid complexes: those of glycine, L-alanine, L-histididne, and L-cysteine, along with diimidazole zinc chloride. The observed static NMR spectra were dominated by the second-order quadrupolar interaction. The EFG tensors were found to be dependent on the local binding environment, with ^{67}Zn quadrupolar coupling constants ranging from 7.05 to 26.4 MHz; the value of C_{Q} for sodium bis(L-cysteinato)zincate(II) hexahydrate, 26.4 MHz, is the second-largest observed to date by ^{67}Zn SSNMR. Moreover, the ^{67}Zn NMR parameters that have been determined for bis(L-alaninato)zinc and bis(glycinato)zinc monohydrate represent the first ^{67}Zn SSNMR study on zinc in pentacoordinated geometry. This study has demonstrated the advantages of very high magnetic fields, in combination with the stepped-frequency technique and the QCPMG pulse sequence, for the collection of extremely wide ^{67}Zn NMR spectra at room temperature under static conditions in the solid state. In some cases, magnetically and chemically different zinc sites could be distinguished and the corresponding NMR parameters for each individual site could be fairly extracted from such ultrawide line shapes. Quantum chemical calculations of the ^{67}Zn NMR parameters in the five complexes, carried out using the B3LYP method and the 6-311G* basis set on zinc atoms, were found to be in good agreement with the experimental values. All together, the present experimental-computational study represents a notable contribution toward an improved understanding of the relationship between ^{67}Zn NMR interaction tensors and molecular structure, and provides good opportunities for the application of ^{67}Zn SSNMR in the investigation of zinc-binding sites in larger and structurally-similar bioinorganic systems.

Chapter 4

Insights into the Zinc-Binding Sites in Insulin Hexamers by High-Field ^{67}Zn Solid-State NMR Spectroscopy

4.1 Introduction

Since 1869, when it was discovered that it was required for the growth of the fungus *Aspergillus niger*, zinc has been known to be essential for life.[111,112,176] As an integral constituent of a large number of enzymes, zinc is an essential cofactor for the observed biological functions of metalloenzymes and proteins, performing either catalytic, cocatalytic, or structural roles.[116,177–179] Due to its closed valence-shell configuration ($[Ar]3d^{10}$), direct characterization of the divalent zinc ion in these enzymes by ultraviolet-visible or electron paramagnetic resonance spectroscopies is impossible. Albeit a good starting point to elucidate the structure of zinc-containing biomaterials, the historical method of replacing the native Zn^{2+} ion with other divalent metals exhibiting either visible-UV transitions (Co^{2+}, Mn^{2+}),[180–182] or with the more friendly spin-$\frac{1}{2}$ $^{113}Cd^{2+}$ ion for solution NMR studies,[183–186] normally results in loss of biological activity of the probed system. Thus direct nuclear

magnetic resonance (NMR) spectroscopy of zinc nuclei should be the method of choice to explore the local structure of zinc in these materials. The greatest impediment to zinc NMR has been the very low intrinsic receptivity of the only magnetic isotope, ^{67}Zn, reflected by its low natural abundance (4.10%),[127] weak magnetic dipole moment (6.25 % that of ^{1}H),[127] and quadrupolar character (nuclear spin $I = \frac{5}{2}$) with a fairly large nuclear quadrupole moment ($Q = 15.0 \times 10^{-30}$ m^2).[126] These discouraging NMR properties translate directly into low sensitivity unless isotopic enrichment and large sample volumes, a remarkably costly process, are employed. Despite these difficulties, a number of ^{67}Zn solid-state NMR (SSNMR) results have been published in the past decades, including some inorganic salts, several zinc organic complexes, and few zinc metalloproteins at cryogenic temperatures (10 K), as has been shown in Table 3.1.

Current advances in SSNMR instrumentation, combined with the development of novel sensitivity improvement techniques based on the quadrupolar Carr-Purcell Meiboom-Gill (QCPMG) pulse sequence,[15–18] have provided excellent opportunities to detect the NMR signals of insensitive half-integer-spin quadrupolar nuclei like ^{67}Zn. The use of ultrahigh magnetic-field strengths increases the Larmor frequency of the observed nucleus. Consequently, in addition to the gain in inherent sensitivity produced by the larger difference in the Boltzmann population, technical problems due to acoustic probe ringing are eliminated at elevated magnetic-field strengths; and the line broadening due to second-order quadrupolar effects is also reduced as it scales inversely, when measured in Hz, with the Larmor frequency. The previous chapter of this thesis discussed the results of a high-field ^{67}Zn SSNMR study on the various zinc sites in several zinc-amino acid coordination complexes, as representatives of the active sites in biologically important materials, employing the QCPMG sequence on stationary powdered samples at room temperature. In the present chapter, we extend our research objectives toward more complex and challeng-

ing systems in an attempt to understand the role played by Zn^{2+} ions in the structural assembly and stability of bioinorganic molecules, where the Zn^{2+} ions are present in very dilute environments. The three polymorphs of the zinc-insulin hexamer are an ideal test case for the potential of solid-state ^{67}Zn NMR spectroscopy to observe dilute Zn^{2+} ions at ambient temperature without any special probe design, particularly that the zinc content in these hexamers is very low (0.4% by weight) even with the use of ^{67}Zn isotopic enrichment. A second goal is the determination of changes in ^{67}Zn NMR spectral characteristics as a function of ligand type and geometry in these systems, as the three polymorphs and their respective conformational transformations have been well-characterized by X-ray crystallography[150–152,187–193] and other spectroscopic methods.[194–197] Herein, we report the results of our ^{67}Zn SSNMR study for the characterization of the various zinc-binding sites in the three polymorphs of the zinc-insulin hexamers.

The biologically active form of insulin (henceforth referred to as IN) is the monomer (MW 5807.6), a polypeptide hormone consisting of two chains: an A chain (21 amino-acid residues) and a B chain (30 residues). The two chains are connected by two disulfide bridges (A7-B7 and A20-Bl9); an additional disulfide bond is present within the A chain connecting A6 to A11, as shown in Figure 4.1 for human insulin. The physiological storage form of this hormone is the zinc-insulin hexamer, and it is the zinc hexamer that is the primary component of all insulin pharmaceutical preparations used for the treatment of *diabetes mellitus*. Historically, the different forms of the zinc-insulin hexamer were named according to their zinc content:[187,190,198] the 2Zn-IN form containing two Zn^{2+} ions per IN hexamer, the 4Zn-IN form containing four Zn^{2+} ions per IN hexamer, and the phenol-stabilized 2Zn-IN form also containing two Zn^{2+} ions per IN hexamer. In 1989, Kaarsholm *et al.*[194] proposed the use of the terms T (tense) and R (relaxed) to describe the conformation of the structures rather than the zinc content. The (T) state describes an extended conformation

of the first eight residues of the B chain N-terminus of the insulin monomer, and the (R) state describes an α-helical confirmation of these residues. Thus, the 2Zn-IN form is now referred to as T_6, the 4Zn-IN form as T_3R_3, and the phenol- or phenolic-derivatives induced 2Zn-IN form as R_6.

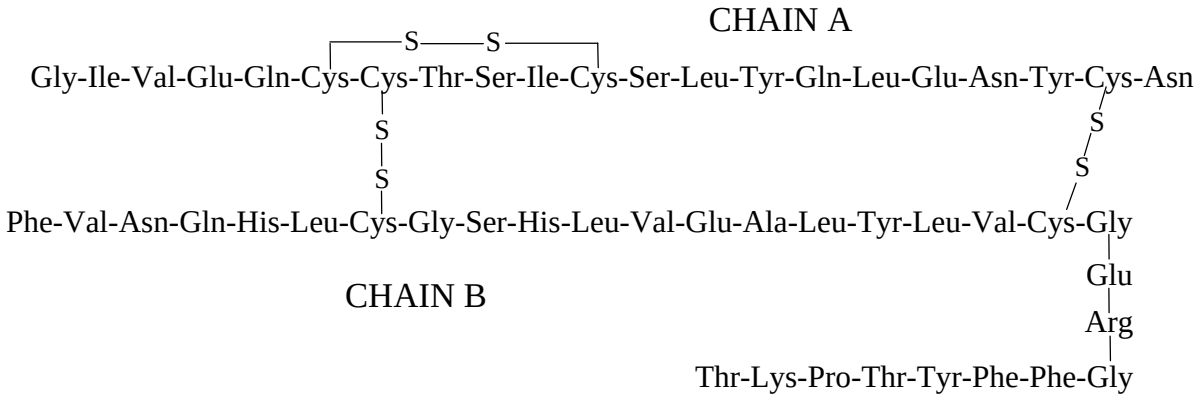

Figure 4.1: The amino-acid sequence of human insulin monomer.

It has been reported that the T_6, T_3R_3, and R_6 hexamers crystallize as rhombohedral crystals, in which the three-fold axis of the hexamer is coincident with the crystallographic three-fold axis, while R_6 insulin hexamer can also crystallize in the monoclinic system. The structure of the T_6 polymorph shows a rhombohedral crystal,[187,190,193] in which three equivalent IN dimers associate on an approximately three-fold axis to form a hexamer. The two monomers forming each dimer have identical conformations and are related to each other by a two-fold axis, which is perpendicular to the crystallographic three-fold axis. Each Zn^{2+} ion lies on a crystallographic three-fold axis in an octahedral environment formed by the three symmetry-related HisB10 residues and three water molecules.

The T_3R_3 form is obtained by the addition of chloride ion to the crystallizing medium, which induces a change in conformation of residues Bl-B8 from an extended conformation to an α helix in three of the six subunits.[188,189] As far as the coordination of Zn^{2+} ions is concerned, there is a single octahedral zinc site at one face of the hexamer as in the T_6 form. At the other face, three tetrahedral cavities, which can be occupied by Zn^{2+} ions, are formed. However, despite the presence of four zinc sites available for binding, less than three Zn^{2+} ions were found to bind to the T_3R_3 hexamer due to disordered zinc-coordinated histidine residues (Smith *et al.* have reported a total occupancy of 2.67).[189]

In the presence of phenol or phenolic-derivatives, added as a preservative, the T to R transition is driven to completion to produce an R_6 hexamer containing also two Zn^{2+} ions per IN hexamer as in T_6.[150,151,192] X-ray studies of the R_6 hexamer structure have shown that the phenol molecule stabilizes this new α-helical conformation. Each Zn^{2+} ion in the hexamer is coordinated to the τ-nitrogens (the imidazole nitrogens that are far from the histidine side chain) of three symmetry-related HisB10 molecules. The coordination sphere of zinc is completed by a chloride ion, resulting in a tetrahedral coordination. The hexameric structures in T_6, T_3R_3, and R_6 crystals are shown in Figure 4.2.

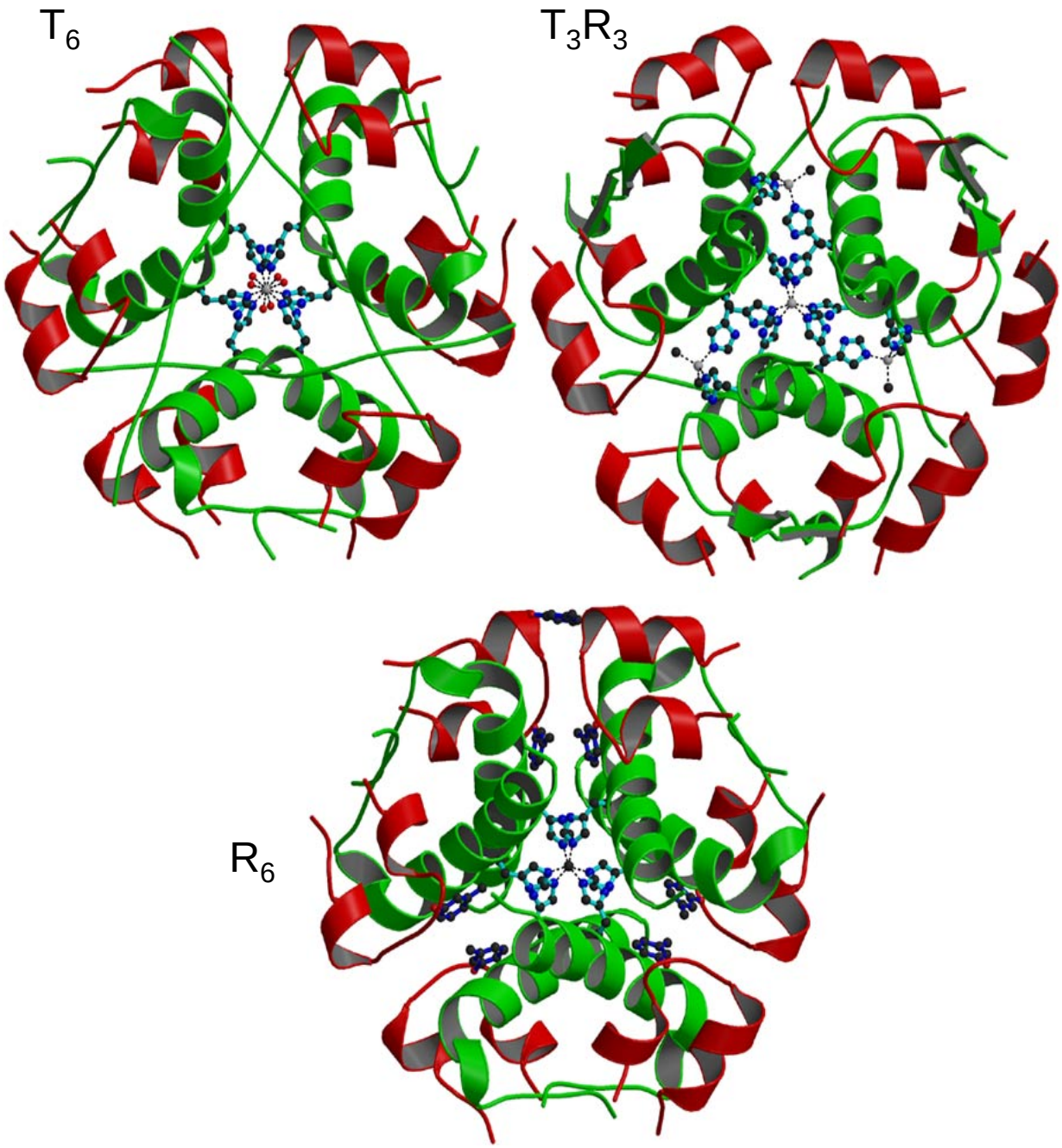

Figure 4.2: The complete hexamer structures in the T_6, T_3R_3, and the R_6 crystals. Ribbon diagrams of the three hexamers, viewed along the crystallographic threefold axes. Residues are colored according to chain type (A chain in red, B chain in green). Zinc ions are shown as grey spheres, along with the residues directly connected to them.

4.2 Experimental Section

4.2.1 Sample Preparation

Zinc-free human insulin was donated by Novo Nordisk A/S, Denmark. ^{67}Zn-enriched (94.2%) zinc oxide was purchased from Trace Sciences International (Ontario, Canada). Other reagents were purchased Sigma-Aldrich and used without further purification. $^{67}Zn(CH_3COO)_2$ aqueous solution (0.15 M) was prepared by dissolving 100 mg of the enriched ZnO completely in enough glacial acetic acid. Deionized water was then added up to a volume of 8 ml.

The three polymorphs of the zinc-insulin hexamers, enriched to 94.2% with ^{67}Zn, were prepared by controlling salt concentration, pH, and the presence of phenol in the aqueous solutions of insulin and zinc, using the methods of Smith and co-workers,[150,152,193] which are based on Schlichtkrull's procedure.[198] Typically, the insulin was first dissolved in the 0.02 M HCl with gentle stirring. The ^{67}Zn-enriched zinc acetate was then added, followed by sodium citrate buffer. The pH then was raised to approximately 8–9 by the addition of 0.75 M NaOH to ensure complete dissolution. The remaining reagents were then added. If the solution became turbid at this point, additional NaOH solution was added until the solution returned clear. The clear solution was then back-titrated with 0.75 M HCl to the final pH listed in Table 4.1. The samples were then warmed to 50 °C, placed in a Dewar, and allowed to cool very slowly to room temperature, then left to dry in air for another week. The resulting solids were dissolved in 0.01 M ammonium acetate, and then centrifuged off to obtain white precipitates that were air dried for several more days.

Table 4.1: Synthesis conditions for T_6, T_3R_3, and R_6 zinc-insulin hexamers.

	T_6	T_3R_3	R_6
Insulin (mg)	240	240	240
0.02 M HCl (ml)	24.0	24.0	24.0
0.15 M zinc acetate (ml)	2.40	2.40	2.40
0.20 M trisodium citrate (ml)	12.0	12.0	12.0
acetone (ml)	8.0	8.0	-
water (ml)	1.60	1.60	-
5% phenol (ml)	-	-	9.60
sodium chloride (g)	-	2.88	2.88
final pH	6.21	6.22	8.52

4.2.2 Solid-State ^{13}C NMR

Natural abundance $^{13}C\{^1H\}$ cross-polarization magic-angle spinning (CP/MAS) NMR spectra of the three zinc-insulin polymorphs, as well as that of zinc-free insulin, were acquired at 11.75 T [$\nu_o(^{13}C)$ = 125.76 MHz] on a Bruker Avance DRX-500 spectrometer with a Bruker 4 mm MAS NMR probe. A ^1H $\pi/2$ pulse width of 4.00 μs, optimized contact time of 2.0 ms, recycle delays of 10 s, and high-power proton decoupling fields of *ca.* 88 kHz using the TPPM sequence,[165] were applied. A spinning speed of 7.0 kHz was used for all samples. Carbon chemical shifts were referenced with respect to TMS using the low frequency chemical shift of solid adamantane (δ_{iso} = 29.5 ppm) as a secondary reference.

4.2.3 Solid-State ^{67}Zn NMR

Zinc-67 NMR experiments were performed at room temperature on a standard-bore 900 MHz (B_o = 21.14 T) Bruker Avance II spectrometer at the *National Ultrahigh-Field NMR Facility for Solids* in Ottawa (http://www.nmr900.ca). ^{67}Zn NMR spectra were acquired

with proton decoupling (*ca.* 30 kHz *rf* field) on a home-built 4 mm H/X low-gamma NMR probe for stationary samples with a dual resonator design.[166] In some cases, when the amount of sample was sufficient, a Bruker single-channel 7 mm MAS probe was also used. The probes were tuned to ^{67}Zn Larmor frequency of 56.316 MHz. Samples were ground into fine powders and packed into either 4 or 7 mm o.d. zirconia rotors. Experimental setup and chemical shift referencing were performed using 1.0 M aqueous $Zn(NO_3)_2$ solution set to 0.0 ppm at room temperature. Spectra of stationary samples were collected using the WURST-QCPMG pulse sequence of O'Dell and Schurko.[96] Two WURST-80 excitation and refocusing pulses, each of duration 50 μs, were swept across a range of 1000 kHz at a rate of 20 MHz/ms. The echo delay between these pulses was optimized to 140 μs. The number of echoes was set to 32, and the acquisition time for each echo was adjusted to 0.5 ms to attain a spikelet separation of 2.0 kHz in the frequency domain. A recycle delay of 0.5 s was sufficient for all samples. Analytical simulations of the experimental NMR spectra were performed using the WSOLIDS1 program[54] developed in the laboratory of Prof. Rod Wasylishen. Spectral stack plots were generated using SpecPlot.[167]

4.2.4 Quantum Chemical Calculations

Quantum chemical calculations were performed on models for the zinc ions binding sites in the three zinc-insulin hexamers using *Gaussian 03*[100] running on SHARCNET.[168] The molecular cluster models for the zinc-binding sites were constructed using atomic coordinates available from X-ray crystallography of the three hexamers: T_6 (PDB code 1MSO, 1.0 Å resolution), T_3R_3 (PDB code 1BEN, 1.4 Å resolution), and R_6 (PDB code 1EV3, 1.78 Å resolution). The models simply consist of a single Zn^{2+} ion coordinated to its primary ligands: the three HisB10 residues and three water molecules for the octahedral sites in T_6 and T_3R_3, and the three HisB10 residues and a chloride ion for the tetrahedral sites in R_6

and T_3R_3, as shown in Figure 4.3. Proton positions were optimized at the B3LYP/6-31G** level, with the positions of the heavy atoms kept frozen during this optimization. Zinc-67 electric field gradient (EFG) and nuclear magnetic shielding tensors were calculated for the resulting models using the density functional theory (DFT) method employing the B3LYP exchange functional.[169,170] The standard 6-311G* basis set was used on the zinc atoms, while the 6-311+G* basis set was used on atoms directly coordinated to zinc, and the 6-31G* basis was used on other atoms including hydrogens. The nuclear magnetic shielding tensors were calculated using the gauge-including atomic orbitals (GIAO) method.[107,108] The computed ^{67}Zn NMR parameters were extracted from the *Gaussian 03* output files using the EFGShield program (version 2.3) developed in the laboratory of D.L. Bryce.[33]

4.3 Results and Discussion

4.3.1 Solid-State NMR

The ^{67}Zn solid-state NMR spectra exhibit anisotropic line shapes that are dominated by the Zeeman, quadrupolar, and the nuclear magnetic shielding (or chemical shift) interactions. Using equations (2.39) and (2.81), one can study the combined influence of the three interactions on the central transition of a ^{67}Zn spin (or any other half-integer quadrupolar spin) in a static solid powder by measuring the NMR frequency response in the presence of the three interactions:

$$\begin{aligned}\nu(\theta,\phi,\vartheta,\varphi) &= \nu_{\mathrm{o}}(\delta_{11}\sin^2\theta\cos^2\phi + \delta_{22}\sin^2\theta\sin^2\phi + \delta_{33}\cos^2\theta) \\ &\quad -\frac{9C_{\mathrm{Q}}^2}{6\nu_{\mathrm{o}}}\frac{\left[I(I+1)-\frac{3}{4}\right]}{\left[2I(2I-1)\right]^2}\left[E(\varphi)\cos^4\vartheta + F(\varphi)\cos^2\vartheta + G(\varphi)\right] \qquad (4.1)\end{aligned}$$

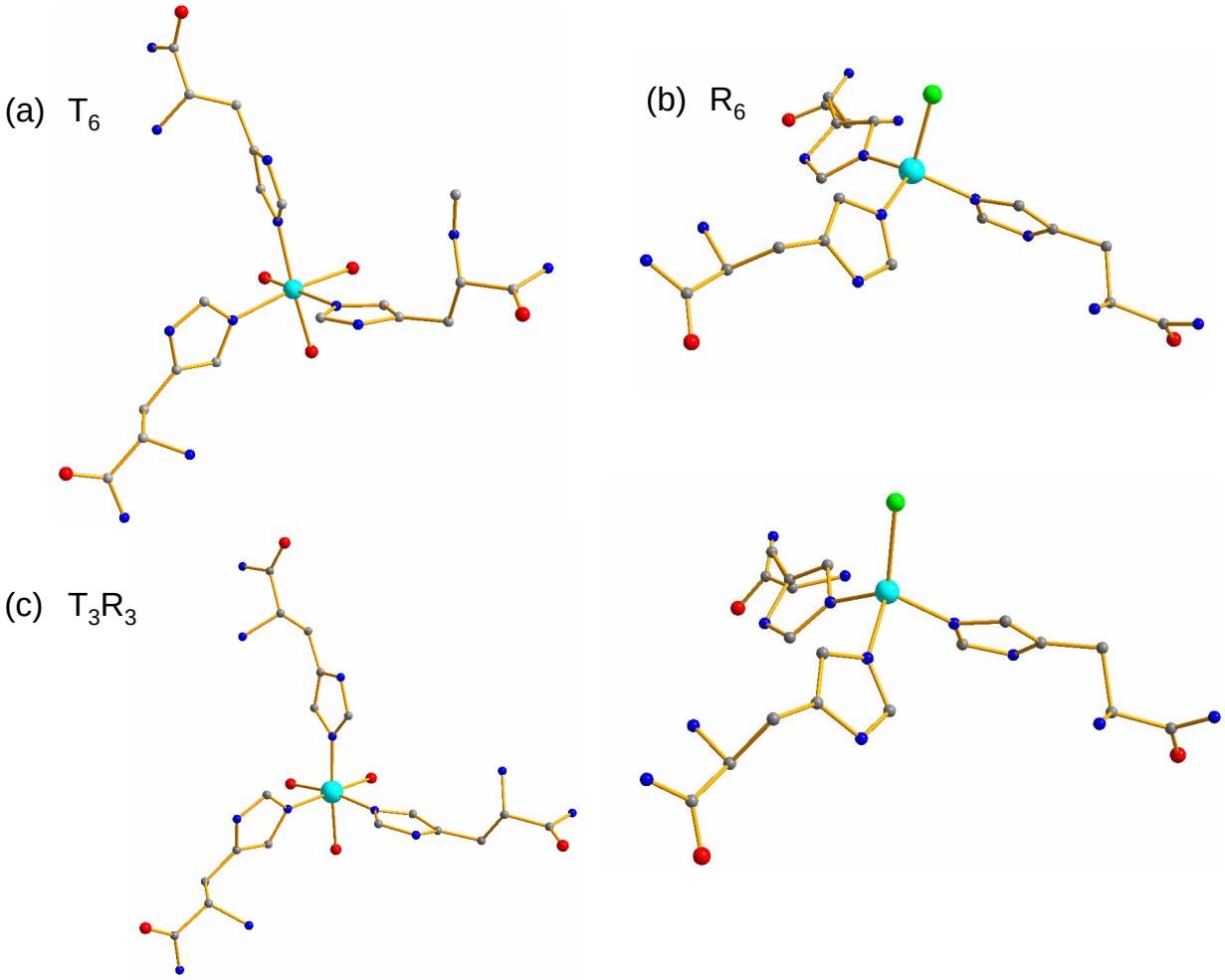

Figure 4.3: Coordination environments of the zinc ions in the zinc-binding sites of the insulin hexamers. (a) The octahedral coordination in T_6, (b) the tetrahedral coordination in R_6, and (c) both the octahedral and tetrahedral coordinations in T_3R_3. These are the models used in quantum chemical calculations of the ^{67}Zn NMR interaction tensors in the present work. Zinc is shown in cyan, chlorine in green, oxygen in red, nitrogen in blue, and carbon in gray. Hydrogens were removed for clarity.

where

$$\begin{aligned} E(\varphi) &= -\frac{27}{8} + \frac{9}{4}\eta_{\mathrm{Q}}\cos 2\varphi - \frac{3}{8}\eta_{\mathrm{Q}}^2\cos^2 2\varphi \\ F(\varphi) &= \frac{30}{8} - \frac{1}{2}\eta_{\mathrm{Q}}^2 - 2\eta_{\mathrm{Q}}\cos 2\varphi + \frac{3}{4}\eta_{\mathrm{Q}}^2\cos^2 2\varphi \\ G(\varphi) &= -\frac{3}{8} + \frac{1}{3}\eta_{\mathrm{Q}}^2 - \frac{1}{4}\eta_{\mathrm{Q}}\cos 2\varphi - \frac{3}{8}\eta_{\mathrm{Q}}^2\cos^2 2\varphi \end{aligned}$$

All parameters have their usual meanings defined in Chapter 2. The angles (θ,ϕ) and (ϑ,φ) describe the respective orientations of the principal axis systems of the chemical shift and quadrupolar coupling tensors with respect to the direction of the external magnetic field, B_{o}.

Solid-state ^{67}Zn NMR spectra of the three zinc-insulin hexamers will be discussed in parallel with their ^{13}C CP/MAS NMR spectra. The ^{67}Zn isotropic chemical shift (δ_{iso}), quadrupolar coupling constant (C_{Q}), and quadrupolar asymmetry parameter (η_{Q}) extracted via spectral simulations for the three zinc-insulin hexamers are listed in Table 4.2. The ^{13}C CP/MAS NMR spectrum of the T_6 sample, Figure 4.4a, shows that it is highly dominated by a citrate-containing impurity. Ideally, this spectrum should exhibit very similar features to that of zinc-free insulin (Figure 4.4b), as both have the same amino acid chains in their backbones. The citrate impurity in the synthesized T_6 sample is confirmed by comparing the T_6 ^{13}C spectrum to that of a commercial zinc citrate dihydrate (Figure 4.4c). It is obvious that this T_6 sample is highly contaminated with zinc citrate, although small differences in the ^{13}C isotropic chemical shifts are noticed between the spectra in (a) and (c). This can be attributed to a different crystallographic form of zinc citrate present in the T_6 sample. Nonetheless, a close examination of both the T_6 and the free insulin spectra reveals that the three main peaks of the insulin are present in the T_6 spectrum, albeit with very low intensities.

Table 4.2: Experimental ^{67}Zn NMR parameters for the zinc sites in the three zinc-insulin hexamers T_6, T_3R_3, and R_6.

polymorph	C_Q (MHz)	η_Q	δ_{iso} (ppm)
T_6	7.3 ± 0.2	0.75 ± 0.05	80 ± 20
T_3R_3	7.4 ± 0.1	0.98 ± 0.02	20 ± 15
R_6	6.4 ± 0.1	0.98 ± 0.02	5 ± 15

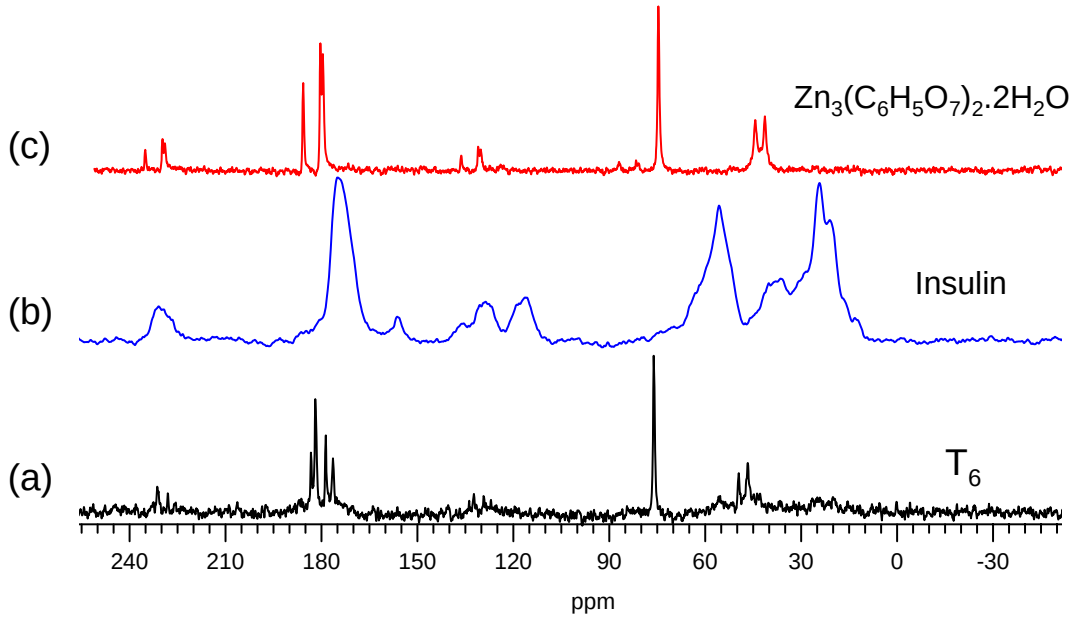

Figure 4.4: Natural abundance solid-state ^{13}C CP/MAS NMR spectra of: (a) T_6 zinc-insulin hexamer, (b) zinc-free insulin, and (c) zinc citrate dihydrate. All spectra were acquired at $B_o = 11.75$ T with a spinning rate of 7.0 kHz.

The presence of zinc citrate impurity imposes major complications on the ^{67}Zn NMR spectrum of the T_6 hexamer. Figure 4.5a shows the ^{67}Zn WURST–QCPMG NMR spectrum of stationary T_6 sample. This spectrum was acquired in about 19.5 h (0.5 s recycle delay, 139 731 transients). Analytical simulation of this line shape gives the following ^{67}Zn NMR parameters: $\delta_{iso} = 70 \pm 15$ ppm, $C_Q = 12.7 \pm 0.2$ MHz, and $\eta_Q = 0.77 \pm 0.05$. The presence of zinc citrate in the T_6 sample used is further confirmed by the ^{67}Zn WURST–

QCPMG NMR spectrum of stationary zinc citrate dihydrate, shown in part (b). The spectrum ascribed to the T_6 sample in (a) most likely does not correspond solely to the actual T_6 hexamer, but includes some spectral features of a zinc citrate polymorph different from the commercial one studied here, as noted in the ^{13}C spectral analysis. The difference spectrum between the T_6 sample and zinc citrate alone is shown in part (c).

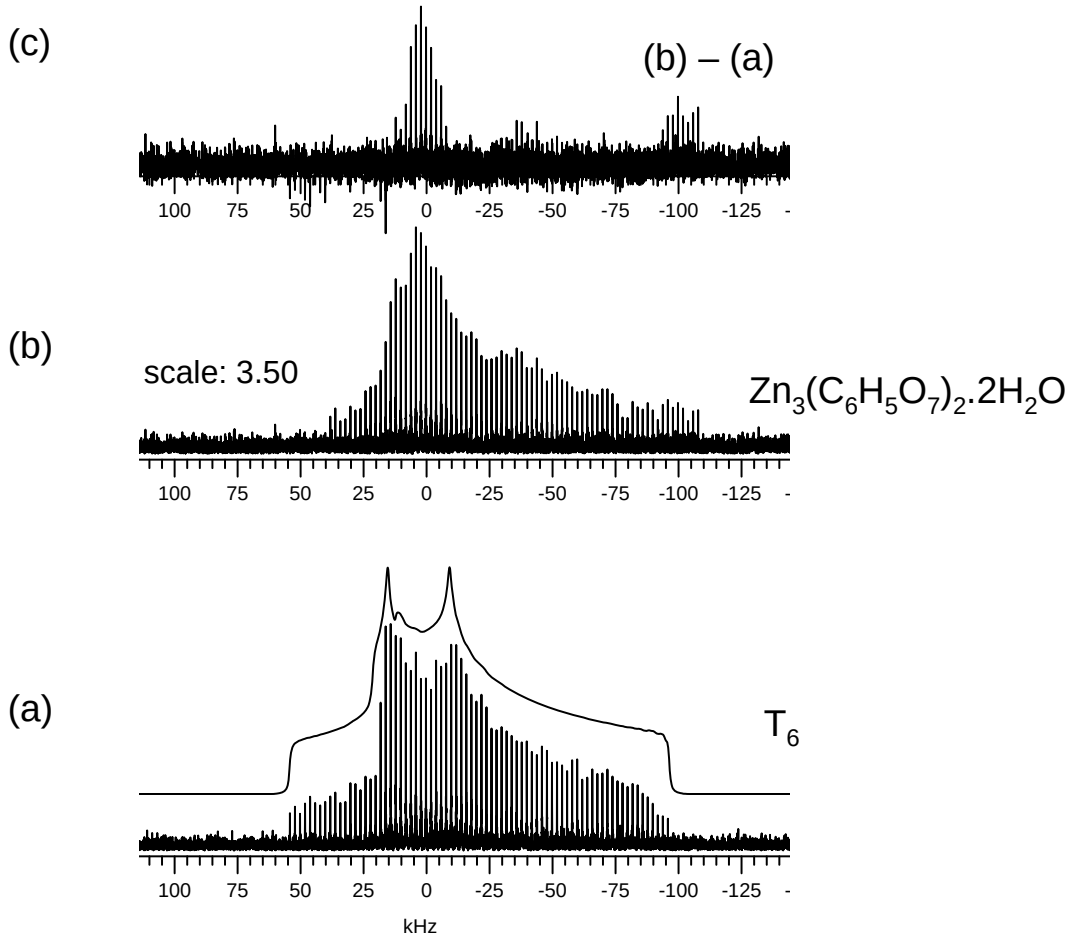

Figure 4.5: (a) Experimental (lower) ^{67}Zn WURST-QCPMG NMR spectrum of stationary T_6 hexamer, with its simulation (upper). (b) Experimental ^{67}Zn WURST-QCPMG NMR spectrum of stationary sample of zinc citrate dihydrate. (c) The difference spectrum.

Seeking a more reliable result for T_6, another sample of this hexamer was prepared using the same procedure outlined in the Experimental section, except that the hexameric solution was air dried without centrifugation. Figure 4.6a shows the ^{13}C CP/MAS NMR spectrum of the new T_6 hexamer. Fortunately, this spectrum is not contaminated with zinc citrate but with sodium citrate buffer, which should not have any negative influence on the ^{67}Zn NMR spectrum of T_6. The similarities in the spectral features between T_6 and free insulin are clearly visible. Figure 4.7 shows the ^{67}Zn WURST–QCPMG NMR spectrum of the new sample acquired at 21.1 T. Although the experimental time for this spectrum was the same as that of the old T_6 sample, the signal-to-noise ratio of the new spectrum is very low due to the small sample volume available. The estimated ^{67}Zn NMR parameters extracted from this spectrum are: $\delta_{iso} = 80 \pm 20$ ppm, $C_Q = 7.3 \pm 0.2$ MHz, and $\eta_Q = 0.75 \pm 0.05$.

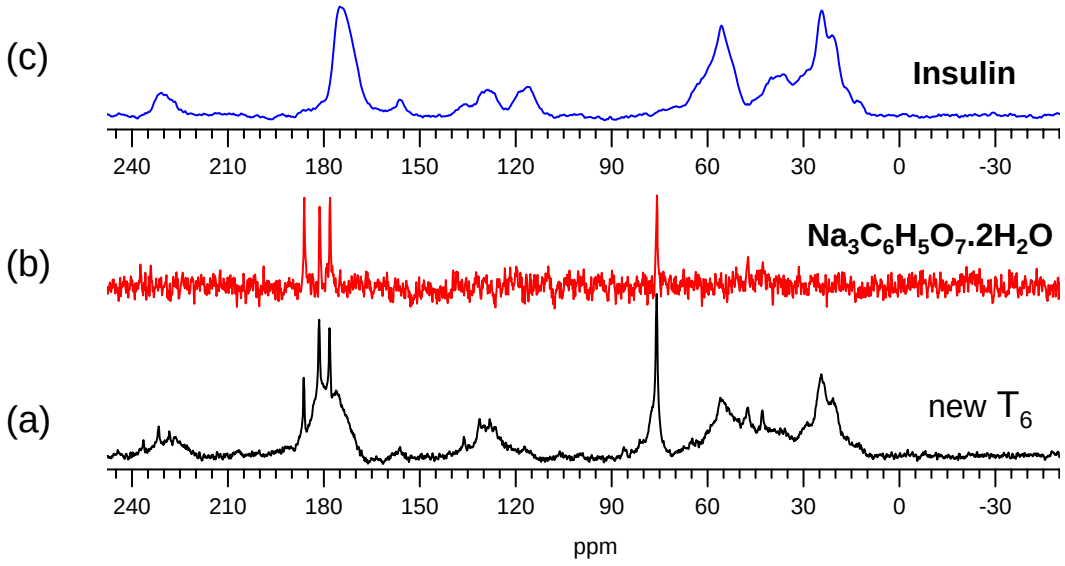

Figure 4.6: Natural abundance solid-state ^{13}C CP/MAS NMR spectra of: (a) new sample of T_6 zinc-insulin hexamer, (b) sodium citrate dihydrate, and (c) zinc-free insulin. All spectra were acquired at $B_o = 11.75$ T with a spinning rate of 7.0 kHz.

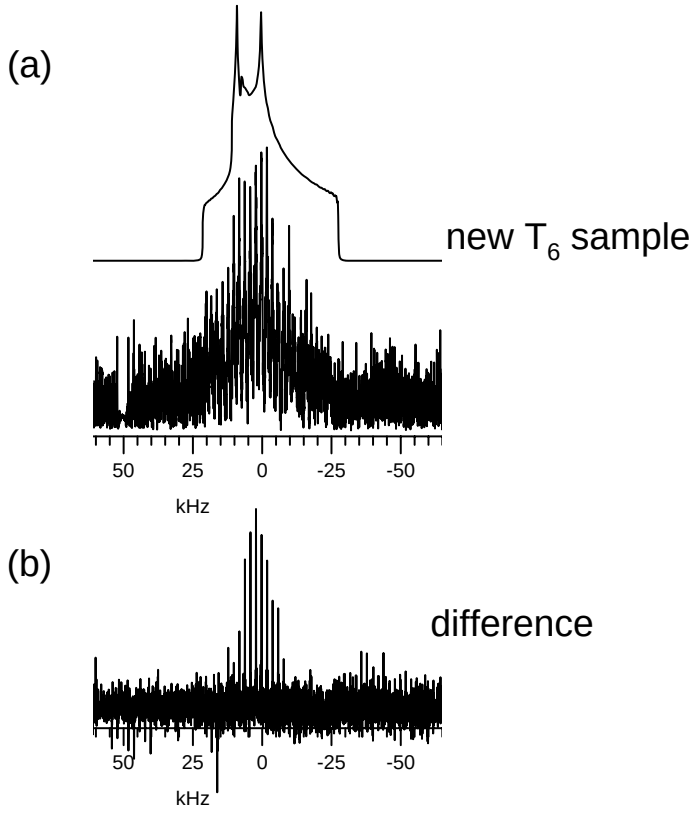

Figure 4.7: (a) Experimental (lower) static ^{67}Zn WURST-QCPMG NMR spectrum of the new sample of T_6 hexamer, with its simulation (upper). (b) The difference ^{67}Zn solid-state NMR spectrum from Figure 4.5.

Figure 4.8a shows the ^{13}C CP/MAS NMR spectrum of the R_6 hexamer. This spectrum is contaminated with sodium citrate buffer, which should not have any negative influence on the ^{67}Zn NMR spectrum of R_6. The similarities in the spectral features between R_6 and free insulin are clearly visible. The ^{67}Zn WURST-QCPMG NMR spectrum of stationary R_6 hexamer is shown in Figure 4.9, along with the simulated spectrum. The experimental ^{67}Zn NMR spectrum was acquired in about 17.5 h (125 510 transients with 0.5 s recycle delay), and exhibits a second-order central-transition quadrupolar line shape corresponding to an EFG tensor with asymmetry parameter η_Q very close to 1.00. The following ^{67}Zn NMR parameters could be extracted from this line shape by analytical simulation: $\delta_{iso} = 5 \pm 15$

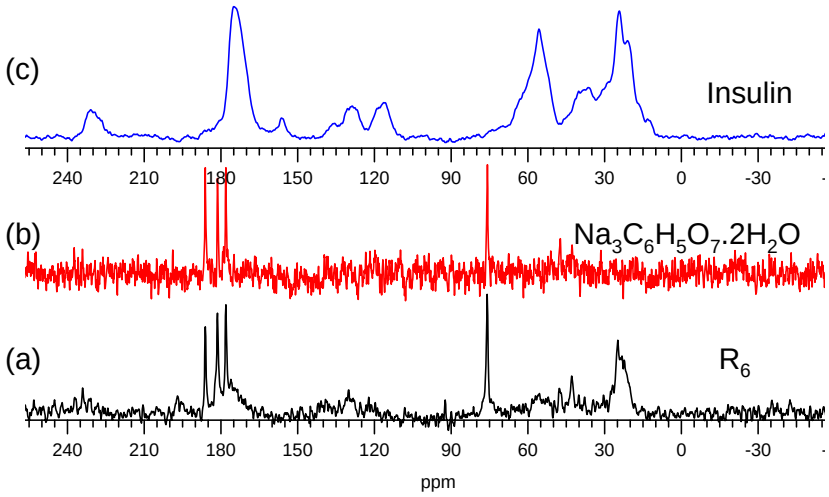

Figure 4.8: Natural abundance solid-state ^{13}C CP/MAS NMR spectra of: (a) R_6 zinc-insulin hexamer, (b) sodium citrate dihydrate, and (c) zinc-free insulin. All spectra were acquired at $B_o = 11.75$ T with a spinning rate of 7.0 kHz.

ppm, $C_Q = 6.4 \pm 0.1$ MHz, and $\eta_Q = 0.98 \pm 0.02$.

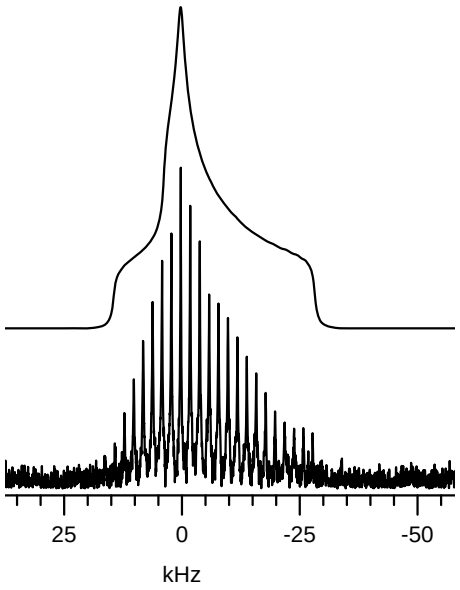

Figure 4.9: Experimental (lower) and simulated (upper) ^{67}Zn solid-state NMR spectra of a stationary powdered sample of the zinc-insulin hexamer R_6 at 21.1 T.

Figure 4.10a shows the ^{13}C CP/MAS NMR spectrum of the T_3R_3 hexamer. The T_3R_3 sample is obviously the purest among the three hexamers studied. The large similarities in the spectral features between T_3R_3 and free insulin are clearly visible. The ^{67}Zn WURST-QCPMG NMR spectrum of stationary T_3R_3 hexamer is shown in Figure 4.11, along with the simulated spectrum. As noted previously in the Introduction, less than three zinc ions have been reported to bind to this hexamer despite the availability of four zinc-binding sites (one octahedral and three tetrahedral), due to the disorder in HisB10 residues. This renders the resolution of the distinct zinc sites in the ^{67}Zn NMR spectrum of this hexamer a very complicated task. The experimental ^{67}Zn NMR spectrum is therefore simulated using single-site NMR parameters, yielding a ^{67}Zn δ_{iso} of 20 ± 15 ppm, C_Q of 7.4 ± 0.1 MHz, and η_Q of 0.98 ± 0.02.

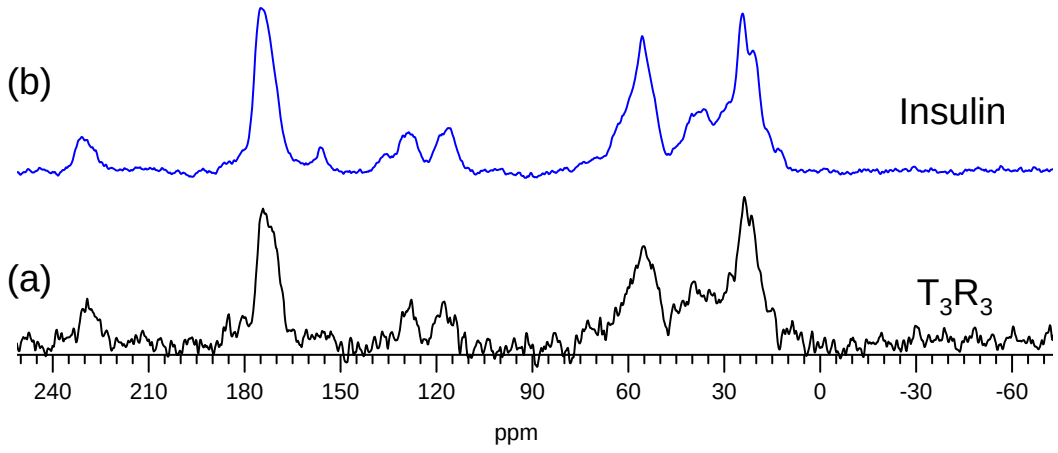

Figure 4.10: Natural abundance solid-state ^{13}C CP/MAS NMR spectra of: (a) T_3R_3 zinc-insulin hexamer and (b) zinc-free insulin. Both spectra were acquired at $B_o = 11.75$ T with a spinning rate of 7.0 kHz.

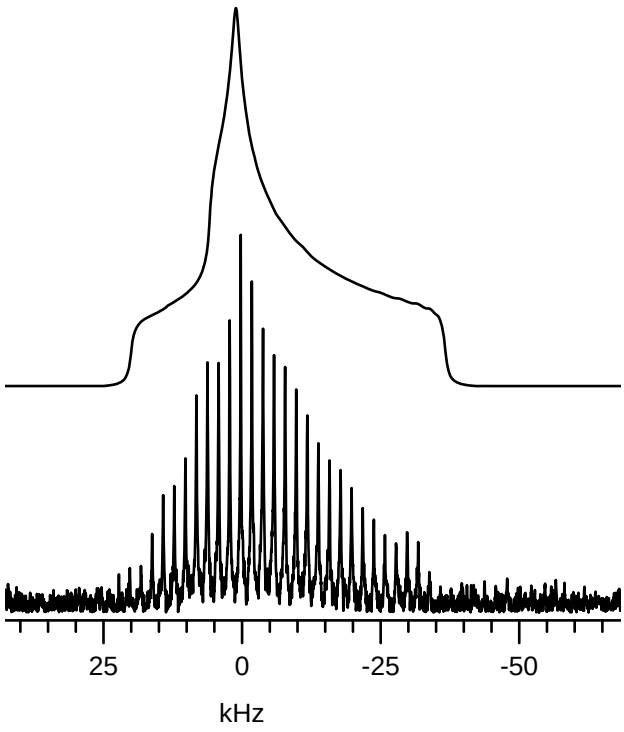

Figure 4.11: Experimental (lower) and simulated (upper) ^{67}Zn solid-state NMR spectra of a stationary powdered sample of the zinc-insulin hexamer T_3R_3 at 21.1 T.

Table 4.3: Calculated ^{67}Zn NMR parameters for models of the zinc sites in the three zinc-insulin hexamers.

	T_6	T_3R_3 (octahedral)	T_3R_3 (tetrahedral)	R_6
C_Q (MHz)	12.39	10.01	5.24	5.46
η_Q	0.16	0.04	0.07	0.52
σ_{iso} (ppm)	1551	1578	1557	1566
δ_{iso} (ppm)[a]	281	254	275	266
Ω (ppm)	146	199	130	158
κ	-0.47	-0.29	0.95	0.94
$\alpha(^\circ)$	71	66	66	123
$\beta(^\circ)$	79	85	2	23
$\gamma(^\circ)$	7	166	103	164

[a] The calculated values of δ_{iso} were determined using the absolute shielding scale for ^{67}Zn:[171,172] $\delta_{iso} = 1831.67 \text{ ppm} - \sigma_{iso}$

4.3.2 Quantum Chemical Calculations

To complement the experimentally determined ^{67}Zn NMR parameters for the zinc active sites in the three zinc-insulin hexamers, and to aid in their interpretation, density-functional theory (DFT) calculations of the ^{67}Zn EFG and nuclear magnetic shielding tensors were also carried out. The results of these calculations are listed in Table 4.3. Among the three hexamers studied, the calculated quadrupolar coupling constant for R_6 shows the best agreement with experiment. For the T_3R_3 hexamer, the experimental C_Q value of 7.4 MHz, determined based on single-site simulation, falls midway between the calculated values of 5.24 and 10.01 MHz for the tetrahedral and octahedral zinc sites. For the T_6 model used, the computed quadrupolar coupling constant is much larger than the experimental value of 7.3 $\pm$ 0.2 MHz. This indicates that the electronic environment around the zinc ions in T_6 is actually less distorted than what is predicted by computations. This disparity between experimental and predicted data for T_6 also indicates that

the coordination geometry of the zinc ions may not be determined sufficiently accurate in the X-ray crystal structure of this hexamer. The calculated ^{67}Zn isotropic chemical shifts follow the same trend as those determined by experiment, as they show an increase from R_6, to T_3R_3, to T_6.

4.4 Conclusions

The results achieved in this chapter have demonstrated the strong potential of solid-state ^{67}Zn NMR spectroscopy for the direct observation of zinc ions in very dilute environments such as metalloproteins using sensitivity enhancement techniques on high magnetic-field NMR spectrometers. The present study also shows that solid-state NMR, in combination with molecular orbital calculations, can provide complementary information concerning the accuracy of the atomic coordinates that are available from the crystal structures determined by diffraction techniques.

Chapter 5

Solid-State ^{27}Al Nuclear Magnetic Resonance Investigation of Three Aluminum-Centered Dyes

A modified version of this chapter has been published as an article in the *Canadian Journal of Chemistry*:
Kamal H. Mroué, Abdul-Hamid M. Emwas, and William P. Power. Solid-state ^{27}Al nuclear magnetic resonance investigation of three aluminum-centered dyes. *Can. J. Chem.* **2010**, *88*, 111–123. DOI: 10.1139/V09-155.

5.1 Introduction

Phthalocyanine complexes (Pcs), and the structurally related naphthalocyanines (Ncs), together with their metal-centered derivatives, constitute an important class of macrocyclic compounds which play a vital role in many modern practical and technological applications.[199] These materials have been intensively used in dyes, pigments, fuel and solar cells, electrophotography, semiconductors, liquid crystals, data-storage devices, photosensitizers for photodynamic therapy, and nonlinear optical materials, among others. This wide variety of applications is due mainly to their intense green-blue color, combined with their

exceptional stability to acids, alkalis, heat, light, and common solvents. These properties and applications, among others as well, are discussed in several excellent monographs about phthalocyanines and their derivatives.[200–206]

Numerous techniques have been used to study these materials, such as X-ray diffraction, mass spectrometry Raman, IR, UV–vis, electronic absorption/emission, Mössbauer, electron paramagnetic and nuclear magnetic resonance (NMR) spectroscopies, among others. Studies of these materials by liquid-state NMR have involved mainly the use of ^{1}H and ^{13}C NMR as identification tools.[207,208] Direct NMR observation of the metal nuclei in solid metal-centered phthalocyanines has been limited to few studies, including a ^{59}Co NMR study of four hexacoordinated cobalt(III) phthalocyanines,[209] a ^{25}Mg NMR study of monopyridinated aqua(magnesium) phthalocyanine,[68] and a recent ^{71}Ga NMR study of gallium phthalocyanine chloride, GaPcCl.[96,210]

From a spectroscopic perspective, solid-state nuclear magnetic resonance (SSNMR) represents an ideal and powerful tool to probe the metal centre in a metallophthalocyanine. The advantages of NMR over other techniques, such as X-ray and neutron diffraction, is that while the latter techniques rely on the long-range order in the crystal lattice and require the availability of high-quality single crystals suitable for analysis, SSNMR focuses on the local electronic environment around the nucleus of interest without the necessity of single crystals. Given the limited solubility of metallophthalocyanines in both inorganic and organic solvents, and their large molecular weights, their analysis by single-crystal X-ray diffraction can be quite cumbersome, if at all possible. Moreover, the ability of SSNMR to characterize disordered and amorphous solid materials has been well-established and demonstrated in numerous instances (*vide infra*). Recently, the increasing availability of ultrahigh-magnetic-field NMR spectrometers, together with the advances in instrumental hardware, and the introduction of new pulse sequences have also facilitated the application

of SSNMR to study such poorly crystalline materials.[175,211]

Among the various metallophthalocyanines, aluminum-centered ones are well-suited for SSNMR experiments. This is due to the very favorable NMR properties that ^{27}Al enjoys, including its high natural abundance (100%),[127] large magnetogyric ratio ($\gamma = 6.9762 \times 10^7\, rad \cdot T^{-1} \cdot s^{-1}$, close to ^{13}C),[127] and a sizable chemical shift range of about 300 ppm.[212] However, the quadrupolar nature of ^{27}Al (spin $I = \frac{5}{2}$) introduces various challenges in SSNMR studies of this nucleus. The most distinctive challenge arises from the non-zero nuclear quadrupole moment [$Q(^{27}\mathrm{Al}) = 14.66\,\mathrm{fm}^2$],[126] which couples strongly with any electric field gradient (EFG) arising naturally from lack of spherical symmetry in charge distribution around the aluminum nucleus. Such quadrupolar interactions have considerable effects on ^{27}Al NMR spectra, often beyond those described under first-order perturbation theory. Usually only the central transition (CT, $+\frac{1}{2} \leftrightarrow -\frac{1}{2}$) is observed in a SSNMR experiment of a polycrystalline powdered sample, and it is unaffected to first order but is substantially broadened by second-order quadrupolar effects.[32,213] In addition to the quadrupolar interaction, ^{27}Al is also sensitive to the chemical shift/shielding interaction. The EFG and chemical shift (CS) are both orientation-dependent NMR interactions that can provide reliable information about the local electronic environment of the nucleus of interest. Indeed, both interactions have been shown to be very sensitive to local structure and bonding, and can potentially yield details and wealth of information not typically available from other techniques.[53,214]

Despite the complications caused by second-order quadrupolar broadening, solid-state ^{27}Al NMR has been used frequently to study a wide variety of materials, most of which are inorganic and disordered solids such as glasses, zeolites, aluminosilicates, molecular sieves, cements, ceramics, as well as natural and synthetic minerals.[64,211,215–228] In these studies, ^{27}Al magic-angle spinning (MAS) NMR has been used primarily to narrow the central tran-

sition line shapes, and to enhance the spectral resolution in order to differentiate among tetrahedral, pentacoordinate, and octahedral local aluminum coordination environments (mainly in $aluminum - (oxygen)_n$ coordination, $n = 4, 5, 6$) based on the different ^{27}Al chemical shift ranges of each environment.[175,229] In the case of disordered and/or amorphous solids, the conventional one-dimensional MAS spectrum does not give well-defined second-order quadrupolar line shapes. These lines are rather featureless and asymmetric, from which it is quite challenging to extract any information related to the chemical shift and quadrupolar interactions arising from overlapping signals.[230–232] For such materials, the two dimensional multiple-quantum magic-angle spinning (MQMAS) experiment[14] is used in order to resolve overlapping resonances in multi-site systems, based on the difference in the chemical shift and quadrupolar parameters experienced by each site. In many instances, MQMAS makes it possible to not only resolve the different sites present in the system, but also allows extraction of sufficient information about the ^{27}Al NMR parameters associated with each unique site.

In contrast to the plethora of inorganic and glassy materials investigated by solid-state ^{27}Al NMR, it is surprising that only a handful of aluminum-containing organic compounds have been studied by this technique. Wasylishen and co-workers reported ^{27}Al NMR spectra of tris(acetylacetonato)aluminum(III), tris(tropolonato)aluminum(III), and tris(2,2,6,6-tetramethyl- 3,5-heptanedionato)aluminum(III).[233] The aluminum atoms in these compounds are each coordinated to six oxygen atoms in a distorted octahedral geometry, where small ^{27}Al CSA values were observed for the three complexes. Gang Wu and co-workers also recorded solid-state ^{27}Al NMR spectra of three blue luminescent aluminum compounds containing terminal 7-azaindole ligands, in which the aluminum ions are in distorted tetrahedral coordination environments.[234] The same group successfully applied ^{27}Al 3QMAS spectroscopy to the identification of disorder and iso-

merism in two blue luminescent aluminum compounds, in which the Al centres exhibit five-coordinated geometries.[235] Utz *et al.* studied the ^{27}Al spectra of three different polymorphs of solid tris(8-hydroxyquinoline)aluminum(III) under MAS conditions.[236] These same systems were reinvestigated recently by Nishiyama *et al.* using ^{27}Al 1D MAS and 2D MQMAS NMR experiments.[237] Schurko *et al.* reported a very small ^{27}Al quadrupolar interaction but a large aluminum chemical shift anisotropy, with a span of 83 ppm, in the bis(pentamethylcyclopentadienyl)aluminum cation.[238] Schurko and co-workers applied the frequency-stepped technique in Hahn-echo and QCPMG pulse sequences to acquire ultrawideline ^{27}Al NMR spectra of stationary samples of three- and five-coordinate organoaluminum complexes.[239]

In this chapter, we investigate the solid-state ^{27}Al NMR spectra of three aluminum-centered organic dyes: aluminum phthalocyanine chloride, AlPcCl (**1**); aluminum-1,8,15,22-tetrakis(phenylthio)-29H,31H-phthalocyanine chloride, AlPc(SPh)$_4$Cl (**2**); and aluminum-2,3-naphthalocyanine chloride, AlNcCl (**3**) (Figure 5.1). In addition to our main interest in the SSNMR of phthalocyanines (for the reasons mentioned above), these compounds have been chosen because they exhibit aluminum in pentacoordinate geometries, which is much less common than the four- and six-coordinate motifs. In all three systems, the Al^{3+} ions are coordinated to four isoindole nitrogen atoms and one chlorine atom in a square-pyramidal geometry. Such coordination geometry is relatively rare in solid-state ^{27}Al NMR studies, both in inorganic and organic systems. We also report extensive density functional theory (DFT) and restricted Hartree-Fock (RHF) quantum chemical calculations of aluminum NMR interactions in molecular models of these complexes in an attempt to examine the orientation of NMR tensors within molecular frames and to help rationalize the origin of experimentally measured aluminum NMR parameters.

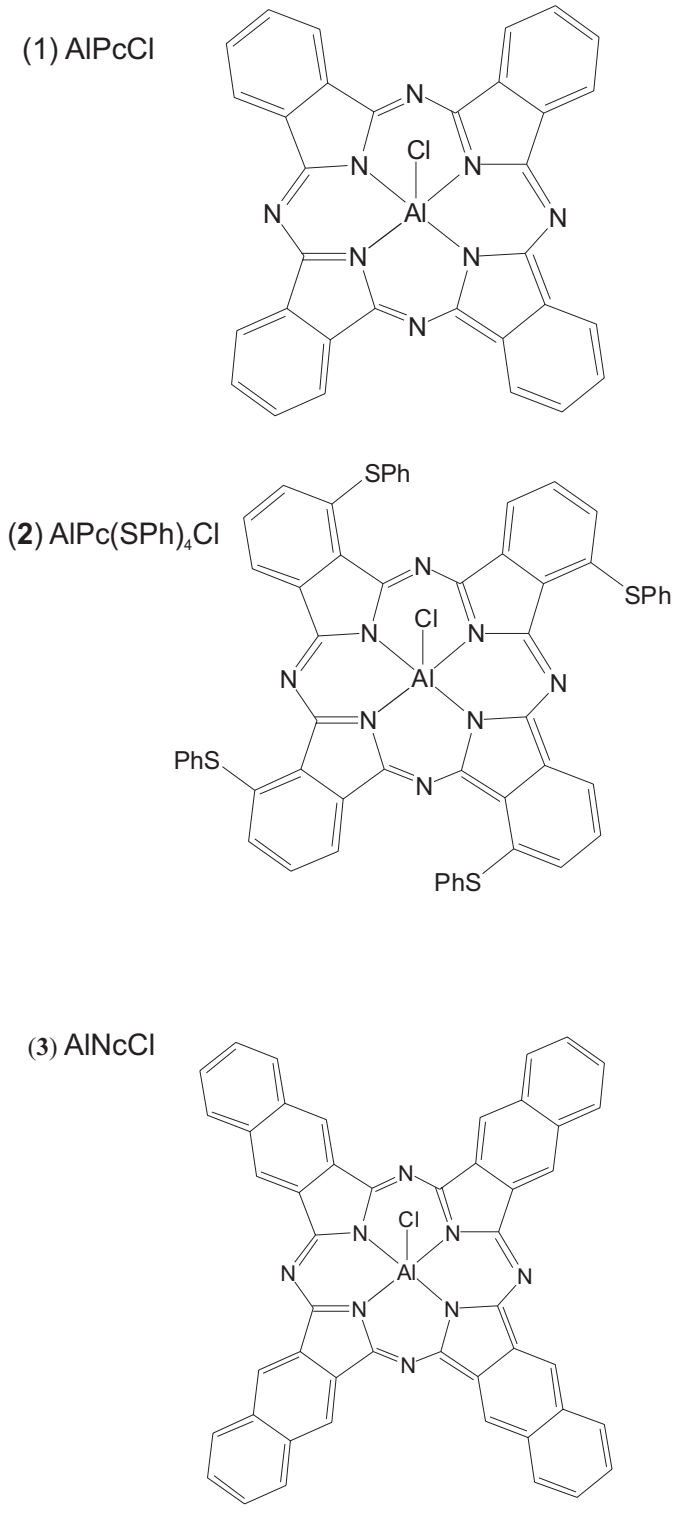

Figure 5.1: Molecular structures of the studied compounds.

5.2 Experimental Section

5.2.1 Sample Preparation

The three complexes were purchased from Aldrich Chemical Company. The dye contents are *ca.* 85%, 90%, and 80% for compounds **1**, **2**, and **3** respectively. Attempts to obtain the pure compounds by recrystallization from a variety of organic solvents or by vacuum sublimation were unfruitful; hence, they were used as purchased. Samples of each complex were ground into fine powders with a mortar and pestle for X-ray powder diffraction experiments, and subsequently packed into 2.5 and 4.0 mm o.d. zirconia rotors for SS-NMR experiments. Powder X-ray diffraction data were collected using an INEL powder diffractometer with a position-sensitive detector and Cu-Kα1 radiation (λ = 1.54056 Å). The operating conditions were 30 kV and 30 mA, with an exposure time of 5–10 min over the 2θ range from 0.0 to 120°.

5.2.2 Solid-State ^{27}Al NMR Spectroscopy

Aluminum-27 solid-state NMR experiments were performed at Larmor frequencies of 130.3 MHz (11.75 T), 156.4 MHz (14.1 T), and 234.5 MHz (21.1 T) using Bruker Avance (11.75 and 14.1 T) and Avance II (21. 1 T) consoles. The experiments at 11.75 and 14.1 T were performed at the University of Waterloo; experiments at 21.1 T were performed at the National Ultrahigh-Field NMR Facility for Solids at the National Research Council (NRC) in Ottawa, Ontario, Canada. Standard Bruker 2.5 mm double-resonance MAS probes were used at 14.1 and 21.1 T, whereas a Bruker 4 mm double-resonance MAS probe was used at 11.75 T. Pulse calibration and chemical shift referencing were performed using a

1.0 M $Al[(H_2O)_6]^{3+}$ aqueous solution set at 0.0 ppm. A solid echo ($\pi/2$ - τ_1 - $\pi/2$ - τ_2 - ACQ) and quadrupolar Carr-Purcell Meiboom-Gill (QCPMG)[15–18] pulse sequences were used to acquire spectra of non-spinning samples. For experiments performed under MAS conditions, the sample spinning speed was 20.0 kHz at 14.1 T and 21.1 T, and 15.0 kHz at 11.75 T. A very short pulse ($\pi/12$) was used in the one-dimensional MAS spectra to ensure quantification of all species. For the solid-echo and QCPMG experiments, a selective $\pi/2$ pulse of 1.20 - 1.40 μs was used.

Two-dimensional ^{27}Al triple-quantum MAS (3QMAS) spectra of the three complexes were obtained at 21.1 T using a spinning rate of 20.0 kHz. The z-filtered 3QMAS pulse sequence was used,[240] consisting of excitation (1.90 μs) followed by evolution of the triple-quantum coherence during t_1 followed by a conversion pulse (0.80 μs), a 20.0μs z-filter, and a selective $\pi/2$ pulse (7.50 μs) followed by acquisition during t_2. A total of 240 transients were obtained for each t_1 increment; 64 complex points were acquired in t_1, with a t_1 increment of 25 μs, which corresponds to half the rotor period. Exponential apodization of 300 Hz was applied in both dimensions prior to zero-filling and Fourier transformation. A shearing transformation was performed during data processing to obtain the isotropic dimension along F1 and the anisotropic MAS dimension along F2. Recycle delays of 2.0 s, 3.0 s, and 5.0 s were sufficient at 11.75, 14.1, and 21.1 T respectively. The 1D NMR spectra used for line shape analysis were simulated with SIMPSON.[55] Spectral simulations were carried out iteratively and simultaneously at multiple fields, and the errors in the extracted parameters were determined by visual comparison of the resulting fit at each field with the corresponding experimental spectrum. Each parameter was optimized independently by varying it in both directions away from its best-fit value, while all other parameters were held fixed, until a visible difference between experimental and simulated spectra was observed. Stack plots were generated with DMFit.[241]

5.2.3 Quantum Chemical Calculations

All quantum chemical calculations were performed using *Gaussian 03*[100] running on the SHARCNET facility for high performance computing.[168] In an attempt to understand the experimentally observed ^{27}Al NMR parameters, three models for calculations of NMR interaction tensors were constructed for compound **1**: The first model was built using atomic coordinates obtained from the X-ray single-crystal study of Hasegawa and Sato,[242,243] and used directly for NMR calculations (Figure 5.2). Two additional models were constructed by the addition of either a chlorine atom or a water molecule below the phthalocyanine ring in an axial position in order to complete the octahedral coordination around the aluminum atom (Figure 5.3). The geometries of both models were then fully optimized at the RHF/6-311G** method. Since there are no crystal structures reported for compounds **2** and **3**, the structures used in NMR calculations were derived from the reported structure of molecule 1 of compound **1** by adding either four thiophenyl groups (**2**) or four naphthalo groups (**3**) in their respective peripheral positions, as depicted in Figures 5.4 and 5.5. The two structures were then fully optimized at the RHF/6-311G** method. Aluminum electric field gradient and nuclear magnetic shielding tensors were subsequently calculated for the resulting structures using both the restricted Hartree-Fock (RHF) and density functional theory (DFT) methods. The B3LYP exchange functional was employed in the DFT calculations.[169,170] The following standard Pople-type basis sets were employed an all atoms: 6-31G**, 6-31++G**, 6-311G**, 6-311++G**, and 6-311+G (2d, p). The nuclear magnetic shielding tensors were calculated using the gauge-including atomic orbitals (GIAO) method.[107,108] Convergence parameters were unchanged and left at their default values. Because there is no established absolute chemical shielding scale for ^{27}Al, the calculated ^{27}Al isotropic chemical shieldings (σ_{iso}) were converted into the corresponding isotropic chemical shifts (δ_{iso}) using the formula $\delta_{\mathrm{iso}} = \sigma_{\mathrm{ref}} - \sigma_{\mathrm{iso}}$, where σ_{ref} is the calculated isotropic shielding

constant of $Al[(H_2O)_6]^{3+}$ cation, the reference species.[212] The geometry of this cation was fully optimized at the RHF/6-311G** level. In order to avoid basis-set dependence of the calculated ^{27}Al chemical shifts, the reference chemical shielding σ_{ref} was computed for each basis set used. The calculated ^{27}Al EFG and CS parameters were extracted from the *Gaussian* output files using the EFGShield program (version 2.3) developed in the laboratory of D.L. Bryce.[33]

5.3 Solid-State ^{27}Al NMR Conventions

Prior to commencing the discussion of the ^{27}Al NMR results of this study, it is convenient to recall some NMR concepts and definitions relevant to the systems currently investigated, keeping in mind that the SSNMR theory for half-integer quadrupolar spins is detailed more elegantly elsewhere.[32,53,213,214] Aside from the Zeeman interaction, the spectrum of a half-integer quadrupolar spin (such as ^{27}Al, $I = \frac{5}{2}$) is dominated by the nuclear quadrupole interaction and the nuclear magnetic shielding interaction. The high-field approximation, in which the Zeeman interaction is assumed to be at least ten times stronger than both interactions, is always applied in the interpretation of SSNMR spectra of these nuclei.

Nuclear magnetic shielding is the interaction between the nuclear spins and the local magnetic field induced by surrounding electrons, and depends on the orientation of the molecule with respect to the external applied magnetic field, B_o; in other words, it is anisotropic. Thus, it can be described by a second-rank tensor, denoted by $\underline{\underline{\sigma}}$. In its principal axis system (PAS), the symmetric component of $\underline{\underline{\sigma}}$ is diagonal, and has three eigenvalues labeled and ordered such that: $\sigma_{11} \leq \sigma_{22} \leq \sigma_{33}$. Experimentally, the magnetic shielding at a nucleus is measured in terms of the chemical shift, δ_{ii}, which gives the difference in ppm between the sample signal and that of a reference compound. Since

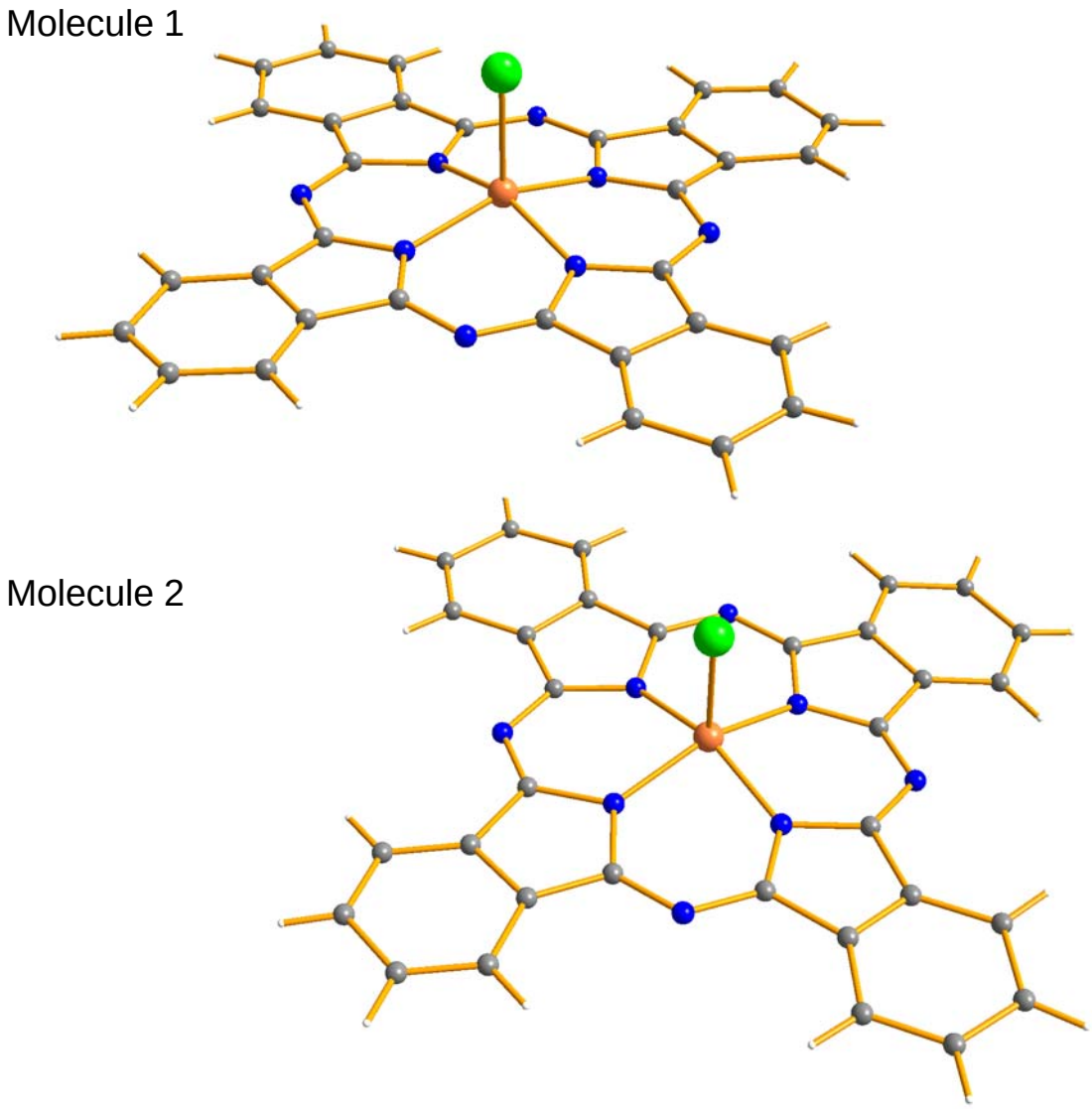

Figure 5.2: Molecular structure of compound **1**. Aluminum is shown in orange, chlorine in green, nitrogen in blue, carbon in gray, and hydrogen in white.

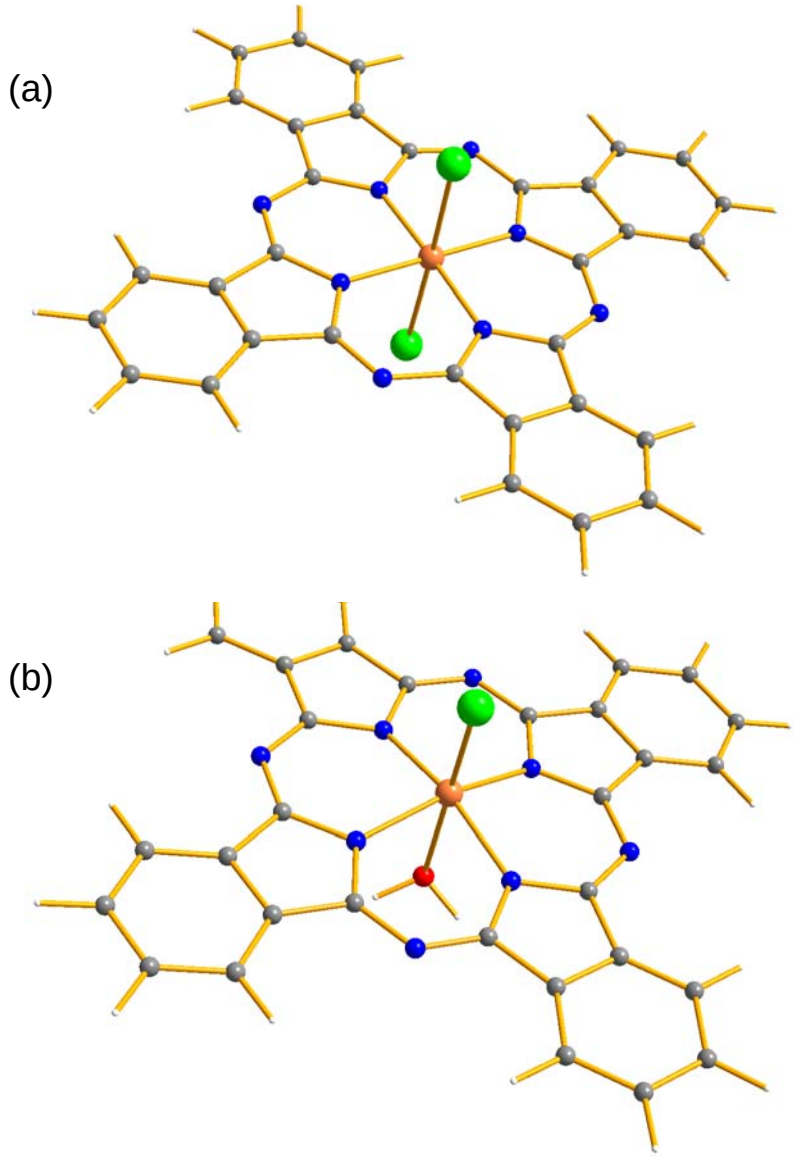

Figure 5.3: Octahedral models of compound **1**: (a) A chlorine atom is added in an axial position below the phthalocyanine ring to complete the octahedral coordination around the aluminum atom. (b) A water molecule is added in an axial position below the phthalocyanine ring in order to complete the octahedral coordination around the aluminum atom. Aluminum is shown in orange, chlorine in green, oxygen in red, nitrogen in blue, carbon in gray, and hydrogen in white.

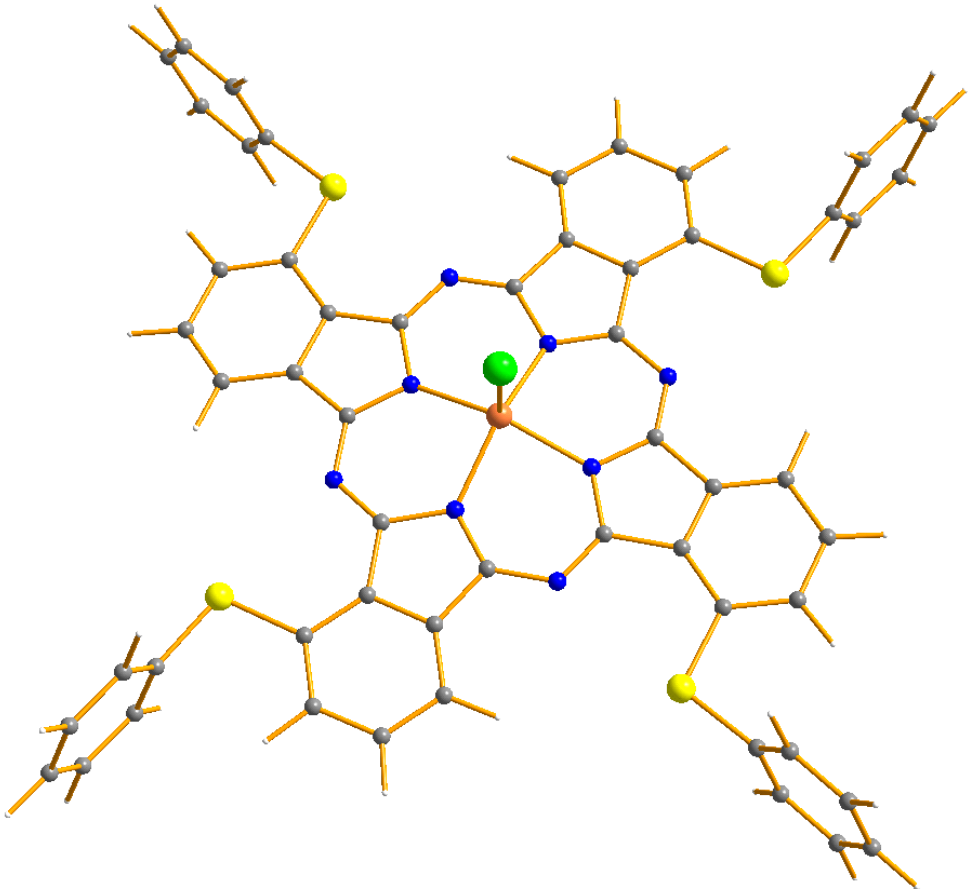

Figure 5.4: Molecular structure of compound **2**. Aluminum is shown in orange, chlorine in green, sulfur in yellow, nitrogen in blue, carbon in gray, and hydrogen in white.

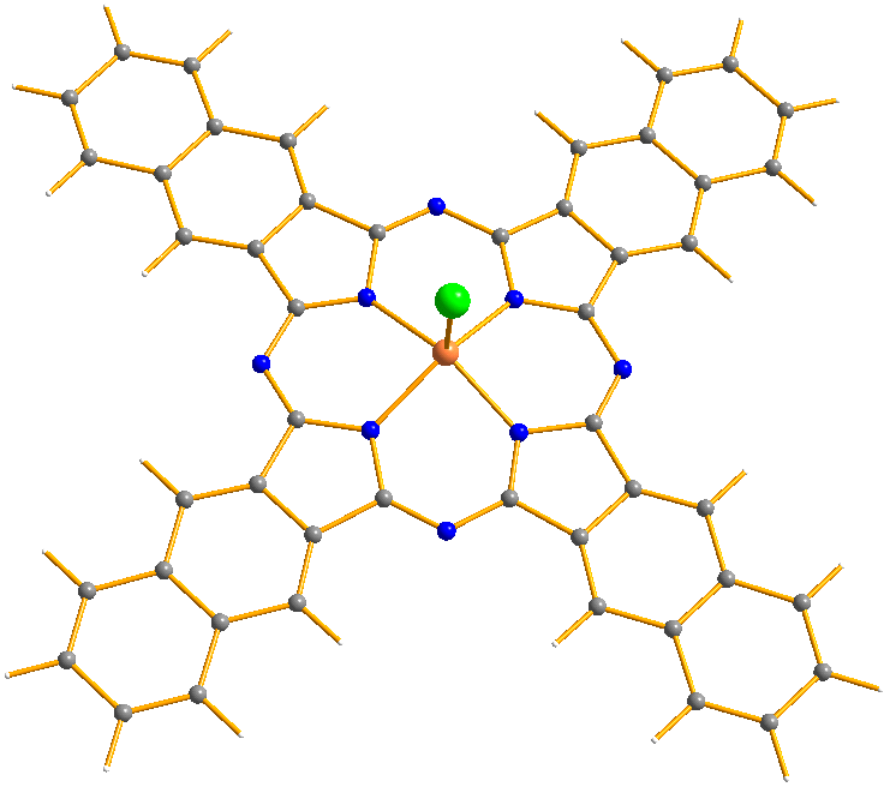

Figure 5.5: Molecular structure of compound **3**. Aluminum is shown in orange, chlorine in green, nitrogen in blue, carbon in gray, and hydrogen in white.

chemical shielding and chemical shift vary conversely with frequency, the three principal components of the chemical shift (CS) tensor will be ordered such that: $\delta_{11} \geq \delta_{22} \geq \delta_{33}$. Although the magnitude of the shielding (or shift) tensor is fully described by its three eigenvalues, an alternative convention is used in which the magnitude of the tensor is fully described by: its isotropic chemical shift $\delta_{\text{iso}} = (\delta_{11} + \delta_{22} + \delta_{33})/3$; its span $\Omega = \sigma_{33} - \sigma_{11} \approx \delta_{11} - \delta_{33}$; and its skew $\kappa = 3(\sigma_{\text{iso}} - \sigma_{22})/\Omega = 3(\delta_{22} - \delta_{\text{iso}})/\Omega$, where $-1.0 \leq \kappa \leq +1.0$.[34,244] The span reflects the breadth of the powder pattern due to shielding anisotropy and has always a positive value when it exists, while the skew describes the shape of the shielding tensor, with $\kappa = \pm\, 1.0$ indicating an axially symmetric CS tensor. It is very important to mention that the span of the CS tensor, represented by Ω, scales linearly (when measured in Hz) with B_{o}. This means that the effects of chemical shift anisotropy (CSA) are observed more clearly at high magnetic fields than at lower ones.

The nuclear quadrupole interaction results from the coupling of the quadrupole moment, eQ, of a nucleus with any electric field gradient (EFG) at that nucleus. The EFG is represented by a symmetric and traceless second-rank tensor. In its PAS, it has three components ordered such that $|V_{33}| \geq |V_{22}| \geq |V_{11}|$, with $V_{11} + V_{22} + V_{33} = 0$. Two parameters are sufficient to quantify the magnitude of the quadrupolar interaction: The quadrupolar coupling constant, C_{Q}, to measure its size (strength), and the asymmetry parameter, η_{Q}, to measure the degree of axial asymmetry of the EFG tensor. They are given by $C_{\text{Q}} = eQV_{33}/h$ and $\eta_{\text{Q}} = (V_{11} - V_{22})/V_{33}$, where e is the electronic charge and h is Planck's constant. C_{Q} is measured in Hz, while η_{Q} is unitless and can take any value between 0 and 1 ($\eta_{\text{Q}} = 0$ corresponds to an axially symmetric EFG tensor). The quadrupolar interaction is treated as a second-order perturbation of the Zeeman interaction when the quadrupolar frequency, $\nu_{\text{Q}} = 3C_{\text{Q}}/(2I(2I-1)) = 0.15\, C_{\text{Q}}$ for ^{27}Al, is less than 10% of the Larmor frequency.[27] This has two direct consequences for solid-state ^{27}Al NMR spectroscopy. First,

the satellite transitions, ($\pm\frac{5}{2} \leftrightarrow \pm\frac{3}{2}$) and ($\pm\frac{3}{2} \leftrightarrow \pm\frac{1}{2}$), often extend over a large spectral range so that they are difficult to both excite and detect; hence, experimentally only the central ($+\frac{1}{2} \leftrightarrow -\frac{1}{2}$) transition is typically observed. Second, the second-order quadrupolar breadth of the central transition line shape is directly proportional to $C_{\mathrm{Q}}^2/\nu_{\mathrm{o}}$, ν_{o} being the Larmor frequency of ^{27}Al.[27,51] This means that the second-order quadrupolar broadening (in Hz) scales inversely with B_{o}, making it advantageous to acquire NMR spectra of half-integer-spin quadrupolar nuclei at the highest possible magnetic field strengths in order to minimize such broadening. Another very important consequence of second-order quadrupolar effects is that the centre of gravity of the central transition (δ_{cg}) does not coincide with the true isotropic chemical shift (δ_{iso}). Rather, it is shifted away by the so-called isotropic second-order quadrupole induced shift (δ_{qis}). For a spin-$\frac{5}{2}$ nucleus like ^{27}Al, δ_{qis} of the central transition is given, in ppm, by:[50,175]

$$\delta_{\mathrm{qis}} = \delta_{\mathrm{cg}} - \delta_{\mathrm{iso}} = -6000\,\frac{P_{\mathrm{Q}}^2}{\nu_{\mathrm{o}}^2} \tag{5.1}$$

where $P_{\mathrm{Q}} = C_{\mathrm{Q}}\sqrt{1+\frac{\eta_{\mathrm{Q}}^2}{3}}$ is the second-order quadrupole effect (SOQE) parameter, and sometimes is simply termed the quadrupolar product.

Of equal importance to the magnitudes of the chemical shift (CS) and quadrupolar interactions is the information pertaining to the relative orientation of these two tensor quantities. This unique information is contained in three fixed Euler angles (α, β, and γ) that describe the counter-clockwise rotations needed to bring the EFG PAS into coincidence with the CS PAS. The so-called *zyz* convention is usually used, where α describes the counterclockwise rotation about the initial z axis (V_{33}) of the coordinate system, followed by a rotation about the new y' axis (V_{22}) by β, followed by a rotation about the new z'' axis (V_{33}) by γ.[245]

5.4 Results and Discussion

Preliminary studies of compounds **1**–**3** using 3QMAS at 21.1 T indicated that both compounds **1** and **2** were composed of multiple components, while compound **3** was composed largely of a single component (Figure 5.6). All three spectra indicate one component with a signal near 30 ± 5 ppm in each dimension, which can be described by an aluminum site with a quadrupolar coupling constant near 10 MHz and an isotropic chemical shift near 27 ppm, as well as a common minor impurity with a narrow peak near 10 ppm (*vide infra*). Therefore, for clarity, compound **3** will be described first, and those results will be used to help illustrate the situation for compounds **1** and **2**. This is completely consistent with the results of powder X-ray diffraction, shown in Figure 5.7, which reveal that compound **1** displays a multi-component nature with a number of overlapping reflections, **2** displays no crystalline reflections (indicating an amorphous nature), while compound **3** displays a clear diffraction pattern consistent with a single-phase crystalline sample.

The sheared 3QMAS spectrum of AlNcCl (compound **3**) at 21.1 T (Figure 5.6C) clearly shows a unique Al site flanked with spinning sidebands. This ridge lies in a direction parallel to the F2 axis, a consequence of the strong quadrupolar interaction experienced by ^{27}Al nuclei in this site. Another small ridge lies at the diagonal CS axis, with a very small intensity relative to the main peak, indicating that it corresponds to an aluminum-containing impurity. This impurity also appears as a low-frequency "shoulder" in the 1D MAS line shape, shown on top of the 2D spectrum. The 1D MAS spectra of AlNcCl at the three magnetic fields are all shown in Figure 5.8, along with their corresponding simulations. Unlike the two other complexes, the MAS spectra of the present compound reveal a polycrystalline and non-disordered powdered sample, despite of the presence of an impurity. It is obvious that the presence of this impurity hinders the exact agreement between the

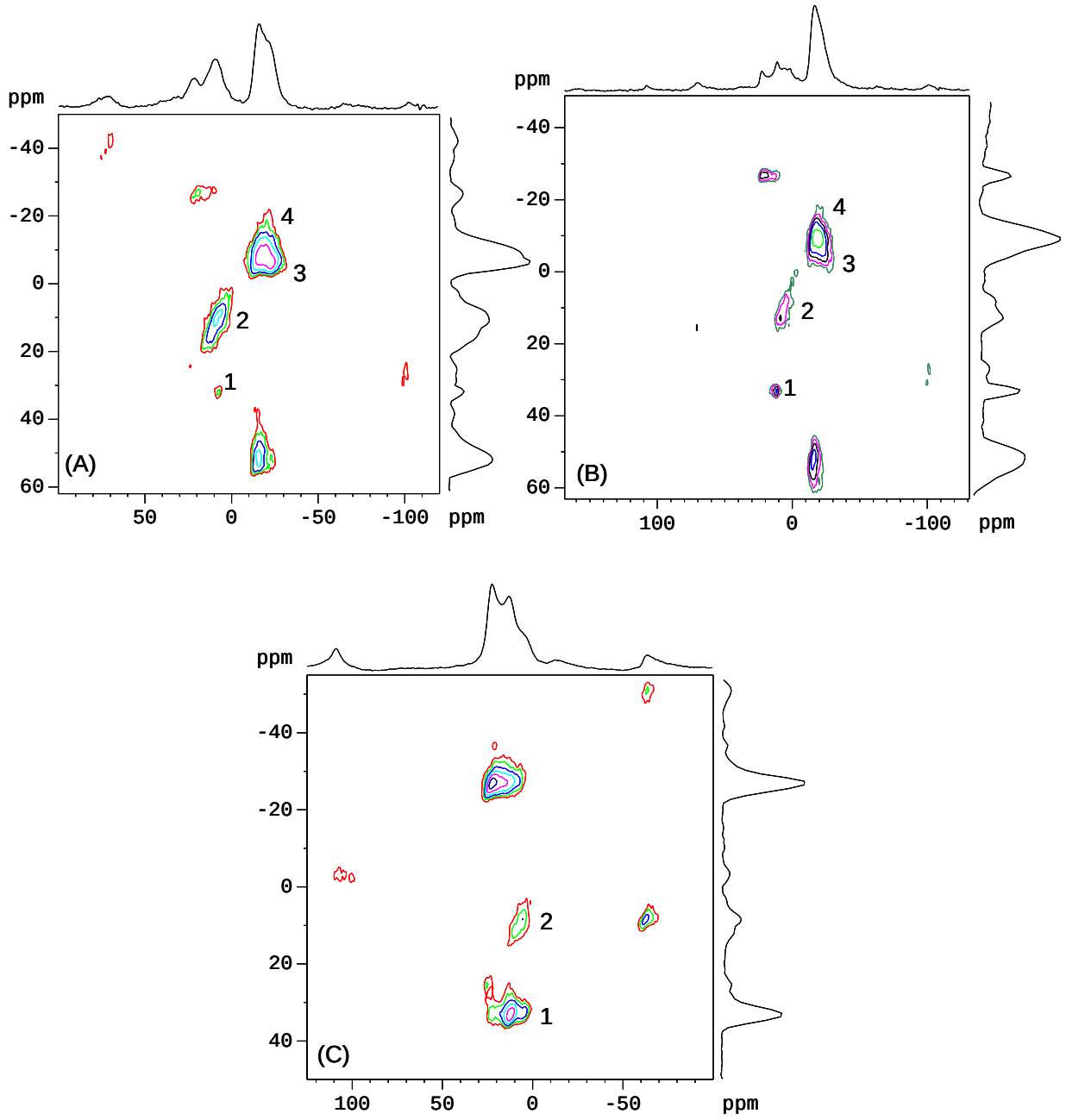

Figure 5.6: Triple-quantum MAS ^{27}Al NMR spectra of the three compounds acquired at 21.1 T with a spinning speed of 20.0 kHz. (A) compound **1**: AlPcCl, (B) compound **2**: $AlPc(SPh)_4Cl$, and (C) **3**: AlNcCl . The unique aluminum sites are marked with numbers. The other peaks are spinning sidebands.

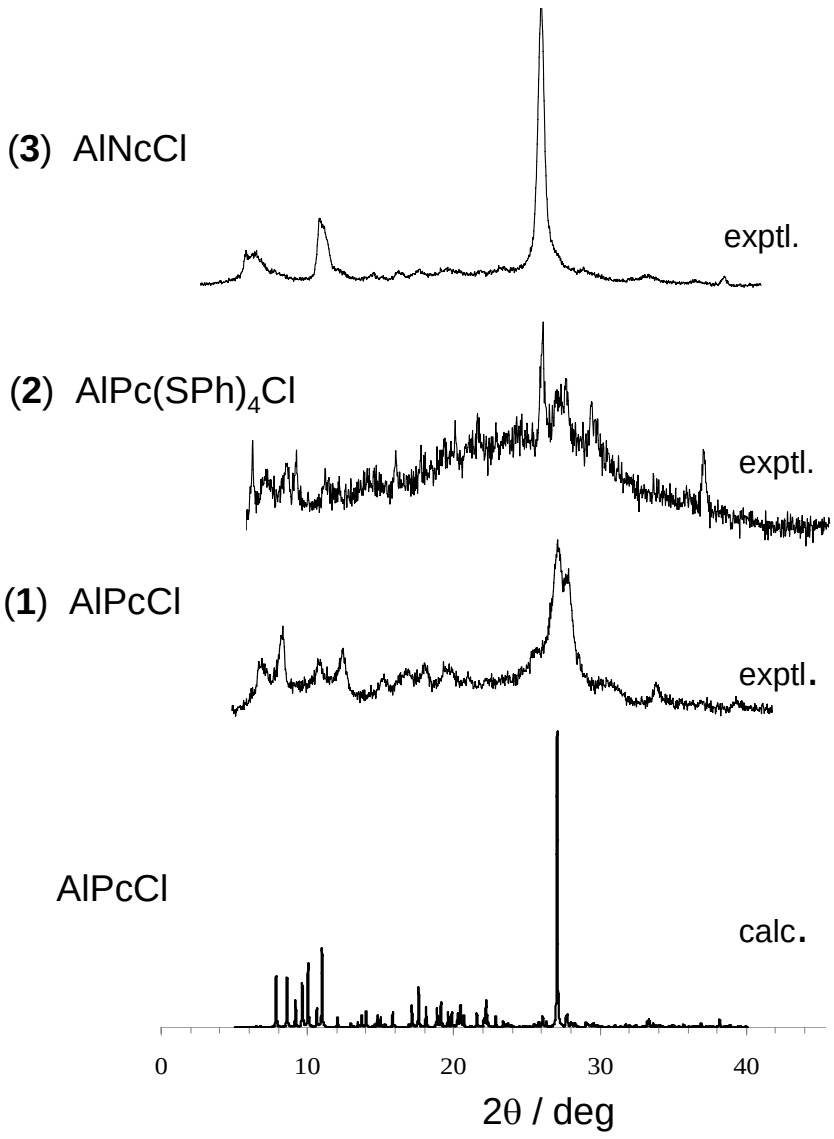

Figure 5.7: Powder X-ray diffraction (PXRD) patterns of the three compounds. (1) Experimental and calculated PXRD pattern of AlPcCl. (2) Experimental PXRD pattern of $AlPc(SPh)_4Cl$. (3) Experimental PXRD pattern of AlNcCl.

Table 5.1: Experimental ^{27}Al solid-state NMR data obtained from the MAS spectra of the three compounds studied. Numbers in parentheses are the estimated uncertainties in the last digits of the extracted parameters.

Compound		Relative Abundance (%)	C_Q (MHz)	η_Q	δ_{iso} (ppm)
(**1**) AlPcCl	site 1	29.4 ± 1.5	9.8 ± 0.4	0.1 ± 0.1	30 ± 3
	site 2	11.8 ± 1.5	5.4 ± 0.4	0.5 ± 0.2	12 ± 1
	site 3	29.4 ± 1.5	6.8 ± 0.4	0.2 ± 0.1	-12 ± 1
	site 4	29.4 ± 1.5	9.1 ± 0.4	0.25 ± 0.15	-12.5 ± 1.0
(**2**) AlPc(SPh)$_4$Cl	site 1	30.3 ± 1.5	10.0 ± 0.4	0.1 ± 0.1	28 ± 2
	site 2	9.1 ± 1.5	5.4 ± 0.4	0.5 ± 0.2	12 ± 1
	site 3	30.3 ± 1.5	6.5 ± 0.2	0.1 ± 0.1	-12.5 ± 1.0
	site 4	30.3 ± 1.5	7.4 ± 0.2	0.1 ± 0.1	-12.5 ± 1.0
(**3**) AlNcCl	site 1	90.9 ± 2.0	9.8 ± 0.2	0.1 ± 0.1	27 ± 1
	site 2	9.1 ± 2.0	5.4 ± 0.4	0.5 ± 0.2	12 ± 1

experimental line shapes and the simulated ones, notably at 21.1 T (Figure 5.8a) due to the inherent higher sensitivity at this ultrahigh field. Simultaneous simulation of the three MAS spectra yields the best-fit values of 27 ppm, 9.8 MHz, and 0.1 for δ_{iso}, C_Q, and η_Q, respectively, for the dominant component (Table 5.1).

In addition to the MAS spectra, ^{27}Al QCPMG and solid-echo NMR spectra of a stationary powder sample of AlNcCl were acquired at 14.1 and 21.1 T, the results of which are shown in Figure 5.9. Comparing the line widths of the static spectra at both fields, it can be readily observed that these line widths are almost equal when measured in Hz. This indicates that chemical shift anisotropy (CSA) has a significant contribution to the powder line shape, and is comparable to the second-order quadrupolar broadening. Had the spectra been dominated by the latter interaction only, then the line width at 21.1 T would have been equal to two-thirds of that at 14.1 T. Clearly, this is not the case. In order to determine the contribution of the CSA to the line shape, the δ_{iso}, C_Q, and η_Q values determined from the MAS experiments were used in the simultaneous simulation of

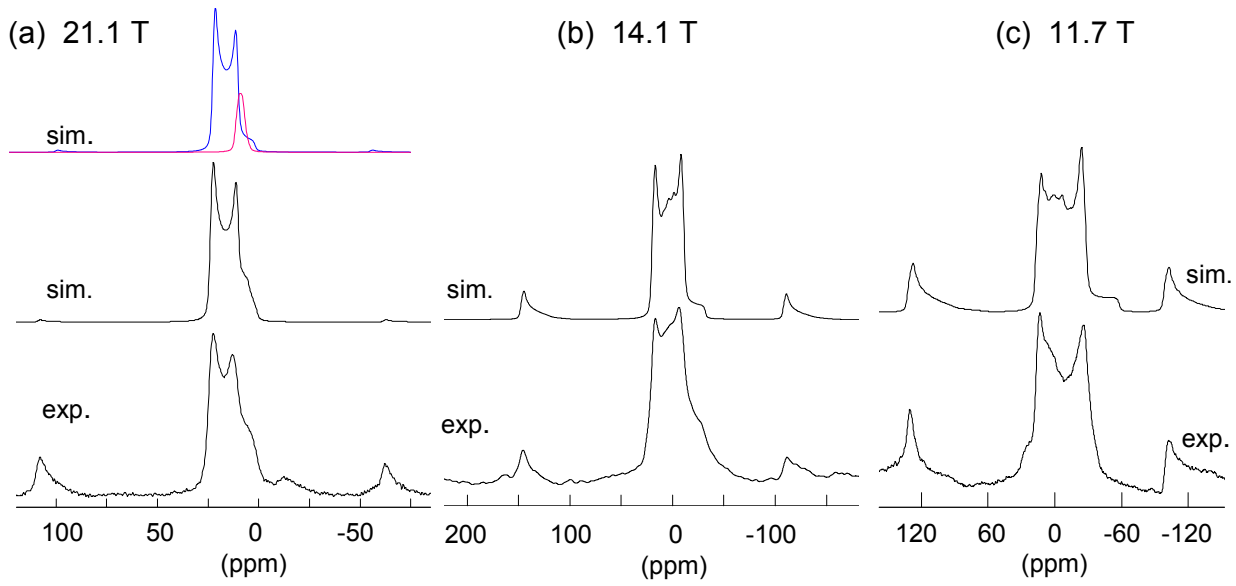

Figure 5.8: Experimental and simulated ^{27}Al MAS NMR spectra of a powder sample of compound **3** acquired at three magnetic fields. Spinning rates are 20.0 kHz in (a) and (b), and 15.0 kHz in (c). The upper trace in (a) shows the simulation for each individual site, where site 1 is in blue and site 2 in red. All simulated spectra were calculated using the parameters reported in Table 5.1.

the static spectra at both fields, and the experimental spectra could be reproduced fairly well with the inclusion of a span of 120 ± 10 ppm and a skew of 0.85 ± 0.10. It is also important to mention that the line shape is very sensitive to the Euler angle β, which is the angle between V_{33} (the largest component of the EFG tensor) and δ_{33} (the most shielded component of the CS tensor). The small experimental value of 5° for this angle indicates that these two components lie almost in the same direction, nearly perpendicular to the plane of the phthalocyanine ring.

A number of studies have noted the presence and characteristics of pentacoordinated Al sites in aluminum-oxide-derived materials.[232,246–250] In accord with the results of those studies, isotropic ^{27}Al chemical shifts of 30 - 40 ppm are observed, falling midway between the common shift ranges of tetrahedral and octahedral aluminum sites encountered in such materials. Quadrupolar coupling constants vary greatly but are generally smaller than what has been observed with these materials, and chemical shift anisotropies in oxide materials are expected to be small.[233] The most relevant comparisons to be made to the results reported here are from other metal-centered complexes involving heterocyclic ligands. Both reports of solid-state ^{27}Al NMR characterizations of pentacoordinated Al sites, in 7-azaindolyl complexes by Aschenhurst *et al.*[235] and in bis-tetrahydrofurfuryloxide complexes by Tang *et al.*,[239] correspond to square-pyramidal geometries about the aluminum centre, similar to the compounds investigated here. However, due to structural distortions in these other compounds, there are some clear differences in the results, particularly with respect to quadrupolar coupling; these were smaller in the azaindolyl complexes, 5.5 - 6.8 MHz, while much larger in tetrahydrofurfuryloxide complexes, 19.6 - 19.9 MHz. Chemical shift data was unreported by Tang *et al.*,[239] as such influences on the acquired NMR spectra were no doubt negligible compared to the very large quadrupolar coupling; however, Aschenhurst *et al.* reported slightly higher ^{27}Al chemical shifts of 43 - 56 ppm in azain-

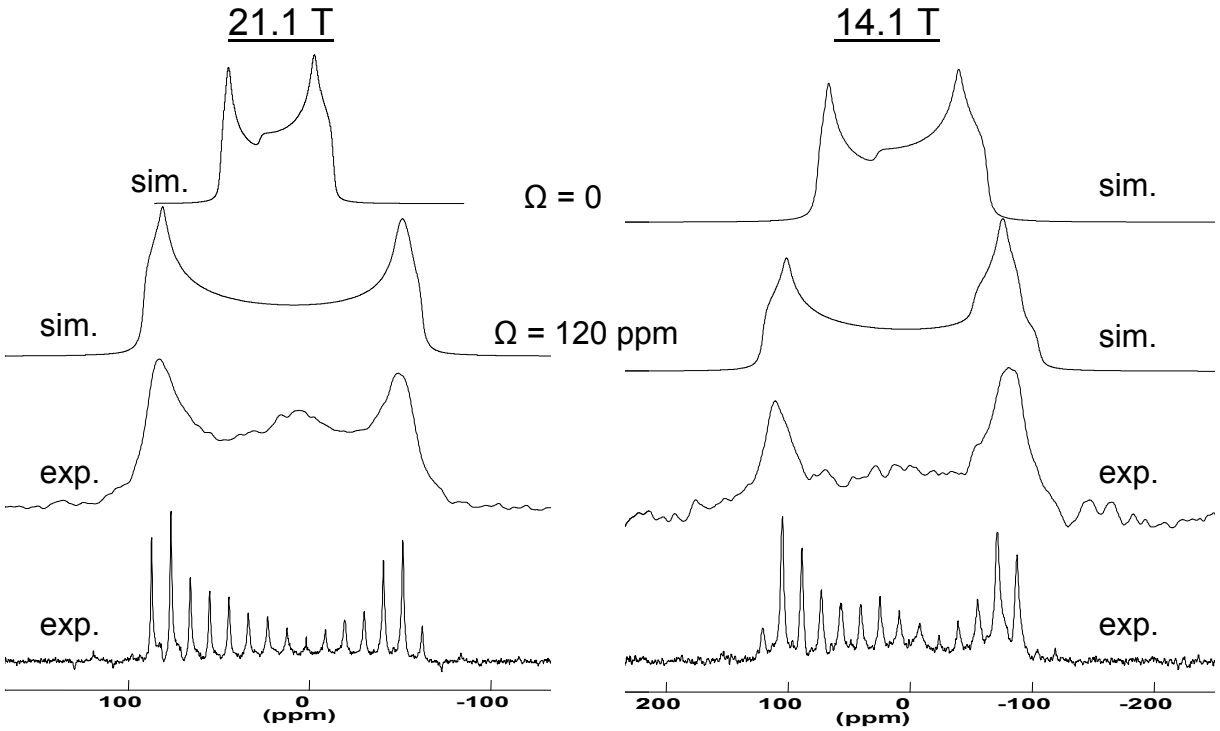

Figure 5.9: Experimental QCPMG and solid-echo ^{27}Al NMR spectra of a stationary powder sample of compound **3** acquired at 21.1 and 14.1 T. Spectra simulated using the experimental parameters with and without CSA are presented above experimental spectra.

dolyl complexes, compared to what has been found here. Of interest in the azaindolyl complexes is the apparent absence of any chemical shift anisotropy; ^{27}Al NMR spectra obtained at 11.7 T could be simulated well without any inclusion of its effects. Clearly, in the square-pyramidal geometry encountered in the phthalocyanine complexes, chemical shift anisotropy has a much greater influence, a fact confirmed by both multiple-field NMR spectra and the computational chemistry results. This may be a reflection of the electron-rich nature of the macrocyclic ring or its rigid steric influence. Indeed, the ^{27}Al chemical shift anisotropy measured for compound **3** and predicted for all compounds from calculations are the largest reported directly from ^{27}Al NMR data of a solid material. The only anisotropies available in the literature that are larger have been derived from gas-phase spin-rotation data for AlNC and AlCl, at 405.6 and 477.4 ppm, respectively.[233]

To gain more insight into the structure of compound **3** and to relate the experimental data to that structure, a series of quantum chemical calculations of the ^{27}Al chemical shielding and EFG tensors was performed using a geometry-optimized model of this compound. The results of these calculations, using various basis sets at the RHF and B3LYP levels, are listed in Table 5.2. Also shown for comparison are the experimentally measured parameters for the major component (site 1) of this compound determined in the present solid-state study. A striking observation of the calculations is the lack of quantitative agreement between the experimental and theoretical values of the ^{27}Al quadrupolar coupling constant. For both the RHF and DFT methods, all of the calculated C_{Q} values are significantly smaller than the experimental value. The largest predicted value of 7.96 MHz, which is obtained with the RHF/6-311+G(2d, p) level, is 17% smaller than the lower experimental limit value of 9.6 MHz. The data also show that for a given basis set, the calculations at the RHF and B3LYP methods give similar results for C_{Q}, with the former method giving slightly larger values. This indicates that electron correlation

Table 5.2: Experimental and calculated ^{27}Al solid-state NMR parameters of compound **3**.

method	basis set	C_Q(MHz)	η_Q	δ_{iso}(ppm)	Ω(ppm)	κ	$\alpha(^\circ)$	$\beta(^\circ)$	$\gamma(^\circ)$
exptl.		9.8 ± 0.2	0.1 ± 0.1	27 ± 1	120 ± 10	0.85 ± 0.10	100 ± 20	5 ± 1	45 ± 20
RHF	6-31G**	5.13	0.36	41	81	0.87	90	15	90
	6-31++G**	5.76	0.33	43	84	0.87	90	15	90
	6-311G**	7.51	0.29	47	100	0.88	90	12	90
	6-311++G**	7.59	0.29	46	100	0.88	90	13	90
	6-311+G(2d, p)	7.96	0.27	47	101	0.88	90	12	90
B3LYP	6-31G**	4.84	0.21	37	104	0.94	90	10	90
	6-31++G**	5.31	0.20	38	101	0.94	90	10	90
	6-311G**	7.26	0.16	41	137	0.95	90	8	90
	6-311++G**	7.32	0.16	40	136	0.94	90	9	90
	6-311+G(2d, p)	7.58	0.16	41	136	0.94	90	8	90

is not important for the system under study. The calculations also indicate that the sign of C_Q is positive. The value of C_Q is also observed to increase as the size of the basis set is increased. The discrepancy between the calculated and observed values of C_Q, and of other reported ^{27}Al NMR parameters as well, may be due to the fact that the atomic coordinates used in the calculations were obtained from a computationally optimized model of the compound, and not from the more realistic single-crystal structure. Other important factors that may cause such discrepancies originate from the fact that calculations were performed on a single isolated rigid molecule in the gas phase (no rovibrational averaging included) and do not take into account the long-range intermolecular interactions in the solid state (which are believed to be very small for the Al site at the centre of the molecule). Also, the limited sizes of the basis sets used may be a factor. It is particularly satisfying to note that theoretical calculations predict an EFG tensor that is nearly axially symmetric, as shown in the tabulated values of the quadrupolar asymmetry parameter. These are in good agreement with the observed value of 0.1 ± 0.1, especially with the B3LYP method employing large basis sets. The calculated B3LYP results for η_Q converge to the value of 0.16, in excellent accord with experiment.

Aside from the isotropic chemical shift values, both RHF and B3LYP calculations of

the ^{27}Al CS tensor parameters show very good agreement with experiment. Both methods overestimate the isotropic chemical shift by at least 10 and 14 ppm for the B3LYP/6-31G** and RHF/6- 31G** methods, respectively. With larger basis sets in both methods, the predicted values become even farther from those observed. The availability of an absolute shielding scale enables the most successful test of the ability of theoretical calculations to reproduce experimentally observed isotropic chemical shifts. In lieu of such a scale for ^{27}Al, it is not surprising to find that the observed isotropic chemical shift, 27 ± 1 ppm, is not well reproduced by the calculations at both levels of theory. As mentioned in the Experimental section of this chapter, the calculated isotropic chemical shifts are derived by subtracting the calculated isotropic ^{27}Al shielding constant in compound **3** from that in $Al[(H_2O)_6]^{3+}$. Hence, the considerable difference between the predicted and observed values of δ_{iso} is attributed to deficiencies in the geometrically optimized model of the reference cation. Geometrical optimization using a larger basis set and/or different theory than RHF (B3LYP or MP2) of this reference compound may be needed to establish better agreement between the experimental and calculated values of δ_{iso}. Sykes *et al.* have reported a series of calculated isotropic shielding constants that converge near 613 ppm for $Al[(H_2O)_6]^{3+}$ at the RHF level (an observation we have confirmed in our own calculations).[251] Using their value as an absolute shielding reference for our calculated results gives δ_{iso} values that are similar to those reported in Table 5.2, with values ranging from 20 to 47 ppm instead of 41 to 47 ppm at the RHF level, but, unsurprisingly, yields δ_{iso} values that are in very poor agreement, ranging from 42 to 80 ppm at the B3LYP level a different computational method in going from the 6-31G** to the 6-311+G(2d, p) basis sets. Our own results indicate a difference between the two computational methods, RHF *vs* B3LYP, of calculating ^{27}Al absolute chemical shielding ranging from 25 to 40 ppm, depending on the basis set used.

As the size of the basis set is augmented, the calculated span of the aluminum CS tensor converges to a value of 100 ppm and 136 ppm at RHF and B3LYP levels, respectively. It is apparent that DFT/B3LYP method yields span values that are closer to the observed one of 120 ± 10 ppm than the RHF method. It is also interesting to find that both methods predict with high accuracy the skew of the aluminum CS tensor. All basis sets, in both methods, yield skew values that fall within the uncertainty limits indicated by the experimental value of 0.85 ± 0.10.

The calculated Euler angles, which define the rotations required to bring the PAS of the EFG tensor into coincidence with that of the CS tensor, are in good agreement with the experimental results at both levels of theory. In particular, calculations predict a small value for angle β, which is the angle between the largest EFG component (V_{33}) and the most shielded CS component (δ_{33}), in close agreement with the observed value of $5 \pm 1°$. Indeed, this is not unexpected, as the observed and predicted pseudo-axial symmetry of both the EFG and CS tensors, with the skew of the latter being close to unity, dictates that approximate coincidence of their unique components, δ_{33} and V_{33}. The absolute orientations of the ^{27}Al EFG and CS tensors in the molecular framework, calculated at the B3LYP/6-311+G(2d, p) level, are shown in Figure 5.10. The most shielded component of the CS tensor, δ_{33}, lies exactly along the Al–Cl bond axis, and the other two CS components, δ_{11} and δ_{22}, are perpendicular to it, and lie in the plane of the naphthalocyanine ring. The EFG tensor exhibits essentially the same orientation as the CS tensor, with V_{33} being 8° off the Al–Cl bond, and the other EFG components (V_{11} and V_{22}) in the plane of the ring. Based on these results and the molecular structure of compound **3**, one can safely suggest that the Al–Cl bond acts as a pseudo-C_4 rotation axis, leading to aluminum being in an approximate square pyramidal coordination environment. These orientations are in line with what has been observed in other phthalocyanine complexes with cobalt,[209]

magnesium[68] and gallium,[96,210] although ring geometry and coordination number can play an important role in the degree of axial symmetry displayed.

In contrast to the two sites observed in compound **3**, Figures 5.6A and 5.6B reveal four distinct aluminum sites in each of compounds **1** and **2**. The presence of four non-equivalent sites, particularly for compound **1**, does not agree with its published crystal structure that reveals two unique and discrete AlPcCl molecules, in which each Al atom is involved in square-pyramidal coordination geometry.[242] Indeed, such disagreement is expected since the samples investigated here are in a poorly crystalline state. An attempt to understand the existence of additional sites in both compounds is discussed later in this chapter (*vide infra*). Estimated values for the isotropic chemical shift (δ_{iso}) and quadrupolar product (P_{Q}) for each site in **1** and **2** were extracted from the sheared 3QMAS spectra using a combination of equation (5.1) and the following equations for a spin-$\frac{5}{2}$ nucleus:[252]

$$\delta_{\mathrm{iso}} = \frac{17\delta_1 + 10\delta_2}{27} \tag{5.2}$$

$$P_{\mathrm{Q}} = \nu_{\mathrm{o}}\sqrt{-\frac{\delta_{\mathrm{qis}}}{6000}} = \nu_{\mathrm{o}}\sqrt{\frac{17(\delta_1 - \delta_2)}{162000}} \tag{5.3}$$

where δ_1 and δ_2 are the experimental chemical shifts for the centre of gravity of the peak in F1 and F2 dimensions of the sheared 3QMAS spectrum; ν_{o} is the Larmor frequency; P_{Q} and ν_{o} are in MHz, and δ is in ppm. These estimated values were subsequently used in the simulation of the one-dimensional MAS spectra acquired at multiple fields. These spectra are shown in Figures 5.11 and 5.12 for compounds **1** and **2**, respectively. The best-fit parameters obtained from the simultaneous simulation of the spectra at three fields are listed in Table 5.1.

Quantum chemical calculations were also performed on compounds **1** and **2**, the results of which are given in Tables 5.3 and 5.4, respectively. Table 5.3 shows the calculated results

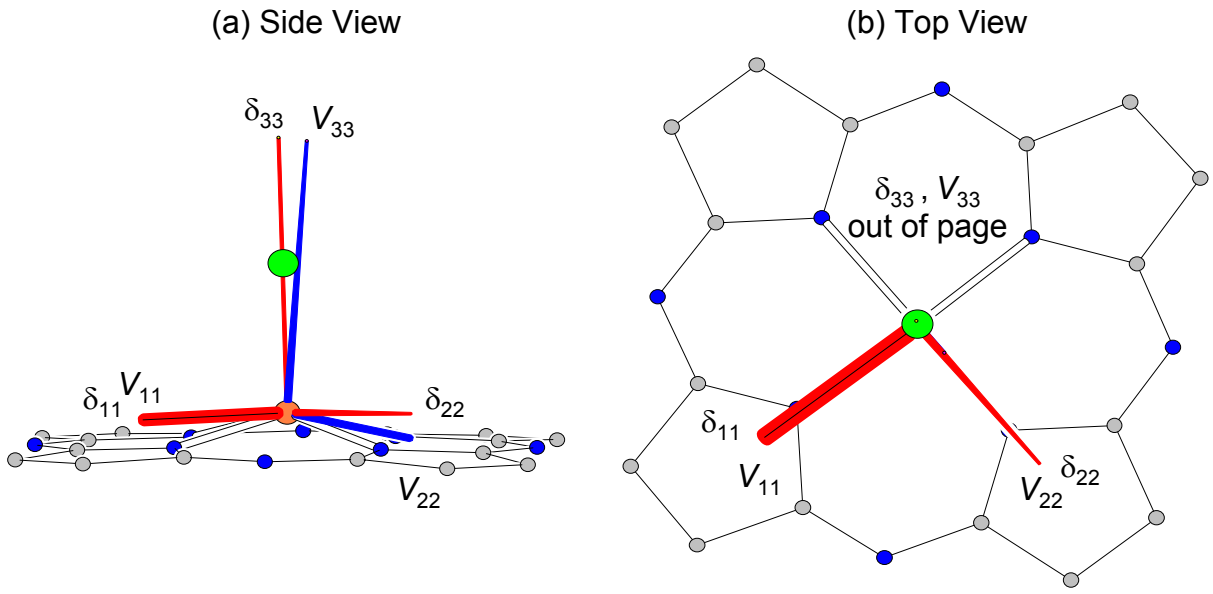

Figure 5.10: Calculated orientations of the ^{27}Al chemical shift (in red) and electric field gradient (in blue) tensors in the molecular frame of compound **3**, as superimposed on views from the (a) side and (b) top. Only part of the molecular structure that depicts aluminum coordination environment is shown. Hydrogens are omitted for clarity. Aluminum is shown in orange, chlorine in green, nitrogen in blue, and carbon in gray.

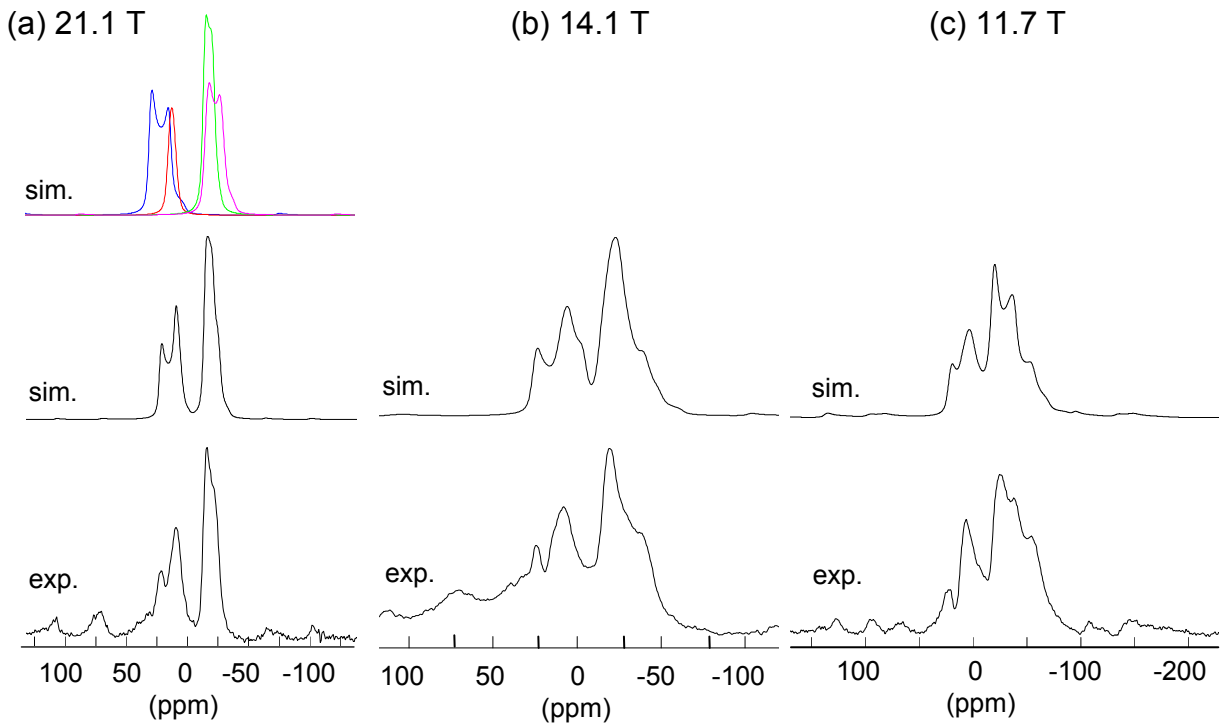

Figure 5.11: Experimental and simulated ^{27}Al MAS NMR spectra of a powder sample of compound **1** acquired at three magnetic fields. Spinning rates are 20.0 kHz in (a) and (b), and 15.0 kHz in (c). The upper trace in (a) shows the simulation for each individual site; site 1 blue, site 2 red, site 3 green, site 4 pink. All simulated spectra were calculated using the parameters reported in Table 5.1.

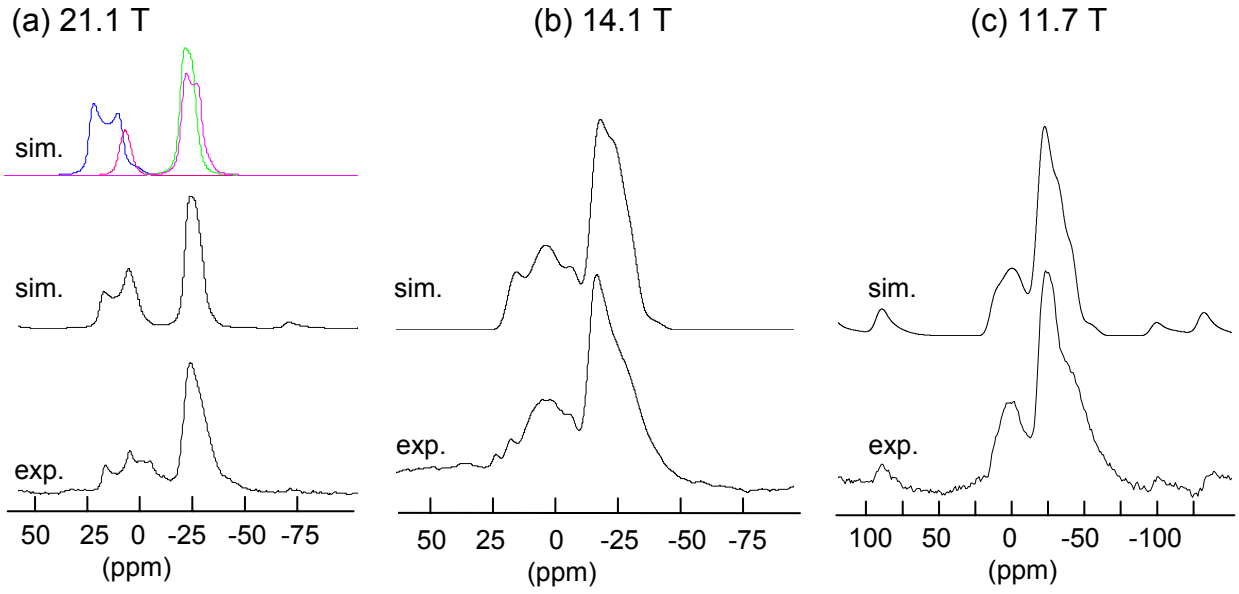

Figure 5.12: Experimental and simulated ^{27}Al MAS NMR spectra of a powder sample of compound **2** acquired at three magnetic fields. Spinning rates are 20.0 kHz in (a) and (b), and 15.0 kHz in (c). The upper trace in (a) shows the simulation for each individual site; site 1 blue, site 2 red, site 3 green, site 4 pink. All simulated spectra were calculated using the parameters reported in Table 5.1.

Table 5.3: Calculated ^{27}Al solid-state NMR parameters of compound **1**.

method	basis set	C_Q(MHz)	η_Q	δ_{iso}(ppm)	Ω(ppm)	κ	$\alpha(^\circ)$	$\beta(^\circ)$	$\gamma(^\circ)$
exptl.(site 1)		9.8 ± 0.4	0.1 ± 0.1	30 ± 3					
Molecule 1									
RHF	6-31G**	6.07	0.10	33	102	0.98	158	1	21
	6-31++G**	6.77	0.09	36	106	0.97	145	0.7	29
	6-311G**	8.94	0.07	39	122	0.98	130	0.6	24
	6-311++G**	9.01	0.07	37	122	0.98	121	0.6	38
	6-311+G(2d, p)	9.39	0.07	39	124	0.98	117	0.6	41
B3LYP	6-31G**	5.83	0.09	33	108	0.98	7	1	172
	6-31++G**	6.38	0.08	43	109	0.92	35	0.8	169
	6-311G**	8.68	0.07	38	141	0.98	171	0.6	159
	6-311++G**	8.74	0.07	37	141	0.98	175	0.8	159
	6-311+G(2d, p)	9.01	0.07	38	141	0.98	173	0.6	159
Molecule 2									
RHF	6-31G**	7.51	0.09	34	99	0.97	121	2.5	39
	6-31++G**	8.24	0.08	36	104	0.95	90	2	32
	6-311G**	10.67	0.06	39	120	0.96	90	1.6	26
	6-311++G**	10.75	0.06	38	120	0.96	90	1.6	27
	6-311+G(2d, p)	11.13	0.06	39	122	0.96	90	1.5	25
B3LYP	6-31G**	7.10	0.08	33	106	0.97	90	2.3	40
	6-31++G**	7.68	0.08	35	106	0.94	95	2	59
	6-311G**	10.24	0.06	38	139	0.95	97	1.5	27
	6-311++G**	10.31	0.06	35	140	0.94	96	1.4	33
	6-311+G(2d, p)	10.58	0.06	37	140	0.96	90	1.4	32

obtained for the two AlPcCl molecules present in the asymmetric unit of compound **1**. Comparing these results with the experimental values obtained for site 1 of this compound, one observes a fair agreement, within experimental error, between the experimental values of δ_{iso}, C_Q, and η_Q and the calculated values at both the RHF and B3LYP levels. Most notably, the calculations predict an almost axially symmetric ^{27}Al EFG tensor, in perfect accord with experiment. The same can be said about the predicted results of compound **2**, as shown in Tables 5.4. The B3LYP calculations accurately reflect the experimental value of 0.1 ± 0.1 for η_Q observed for site 1 of **2** at all basis sets used, though it should be noted that they were carried out on a geometrically optimized model, and not on an actual crystal structure as none exists.

Table 5.4: Calculated ^{27}Al solid-state NMR parameters of compound **2**.

method	basis set	C_Q(MHz)	η_Q	δ_{iso}(ppm)	Ω(ppm)	κ	$\alpha(^\circ)$	$\beta(^\circ)$	$\gamma(^\circ)$
exptl.(site 1)		10.0 ± 0.4	0.1 ± 0.1	28 ± 2					
RHF	6-31G**	5.39	0.35	39	86	0.87	87	14	93
	6-31++G**	6.05	0.31	41	91	0.88	87	13	93
	6-311G**	7.80	0.28	45	107	0.88	87	11	93
	6-311++G**	7.90	0.28	43	106	0.88	87	11	93
	6-311+G(2d, p)	8.25	0.28	44	106	0.88	87	11	93
B3LYP	6-31G**	5.11	0.21	35	108	0.94	86	9	94
	6-31++G**	5.64	0.19	37	107	0.94	86	9	93
	6-311G**	7.55	0.16	39	142	0.94	86	7	94
	6-311++G**	7.63	0.16	37	143	0.94	86	7	94
	6-311+G(2d, p)	7.88	0.16	38	142	0.94	86	7	94

In light of this successful agreement between experiment and calculation for the major component of **3**, attempts were then made to use calculated predictions to guide interpretation of both the impurity peak common to all three compounds, and to the additional sites apparent in compounds **1** and **2**. Based on both the simulated best-fit parameters for these additional sites, as given in Table 5.1, with ^{27}Al chemical shifts falling in the expected range for octahedral Al species, and the chemical nature of these related dye molecular frameworks, it was appropriate to focus on possible octahedral derivatives of the parent pentacoordinate species. Calculated results were obtained for optimized structures composed of the original species with an additional axial ligand, either chlorine atom or H_2O, completing the octahedral coordination of Al by occupying the empty site below the phthalocyanine ring. These calculated results are given in Tables 5.5 and 5.6. While exact agreement is not possible, it is clear that the trends are consistent with two likely assignments: sites 3 and 4 of compounds **1** and **2** are likely associated with additional Cl ligands interacting with the central Al, resulting in a low frequency movement of the ^{27}Al chemical shift to approximately -12 ppm; and site 2 of all three compounds is likely associated with a different ligand, possibly H_2O or another light coordinating atom (OH, NH_3, etc.) resulting in a ^{27}Al chemical shift near 12 ppm. In each case, it seems quite

Table 5.5: Calculated ^{27}Al solid-state NMR parameters of a theoretical octahedral model of compound **1**, in which an additional axial chlorine is coordinated to Al.

method	basis set	C_Q(MHz)	η_Q	δ_{iso}(ppm)	Ω(ppm)	κ	$\alpha(^\circ)$	$\beta(^\circ)$	$\gamma(^\circ)$
RHF	6-31G**	9.02	0.14	-15	33	0.83	91	0	89
	6-31++G**	10.05	0.13	-7	38	0.86	86	0	94
	6-311G**	12.62	0.13	+5	45	0.87	90	0	90
	6-311++G**	12.66	0.13	+7	48	0.88	91	0	89
	6-311+G(2d, p)	12.82	0.13	+8	46	0.87	90	0	90
B3LYP	6-31G**	7.99	0.08	+3	45	0.95	85	0	95
	6-31++G**	8.66	0.07	+8	34	0.93	125	0	55
	6-311G**	11.34	0.07	-1	74	0.97	92	0	88
	6-311++G**	11.31	0.07	0	59	0.96	97	0	83
	6-311+G(2d, p)	11.43	0.07	-1	52	0.96	102	0	78

Table 5.6: Calculated ^{27}Al solid-state NMR parameters of a theoretical octahedral model of compound **1**, in which an additional axial H_2O is coordinated to Al.

method	basis set	C_Q(MHz)	η_Q	δ_{iso}(ppm)	Ω(ppm)	κ	$\alpha(^\circ)$	$\beta(^\circ)$	$\gamma(^\circ)$
RHF	6-31G**	7.48	0.03	+3	76	0.99	174	1	74
	6-31++G**	8.15	0.02	+18	85	0.98	175	2	5
	6-311G**	9.87	0.02	+8	93	0.99	176	1	83
	6-311++G**	9.95	0.02	+16	93	0.99	176	1	85
	6-311+G(2d, p)	10.29	0.02	+17	94	0.99	175	1	84
B3LYP	6-31G**	7.36	0.02	+8	75	0.99	176	2	13
	6-31++G**	7.77	0.02	+17	80	0.92	174	2	7
	6-311G**	9.43	0.02	+14	106	0.99	177	2	88
	6-311++G**	9.52	0.02	+13	106	0.99	176	2	80
	6-311+G(2d, p)	9.76	0.02	+13	106	0.99	173	2	87

clear that a completion of the octahedral coordination sphere of Al is responsible for the additional components.

5.5 Conclusions

A combination of solid-state ^{27}Al NMR experiments and quantum chemical calculations has been used to study anisotropic ^{27}Al NMR interaction tensors in three commercially

obtained aluminum-centered phthlaocyanine dyes. The ^{27}Al CS and EFG tensors, including their relative orientations, were determined for aluminum-2,3-naphthalocyanine chloride. The span of the aluminum chemical shift tensor in this compound is the largest measured directly by ^{27}Al SSNMR spectroscopy. RHF and DFT calculations have provided more insight into the aluminum CS and EFG tensors, and their orientation with respect to the molecular frame, indicating that their largest components, δ_{33} and V_{33}, are perpendicular to the macrocyclic ring of this compound. The use of a 21.1 T NMR spectrometer has offered an excellent opportunity for visible manifestation of the aluminum chemical shift anisotropy in experiments performed on stationary polycrystalline samples. In addition, the use of such an ultrahigh-field magnet, combined with the state-of-art triple-quantum MAS experiment, was very vital for the resolution of the different non-equivalent aluminum sites present in powder samples of the three related compounds.

Chapter 6

Concluding Remarks

6.1 Thesis Contributions

The application of solid-state NMR methodology, involving the employment of several techniques aimed at the observation of the two spin-$\frac{5}{2}$ ^{67}Zn and ^{27}Al nuclei as well as at the investigation of their corresponding NMR quadrupolar and shielding tensors, enabled an extensive characterization of local electronic structures about the two metal centres in several model zinc coordination complexes and in the three biologically important zinc-insulin hexamers, in addition to three multi-component aluminum-phthalocyanine and -naphthalocyanine commercial dyes. In addition to the specific conclusions achieved in the different cases investigated, which have been reported in the end of the single chapters, some general conclusions can be drawn from this thesis, and are highlighted here.

The first study examined ^{67}Zn NMR in model coordination compounds. The systems investigated were specifically selected for their relevance in bioinorganic chemistry, and in two cases for the lack of NMR data for pentacoordinated zinc sites. In all cases, the

quadrupolar interaction was found to dominate the central-transition ^{67}Zn NMR spectra; no convincing effects from chemical shift anisotropy (CSA) on the NMR spectra of the five complexes could be reliably detected at the applied field strength. The Zn quadrupolar interaction proved to be extremely sensitive to changes in the local zinc environment. The feasibility and practicality of solid-state ^{67}Zn NMR experiments was demonstrated by this work, allowing pertinent information about the electronic and molecular structure to be obtained in reasonable experimental times.

The second study represented an extension of the first work toward the NMR observation of zinc ions in larger and more complex systems of biological relevance, as in the three zinc-insulin hexamers. Preliminary ^{67}Zn NMR studies on these systems involved characterization of the isotropic chemical shifts and quadrupolar parameters for powdered samples, thus demonstrating the great potential borne by solid-state NMR to tackle such challenging and demanding issues as the presence of zinc ions in very dilute environments.

The third study demonstrated the ability of solid-state ^{27}Al NMR to investigate the high degree of complexity in many multi-component materials, such as the aluminum-phthalocyanine dyes, which is due to the presence of different chemical components and phases, arising from the usual lack of structural order as well as from the coexistence of sample fractions exhibiting different coordination environments. These complications often hampered detailed information from being obtained from a single NMR experiment. To this regard, the employment of a combined multi-experiment NMR approach, together with *ab initio* and density functional theory (DFT) computations, enabled the extraction of reliable information on important specific aspects, such as the nature and the number of the components coexisting in the different materials.

In the past, solid-state NMR studies of ^{67}Zn were greatly discouraged due to the lack of adequate resources, such as super-conducting high-field magnets and reliable pulse se-

quences. Fortunately, the ever-growing use of NMR as a successful tool in various aspects of scientific research has been the driving force behind many advances in this field. In our case, for example, the use of a 21.1 T magnetic field, with the QCPMG and WURST-QCPMG experiments and stepped-frequency techniques, has ultimately paved the way to the success of the NMR investigations that have been reported in this thesis. Of particular interest is the recently introduced WURST-QCPMG experiment that has provided promising results by producing spectra of unreceptive nuclei with higher signal-to-noise in a much shorter time than the standard QCPMG experiment. More progress in the area of difficult nuclei is expected in the future. Consequently, this progress must necessarily be accompanied with the production of magnets with much higher field strengths and with the development of new and improved sensitivity-enhancement techniques. It is hoped that the research presented in this thesis will stimulate more interest in this area toward studying more challenging nuclei in more complex and important systems.

6.2 Further Research Work

Based on the present solid-state ^{67}Zn NMR studies, an important course of research can be proposed that involves the zinc binding motifs in zinc finger proteins. The zinc finger domains, consisting of approximately 30 amino acids,[253] with a systematic placement for Cys and/or His residues within the sequence, are excellent candidates to investigate by solid-state ^{67}Zn NMR. The consensus sequences normally studied are: $X_3-Cys-X_4-Cys-X_{12}-His-X_3-His-X$ (where X is a non-Cys/His amino acid) for Cys_2His_2 binding motifs, and $X_2-Cys-X_2-Cys-X_4-His-X_4-Cys-X_2$ for Cys_3His binding motifs, although shorter sequences can also be used. Another interesting peptide that have appeared in the literature is the GAL4 motif,[254] which constitutes a binuclear Zn_2Cys_6

complex at its core, incorporating two bridging Cys residues in a Zn_2S_2 four-membered ring. The application of solid-state ^{67}Zn NMR methods to the zinc finger domains will be helpful to better understand the role played by zinc ions in stabilizing their folds, and to further characterize the nature of the coordination environments around the zinc ions in these systems, as this important information is sometimes not precisely determined by diffraction techniques, as in the case of the T_6 zinc-insulin hexamer.

APPENDICES

Appendix A

Supplementary Data for Chapter 3

Single-crystal X-ray Structure of Bis(imidazole)zinc(II) Chloride

Table A.1: Crystallographic data and structure refinement for bis(imidazole)zinc(II) chloride.

	$Zn(imidazole)_2Cl_2$
Empirical formula	$C_6H_8N_4Cl_2Zn$
Formula weight	272.43
Temperature (K)	243(1)
Wavelength (Å)	0.71073
Crystal size (mm^3)	0.30 x 0.26 x 0.23
Crystal system, space group	Monoclinic, $P2_1/n$
Unit cell dimensions	
a (Å)	7.9306(3)
b (Å)	11.7739(4)
c (Å)	11.4156(4)
α (°)	90.0
β (°)	105.441(1)
γ (°)	90.0
Volume ($Å^3$)	1027.45(6)
Z	4
Calculated density ($g.cm^{-3}$)	1.761
Absorption coefficient (mm^{-1})	2.869
$F(000)$	544
θ range for data collection(°)	2.53 to 30.00
Limiting indices	$-11 \leq h \leq 10$; $-16 \leq k \leq 16$; $-16 \leq l \leq 15$
Reflections collected	8289
Unique reflections	2970 [$R_{\text{int}} = 0.0153$]
Absorption correction	Empirical
Max. and min. transmission	1.000 and 0.825
Refinement method	Full-matrix least-squares on F^2
Data/restraints/parameters	2970 / 0 / 119
Goodness-of-fit on F^2	1.968
Final R indices [$I > 2\sigma(I)$]	$R_1 = 0.0211$, $wR_2 = 0.0528$
R indices (all data)	$R_1 = 0.0228$, $wR_2 = 0.0531$
Extinction coefficient	0.0140(8)
Largest diff. peak and hole (e $Å^{-3}$)	0.278 and -0.334

Table A.2: Atomic Cartesian coordinates (x 10^4) and equivalent isotropic displacement parameters (Å^2 x 10^3) for bis(imidazole)zinc(II) chloride. U(eq) is defined as one third of the trace of the orthogonalized U_{ij} tensor.

	x	y	z	U(eq)
Zn(1)	4934(1)	1808(1)	2494(1)	26(1)
Cl(1)	5343(1)	3611(1)	3191(1)	30(1)
Cl(2)	2082(1)	1373(1)	1906(1)	35(1)
N(1)	6349(1)	830(1)	3835(1)	27(1)
C(2)	6760(2)	1077(1)	5004(1)	34(1)
N(3)	7684(2)	244(1)	5653(1)	39(1)
C(4)	7888(2)	-585(1)	4880(1)	42(1)
C(5)	7070(2)	-218(1)	3754(1)	36(1)
N(6)	5938(1)	1555(1)	1083(1)	28(1)
C(7)	7609(2)	1435(1)	1133(1)	37(1)
N(8)	7822(2)	1318(1)	23(1)	41(1)
C(9)	6219(2)	1363(1)	-787(1)	42(1)
C(10)	5056(2)	1509(1)	-128(1)	34(1)
H(2)	6442	1751	5333	41
H(3)	8089	232	6440	47
H(4)	8482	-1278	5087	51
H(5)	7004	-615	3029	44
H(7)	8522	1433	1854	44
H(8)	8815	1228	-154	50
H(9)	5971	1304	-1637	50
H(10)	3838	1569	-445	40

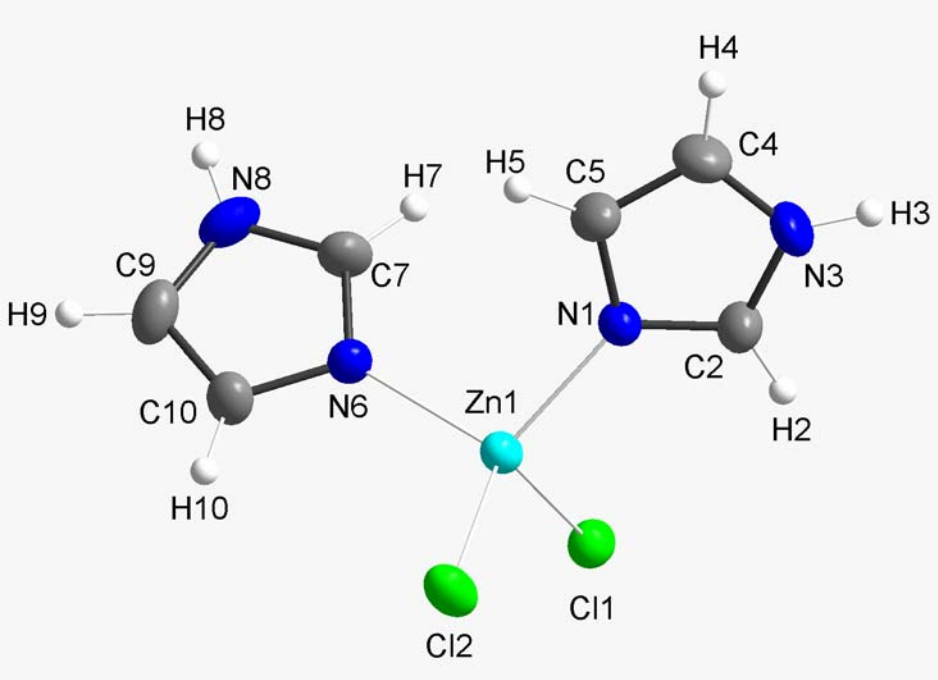

Figure A.1: Molecular structure of bis(imidazole)zinc(II) chloride determined by single-crystal X-ray diffraction experiment. Heavy atoms are drawn with 50 % probability ellipsoids.

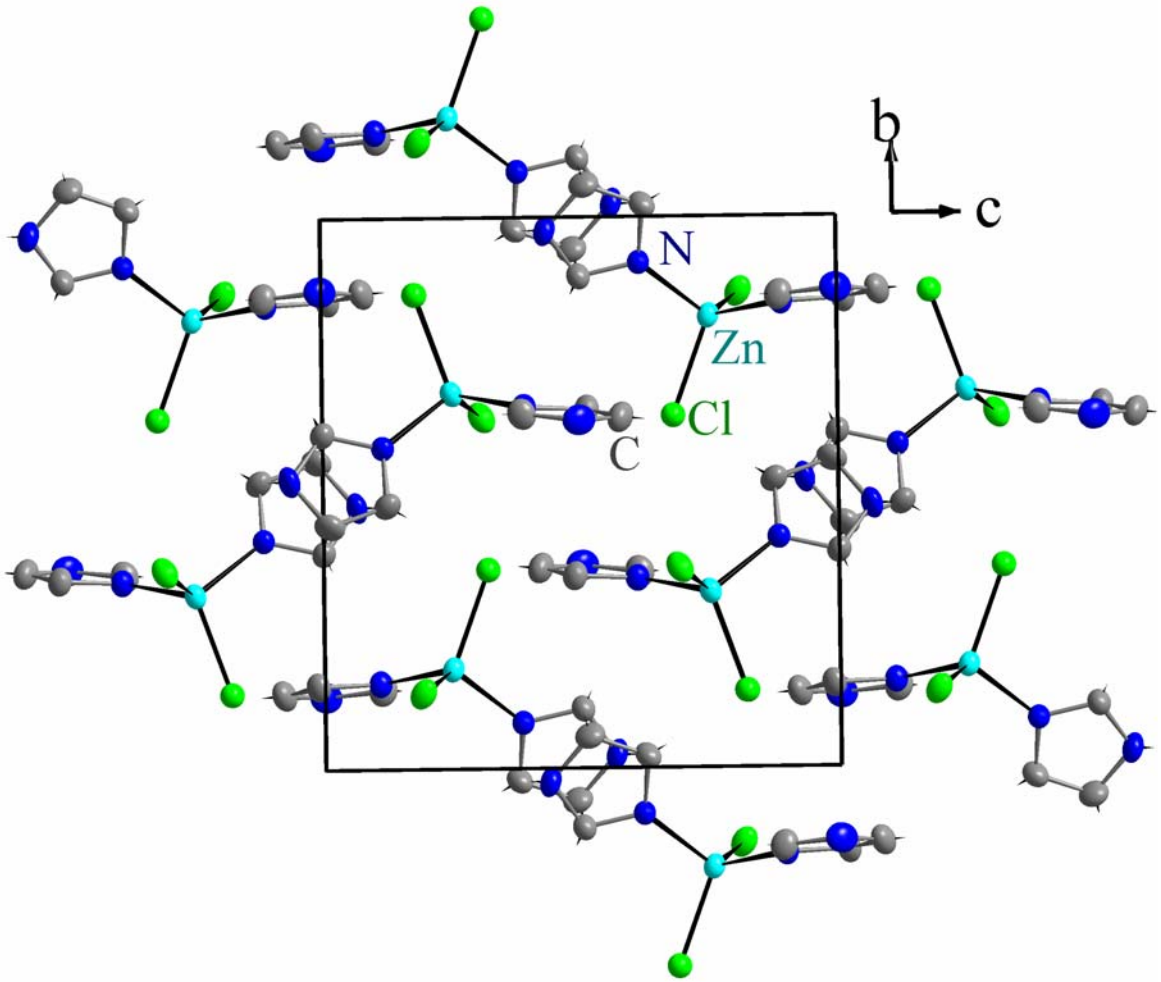

Figure A.2: Crystal packing of bis(imidazole)zinc(II) chloride, in projection along the *a* axis.

Table A.3: Bond lengths [Å] and angles [°] for bis(imidazole)zinc(II) chloride.

Bond	Distance(Å)	Bond angle	Angle(°)
Zn(1)-N(1)	2.0032(10)	N(1)-Zn(1)-N(6)	105.55(4)
Zn(1)-N(6)	2.0005(10)	N(6)-Zn(1)-Cl(2)	108.12(3)
Zn(1)-Cl(1)	2.2597(3)	N(1)-Zn(1)-Cl(2)	114.39(3)
Zn(1)-Cl(2)	2.2403(4)	N(6)-Zn(1)-Cl(1)	111.88(3)
N(1)-C(2)	1.3189(16)	N(1)-Zn(1)-Cl(1)	105.77(3)
N(1)-C(5)	1.3738(16)	Cl(2)-Zn(1)-Cl(1)	111.049(14)
C(2)-N(3)	1.3262(17)	C(2)-N(1)-C(5)	105.69(11)
N(3)-C(4)	1.354(2)	C(2)-N(1)-Zn(1)	125.75(9)
C(4)-C(5)	1.3469(19)	C(5)-N(1)-Zn(1)	128.56(9)
N(6)-C(7)	1.3187(17)	N(1)-C(2)-N(3)	110.69(12)
N(6)-C(10)	1.3736(17)	C(2)-N(3)-C(4)	108.25(12)
C(7)-N(8)	1.3299(19)	C(5)-C(4)-N(3)	106.23(13)
N(8)-C(9)	1.360(2)	C(4)-C(5)-N(1)	109.13(12)
C(9)-C(10)	1.347(2)	C(7)-N(6)-C(10)	106.03(11)
		C(7)-N(6)-Zn(1)	126.26(10)
		C(10)-N(6)-Zn(1)	127.68(9)
		N(6)-C(7)-N(8)	110.55(13)
		C(7)-N(8)-C(9)	108.10(13)
		C(10)-C(9)-N(8)	106.27(13)
		C(9)-C(10)-N(6)	109.05(13)

Single-crystal X-ray Structure of Sodium Bis(L-cysteinato)zincate(II) Hexahydrate

Table A.4: Crystallographic data and structure refinement for sodium bis(L-cysteinato)zincate(II) hexahydrate.

	$Na_2Zn(L{-}Cys)_2 \cdot 6\,H_2O$
Empirical formula	$C_6H_{22}N_2O_{10}S_2Na_2Zn$
Formula weight	457.73
Temperature (K)	200(2)
Wavelength (Å)	0.71073
Crystal size (mm^3)	0.50 x 0.10 x 0.02
Crystal system, space group	Monoclinic, *C2*
Unit cell dimensions	
a (Å)	5.1893(2)
b (Å)	23.2065(8)
c (Å)	15.0008(5)
α (°)	90.0
β (°)	92.5610(10)
γ (°)	90.0
Volume ($Å^3$)	1804.67(11)
Z	4
Calculated density ($g.cm^{-3}$)	1.685
Absorption coefficient (mm^{-1})	1.685
$F(000)$	944
θ range for data collection (°)	3.24 to 29.99
Limiting indices	$-7 \leq h \leq 7$; $-32 \leq k \leq 32$; $-20 \leq l \leq 21$
Reflections collected	11986
Unique reflections	5220 [$R_{\text{int}} = 0.0246$]
Absorption correction	Empirical
Max. and min. transmission	0.9666 and 0.4817
Refinement method	Full-matrix least-squares on F^2
Data/restraints/parameters	5220 / 13 / 262
Goodness-of-fit on F^2	1.377
Final R indices [$I > 2\sigma(I)$]	$R_1 = 0.0355$, $wR_2 = 0.0887$
R indices (all data)	$R_1 = 0.0379$, $wR_2 = 0.0898$
Absolute structure parameter	0.007(10)
Largest diff. peak and hole ($e\ Å^{-3}$)	1.618 and -0.872

Table A.5: Atomic Cartesian coordinates (x 10^4) and equivalent isotropic displacement parameters ($Å^2$ x 10^3) for sodium bis(L-cysteinato)zincate(II) hexahydrate. U(eq) is defined as one third of the trace of the orthogonalized U_{ij} tensor.

	x	y	z	U(eq)
Zn(1)	-5000	4993(1)	0	19(1)
S(1)	-2563(2)	5387(1)	-1089(1)	22(1)
O(1)	-3120(4)	3807(1)	-1021(2)	23(1)
O(2)	-2365(6)	4025(1)	-2430(2)	42(1)
N(1)	-7149(5)	4528(1)	-928(2)	18(1)
C(1)	-3572(6)	4079(1)	-1733(2)	20(1)
C(2)	-5790(6)	4515(1)	-1774(2)	19(1)
C(3)	-4794(7)	5117(1)	-1976(2)	23(1)
Na(1)	-5000	3178(1)	0	18(1)
Na(2)	0	2279(1)	0	19(1)
O(3)	-1197(4)	3134(1)	859(1)	20(1)
O(4)	-3861(5)	2371(1)	-939(2)	23(1)
O(5)	-1530(5)	1740(1)	1199(2)	23(1)
Zn(2)	-5000	1284(1)	-5000	20(1)
S(2)	-2532(2)	886(1)	-3860(1)	24(1)
O(6A)	-2810(30)	2470(8)	-4061(8)	37(4)
O(6B)	-3500(20)	2668(7)	-3873(8)	19(3)
O(7)	-1550(4)	2256(1)	-2667(1)	23(1)
N(2)	-6911(5)	1798(1)	-4122(2)	21(1)
C(4)	-3142(6)	2241(1)	-3323(2)	22(1)
C(5)	-5387(6)	1820(1)	-3262(2)	18(1)
C(6)	-4485(6)	1214(2)	-3002(2)	24(1)
Na(3)	1470(5)	3218(1)	-2703(2)	32(1)
O(8)	4198(6)	3584(1)	-3807(2)	43(1)
Na(4)	1883(5)	4067(1)	-4984(2)	13(1)
O(9A)	670(30)	4595(4)	-6029(7)	31(3)
O(9B)	-520(40)	4485(4)	-6216(6)	30(3)
O(10)	5000	4844(3)	-5000	34(2)
O(11)	622(8)	3215(2)	-4838(3)	24(1)
O(12)	5000	4174(3)	-5000	25(1)

Table A.6: Hydrogen Cartesian coordinates (x 10^4) and equivalent isotropic displacement parameters ($Å^2$ x 10^3) for sodium bis(L-cysteinato)zincate(II) hexahydrate. U(eq) is defined as one third of the trace of the orthogonalized U_{ij} tensor.

	x	y	z	U(eq)
H(1A)	-7374	4166	-729	22
H(1B)	-8712	4691	-1019	22
H(2A)	-7024	4401	-2256	23
H(3A)	-6244	5379	-2048	28
H(3B)	-3920	5109	-2534	28
H(3X)	130(80)	3350(17)	860(30)	24
H(4X)	-5250(90)	2468(18)	-1030(30)	28
H(4Y)	-3440(90)	2420(20)	-1310(30)	28
H(5X)	-610(80)	1801(19)	1590(30)	27
H(5Y)	-1600(70)	1400(20)	1110(30)	27
H(2X)	-7102	2156	-4347	25
H(2Y)	-8489	1653	-4035	25
H(5A)	-6515	1960	-2802	22
H(6A)	-5978	973	-2911	28
H(6B)	-3474	1232	-2443	28
H(9X)	50(120)	4780(20)	-6080(40)	36
H(11X)	980(70)	2891(16)	-5500(20)	28

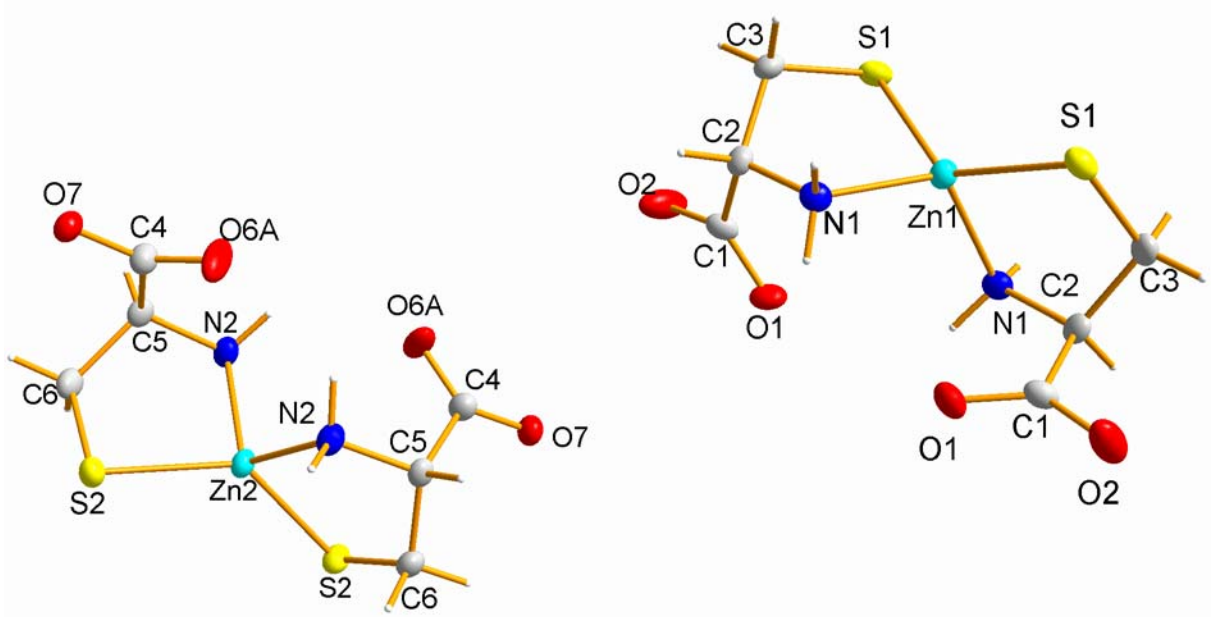

Figure A.3: Molecular structure of each of the independent $[Zn(L{-}Cys)_2]^{2-}$ anions of sodium bis(L-cysteinato)zincate(II) hexahydrate determined by single-crystal X-ray diffraction experiment. Heavy atoms are drawn with 50 % probability ellipsoids.

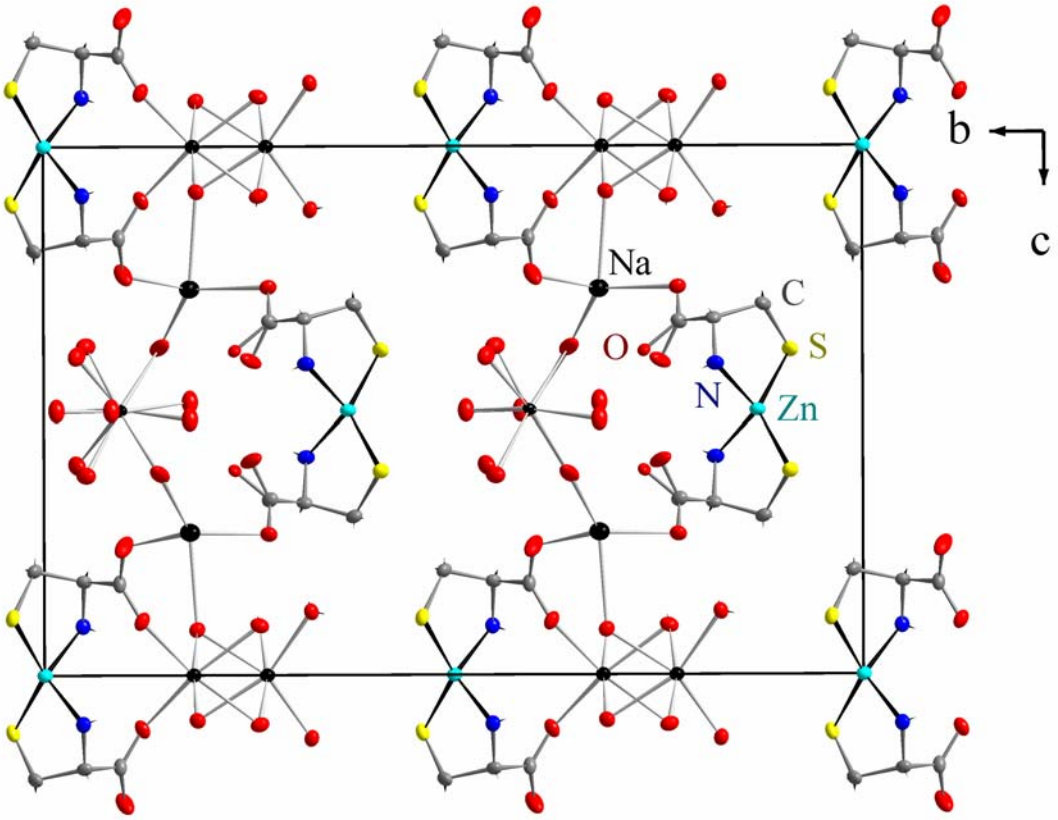

Figure A.4: Crystal packing of sodium bis(L-cysteinato)zincate(II) hexahydrate, in projection along the *a* axis.

Table A.7: Bond lengths [Å] and angles [°] for sodium bis(L-cysteinato)zincate(II) hexahydrate.

Bond	Distance(Å)	Bond angle	Angle(°)
Zn(1)-N(1)#1	2.052(3)	N(1)#1-Zn(1)-N(1)	116.53(14)
Zn(1)-N(1)	2.052(3)	N(1)#1-Zn(1)-S(1)#1	91.51(7)
Zn(1)-S(1)#1	2.3001(8)	N(1)-Zn(1)-S(1)#1	113.07(7)
Zn(1)-S(1)	2.3001(8)	N(1)#1-Zn(1)-S(1)	113.07(7)
S(1)-C(3)	1.834(3)	N(1)-Zn(1)-S(1)	91.51(7)
O(1)-C(1)	1.254(4)	S(1)#1-Zn(1)-S(1)	133.14(4)
O(2)-C(1)	1.249(4)	C(3)-S(1)-Zn(1)	91.71(11)
N(1)-C(2)	1.479(4)	C(2)-N(1)-Zn(1)	109.11(18)
C(1)-C(2)	1.531(4)	O(1)-C(1)-O(2)	125.5(3)
C(2)-C(3)	1.525(4)	O(1)-C(1)-C(2)	118.6(3)
Zn(2)-N(2)	2.064(3)	O(2)-C(1)-C(2)	115.9(3)
Zn(2)-N(2)#5	2.064(3)	N(1)-C(2)-C(3)	109.3(2)
Zn(2)-S(2)#5	2.2850(7)	N(1)-C(2)-C(1)	111.4(2)
Zn(2)-S(2)	2.2851(7)	C(3)-C(2)-C(1)	110.6(2)
S(2)-C(6)	1.838(3)	N(2)-Zn(2)-N(2)#5	109.35(16)
O(6A)-C(4)	1.248(8)	N(2)-Zn(2)-S(2)#5	116.24(7)
O(6B)-C(4)	1.298(9)	N(2)#5-Zn(2)-S(2)#5	91.46(7)
O(7)-C(4)	1.257(3)	N(2)-Zn(2)-S(2)	91.46(7)
N(2)-C(5)	1.483(4)	N(2)#5-Zn(2)-S(2)	116.24(7)
C(4)-C(5)	1.526(4)	S(2)#5-Zn(2)-S(2)	132.31(5)
C(5)-C(6)	1.528(5)	C(6)-S(2)-Zn(2)	92.76(10)
		C(4)-O(7)-Na(3)	111.5(2)
		C(5)-N(2)-Zn(2)	108.77(18)
		O(6A)-C(4)-O(7)	124.7(5)
Symmetry transformations:		O(6A)-C(4)-O(6B)	29.8(5)
#1 -x-1, y, -z		O(7)-C(4)-O(6B)	123.1(5)
#2 x-1, y, z		O(6A)-C(4)-C(5)	117.6(3)
#3 -x, y, -z		O(7)-C(4)-C(5)	116.6(3)
#4 x+1, y, z		O(6B)-C(4)-C(5)	116.0(4)
#5 -x-1, y, -z-1		N(2)-C(5)-C(4)	110.4(2)
#6 -x+1, y, -z-1		N(2)-C(5)-C(6)	109.6(2)
#7 -x, y, -z-1		C(4)-C(5)-C(6)	112.2(3)
		C(5)-C(6)-S(2)	112.0(2)

Single-crystal X-ray Structure of Bis(glycinato)zinc(II) Monohydrate

Table A.8: Crystallographic data and structure refinement for bis(glycinato)zinc(II) monohydrate.

	$Zn(Gly)_2 \cdot H_2O$
Empirical formula	$C_4H_{10}N_2O_5Zn$
Formula weight	231.51
Temperature (K)	200(2)
Wavelength (Å)	0.71073
Crystal size (mm^3)	0.52 x 0.12 x 0.02
Crystal system, space group	Triclinic, $P\bar{1}$
Unit cell dimensions	
a (Å)	9.090(3)
b (Å)	9.537(3)
c (Å)	10.420(5)
α (°)	106.112(7)
β (°)	105.815(7)
γ (°)	106.854(5)
Volume ($Å^3$)	766.9(5)
Z	4
Calculated density ($g.cm^{-3}$)	2.005
Absorption coefficient (mm^{-1})	3.189
$F(000)$	472
θ range for data collection (°)	3.48 to 27.99
Limiting indices	$-11 \leq h \leq 11$; $-12 \leq k \leq 12$; $-13 \leq l \leq 13$
Reflections collected	6515
Unique reflections	3628 [$R_{\text{int}} = 0.0212$]
Absorption correction	Empirical
Max. and min. transmission	0.9390 and 0.2879
Refinement method	Full-matrix least-squares on F^2
Data/restraints/parameters	3628 / 0 / 230
Goodness-of-fit on F^2	1.302
Final R indices [$I > 2\sigma(I)$]	$R_1 = 0.0348$, $wR_2 = 0.0897$
R indices (all data)	$R_1 = 0.0381$, $wR_2 = 0.0957$
Largest diff. peak and hole (e $Å^{-3}$)	1.823 and -0.932

Table A.9: Atomic Cartesian coordinates (x 10^4) and equivalent isotropic displacement parameters (Å^2 x 10^3) for bis(glycinato)zinc(II) monohydrate. U(eq) is defined as one third of the trace of the orthogonalized U_{ij} tensor.

	x	y	z	U(eq)
Zn(1)	9976(1)	9347(1)	7536(1)	17(1)
Zn(2)	5102(1)	5584(1)	2786(1)	19(1)
O(1)	11862(3)	10795(3)	9608(3)	23(1)
O(2)	14617(3)	11933(4)	10721(3)	32(1)
O(3)	8084(3)	8378(3)	5372(2)	19(1)
O(4)	5340(3)	7567(3)	4329(3)	24(1)
O(5)	6948(3)	6356(3)	2023(3)	21(1)
O(6)	9623(3)	6839(4)	2508(3)	30(1)
O(7)	3099(3)	3961(3)	3110(3)	22(1)
O(8)	334(3)	2667(3)	2139(3)	22(1)
N(1)	11916(3)	9981(3)	6930(3)	18(1)
N(2)	8340(4)	10284(4)	7922(3)	24(1)
N(3)	6640(4)	4629(4)	3657(4)	27(1)
N(4)	3129(3)	5065(3)	980(3)	17(1)
C(1)	13489(4)	10540(4)	8170(4)	20(1)
C(2)	13310(4)	11149(4)	9619(4)	20(1)
C(3)	6678(4)	9423(4)	6761(4)	20(1)
C(4)	6729(4)	8391(4)	5394(3)	16(1)
C(5)	8290(4)	5310(4)	3617(4)	20(1)
C(6)	8291(4)	6239(4)	2648(3)	18(1)
C(7)	1534(4)	4349(4)	1093(4)	19(1)
C(8)	1700(4)	3601(4)	2198(4)	17(1)
O(9)	17553(4)	12388(4)	15196(3)	36(1)
O(10)	7395(3)	2515(4)	96(3)	30(1)

Table A.10: Hydrogen Cartesian coordinates (x 10^4) and equivalent isotropic displacement parameters (Å^2 x 10^3) for bis(glycinato)zinc(II) monohydrate. U(eq) is defined as one third of the trace of the orthogonalized U_{ij} tensor.

	x	y	z	U(eq)
H(1X)	11829	9125	6192	21
H(1Y)	11901	10777	6596	21
H(2X)	8263	10264	8779	28
H(2Y)	8732	11329	8022	28
H(3X)	6747	4818	4600	32
H(3Y)	6184	3546	3150	32
H(4X)	3192	5981	827	21
H(4Y)	3182	4374	195	21
H(1B)	14352	11405	8110	24
H(1C)	13863	9657	8122	24
H(3B)	6219	10196	6555	24
H(3C)	5929	8751	7084	24
H(5A)	8650	4443	3263	24
H(5B)	9102	6023	4611	24
H(7A)	723	3529	137	22
H(7B)	1098	5177	1368	22
H(9A)	16650(50)	12420(50)	15390(40)	15
H(9B)	18190(50)	12490(50)	15780(50)	15
H(10A)	7990(50)	2530(50)	580(50)	15
H(10B)	6580(50)	2230(50)	520(40)	15

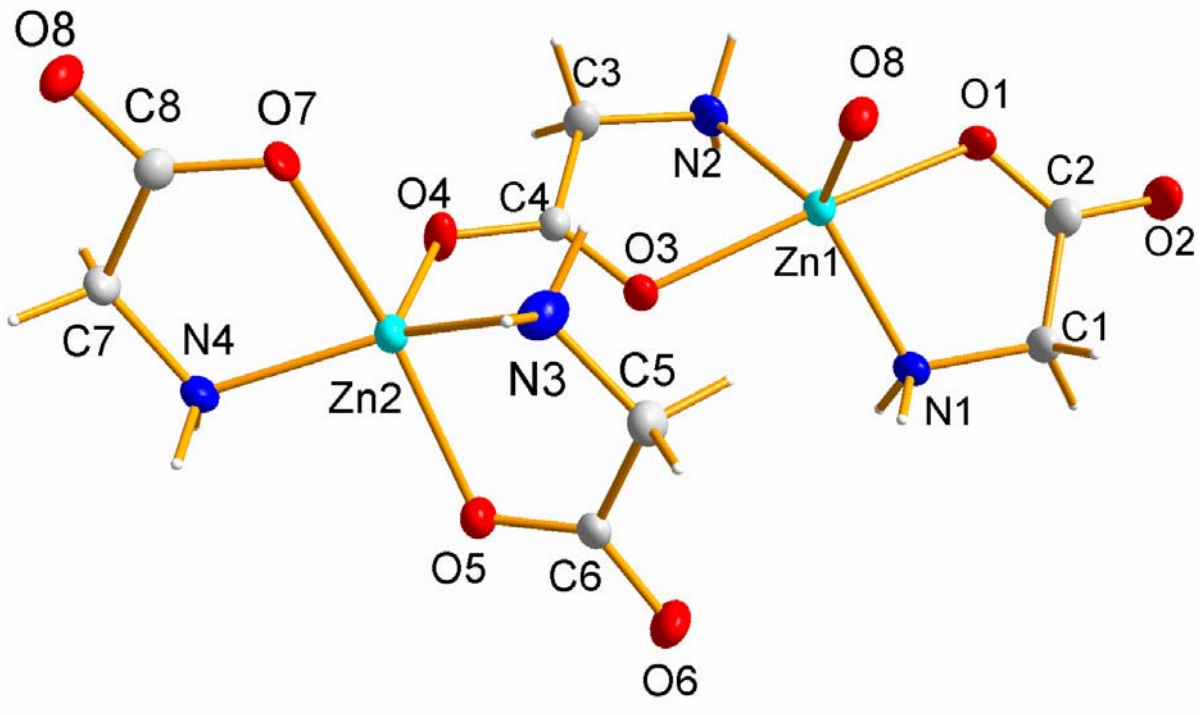

Figure A.5: The coordination environments of Zn(1) and Zn(2) in bis(glycinato)zinc(II) monohydrate determined by single-crystal X-ray diffraction experiment. Heavy atoms are drawn with 50 % probability ellipsoids.

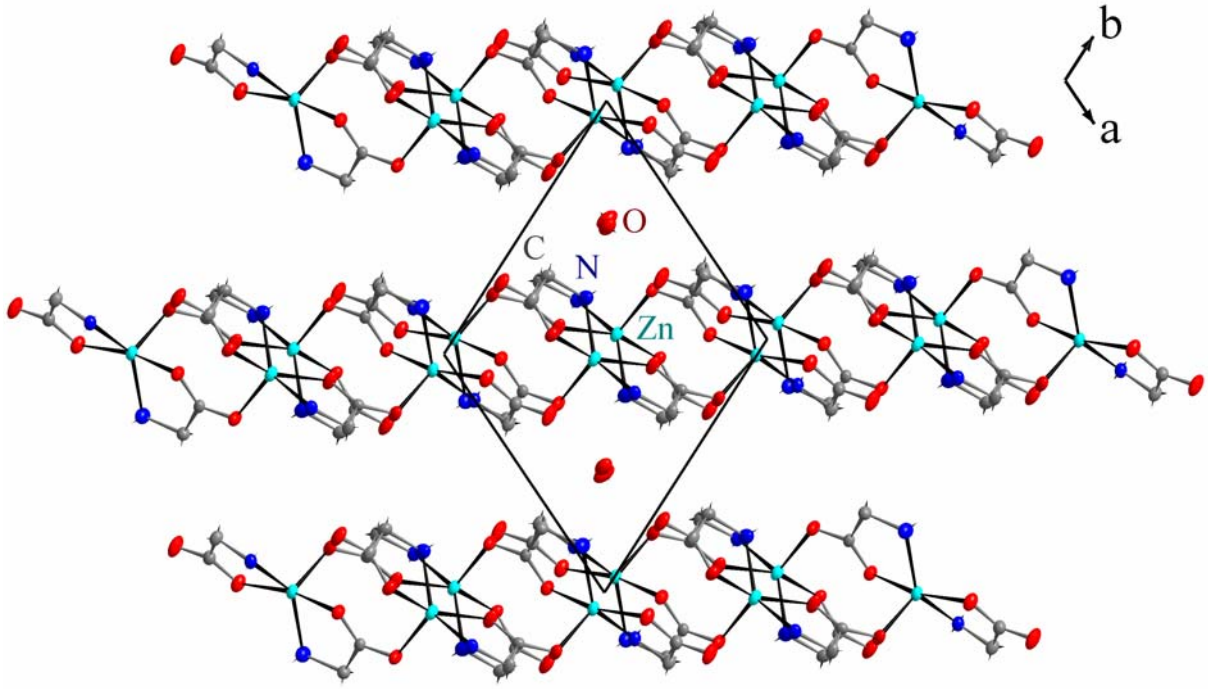

Figure A.6: Crystal packing of bis(glycinato)zinc(II) monohydrate, in projection along the c axis.

Table A.11: Bond lengths [Å] and angles [°] for bis(glycinato)zinc(II) monohydrate.

Bond	Distance(Å)	Bond angle	Angle(°)
Zn(1)-O(8)#1	1.996(2)	N(1)-Zn(1)-O(8)#1	111.01(11)
Zn(1)-N(1)	2.019(3)	N(2)-Zn(1)-O(8)#1	113.72(12)
Zn(1)-N(2)	2.016(3)	N(2)-Zn(1)-N(1)	135.25(13)
Zn(1)-O(1)	2.113(3)	O(8)#1-Zn(1)-O(1)	94.17(11)
Zn(1)-O(3)	2.169(2)	N(2)-Zn(1)-O(1)	94.03(11)
Zn(2)-O(4)	2.023(3)	N(1)-Zn(1)-O(1)	81.56(11)
Zn(2)-N(3)	2.029(3)	O(8)#1-Zn(1)-O(3)	98.86(10)
Zn(2)-N(4)	2.032(3)	N(2)-Zn(1)-O(3)	79.33(11)
Zn(2)-O(5)	2.080(2)	N(1)-Zn(1)-O(3)	95.12(10)
Zn(2)-O(7)	2.195(2)	O(1)-Zn(1)-O(3)	166.87(10)
O(1)-C(2)	1.256(4)	O(4)-Zn(2)-N(3)	110.04(13)
O(2)-C(2)	1.247(4)	O(4)-Zn(2)-N(4)	107.43(11)
O(3)-C(4)	1.241(4)	N(3)-Zn(2)-N(4)	141.50(13)
O(4)-C(4)	1.273(4)	O(4)-Zn(2)-O(5)	105.00(10)
O(5)-C(6)	1.270(4)	N(3)-Zn(2)-O(5)	81.80(11)
O(6)-C(6)	1.247(4)	N(4)-Zn(2)-O(5)	96.90(11)
O(7)-C(8)	1.243(4)	O(4)-Zn(2)-O(7)	95.07(10)
O(8)-C(8)	1.275(4)	N(3)-Zn(2)-O(7)	88.51(11)
N(1)-C(1)	1.472(4)	N(4)-Zn(2)-O(7)	79.68(10)
N(2)-C(3)	1.468(4)	O(5)-Zn(2)-O(7)	159.69(10)
N(3)-C(5)	1.469(4)	C(2)-O(1)-Zn(1)	113.7(2)
N(4)-C(7)	1.465(4)	C(4)-O(3)-Zn(1)	111.8(2)
C(1)-C(2)	1.531(5)	C(4)-O(4)-Zn(2)	119.0(2)
C(3)-C(4)	1.512(4)	C(6)-O(5)-Zn(2)	113.5(2)
C(5)-C(6)	1.517(5)	C(8)-O(7)-Zn(2)	112.5(2)
C(7)-C(8)	1.510(4)	C(8)-O(8)-Zn(1)#1	124.4(2)
		C(1)-N(1)-Zn(1)	109.8(2)
		C(3)-N(2)-Zn(1)	112.5(2)
		C(5)-N(3)-Zn(2)	111.1(2)
		C(7)-N(4)-Zn(2)	112.3(2)
		N(1)-C(1)-C(2)	112.1(3)
		O(2)-C(2)-O(1)	125.2(3)
		O(2)-C(2)-C(1)	117.2(3)
		O(1)-C(2)-C(1)	117.6(3)
		N(2)-C(3)-C(4)	111.5(3)
		O(3)-C(4)-O(4)	124.2(3)

Table A.11 – *Continued*

Bond	Distance(Å)	Bond angle	Angle(°)
		O(3)-C(4)-C(3)	119.4(3)
		O(4)-C(4)-C(3)	116.4(3)
		N(3)-C(5)-C(6)	112.1(3)
Symmetry transformations:		O(6)-C(6)-O(5)	123.9(3)
#1 -x+1, -y+1, -z+1		O(6)-C(6)-C(5)	117.5(3)
		O(5)-C(6)-C(5)	118.6(3)
		N(4)-C(7)-C(8)	111.9(3)
		O(7)-C(8)-O(8)	124.9(3)
		O(7)-C(8)-C(7)	119.7(3)
		O(8)-C(8)-C(7)	115.4(3)

Sample *Gaussian 03* input file for the calculation of the ^{67}Zn EFG and chemical shift parameters of diimidazole zinc chloride

```
%rwf=/scratch/kmroue/ZnHimCl2-6311gs-6311pgs
%scr=/scratch/kmroue/ZnHimCl2-6311gs-6311pgs
%nosave
%mem=200MB
%chk=/scratch/kmroue/ZnHimCl2-6311gs-6311pgs
%nproc=4
# nmr=giao b3lyp/gen Density=Current prop=efg

NMR calculations of Zinc Diimidazole dichloride using atomic coordinates from our
X-ray single-crystal structure

0 1
Zn      3.154942      2.128721      2.744287
Cl      3.267461      4.251555      3.511235
Cl      1.071849      1.616556      2.097278
N       3.869544      0.977234      4.219863
C       3.840191      1.268049      5.506179
H       3.488003      2.061610      5.868196
N       4.375724      0.287283      6.220310
H       4.457716      0.273154      7.086290
C       4.772451     -0.688773      5.369735
H       5.180614     -1.504704      5.597509
C       4.465960     -0.256671      4.130735
H       4.633971     -0.724095      3.332977
N       4.380028      1.830841      1.191685
C       5.690034      1.689555      1.246703
H       6.194961      1.687200      2.040059
N       6.196325      1.551800      0.025308
H       7.037630      1.445835     -0.169455
C       5.171238      1.604783     -0.865980
H       5.232904      1.535317     -1.801282
C       4.048615      1.776682     -0.140846
H       3.179016      1.847325     -0.489658

Zn 0
```

6-311G*
****
2 3 4 13 0
6-311+G*
*****
7 16 0
6-31G*
****
H C 0
6-31G*
****

Sample *Gaussian 03* input file for the calculation of the ^{67}Zn EFG and chemical shift parameters of zinc L-alaninate

nmr=giao b3lyp/gen Density=Current prop=efg

NMR calculation of Zinc alaninate

-1 1

Zn	3.81207	-3.01419	2.09842
O	4.35553	-1.85300	0.40142
O	5.99956	-1.57830	-1.06248
N	5.85203	-3.08139	2.23801
H	6.11461	-2.56614	2.92780
H	6.10484	-3.92682	2.41621
C	5.52964	-1.98688	0.05940
C	6.53765	-2.62481	1.01170
H	7.16560	-1.92127	1.27804
C	7.36119	-3.74280	0.38035
H	7.74719	-3.43183	-0.44070
H	6.79315	-4.49648	0.20215
H	8.06045	-4.00469	0.98392
O	3.39759	-3.76520	4.02765
O	2.39939	-3.20514	5.93704

N	2.99476	-1.35161	2.97667
H	3.64911	-0.82675	3.30336
H	2.53393	-0.87956	2.36447
C	2.68667	-2.98698	4.74044
C	2.09668	-1.76232	4.06597
H	2.01834	-1.03531	4.71840
C	0.72604	-2.09942	3.51317
H	0.30835	-1.29934	3.18456
H	0.18538	-2.48080	4.20776
H	0.81688	-2.73042	2.79464
O	2.63704	-4.24525	1.06248
O	4.28107	-4.51995	-0.40142
C	3.10696	-4.65383	-0.05940
C	2.09895	-5.29176	-1.01170
N	2.78457	-5.74834	-2.23801
H	2.52199	-5.23309	-2.92780
H	2.53176	-6.59377	-2.41621
H	1.47100	-4.58822	-1.27804
C	1.27540	-6.40975	-0.38035
H	0.88941	-6.09878	0.44070
H	1.84345	-7.16343	-0.20215
H	0.57615	-6.67164	-0.98392

Zn 0
6-31G*
****

2 4 14 16 26 0
6-311+G*
*****

3 15 27 30 0
6-31G*
****

H C 0
6-31G*
****

Sample *Gaussian 03* input file for the calculation of the ^{67}Zn EFG and chemical shift parameters of bis(L-histidinato)zinc(II) dihydrate

```
# nmr=giao b3lyp/gen Density=Current prop=efg

NMR calculations of Bis(L-Histidinato)zinc(II) Dihydrate

-1 1
C      -0.01077400      2.53626400      1.81154500
C       1.44006600      2.43132000      1.24054400
C       1.50755100      3.18458200     -0.10253600
C       0.45007000      2.79166100     -1.09792500
C      -0.91949900      1.51942900     -2.20248600
C      -0.22314800      3.60307400     -1.97529000
H       2.10952000      2.93949200      1.94467300
H       1.39982800      4.25143400      0.11409100
H       2.50920800      3.04971900     -0.54235300
H      -1.48092300      0.66726500     -2.55658700
H      -0.17584100      4.66661100     -2.15163600
H       2.69936900      0.93987500      0.52499900
H       1.95609000      0.53353000      1.92567100
H      -1.74748500      3.07014800     -3.37851700
N       1.82201800      1.01925200      1.03838200
N       0.00000000      1.48794200     -1.25557900
N      -1.08477400      2.77942200     -2.67440500
O      -0.75398600      1.50320100      1.60464000
O      -0.31927700      3.60002400      2.34194600
Zn      0.00000000      0.00000000      0.44967100
N      -1.82201800     -1.01925200      1.03838200
N       0.00000000     -1.48794200     -1.25557900
C      -1.44006600     -2.43132000      1.24054400
H      -2.69936900     -0.93987500      0.52499900
H      -1.95609000     -0.53353000      1.92567100
C      -0.45007000     -2.79166100     -1.09792500
C       0.91949900     -1.51942900     -2.20248600
C       0.01077400     -2.53626400      1.81154500
C      -1.50755100     -3.18458200     -0.10253600
H      -2.10952000     -2.93949200      1.94467300
```

C	0.22314800	-3.60307400	-1.97529000
H	1.48092300	-0.66726500	-2.55658700
N	1.08477400	-2.77942200	-2.67440500
O	0.75398600	-1.50320100	1.60464000
O	0.31927700	-3.60002400	2.34194600
H	-1.39982800	-4.25143400	0.11409100
H	-2.50920800	-3.04971900	-0.54235300
H	0.17584100	-4.66661100	-2.15163600
H	1.74748500	-3.07014800	-3.37851700

Zn 0
6-311G*
****
15 16 21 22 0
6-311+G*
*****
17 33 0
6-31G*
****
H C 0
6-31G*
****

Sample *Gaussian 03* input file for the calculation of the ^{67}Zn EFG and chemical shift parameters of sodium bis(L-cysteinato)zincate(II) hexahydrate

```
# nmr=giao b3lyp/gen Density=Current prop=efg

efg calculation of site (1) of Sodium Bis(L-cysteinato)zincate(II) hexahydrate

-4 1
Zn    -2.59465      11.58700      0.00000
S     -1.25691      12.50157     -1.63226
S     -3.93239      12.50157      1.63226
N     -3.64760      10.50790     -1.39128
N     -1.54170      10.50790      1.39128
H     -3.77773      9.66783      -1.09247
H     -1.41157      9.66783      1.09247
H     -4.45262      10.88617     -1.52705
H     -0.73668      10.88617      1.52705
C     -2.30360      10.47750      2.65848
C     -2.88570      10.47750     -2.65848
C     -1.73746      9.46640      -2.59704
H     -3.49375      10.21318     -3.38080
C     -2.35530      11.87523     -2.96120
C     -2.83400      11.87523      2.96120
H     -2.08637      12.48277      3.06910
H     -3.32494      11.85620      3.79741
C     -3.45184      9.46640      2.59704
H     -1.69555      10.21318      3.38080
O     -3.63867      8.83495      1.53005
O     -4.12489      9.33992      3.64110
O     -1.55063      8.83495     -1.53005
O     -1.06441      9.33992     -3.64110
H     -3.10293      12.48277     -3.06910
H     -1.86436      11.85620     -3.79741
Zn    -2.25951      2.97902     -7.49291
S     -1.05498      2.05517     -5.78497
S     -3.46405      2.05517     -9.20084
N     -3.31007      4.17276     -6.17640
N     -1.20895      4.17276     -8.80941
```

H	-3.39407	5.00332	-6.51433
H	-1.12495	5.00332	-8.47148
H	-4.13474	3.83603	-6.04678
H	-0.38428	3.83603	-8.93904
C	-1.94220	4.22312	-10.09714
C	-2.57682	4.22312	-4.88867
C	-3.11128	5.19965	-10.00603
H	-1.32600	4.54847	-10.78679
C	-2.39284	2.81634	-10.48707
O	-2.96236	6.19149	-9.18181
O	-3.89345	5.23562	-10.98895
C	-1.40774	5.19965	-4.97979
H	-3.19302	4.54847	-4.19903
C	-2.12618	2.81634	-4.49874
H	-1.61198	2.25799	-10.62345
H	-2.88001	2.85904	-11.32478
H	-2.90705	2.25799	-4.36237
H	-1.63901	2.85904	-3.66104
O	-1.55666	6.19149	-5.80401
O	-0.62557	5.23562	-3.99687

Zn 0
6-311G*
****
N S 0
6-311+G*
*****
H C O 0
6-31G*
****

Sample *Gaussian 03* input file for the calculation of the ^{67}Zn EFG and chemical shift parameters of bis(glycinato)zinc(II) monohydrate

nmr=giao b3lyp/gen Density=Current prop=efg

NMR calculation of both sites of Bis(Glycinato)zinc Monohydrate

0 1

Zn	4.34320000	5.60640000	6.96580000
Zn	2.30200000	4.01570000	2.57520000
O	5.06920000	6.12330000	8.88120000
O	3.50590000	5.56120000	4.96660000
O	4.52640000	3.64160000	7.26640000
N	6.10380000	6.41990000	6.40580000
N	2.48780000	6.31140000	7.32280000
C	7.02700000	6.44880000	7.55200000
C	6.28440000	6.44220000	8.89140000
C	2.26470000	5.56490000	4.98600000
O	1.53240000	5.22620000	4.00150000
O	3.98370000	5.01610000	1.87000000
O	0.83860000	2.40810000	2.87480000
N	3.71700000	2.80510000	3.38130000
N	1.16520000	4.24220000	0.90680000
C	5.05940000	4.66670000	2.44770000
C	3.55970000	2.81200000	7.21180000
C	1.54480000	5.97750000	6.24870000
O	6.94270000	6.73000000	9.91000000
C	-0.11850000	3.54520000	1.01030000
C	5.04020000	3.44260000	3.34340000
C	-0.07460000	2.43350000	2.03170000
O	-1.04130000	1.60390000	1.97720000
O	6.14400000	5.26860000	2.31830000
O	2.64660000	2.83740000	6.36880000
C	3.60360000	1.70030000	8.23330000
N	2.32000000	1.00340000	8.33680000
H	2.47220000	0.10750000	8.47910000
H	1.85750000	1.32890000	9.06330000
H	3.84260000	2.07770000	9.11690000

H	4.30700000	1.05140000	7.97910000
H	6.47130000	5.92420000	5.72360000
H	5.96490000	7.27610000	6.09710000
H	7.58870000	7.26200000	7.49560000
H	7.62470000	5.66150000	7.50760000
H	2.17990000	5.96050000	8.11490000
H	2.52670000	7.22640000	7.41520000
H	0.97320000	6.76300000	6.05820000
H	0.95830000	5.23790000	6.54720000
H	3.49480000	2.61250000	4.25300000
H	3.74590000	2.01340000	2.91270000
H	5.70770000	2.78870000	3.01620000
H	5.29920000	3.70790000	4.26130000
H	1.01290000	5.13800000	0.76440000
H	1.62760000	3.91660000	0.18020000
H	-0.35750000	3.16790000	0.12660000
H	-0.82190000	4.19420000	1.26450000
Zn	1.18320000	1.22980000	6.66840000
O	-0.49860000	0.22950000	7.37360000
N	-0.23190000	2.44050000	5.86230000
H	-0.00970000	2.63310000	4.99060000
H	-0.26080000	3.23210000	6.33090000
C	-1.57430000	0.57890000	6.79590000
C	-1.55510000	1.80300000	5.90020000
H	-2.22260000	2.45690000	6.22740000
H	-1.81400000	1.53770000	4.98230000
O	-2.65890000	-0.02310000	6.92530000
O	1.95270000	0.01930000	5.24200000
C	1.22040000	-0.31940000	4.25760000
Zn	-0.85810000	-0.36080000	2.27780000
O	-0.02080000	-0.31570000	4.27700000
C	1.94030000	-0.73200000	2.99490000
O	-1.58410000	-0.87780000	0.36230000
N	-2.61870000	-1.17440000	2.83780000
H	-2.98620000	-0.67860000	3.52000000
H	-2.47980000	-2.03060000	3.14650000
N	0.99740000	-1.06590000	1.92080000
H	1.30520000	-0.71490000	1.12860000
H	0.95840000	-1.98080000	1.82840000
C	-3.54190000	-1.20320000	1.69160000

C	-2.79930000	-1.19660000	0.35220000
H	-4.10360000	-2.01640000	1.74800000
H	-4.13960000	-0.41590000	1.73590000
O	-3.45760000	-1.48440000	-0.66650000
H	2.51190000	-1.51750000	3.18530000
H	2.52680000	0.00770000	2.69640000

Zn 0
6-311G*
****
3 4 5 6 7 11 12 13 14 15 0
6-311+G*
*****
19 23 24 25 27 49 50 57 58 61 63 64 67 74 0
6-31G*
****
H C 0
6-31G*
****

Appendix B

Supplementary Data for Chapter 4

Sample *Gaussian 03* input file for the calculation of the ^{67}Zn EFG and chemical shift parameters in the model of the octahedral zinc binding site in the zinc-insulin hexamer T_6

```
%rwf=/scratch/kmroue/T6-1MSO-6311gs-6311pgs-631gs
%nosave
%mem=24GB
%chk=/scratch/kmroue/T6-1MSO-6311gs-6311pgs-631gs
%NProc=4
#nmr=giao b3lyp/gen density=current prop=efg

NMR calculations with coordinates from optimized job T6-1MSO-popt.log

2 1
Zn      0.26414400      -0.22068400      0.56561300
N      -0.68844300      -1.85268300      -0.07588500
N      -1.08972300      1.24233800      0.56814600
N      1.88449700      0.27840500      -0.49345300
O      3.51297900      -1.51528200      2.44452000
O      -0.81115000      -1.46706800      4.00214200
```

O	1.07112800	-0.49100400	2.34746200
C	3.07905200	-0.42016600	-0.40425700
C	2.16042400	1.42386500	-1.10642800
N	3.47642400	1.47762900	-1.39959400
H	1.45711600	2.21173700	-1.33251300
C	-1.78879600	-2.41838600	0.55290800
C	-0.54878500	-2.48570100	-1.23620800
C	-0.84989700	2.58959100	0.79534800
C	-2.38862400	1.12727500	0.29929800
C	4.09180700	0.31705700	-0.95481500
H	3.13276500	-1.38077800	0.08109400
H	3.93512400	2.23918200	-1.88225100
C	5.55880000	0.07523700	-1.11413600
C	6.09463000	-1.16275500	-0.37301500
N	6.00512600	-1.01763500	1.09472900
C	7.48148900	-1.49689000	-0.99222200
H	5.47220400	-2.02377800	-0.64525200
O	7.57156100	-1.58270700	-2.20649800
N	8.51702400	-1.72354900	-0.14442000
N	-2.96828100	2.34274200	0.34824000
H	-2.91928000	0.21015300	0.08598600
C	-2.01496600	3.29862300	0.66320100
H	0.13134600	2.96242400	1.04236700
C	-2.33671400	4.75278300	0.75130600
C	-2.01028300	5.53931800	-0.54335100
N	-0.56386100	5.67724000	-0.69862000
C	-2.90245500	6.81227000	-0.55256500
H	-2.37066300	4.95214600	-1.39783300
O	-4.08413000	6.72046900	-0.24937600
N	-2.31235600	7.97228400	-0.93070700
H	-0.18130600	6.34354400	-0.03111900
H	-1.34620500	8.02915600	-1.20425900
H	8.48594800	-1.52872100	0.84189400
H	6.52170800	-0.19716300	1.41049700
C	-2.32442300	-3.39803000	-0.24088900
H	-2.10844300	-2.09619600	1.53236600
C	-3.53059900	-4.26148200	-0.09913600
N	-1.51384300	-3.41803400	-1.36543100
H	0.21542700	-2.29886500	-1.97528700
C	-4.78391800	-3.68532700	-0.80803800

N	-5.23798100	-2.46898100	-0.13582200
C	-5.77916700	-4.86145800	-1.01180700
H	-4.49564500	-3.39741200	-1.82750800
O	-5.36219300	-5.93351300	-1.42655100
N	-7.08303500	-4.62024500	-0.72936800
H	-7.42086800	-3.71949000	-0.43609100
H	-5.66667300	-2.68039900	0.76280800
H	-3.95007200	2.53169700	0.19253500
H	-1.61588400	-4.05109200	-2.14862400
H	6.11463400	0.96458700	-0.78387000
H	5.81044300	-0.07240100	-2.17024500
H	6.43018600	-1.82866100	1.54188200
H	9.41547500	-1.93413000	-0.55713000
H	-3.35028900	-5.25836200	-0.51085000
H	-3.75098700	-4.39171700	0.96584500
H	-5.91978000	-1.96546600	-0.69635700
H	-7.75175700	-5.35594300	-0.90812800
H	-1.78169200	5.19722800	1.58483500
H	-3.39939100	4.89594900	0.96379400
H	-0.31417000	5.98926800	-1.63276600
H	-2.88544100	8.80189900	-0.98919700
H	2.00578400	-0.83263100	2.43232200
H	0.49738500	-0.87549400	3.05252500
H	-0.74282400	-2.34059600	4.41142300
H	-1.12331600	-0.87976900	4.70453100
H	3.80321200	-1.96749800	3.24633800
H	4.33176900	-1.18056200	1.99837700

Zn 0
6-311G*
****
2 3 4 5 6 7 0
6-311+G*
****
10 21 24 25 26 32 35 36 28 44 47 50 51 0
6-31G*
****
H C 0
6-31G*
****

Sample *Gaussian 03* input file for the calculation of the ^{67}Zn EFG and chemical shift parameters in the octahedral model of the zinc binding site in the zinc-insulin hexamer T_3R_3

%rwf=/scratch/kmroue/T3R3-1BEN-octa-6311gs-6311pgs-631gs
%nosave
%mem=24GB
%chk=/scratch/kmroue/T3R3-1BEN-octa-6311gs-6311pgs-631gs
%NProc=4
#nmr=giao b3lyp/gen prop=efg density=current

NMR calculations using coordinates from optimized job T3R3-1BEN-octa-popt.log

2 1

Zn	-0.00008400	-0.00033900	2.06447700
N	-0.77444600	1.69867000	1.07550000
N	1.85801500	-0.17889100	1.07437700
N	-1.08431500	-1.51989600	1.07472000
O	1.13641000	1.17747900	3.63709900
O	0.45335000	-1.57540000	3.63634600
O	-1.58935200	0.39384700	3.63753000
C	2.72734200	-1.25406100	1.13795400
C	2.34294000	0.61746700	0.16398900
N	3.46256100	0.11703900	-0.35510600
H	1.92316600	1.55369700	-0.14021800
C	-0.27748800	2.98892700	1.13876700
C	-1.70672100	1.72064700	0.16525700
C	-2.45013300	-1.73497200	1.13817700
C	-0.63721400	-2.33780500	0.16407800
C	3.72947900	-1.09050000	0.25256400
H	2.56661900	-2.06614900	1.81233000
H	4.02757100	0.55719500	-1.04976200
C	4.90977900	-1.92813500	-0.12327900
C	4.68880100	-2.73512900	-1.41851500
H	5.12732000	-2.61043600	0.69133100
H	5.77828800	-1.29658100	-0.24989100
N	3.74309500	-3.80697400	-1.17830100

C	6.06662500	-3.07455300	-2.01224300
H	4.24493700	-2.07882800	-2.16005500
H	4.11086200	-4.51083900	-0.56668700
O	6.85414300	-2.18422900	-2.17510700
N	6.31927400	-4.35293500	-2.33606600
H	5.65209500	-5.08166400	-2.25613800
N	-1.63050900	-3.05686600	-0.35530900
H	0.38347900	-2.44251200	-0.14005300
C	-2.80968800	-2.68422500	0.25241000
H	-1.53191200	-3.76609900	-1.05014000
C	-4.12534700	-3.28720200	-0.12369400
C	-4.71357600	-2.69174300	-1.41872900
H	-4.82500200	-3.13461200	0.69094900
H	-4.01284700	-4.35510300	-0.25069100
N	-5.16862500	-1.33677800	-1.17804000
C	-5.69668800	-3.71481700	-2.01279900
H	-3.92325800	-2.63546100	-2.16025400
O	-5.31979000	-4.84211700	-2.17566000
N	-6.92989600	-3.29392700	-2.33684200
H	-7.22709000	-2.35167900	-2.25682300
H	-5.96207600	-1.30332700	-0.56642700
C	-0.92003900	3.77511700	0.25334400
H	0.50640100	3.25560600	1.81294900
N	-1.83281000	2.94045700	-0.35398000
H	-2.30800500	0.88918600	-0.13871800
H	-2.49656100	3.20985800	-1.04851600
C	-0.78428500	5.21599200	-0.12275800
C	0.02503800	5.42758400	-1.41811100
H	-0.30188700	5.74549100	0.69171500
H	-1.76533900	5.65269100	-0.24934100
N	1.42603800	5.14393700	-1.17798300
C	-0.36944000	6.79057800	-2.01204500
H	-0.32177300	4.71506600	-2.15950500
O	-1.53417700	7.02786500	-2.17474800
N	0.61163200	7.64818800	-2.33599100
H	1.85204800	5.81421200	-0.56643000
H	1.57624500	7.43443800	-2.25602800
H	-3.07304300	-1.18980100	1.81262600
H	7.19422900	-4.56215300	-2.76560100
H	3.44436200	-4.24854400	-2.02586700

H -5.40153400 -0.85694500 -2.02545200
H -7.54873000 -3.94678100 -2.76654500
H 0.35564200 8.51061100 -2.76554000
H 1.95773400 5.10575400 -2.02558900
H 0.71732300 1.66152400 4.33920900
H 2.04100000 1.46318900 3.58277200
H 0.24807200 -2.50158600 3.58237100
H 1.08184600 -1.45461000 4.33869500
H -2.28902700 1.03448600 3.58349200
H -1.79971700 -0.21186700 4.33878700

Zn 0
6-311G*
****
2 3 4 5 6 7 0
6-311+G*
****
10 23 27 28 30 38 41 42 47 54 57 58 0
6-31G*
****
H C 0
6-31G*
****

Sample *Gaussian 03* input file for the calculation of the ^{67}Zn EFG and chemical shift parameters in the tetrahedral model of the zinc binding site in the zinc-insulin hexamer T_3R_3

%rwf=/scratch/kmroue/T3R3-1BEN-tetra-6311gs-6311pgs-631gs
%nosave
%mem=24GB
%chk=/scratch/kmroue/T3R3-1BEN-tetra-6311gs-6311pgs-631gs
%NProc=4
#nmr=giao b3lyp/gen prop=efg density=current

NMR calculations using coordinates from optimized job T3R3-1BEN-tetra-popt.log

1 1

Zn	0.00000400	-0.00000700	0.98370000
N	-0.92329300	1.67769700	0.20275500
N	-0.99129100	-1.63844700	0.20274300
N	1.91458100	-0.03926200	0.20273900
Cl	0.00001900	-0.00001600	3.21378700
C	-0.81125600	2.93549900	0.76363600
C	-1.80610700	1.78009500	-0.74640400
C	-2.13659400	-2.17032400	0.76362700
C	-0.63857200	-2.45417700	-0.74642600
C	2.94786100	-0.76516200	0.76363700
C	2.44465400	0.67405300	-0.74644600
C	-1.63420000	3.79119600	0.12927100
H	-0.15833200	3.11987600	1.58890400
N	-2.25855100	3.02846800	-0.83828500
H	-2.14653900	0.98090300	-1.37023800
C	-2.46618800	-3.31085300	0.12925100
H	-2.62272200	-1.69707200	1.58890500
N	-1.49348100	-3.47018400	-0.83831800
H	0.22376100	-2.34939900	-1.37026500
C	4.10038100	-0.48033200	0.12925300
H	2.78108600	-1.42277100	1.58892900
N	3.75199900	0.44169600	-0.83833700
H	1.92273900	1.36844800	-1.37029800

H	4.37937700	0.89164400	-1.46860300
C	-1.93151800	5.24624900	0.30600500
H	-1.41749900	-4.23849300	-1.46857200
C	-3.57764500	-4.29586100	0.30598100
C	-4.75889400	-4.06952300	-0.65822800
H	-3.93558200	-4.23469600	1.32816500
H	-3.19764800	-5.29863000	0.16379200
N	-5.48383900	-2.87921900	-0.27496700
C	-5.53163800	-5.39045600	-0.79819700
H	-4.36064500	-3.89739100	-1.65281200
O	-4.94016000	-6.38116800	-1.13078100
N	-6.85393800	-5.37367600	-0.55451600
H	-5.92206900	-2.95421900	0.62213900
H	-7.35100300	-4.55222100	-0.30917100
C	5.50915800	-0.95035600	0.30599200
C	5.90377300	-2.08654900	-0.65817900
H	5.63516600	-1.29088400	1.32818700
H	6.18757300	-0.11988300	0.16376900
N	5.23542400	-3.30951300	-0.27487000
C	7.43410600	-2.09529100	-0.79815500
H	5.55556900	-1.82776000	-1.65277000
H	5.51950200	-3.65149900	0.62224500
O	7.99633900	-1.08771300	-1.13079600
N	8.08073400	-3.24881400	-0.55444100
H	7.61787300	-4.09000500	-0.30905500
H	-2.96192900	3.34681700	-1.46852800
C	-1.14488300	6.15607600	-0.65820400
H	-1.69957400	5.52564800	1.32818800
H	-2.98994000	5.41854400	0.16382100
N	0.24842500	6.18874200	-0.27495000
C	-1.90247000	7.48576200	-0.79816700
H	-1.19493900	5.72512000	-1.65278900
H	0.40259200	6.60576700	0.62215200
O	-3.05619000	7.46889000	-1.13075400
N	-1.22679000	8.62251300	-0.55446400
H	-0.26685900	8.64225100	-0.30910700
H	-6.16081900	-2.59214800	-0.95293700
H	-7.36429500	-6.22068800	-0.67342100
H	0.83552600	6.63148000	-0.95292500
H	-1.70514300	9.48800300	-0.67336000

H 5.32530100 -4.03935300 -0.95281600
H 9.06944400 -3.26729000 -0.67336000

Zn 0
6-311G*
****
2 3 4 5 0
6-311+G*
****
14 18 22 31 35 42 47 53 58 0
6-31G*
****
H C O 0
6-31G*
****

Sample *Gaussian 03* input file for the calculation of the ^{67}Zn EFG and chemical shift parameters in the tetrahedral model of the zinc binding site in the zinc-insulin hexamer R_6

%rwf=/scratch/kmroue/R6-1EV3-6311gs-6311pgs-631gs
%nosave
%mem=24GB
%chk=/scratch/kmroue/R6-1EV3-6311gs-6311pgs-631gs
%NProc=4
#nmr=giao b3lyp/gen prop=efg density=current

NMR calculations with coordinates from optimized job R6-1EV3-popt.log

1 1

Zn	0.14884300	-0.08857100	-0.03571600
Cl	0.27775900	-0.05786900	2.18609300
C	4.19932400	0.59537100	-0.78197200
C	3.09205300	0.27721700	-0.03657000
C	2.37081100	0.64626800	-2.05688600
N	1.96378600	0.30734200	-0.84072900
N	-1.20036000	1.33739500	-0.57195800
N	-0.45881300	-1.89797000	-0.69146100
C	5.65556400	0.73363700	-0.46332700
N	3.70954900	0.82463500	-2.05909800
C	-1.29939700	-2.70501000	0.05832800
C	-0.12381700	-2.59390800	-1.76943500
C	-1.48210500	-3.90407300	-0.58267000
N	-0.72372400	-3.80298700	-1.73960300
C	-2.25062600	-5.14584800	-0.25236000
C	-3.63812000	-4.88165900	0.36543500
N	-3.50191800	-4.25807600	1.67685300
C	-4.46601400	-6.19013500	0.24747500
O	-4.44954600	-6.84077500	-0.78920800
N	-5.20982800	-6.53308600	1.33018700
C	6.19148800	-0.34279300	0.50177900
N	5.58288000	-0.19547700	1.81830400
C	7.74098600	-0.34407300	0.39759200

O	8.28891600	-0.25342300	-0.69338900
N	8.42209000	-0.47715100	1.56429200
C	-1.68413600	2.22468200	0.37613700
C	-1.82131100	1.62372300	-1.70710200
N	-2.67144700	2.65718300	-1.52332100
C	-2.60840300	3.06006500	-0.19686700
C	-3.42629000	4.19017600	0.33823200
C	-2.90490400	5.59002300	-0.06787400
N	-1.68733100	5.91678300	0.67245400
C	-4.04440900	6.59899500	0.19137000
O	-5.05448800	6.56282600	-0.49928600
N	-3.82452800	7.45676000	1.21318000
H	-1.69671500	1.11275800	-2.64976700
H	-1.34680800	2.17157800	1.40084800
H	-3.27810300	3.05516100	-2.22748000
H	-3.44593300	4.12680400	1.43064600
H	-4.45899300	4.10859000	-0.01600100
H	-2.77581800	5.59886900	-1.16244000
H	-1.05832400	5.11809700	0.70404400
H	-1.18186500	6.67092300	0.21455000
H	-2.99821500	7.33898100	1.78260700
H	-4.55307200	8.10312300	1.47513200
H	-1.70115800	-2.39043600	1.00754600
H	0.53726100	-2.27042800	-2.55861800
H	-0.63311900	-4.52299400	-2.44276200
H	-2.40599900	-5.74673800	-1.15257900
H	-1.67007200	-5.77028200	0.44140100
H	-4.15875400	-4.16220000	-0.27930200
H	-3.12356200	-4.89267300	2.37454000
H	-4.37026800	-3.86125000	2.01994800
H	-5.78229800	-7.36217900	1.27464600
H	-5.20344400	-5.99476700	2.17959500
H	9.42961400	-0.51930300	1.52878300
H	7.95653200	-0.55101600	2.45267500
H	5.69429500	-1.01519100	2.40497900
H	5.91545100	0.62521800	2.31629600
H	5.88331800	-1.32197000	0.11370300
H	5.85048200	1.72374700	-0.02769200
H	6.25221000	0.67582000	-1.37790700
H	4.26820400	1.08245700	-2.86071100

H 3.03379800 0.04234000 1.01404000
H 1.74842600 0.77543600 -2.92916700

Zn 0
6-311G*
****
2 6 7 8 0
6-311+G*
****
10 14 17 20 22 25 28 32 32 35 0
6-31G*
****
H C O 0
6-31G*
****

Appendix C

Supplementary Data for Chapter 5

Cartesian atomic coordinates employed in *Gaussian 03* calculations of the ^{27}Al EFG and chemical shift parameters of compound 1, AlPcCl

Molecule 1

Cl	10.89846	10.08872	5.79711
Al	10.87539	7.94651	5.45347
N	11.71775	7.80885	3.69994
N	9.12123	7.70837	4.57738
N	10.03475	7.29656	7.09698
N	12.58375	7.41400	6.23040
N	14.04206	7.71065	4.30573
N	9.78883	7.94524	2.25745
N	7.67308	7.43231	6.43822
N	11.94211	6.96470	8.50280
C	11.09625	8.00490	2.49922
C	8.91921	7.83056	3.19194
C	7.51212	7.80197	2.94745
C	6.73722	7.87492	1.79292
C	5.34829	7.77809	1.90158
C	4.77607	7.69246	3.13761

C	5.47774	7.62860	4.31931
C	6.82993	7.71845	4.16990
C	7.87473	7.60633	5.14786
C	8.66740	7.32166	7.32110
C	8.40515	6.98842	8.69295
C	7.25033	6.85534	9.54867
C	7.40075	6.57474	10.83903
C	8.65630	6.50845	11.43667
C	9.79286	6.63372	10.71678
C	9.65115	6.86249	9.33134
C	10.63656	7.03846	8.28547
C	12.82680	7.14131	7.53842
C	14.25605	7.05699	7.82366
C	15.03012	6.87046	8.93744
C	16.38651	6.91124	8.76087
C	16.99631	7.11743	7.60633
C	16.26798	7.3033	6.41105
C	14.90710	7.27374	6.60121
C	13.86763	7.49666	5.59609
C	13.05699	7.83251	3.43643
C	13.31841	8.04374	2.07816
C	14.48219	8.13749	1.30394
C	14.32198	8.34595	-0.12224
C	13.12168	8.44377	-0.66555
C	11.90741	8.34303	0.06791
C	12.08587	8.1318	1.42619
H	7.16433	7.99649	0.94264
H	4.80174	7.75838	1.12873
H	3.81381	7.67579	3.21911
H	5.06076	7.51686	5.14922
H	6.38421	6.95200	9.16699
H	6.60572	6.43494	11.35245
H	8.70388	6.37349	12.39018
H	10.64515	6.58444	11.13649
H	14.65594	6.71677	9.79723
H	16.93378	6.77375	9.50792
H	17.96765	7.11457	7.58189
H	16.68489	7.47003	5.57028
H	15.33788	8.05274	1.70328
H	15.10820	8.41109	-0.66963

H	13.06473	8.61280	-1.60684
H	11.05532	8.35754	-0.36809

Molecule 2

Cl	5.23709	4.13895	1.29715
Al	5.19418	1.97788	0.95487
N	6.03534	1.86124	-0.77965
N	3.52200	1.73688	0.05433
N	4.33854	1.34497	2.59159
N	6.89368	1.42378	1.72501
N	8.39177	1.63744	-0.16299
N	4.10928	2.15348	-2.28190
N	2.01353	1.34367	1.98308
N	6.27947	1.08500	4.07482
C	5.41904	2.02220	-2.03741
C	3.21056	1.93056	-1.27678
C	1.75802	1.95314	-1.50768
C	1.05690	2.09483	-2.67580
C	-0.31323	2.06249	-2.55356
C	-0.94605	1.83031	-1.31753
C	-0.18994	1.68862	-0.14941
C	1.22143	1.72307	-0.28524
C	2.27549	1.62639	0.67914
C	2.98457	1.18396	2.83879
C	2.74587	0.93763	4.25140
C	1.59026	0.71634	4.90337
C	1.67221	0.46303	6.27523
C	2.94150	0.39251	6.90003
C	4.13388	0.63347	6.20731
C	4.00170	0.90920	4.86262
C	4.96466	1.14967	3.83033
C	7.16387	1.22376	3.09686
C	8.60689	1.15211	3.30061
C	9.33494	0.93048	4.46872
C	10.75949	0.87654	4.38723
C	11.34631	1.09475	3.06970
C	10.55877	1.31914	1.96950
C	9.13844	1.32401	2.02383
C	8.10316	1.48097	1.10020

C	7.44373	1.81471	-1.04587
C	7.65018	2.04283	-2.51281
C	8.79993	2.09028	-3.24627
C	8.67645	2.29306	-4.55022
C	7.38947	2.45261	-5.14786
C	6.25797	2.39396	-4.42797
C	6.35843	2.16729	-3.05612
H	1.49139	2.22116	-3.51386
H	-0.82158	2.20078	-3.34000
H	-1.88451	1.75359	-1.30394
H	-0.60262	1.60085	0.70630
H	0.73208	0.71177	4.47008
H	0.91862	0.28424	6.79952
H	3.01145	0.18359	7.82366
H	4.99276	0.61056	6.62023
H	8.88990	0.80346	5.30270
H	11.29178	0.69101	5.15193
H	12.28139	1.09307	2.96919
H	10.98802	1.48060	1.13688
H	9.65043	1.98569	-2.85645
H	9.42318	2.34657	-5.10847
H	7.31115	2.58028	-6.09729
H	5.40191	2.49287	-4.83274

Cartesian atomic coordinates employed in *Gaussian 03* calculations of the ^{27}Al EFG and chemical shift parameters of the octahedral model of compound 1, in which additional axial chlorine is coordinated to Al

Cl	0.32373	0.42761	0.34016
Al	2.63616	-0.08763	-0.0875
N	3.11647	1.79473	0.03675
N	2.31757	0.08172	-2.01365
N	2.15129	-1.99006	-0.21328

N	2.93725	-0.33039	1.83356
N	3.5847	1.90456	2.39519
N	2.83246	2.40478	-2.27424
N	1.67538	-2.15499	-2.54387
N	2.41738	-2.64846	2.06296
C	3.48243	2.43517	1.16206
C	3.75641	3.79638	0.86151
C	4.16859	4.89194	1.64303
C	4.3443	6.09377	1.02335
C	4.11945	6.24328	-0.37204
C	3.72005	5.1902	-1.14066
C	3.53485	3.94373	-0.51382
C	3.13595	2.66561	-0.98875
C	2.47376	1.27085	-2.72216
C	2.1455	0.99514	-4.12087
C	2.1273	1.793	-5.25497
C	1.76073	1.19984	-6.44639
C	1.41923	-0.15586	-6.51282
C	1.4389	-0.94605	-5.38131
C	1.80763	-0.3453	-4.18799
C	1.93531	-0.86768	-2.82604
C	1.7852	-2.62378	-1.34738
C	1.50058	-4.03935	-1.03025
C	1.09631	-5.09853	-1.81588
C	0.9167	-6.32143	-1.18781
C	1.13695	-6.4679	0.17999
C	1.54322	-5.39574	0.95948
C	1.71861	-4.18435	0.32366
C	2.13454	-2.85612	0.82184
C	2.79486	-1.43931	2.50994
C	3.11404	-1.21403	3.92114
C	3.11444	-2.06024	5.01879
C	3.4736	-1.52191	6.23794
C	3.82245	-0.17111	6.35025
C	3.82031	0.66719	5.25347
C	3.45878	0.12183	4.03077
C	3.34531	0.69127	2.68799
H	4.33744	4.77422	2.69789
H	4.65913	6.95082	1.59388
H	4.26976	7.2097	-0.82213

H	3.54887	5.29858	-2.19614
H	2.39001	2.83279	-5.1997
H	1.7356	1.78928	-7.34652
H	1.1388	-0.58225	-7.45983
H	1.17976	-1.98774	-5.41516
H	0.92975	-4.97323	-2.8691
H	0.60192	-7.17402	-1.76338
H	0.98821	-7.43093	0.63576
H	1.71614	-5.49615	2.01434
H	2.84409	-3.09449	4.91554
H	3.48721	-2.14381	7.11563
H	4.09783	0.21853	7.31495
H	4.0873	1.70414	5.33536
Cl	4.92703	-0.68952	-0.52108

Cartesian atomic coordinates employed in *Gaussian 03* calculations of the ^{27}Al EFG and chemical shift parameters of the octahedral model of compound 1, in which an additional axial H_2O is coordinated to Al

Al	0.00761	0.0243	-0.13929
N	1.98696	-0.04186	-0.02535
N	0.11547	2.00398	-0.08117
N	-1.84671	0.19097	-0.79359
N	0.0267	-1.85785	-0.73461
N	2.35117	-2.42029	-0.34054
N	2.46356	2.2874	0.46248
N	-2.20968	2.56785	-0.48489
N	-2.30537	-2.12616	-1.34214
C	2.74936	-1.19082	-0.04281
C	4.12292	-0.86248	0.30519
C	5.27389	-1.64406	0.42398
C	6.45613	-1.0009	0.7821
C	6.4902	0.38854	1.01497

C	5.34296	1.16897	0.8955
C	4.1569	0.52482	0.53754
C	2.8032	1.01343	0.32782
C	1.2293	2.73411	0.27948
C	0.85896	4.13221	0.43271
C	1.59693	5.26753	0.77363
C	0.92037	6.48345	0.83189
C	-0.45908	6.56576	0.55577
C	-1.19578	5.43411	0.21483
C	-0.51844	4.21445	0.15738
C	-0.95892	2.86481	-0.15902
C	-2.60701	1.3389	-0.78153
C	-3.97077	1.01866	-1.17908
C	-5.11461	1.80352	-1.32905
C	-6.28418	1.16677	-1.73988
C	-6.30994	-0.21764	-1.99684
C	-5.16679	-1.00082	-1.84917
C	-3.99651	-0.36351	-1.4357
C	-2.64868	-0.85583	-1.18656
C	-1.07623	-2.57585	-1.13611
C	-0.70052	-3.96988	-1.32838
C	-1.42877	-5.09217	-1.72415
C	-0.74815	-6.30519	-1.81059
C	0.62507	-6.39413	-1.51143
C	1.35283	-5.27246	-1.11844
C	0.67043	-4.05876	-1.02939
C	1.10055	-2.71629	-0.66377
Cl	-0.43113	-0.31738	2.00699
H	-5.17663	-2.06784	-2.04404
H	-7.23977	-0.67988	-2.31456
H	-7.19472	1.74533	-1.86400
H	-5.08566	2.86907	-1.12785
H	-2.25845	5.48712	0.00363
H	-0.9536	7.53082	0.61315
H	1.46185	7.38665	1.09691
H	2.65783	5.19406	0.98763
H	5.3588	2.23846	1.07613
H	7.42994	0.85515	1.29493
H	7.37021	-1.57763	0.88713
H	5.2372	-2.71343	0.24576

H	2.41048	-5.33176	-0.88487
H	1.12244	-7.3564	-1.58818
H	-1.28336	-7.20043	-2.11272
H	-2.4864	-5.01358	-1.95186
O	0.46684	0.3808	-2.41234
H	1.40768	0.20699	-2.55675
H	0.34638	1.32183	-2.60219

Cartesian atomic coordinates employed in *Gaussian 03* calculations of the ^{27}Al EFG and chemical shift parameters of compound 2, $AlPc(SPh)_4Cl$

Cl	-0.01173800	-0.03409000	2.69711600
Al	0.00868500	0.04905300	0.52114400
N	-0.00350800	1.94780300	0.08169300
N	-1.91503500	-0.00496600	0.06542900
N	0.02433200	-1.88182700	0.04951600
N	1.93455000	0.02194000	0.09206500
N	2.36033700	2.37480800	0.04204000
N	-2.38344100	2.33415300	0.00911400
N	-2.30637100	-2.35931300	-0.00770600
N	2.37051600	-2.31488900	0.02725100
C	1.08036400	2.76795700	0.03743300
C	0.67167700	4.11966200	-0.04641800
C	1.36352900	5.36364700	-0.12344000
C	0.60270900	6.49159400	-0.20218100
C	-0.82002600	6.44527700	-0.21016900
C	-1.49748900	5.27276800	-0.14033800
C	-0.72966700	4.09336000	-0.05588800
C	-1.10614900	2.73749900	0.02253300
C	-2.75027300	1.12142700	0.01953500
C	-4.13606700	0.66924100	-0.05670500
C	-5.36216100	1.33976300	-0.12004200
C	-6.49292700	0.54273800	-0.19678800
C	-6.42319700	-0.85297900	-0.21309400

C	-5.21573300	-1.51066800	-0.15365600
C	-4.08535300	-0.71391800	-0.07484500
C	-2.67994700	-1.07728600	0.00270800
C	-1.06889000	-2.70071800	0.00239300
C	-0.64162800	-4.10734600	-0.05703700
C	-1.34035200	-5.31103200	-0.11834600
C	-0.55997500	-6.46443900	-0.16589300
C	0.82845100	-6.41623900	-0.15539000
C	1.51449200	-5.21500900	-0.09731100
C	0.73950400	-4.07947300	-0.04778100
C	1.13258900	-2.66555000	0.01825600
C	2.73311200	-1.03394700	0.04252000
C	4.13483400	-0.63743500	-0.01428200
C	5.33670100	-1.35940600	-0.07677800
C	6.49827900	-0.60884000	-0.11881000
C	6.47208200	0.78892400	-0.10294200
C	5.29315700	1.49691700	-0.04532100
C	4.13008800	0.74819800	0.00099600
C	2.73608200	1.16510300	0.05715700
H	1.07161900	7.45372200	-0.25966300
H	-1.35490900	7.37632600	-0.27323900
H	-2.56975500	5.22787400	-0.14560500
H	-7.46080500	1.00085100	-0.24463700
H	-7.33952200	-1.41189300	-0.27295400
H	-5.14164400	-2.58080000	-0.16485900
H	-1.03517400	-7.42356600	-0.21125800
H	1.37351600	-7.34217600	-0.19316800
H	2.58565100	-5.16151700	-0.08854700
H	7.44995300	-1.09825100	-0.16440900
H	7.40952000	1.31506300	-0.13713500
H	5.26359800	2.56915000	-0.03389000
S	3.15132400	5.36788300	-0.11112700
C	3.55952500	7.10410700	-0.17750800
C	3.72903500	7.82593300	0.99674000
C	3.78525200	7.72223900	-1.40012100
C	4.10848300	9.15657700	0.94712600
H	3.56118000	7.34434900	1.94230700
C	4.16551400	9.05305600	-1.44793000
H	3.66043100	7.16089400	-2.30763800
C	4.32660500	9.77109300	-0.27485300

H	4.23662700	9.70968100	1.86039800
H	4.33781800	9.52553700	-2.39848700
H	4.62395000	10.80402000	-0.31243500
S	5.32426000	-3.14342100	-0.09880200
C	7.05727900	-3.56905100	-0.14972700
C	7.75669800	-3.77853500	1.03146500
C	7.68904400	-3.77383500	-1.36906600
C	9.08285100	-4.17438700	0.99191400
H	7.26292500	-3.62998300	1.97398800
C	9.01526200	-4.17028300	-1.40595500
H	7.14330000	-3.62129300	-2.28186000
C	9.71267000	-4.36947300	-0.22614200
H	9.62003300	-4.33362700	1.90956400
H	9.49991700	-4.32622000	-2.35298600
H	10.74191900	-4.67962200	-0.25569100
S	-3.12124600	-5.32914400	-0.13198800
C	-3.51515400	-7.07012500	-0.17827400
C	-3.71707200	-7.70621300	-1.39587400
C	-3.70503000	-7.77106500	1.00538200
C	-4.08922300	-9.03955800	-1.42856800
H	-3.58315000	-7.15830600	-2.31031200
C	-4.07652200	-9.10432800	0.96965600
H	-3.56223900	-7.27292700	1.94651700
C	-4.26747600	-9.73898900	-0.24658300
H	-4.24389900	-9.52776900	-2.37390500
H	-4.22145600	-9.64287400	1.88880100
H	-4.55955700	-10.77354000	-0.27298300
S	-5.40014500	3.12232900	-0.09868500
C	-7.14640300	3.49370100	-0.12257400
C	-7.84491900	3.63370900	1.06963300
C	-7.79308100	3.72540600	-1.32917800
C	-9.18385100	3.98540000	1.05286100
H	-7.33918500	3.46797100	2.00291400
C	-9.13220900	4.07832600	-1.34337900
H	-7.24782600	3.62967100	-2.24996500
C	-9.82821000	4.20688800	-0.15315600
H	-9.71948300	4.09182300	1.97908000
H	-9.62754000	4.25663200	-2.28094500
H	-10.86723000	4.48404900	-0.16482400

Cartesian atomic coordinates employed in *Gaussian 03* calculations of the ^{27}Al EFG and chemical shift parameters of compound 3, AlNcCl

Cl	-0.00002300	-0.04286400	2.65831100
Al	0.00000900	0.05461200	0.48524900
N	-0.00102300	1.96234600	0.05921300
N	-1.93385700	0.01268800	0.04832200
N	0.00100200	-1.88642100	0.01058100
N	1.93390600	0.01467700	0.04839800
N	2.37597400	2.36756900	0.00611700
N	-2.37844000	2.36509900	0.00613000
N	-2.34359300	-2.33873400	-0.02734500
N	2.34607100	-2.33634800	-0.02722600
C	1.09647800	2.76202600	0.01038100
C	0.70276500	4.12072300	-0.06671100
C	1.41736400	5.31063100	-0.14150100
C	-1.42291800	5.30908800	-0.14154100
C	-0.70701900	4.11997200	-0.06672500
C	-1.09927600	2.76085300	0.01037200
C	-2.75343400	1.15626800	0.01431900
C	-4.14449000	0.72222700	-0.04939100
C	-5.32121600	1.40327400	-0.09636400
C	-5.24675500	-1.43329000	-0.13833800
C	-4.11376200	-0.68160500	-0.07131500
C	-2.70792200	-1.05568200	-0.00968600
C	-1.10532700	-2.68477200	-0.03005800
C	-0.69904100	-4.09364700	-0.09663500
C	-1.41731000	-5.23935600	-0.15266200
C	1.42274700	-5.23792300	-0.15254400
C	0.70334500	-4.09294600	-0.09659300
C	1.10821800	-2.68367200	-0.02995200
C	2.70909400	-1.05287400	-0.00960300
C	4.11450500	-0.67734000	-0.07126900
C	5.24830300	-1.42784200	-0.13831300
C	5.31979400	1.40879200	-0.09637500
C	4.14376100	0.72653800	-0.04936100
C	2.75229300	1.15912500	0.01436700

H	2.49189300	5.30675000	-0.14145100
H	-2.49744300	5.30402200	-0.14147400
H	-5.34540700	2.47692200	-0.08070100
H	-5.20452100	-2.50643700	-0.15392700
H	-2.49116600	-5.22905500	-0.15180900
H	2.49659400	-5.22652600	-0.15176400
H	5.20719000	-2.50103500	-0.15389700
H	5.34286800	2.48246600	-0.08080100
C	0.71204000	-6.46672100	-0.20986000
C	1.39710700	-7.70866600	-0.26694200
C	-0.70536900	-6.46743800	-0.20990700
C	0.71238700	-8.87898300	-0.32095200
H	2.47249000	-7.70672800	-0.26588500
C	-1.38918200	-7.71007100	-0.26699200
C	-0.70327000	-8.87970200	-0.32098000
H	1.24225400	-9.81329600	-0.36339700
H	-2.46456700	-7.70921900	-0.26599300
H	-1.23218600	-9.81455400	-0.36341500
C	6.48724200	-0.75402000	-0.18448500
C	7.71645200	-1.47066600	-0.25182300
C	6.52050600	0.66633200	-0.16330600
C	8.90133600	-0.81829700	-0.29560900
H	7.68540700	-2.54585000	-0.26656800
C	7.78735600	1.31652800	-0.21058800
C	8.93535300	0.60179200	-0.27450800
H	9.82300000	-1.36931200	-0.34582900
H	7.81513100	2.39142800	-0.19379500
H	9.88378600	1.10715400	-0.30919000
C	-0.72331800	6.50004700	-0.21326200
C	-1.40421300	7.76744700	-0.28954900
C	0.71646300	6.50082200	-0.21322700
C	-0.72349400	8.92336300	-0.35949000
H	-2.48020500	7.76635600	-0.28853900
C	1.39598400	7.76896400	-0.28945800
C	0.71400900	8.92413800	-0.35943800
H	-1.24824300	9.86046200	-0.41546200
H	2.47197700	7.76904500	-0.28838900
H	1.23774700	9.86180500	-0.41537700
C	-6.52117800	0.65955100	-0.16328700
C	-7.78870300	1.30842500	-0.21051800

C	-6.48641900	-0.76075000	-0.18448500
C	-8.93595600	0.59248700	-0.27443200
H	-7.81759600	2.38329300	-0.19369600
C	-7.71487000	-1.47868700	-0.25181100
C	-8.90044200	-0.82755800	-0.29558100
H	-9.88492300	1.09684900	-0.30908500
H	-7.68268700	-2.55383600	-0.26662200
H	-9.82152600	-1.37953900	-0.34584600

Sample *Gaussian 03* input file for the calculation of the ^{27}Al EFG and chemical shift parameters of compound 1

nmr=giao b3lyp/6-311+G(2d,p) density=current prop

NMR calculation of monohydrated AlPcCl

0 1

Al	0.00761000	0.02429800	-0.13928600
N	1.98696300	-0.04186400	-0.02535400
N	0.11547200	2.00398100	-0.08116900
N	-1.84671400	0.19097300	-0.79359200
N	0.02670100	-1.85784800	-0.73461200
N	2.35116700	-2.42028900	-0.34053700
N	2.46356400	2.28740400	0.46248300
N	-2.20968200	2.56785300	-0.48488600
N	-2.30536700	-2.12615700	-1.34213500
C	2.74936300	-1.19082100	-0.04280800
C	4.12292000	-0.86248400	0.30519000
C	5.27389200	-1.64405500	0.42397600
C	6.45613100	-1.00090500	0.78209600
C	6.49020100	0.38854000	1.01497500
C	5.34295600	1.16897200	0.89549800
C	4.15689900	0.52481600	0.53754000
C	2.80319800	1.01343400	0.32782200

C	1.22929700	2.73411100	0.27947500
C	0.85895800	4.13221000	0.43270900
C	1.59693000	5.26752800	0.77362600
C	0.92036600	6.48344600	0.83188500
C	-0.45907600	6.56576400	0.55577000
C	-1.19577800	5.43411300	0.21483400
C	-0.51843700	4.21444500	0.15737800
C	-0.95892400	2.86481300	-0.15901600
C	-2.60700900	1.33889600	-0.78153100
C	-3.97077300	1.01866500	-1.17908400
C	-5.11461100	1.80352200	-1.32904700
C	-6.28417500	1.16676600	-1.73988200
C	-6.30994000	-0.21763800	-1.99684000
C	-5.16678700	-1.00081600	-1.84917300
C	-3.99651200	-0.36350500	-1.43570000
C	-2.64867500	-0.85583400	-1.18655900
C	-1.07622700	-2.57584900	-1.13611500
C	-0.70052000	-3.96987800	-1.32837500
C	-1.42877400	-5.09217400	-1.72415100
C	-0.74814700	-6.30519300	-1.81058700
C	0.62507100	-6.39413300	-1.51143100
C	1.35282700	-5.27246200	-1.11843600
C	0.67042500	-4.05876400	-1.02939300
C	1.10055000	-2.71628800	-0.66376900
Cl	-0.43113300	-0.31737900	2.00699200
H	-5.17663100	-2.06783800	-2.04403500
H	-7.23976500	-0.67988100	-2.31455700
H	-7.19471900	1.74533000	-1.86400100
H	-5.08566000	2.86906500	-1.12785100
H	-2.25844500	5.48711700	0.00362800
H	-0.95360100	7.53082400	0.61314800
H	1.46184600	7.38665000	1.09690700
H	2.65783100	5.19406100	0.98762700
H	5.35879900	2.23846400	1.07612900
H	7.42994100	0.85515100	1.29492900
H	7.37021400	-1.57763100	0.88712800
H	5.23720200	-2.71342800	0.24576000
H	2.41048000	-5.33175500	-0.88486500
H	1.12243600	-7.35640200	-1.58818200
H	-1.28336300	-7.20043400	-2.11271700

H	-2.48640000	-5.01357800	-1.95186200
O	0.46684200	0.38079700	-2.41233700
H	1.40767900	0.20698800	-2.55674700
H	0.34638400	1.32183200	-2.60219300

Sample *SIMPSON* input file for the simulation of 1D MAS spectrum with multiple sites

```
# Al-27 MAS spectrum of Aluminum phthalocyanine chloride on 900 spectrometer

spinsys {
channels 27Al
nuclei 27Al
shift 1 0.0p 0.0p 0.0 0 0 0
quadrupole 1 2 0.0e6 0.0 0 0 0
}
par {
start_operator I1x
detect_operator I1c
spin_rate 20000
gamma_angles 12
sw 240000
crystal_file C:/cygnus/cygwin-b20/simpson-1.1.1/cryst/zcw28656
np 2048
method gcompute
proton_frequency 900.080000e6
verbose 1101
}
proc pulseq {} {
global par
delay 9999
}
proc main {} {
global par
set cq(1) 10.0e6
```

```
set cq(2) 5.40e6
set cq(3) 6.80e6
set cq(4) 9.00e6
set etq(1) 0.00
set etq(2) 0.50
set etq(3) 0.20
set etq(4) 0.25
set shift(1) 27.0p
set shift(2) 12.0p
set shift(3) -12.0p
set shift(4) -12.5p
set aniso(1) 0.0p
set aniso(2) 0.0p
set aniso(3) 0.0p
set aniso(4) 0.0p
set etc(1) 0.0
set etc(2) 0.0
set etc(3) 0.0
set etc(4) 0.0
set alphac(1) 0
set betac(1) 0
set gammac(1) 0
set alphac(2) 0
set betac(2) 0
set gammac(2) 0
set alphac(3) 0
set betac(3) 0
set gammac(3) 0
set alphac(4) 0
set betac(4) 0
set gammac(4) 0
set scale(1) 1.0
set scale(2) 0.4
set scale(3) 1.0
set scale(4) 1.0
for {set i 1} {$i <= 4} {incr i} {
set g [fsimpson [list \
[list shift_1_iso $shift($i) ] \
[list shift_1_aniso $aniso($i)] \
[list shift_1_eta $etc($i)] \
```

```
[list shift_1_alpha $alphac($i)] \
[list shift_1_beta $betac($i)] \
[list shift_1_gamma $gammac($i)] \
[list quadrupole_1_aniso $cq($i)] \
[list quadrupole_1_eta $etq($i)] \
]]
fphase $g -scale $scale($i)
if [info exists f] {
fadd $f $g
funload $g
} else {
set f $g
}
}
fsave $f $par(name).fid
fzerofill $f 4096
faddlb $f 1000.0 0.5
fft $f
fphase $f -rp 0 -scale 250000
fsave $f $par(name).spe
funload $f
}
```

Sample *SIMPSON* input file for the simulation of 1D static spectrum with multiple sites

```
# Al-27 static spectrum of Aluminum phthalocyanine chloride on 900 spectrometer

spinsys {
channels 27Al
nuclei 27Al
shift 1 0.0p 0.0p 0.0 0 0 0
quadrupole 1 2 0.0e6 0.0 0 0 0
}
par {
start_operator I1x
detect_operator I1c
spin_rate 0
gamma_angles 1
sw 500000
crystal_file C:/cygnus/cygwin-b20/simpson-1.1.1/cryst/zcw28656
np 2048
method direct
proton_frequency 900.080000e6
verbose 1101
}
proc pulseq {} {
global par
reset
delay [expr 1.0e6/$par(sw)]
store 1
reset
acq $par(np) 1
}
proc main {} {
global par
set cq(1) 10.0e6
set cq(2) 5.40e6
set cq(3) 6.80e6
set cq(4) 9.00e6
set etq(1) 0.00
```

```
set etq(2) 0.50
set etq(3) 0.20
set etq(4) 0.25
set shift(1) 27.0p
set shift(2) 12.0p
set shift(3) -12.0p
set shift(4) -12.5p
set aniso(1) 0.0p
set aniso(2) 0.0p
set aniso(3) 0.0p
set aniso(4) 0.0p
set etc(1) 0.0
set etc(2) 0.0
set etc(3) 0.0
set etc(4) 0.0
set alphac(1) 0
set betac(1) 0
set gammac(1) 0
set alphac(2) 0
set betac(2) 0
set gammac(2) 0
set alphac(3) 0
set betac(3) 0
set gammac(3) 0
set alphac(4) 0
set betac(4) 0
set gammac(4) 0
set scale(1) 1.0
set scale(2) 0.4
set scale(3) 1.0
set scale(4) 1.0
for {set i 1} {$i <= 4} {incr i} {
set g [fsimpson [list \
[list shift_1_iso $shift($i) ] \
[list shift_1_aniso $aniso($i)] \
[list shift_1_eta $etc($i)] \
[list shift_1_alpha $alphac($i)] \
[list shift_1_beta $betac($i)] \
[list shift_1_gamma $gammac($i)] \
[list quadrupole_1_aniso $cq($i)] \
```

```
[list quadrupole_1_eta $etq($i)] \
]]
fphase $g -scale $scale($i)
if [info exists f] {
fadd $f $g
funload $g
} else {
set f $g
}
}
fsave $f $par(name).fid
fzerofill $f 4096
faddlb $f 1000.0 0.5
fft $f
fphase $f -rp -90
fsave $f $par(name).spe
funload $f
}
```

References

[1] Belz, M. H. *Phil. Mag.* **1922**, *44*, 479–501.

[2] (a) Rabi, I. I.; Zacharias, J. R.; Millman, S.; Kusch, P. *Phys. Rev.* **1938**, *53*, 318–318; (b) Rabi, I. I.; Millman, S.; Kusch, P.; Zacharias, J. R. *Phys. Rev.* **1939**, *55*, 526–535.

[3] Purcell, E. M.; Torrey, H. C.; Pound, R. V. *Phys. Rev.* **1946**, *69*, 37–38.

[4] Bloch, F.; Hansen, W. W.; Packard, M. *Phys. Rev.* **1946**, *69*, 127–127.

[5] Laws, D. D.; Bitter, H. M. L.; Jerschow, A. *Angew. Chem. Int. Ed.* **2002**, *41*, 3096–3129.

[6] (a) Proctor, W.; Yu, F. *Phys. Rev.* **1950**, *77*, 717–717; (b) Dickinson, W. C. *Phys. Rev.* **1950**, *77*, 736–737; (c) Arnold, J. T.; Dharmatti, S. S.; Packard, M. E. *J. Chem. Phys.* **1951**, *19*, 507–507.

[7] (a) Gutowsky, H. S.; McCall, D. W. *Phys. Rev.* **1951**, *82*, 748–749; (b) Gutowsky, H. S.; McCall, D. W.; Slichter, C. P. *Phys. Rev.* **1951**, *84*, 589–590; (c) Proctor, W. G.; Yu, F. C. *Phys. Rev.* **1951**, *81*, 20–30; (d) Andrew, E. R. *Phys. Rev.* **1951**, *82*, 443–444.

[8] (a) Hahn, E. L. *Phys. Rev.* **1950**, *77*, 297–298; (b) Hahn, E. L. *Phys. Rev.* **1950**, *80*, 580–594.

[9] (a) Andrew, E.; Bradbury, A.; Eades, R. *Nature(London)* **1958**, *182*, 1659–1659; (b) Andrew, E.; Bradbury, A.; Eades, R. *Nature(London)* **1959**, *183*, 1802–1803; (c) Lowe, I. *Phys. Rev. Lett.* **1959**, *2*, 285–287.

[10] (a) Pines, A.; Gibby, M. G.; Waugh, J. S. *J. Chem. Phys.* **1972**, *56*, 1776–1777; (b) Pines, A.; Gibby, M. G.; Waugh, J. S. *J. Chem. Phys.* **1973**, *59*, 569–590.

[11] Samoson, A.; Lippmaa, E.; Pines, A. *Mol. Phys.* **1988**, *65*, 1013–1018.

[12] Chmelka, B. F.; Mueller, K. T.; Pines, A.; Stebbins, J.; Wu, Y.; Zwanziger, J. W. *Nature* **1989**, *339*, 42–43.

[13] (a) Llor, A.; Virlet, J. *Chem. Phys. Lett.* **1988**, *152*, 248–253; (b) Mueller, K. T.; Sun, B. Q.; Chingas, G. C.; Zwanziger, J. W.; Terao, T.; Pines, A. *J. Magn. Reson.* **1990**, *86*, 470–487.

[14] (a) Frydman, L.; Harwood, J. S. *J. Am. Chem. Soc.* **1995**, *117*, 5367–5368; (b) Medek, A.; Harwood, J. S.; Frydman, L. *J. Am. Chem. Soc.* **1995**, *117*, 12779–12787.

[15] Carr, H. Y.; Purcell, E. M. *Phys. Rev.* **1954**, *94*, 630–638.

[16] Meiboom, S.; Gill, D. *Rev. Sci. Instrum.* **1958**, *29*, 688–691.

[17] Cheng, J. T.; Ellis, P. D. *J. Phys. Chem.* **1989**, *93*, 2549–2555.

[18] Larsen, F. H.; Jakobsen, H. J.; Ellis, P. D.; Nielsen, N. C. *J. Phys. Chem. A* **1997**, *101*, 8597–8606.

[19] Abragam, A. *The Principles of Nuclear Magnetism*; Clarendon Press: Oxford, 1961.

[20] Slichter, C. P. *Principles of Magnetic Resonance*, 3rd ed.; Springer-Verlag: New York, 1990.

[21] Haeberlen, U. In *Advances in Magnetic Resonance, Supplement 1*; Waugh, J. S., Ed.; Academic Press: New York, 1976.

[22] Mehring, M. *Principles of High Resolution NMR in Solids*, 2nd ed.; Springer-Verlag: Berlin, 1983.

[23] Ernst, R. R.; Bodenhausen, G.; Wokaun, A. *Principles of Nuclear Magnetic Resonance in One and Two Dimensions*; Clarendon Press: Oxford, 1987.

[24] Harris, R. K. *Nuclear Magnetic Resonance Spectroscopy*; Longman Scientific & Technical: UK, 1986.

[25] Levitt, M. H. *Spin Dynamics: Basics of Nuclear Magnetic Resonance*; John Wiley & Sons: Chichester, 2001.

[26] Schmidt-Rohr, K.; Spiess, H. W. *Multidimensional Solid-state NMR and Polymers*; Academic Press: London, 1994.

[27] Duer, M. J. *Introduction to Solid-State NMR Spectroscopy*; Blackwell Publishing Ltd.: Oxford, 2004.

[28] Cohen, M. H.; Reif, F. In *Solid State Physics*; Seitz, F., Turnbull, D., Eds.; Academic Press: New York, 1957; Vol. 5, pp 321–438.

[29] Taylor, P. C.; Baugher, J. F.; Kriz, H. M. *Chem. Rev.* **1975**, *75*, 203–240.

[30] Vaughan, R. W. *Ann. Rev. Phys. Chem.* **1978**, *29*, 397–419.

[31] Man, P. P. In *Encyclopedia of Nuclear Magnetic Resonance*; Grant, D. M., Harris, R. K., Eds.; Wiley: Chichester, UK, 1996; Vol. 6, pp 3838–3847.

[32] Vega, A. J. In *Encyclopedia of Nuclear Magnetic Resonance*; Grant, D. M., Harris, R. K., Eds.; Wiley: Chichester, UK, 1996; Vol. 6, pp 3869–3889.

[33] Adiga, S.; Aebi, D.; Bryce, D. L. *Can. J. Chem.* **2007**, *85*, 496–505.

[34] Mason, J. *Solid State Nucl. Magn. Reson.* **1993**, *2*, 285–288.

[35] (a) Ramsey, N. F. *Phys. Rev.* **1950**, *78*, 699–703; (b) Ramsey, N. F. *Phys. Rev.* **1950**, *77*, 567; (c) Ramsey, N. F. *Phys. Rev.* **1951**, *83*, 540–541; (d) Ramsey, N. F. *Phys. Rev.* **1952**, *86*, 243–246.

[36] Malli, G.; Froese, C. *Int. J. Quantum Chem.* **1967**, *S1*, 95–98.

[37] Kolb, D.; Johnson, W. R.; Shorer, P. *Phys. Rev. A* **1982**, *26*, 19–31.

[38] Duncan, T. M. *A Compilation of Chemical Shift Anisotropies*; Farragut Press: Chicago, 1990.

[39] Herzfeld, J.; Berger, A. E. *J. Chem. Phys.* **1980**, *73*, 6021–6030.

[40] Power, W. P.; Mooibroek, S.; Wasylishen, R. E.; Cameron, T. S. *J. Phys. Chem.* **1994**, *98*, 1552–1560.

[41] *National Institute of Standards and Technology (NIST)*, URL: *http://physics.nist.gov/constants*. Accessed on 2007, July 19.

[42] Power, W. P.; Wasylishen, R. E. *Annu. Rep. Nucl. Magn. Spectrosc.* **1991**, *23*, 1–84.

[43] Pake, G. E. *J. Chem. Phys.* **1948**, *16*, 327–336.

[44] Spiess, H. W. In *NMR Basic Principles and Progress*; Diehl, P., Fluck, E., Kosfeld, R., Eds.; Springer-Verlag: Berlin, 1978; Vol. 15, pp 55–214.

[45] Bryce, D. L.; Wasylishen, R. E. *J. Am. Chem. Soc.* **2000**, *122*, 11236–11237.

[46] Buckingham, A. D.; Love, I. *J. Magn. Reson.* **1970**, *2*, 338–351.

[47] Vaara, J.; Jokisaari, J.; Wasylishen, R. E.; Bryce, D. L. *Prog. Nucl. Magn. Reson. Spectrosc.* **2002**, *41*, 233–304.

[48] Zare, R. N. *Angular Momentum - Understanding Spatial Aspects in Chemistry and Physics*; John Wiley & Sons: New York, 1988.

[49] Bain, A. D.; Khasawneh, M. *Concepts Magn. Reson.* **2004**, *22A*, 69–78.

[50] Samoson, A. *Chem. Phys. Lett.* **1985**, *119*, 29–32.

[51] Amoureux, J. P.; Fernandez, C.; Granger, P. In *Multinuclear Magnetic Resonance in Liquids and Solids - Chemical Applications*; Granger, P., Harris, R. K., Eds.; Kluwer Academic Publishers: Dordrecht, The Netherlands, 1990; Vol. 322, Chapter XXII, pp 409–424.

[52] Smith, M. E.; van Eck, E. R. H. *Prog. Nucl. Magn. Reson. Spectrosc.* **1999**, *34*, 159–201.

[53] Power, W. P.; Wasylishen, R. E.; Mooibroek, S.; Pettitt, B. A.; Danchura, W. *J. Phys. Chem.* **1990**, *94*, 591–598.

[54] Eichele, K.; Wasylishen, R. E. *WSOLIDS1: Solid-State NMR Spectrum Simulation, version 1.19.11*, Universität Tübingen, Tübingen, Germany, 2009.

[55] Bak, M.; Rasmussen, J. T.; Nielsen, N. C. *J. Magn. Reson.* **2000**, *147*, 296–330.

[56] Power, W. P.; Kirby, C. W.; Taylor, N. J. *J. Am. Chem. Soc.* **1998**, *120*, 9428–9434.

[57] Kirby, C. W.; Power, W. P. *Can. J. Chem.* **2001**, *79*, 296–303.

[58] Rose, M. E. *Elementary Theory of Angular Momentum*; Wiley: New York, 1957.

[59] Man, P. P.; Klinowski, J.; Trokiner, A.; Zanni, H.; Papon, P. *Chem. Phys. Lett.* **1988**, *151*, 143–150.

[60] Kundla, E.; Samoson, A.; Lippmaa, E. *Chem. Phys. Lett.* **1981**, *83*, 229–232.

[61] Samoson, A.; Kundla, E.; Lippmaa, E. *J. Magn. Reson.* **1982**, *49*, 350–357.

[62] Vaughn, M. T.; Weidner, D. J. *Phys. Chem. Miner.* **1978**, *3*, 133–144.

[63] Gu, J.; Power, W. P. *Solid State Nucl. Magn. Reson.* **2005**, *27*, 192–199.

[64] Rocha, J. *Chem. Commun.* **1998**, 2489–2490.

[65] Gerothanassis, I. P. *Prog. Nucl. Magn. Reson. Spectrosc.* **1987**, *19*, 267–329.

[66] Bodart, P. R.; Amoureux, J. P.; Dumazy, Y.; Lefort, R. *Mol. Phys.* **2000**, *98*, 1545–1551.

[67] Larsen, F. H.; Skibsted, J.; Jakobsen, H. J.; Nielsen, N. C. *J. Am. Chem. Soc.* **2000**, *122*, 7080–7086.

[68] Wong, A.; Ida, R.; Mo, X.; Gan, Z.; Poh, J.; Wu, G. *J. Phys. Chem. A* **2006**, *110*, 10084–10090.

[69] Zhu, J.; Lin, Z.; Yan, Z.; Huang, Y. *Chem. Phys. Lett.* **2008**, *461*, 260–265.

[70] Sutrisno, A.; Terskikh, V. V.; Huang, Y. *Chem. Commun.* **2009**, 186–188.

[71] Moudrakovski, I.; Lang, S.; Patchkovskii, S.; Ripmeester, J. *J. Phys. Chem. A* **2010**, *114*, 309–316.

[72] Bryce, D. L.; Gee, M.; Wasylishen, R. E. *J. Phys. Chem. A* **2001**, *105*, 10413–10421.

[73] Chapman, R.; Bryce, D. *Phys. Chem. Chem. Phys.* **2009**, *11*, 6987–6998.

[74] Rossini, A. J.; Mills, R. W.; Briscoe, G. A.; Norton, E. L.; Geier, S. J.; Hung, I.; Zheng, S.; Autschbach, J.; Schurko, R. W. *J. Am. Chem. Soc.* **2009**, *131*, 3317–3330.

[75] Forgeron, M. A. M.; Wasylishen, R. E. *Magn. Reson. Chem.* **2008**, *46*, 206–214.

[76] Larsen, F. H.; Lipton, A. S.; Jakobsen, H. J.; Nielsen, N. C.; Ellis, P. D. *J. Am. Chem. Soc.* **1999**, *121*, 3783–3784.

[77] Lipton, A. S.; Wright, T. A.; Bowman, M. K.; Reger, D. L.; Ellis, P. D. *J. Am. Chem. Soc.* **2002**, *124*, 5850–5860.

[78] Lipton, A. S.; Buchko, G. W.; Sears, J. A.; Kennedy, M. A.; Ellis, P. D. *J. Am. Chem. Soc.* **2001**, *123*, 992–993.

[79] Lipton, A. S.; Ellis, P. D. *J. Am. Chem. Soc.* **2007**, *129*, 9192–9200.

[80] Lipton, A. S.; Bergquist, C.; Parkin, G.; Ellis, P. D. *J. Am. Chem. Soc.* **2003**, *125*, 3768–3772.

[81] Lipton, A. S.; Morlok, M. M.; Parkin, G.; Ellis, P. D. *Inorg. Chem.* **2008**, *47*, 5184–5189.

[82] Lipton, A. S.; Heck, R. W.; ; Ellis, P. D. *J. Am. Chem. Soc.* **2004**, *126*, 4735–4739.

[83] Lipton, A. S.; Heck, R. W.; Staeheli, G. R.; Valiev, M.; De Jong, W. A.; Ellis, P. D. *J. Am. Chem. Soc.* **2008**, *130*, 6224–6230.

[84] Lipton, A. S.; Heck, R. W.; Hernick, M.; Fierke, C. A.; Ellis, P. D. *J. Am. Chem. Soc.* **2008**, *130*, 12671–12679.

[85] Bowers, G. M.; Lipton, A. S.; Mueller, K. T. *Solid State Nucl. Magn. Reson.* **2006**, *29*, 95–103.

[86] Hung, I.; Schurko, R. W. *J. Phys. Chem. B* **2004**, *108*, 9060–9069.

[87] Forgeron, M. A. M.; Wasylishen, R. E. *J. Am. Chem. Soc.* **2006**, *128*, 7817–7827.

[88] Forgeron, M. A. M.; Wasylishen, R. E. *Phys. Chem. Chem. Phys.* **2008**, *10*, 574–581.

[89] Forgeron, M. A. M.; Wasylishen, R. E.; Gerken, M.; Schrobilgens, G. J. *Inorg. Chem* **2007**, *46*, 3585–3592.

[90] Yao, Z.; Kwak, H. T.; Sakellariou, D.; Emsley, L.; Grandinetti, P. J. *Chem. Phys. Lett.* **2000**, *327*, 85–90.

[91] Schurko, R. W.; Hung, I.; Widdifield, C. M. *Chem. Phys. Lett.* **2003**, *379*, 1–10.

[92] Kentgens, A. P. M.; Verhagen, R. *Chem. Phys. Lett.* **1999**, *300*, 435–443.

[93] Siegel, R.; Nakashima, T. T.; Wasylishen, R. E. *Chem. Phys. Lett.* **2004**, *388*, 441–445.

[94] Siegel, R.; Nakashima, T. T.; Wasylishen, R. E. *Chem. Phys. Lett.* **2006**, *421*, 529–533.

[95] Siegel, R.; Nakashima, T. T.; Wasylishen, R. E. *J. Magn. Reson.* **2007**, *184*, 85–100.

[96] O'Dell, L. A.; Schurko, R. W. *Chem. Phys. Lett.* **2008**, *464*, 97–102.

[97] Bhattacharyya, R.; Frydman, L. *J. Chem. Phys.* **2007**, *127*, 194503–94510.

[98] O'Dell, L. A.; Rossini, A. J.; Schurko, R. W. *Chem. Phys. Lett.* **2009**, *468*, 330–335.

[99] Kennedy, M. A.; Vold, R. L.; Vold, R. R. *J. Magn. Reson.* **1991**, *92*, 320–331.

[100] Frisch, M. J.; Trucks, G. W.; Schlegel, H. B.; Scuseria, G. E.; Robb, M. A.; Cheeseman, J. R.; Montgomery,; Jr.,; A., J.; Vreven, T.; Kudin, K. N.; Burant, J. C.; Millam, J. M.; Iyengar, S. S.; Tomasi, J.; Barone, V.; Mennucci, B.; Cossi, M.; Scalmani, G.; Rega, N.; Petersson, G. A.; Nakatsuji, H.; Hada, M.; Ehara, M.; Toyota, K.; Fukuda, R.; Hasegawa, J.; Ishida, M.; Nakajima, T.; Honda, Y.; Kitao, O.; Nakai, H.; Klene, M.; Li, X.; Knox, J. E.; Hratchian, H. P.; Cross, J. B.; Bakken, V.; Adamo, C.; Jaramillo, J.; Gomperts, R.; Stratmann, R. E.; Yazyev, O.; Austin, A. J.; Cammi, R.; Pomelli, C.; Ochterski, J. W.; Ayala, P. Y.; Morokuma, K.; Voth, G. A.; Salvador, P.; Dannenberg, J. J.; Zakrzewski, V. G.; Dapprich, S.; Daniels, A. D.; Strain, M. C.; Farkas, O.; Malick, D. K.; Rabuck, A. D.; Raghavachari, K.; Foresman, J. B.; Ortiz, J. V.; Cui, Q.; Baboul, A. G.; Clifford, S.; Cioslowski, J.; Stefanov, B. B.; Liu, G.; Liashenko, A.; Piskorz, P.; Komaromi, I.; Martin, R. L.; Fox, D. J.; Keith, T.; Al-Laham, M. A.; Peng, C. Y.; Nanayakkara, A.; Challacombe, M.; Gill, P. M. W.; Johnson, B.; Chen, W.; Wong, M. W.; Gonzalez, C.; Pople, J. A. *Gaussian 03*; Gaussian, Inc.: Wallingford, CT, 2004.

[101] *Calculation of NMR and EPR Parameters: Theory and Applications*; Kaupp, M., Bühl, M., Malkin, V. G., Eds.; Wiley-VCH: Weinheim, Germany, 2004.

[102] Young, D. C. *Computational Chemistry: A Practical Guide for Applying Techniques to Real World Problems*; John Wiley & Sons: Toronto, 2001.

[103] Autschbach, J. *Structure and Bonding* **2004**, *112*, 1–48.

[104] Helgaker, T.; Jaszunski, M.; Ruud, K. *Chem. Rev.* **1999**, *99*, 293–352.

[105] Vaara, J. *Phys. Chem. Chem. Phys.* **2007**, *9*, 5399–5418.

[106] Facelli, J. C. *Concepts Magn. Reson.* **2004**, *20*, 42–69.

[107] Ditchfield, R. *Mol. Phys.* **1974**, *27*, 789–807.

[108] Wolinski, K.; Hinton, J. F.; Pulay, P. *J. Am. Chem. Soc.* **1990**, *112*, 8251–8260.

[109] Cheeseman, J. R.; Trucks, G. W.; Keith, T. A.; Frisch, M. J. *J. Chem. Phys.* **1996**, *104*, 5497–5509.

[110] Parkin, G. *Chem. Rev.* **2004**, *104*, 699–767, and references therein.

[111] Berg, J. M.; Shi, Y. *Science* **1996**, *271*, 1081–1085.

[112] Coleman, J. E. *Annu. Rev. Biochem.* **1992**, *61*, 897– 946.

[113] Mills, C. F. *Zinc in Human Biology*; Springer-Verlag: London, 1989.

[114] Parkin, G. *Chem. Commun.* **2000**, 1971–1985.

[115] Alberts, I. L.; Nadassy, K.; Wodak, S. J. *Protein Sci.* **1998**, *7*, 1700–1716.

[116] Vallee, B. L.; Auld, D. S. *Biochemistry* **1990**, *29*, 5647–5659.

[117] McCall, K. A.; Huang, C.; Fierke, C. A. *J. Nutr.* **2000**, *130*, 1437S–1446S.

[118] Lipscomb, W. N.; Sträter, N. *Chem. Rev.* **1996**, *96*, 2375–2434.

[119] Bertini, I.; Gray, H. B.; Lippard, S. J.; Valentine, J. S. *Bioinorganic Chemistry*; University Science Books: Mill Valley, CA, 1994.

[120] Bode, W.; Gomis-Rüth, F. X.; Huber, R.; Zwilling, R.; StÖcker, W. *Nature (London, U.K.)* **1992**, *358*, 164–167.

[121] Ippolito, J. A.; Christianson, D. W. *Biochemistry* **1994**, *33*, 15241–15249.

[122] Kiefer, L. L.; Ippolito, J. A.; Fierke, C. A.; Christianson, D. W. *J. Am. Chem. Soc.* **1993**, *115*, 12581–12582.

[123] Lippard, S. J.; Berg, J. M. *Principles of Bioinorganic Chemistry*; University Science Books: Mill Valley, CA, 1994.

[124] Vallee, B. L.; Coleman, J. E.; Auld, D. S. *Proc. Natl. Acad. Sci. U.S.A.* **1991**, *88*, 999–1003.

[125] Berg, J. M.; Godwin, H. A. *Annu. Rev. Biophys. Biomol. Struct.* **1997**, *26*, 357–371.

[126] Pyykkö, P. *Mol. Phys.* **2008**, *106*, 1965–1974.

[127] Harris, R. K.; Becker, E. D.; Cabral de Menezes, S. M.; Goodfellow, R.; Granger, P. *Pure Appl. Chem.* **2001**, *73*, 1795–1818.

[128] Bryce, D. L.; Sward, G. D.; Adiga, S. *J. Am. Chem. Soc.* **2006**, *128*, 2121–2134.

[129] Herberg, H.; Abart, J.; Voitländer, J. *Z. Naturforsch., A: Phys. Sci.* **1979**, *34*, 1029–1030.

[130] Abart, J.; Palangié, E.; Socher, W.; Voitländer, J. *J. Chem. Phys.* **1983**, *78*, 5468–5473.

[131] Bastow, T. J. *J. Phys. Condens. Matter.* **1996**, *8*, 11309–11315.

[132] Bennett, L. H. *Phys. Rev.* **1966**, *150*, 418–420.

[133] Bastow, T. J. *Chem. Phys. Lett.* **2003**, *380*, 516–520.

[134] Wu, G. *Chem. Phys. Lett.* **1998**, *298*, 375–380.

[135] Sham, S.; Wu, G. *Can. J. Chem.* **1999**, *77*, 1782–1787.

[136] Bastow, T. J.; Stuart, S. N. *Phys. Stat. Sol. (b)* **1988**, *145*, 719–728.

[137] Dec, S. F.; Davis, M. F.; Maciel, G. E.; Bronnimann, C. E.; Fitzgerald, J. J.; Han, S. *Inorg. Chem.* **1993**, *32*, 955–959.

[138] Hayes, C. E.; Pound, R. V. *Bull. Am. Phys. Soc.* **1972**, *17*, 330.

[139] Haller, M.; Hertler, W. E.; Lutz, O.; Nolle, A. *Solid State Commun.* **1980**, *33*, 1051–1053.

[140] Wu, G.; Kroeker, S.; Wasylishen, R. E. *Inorg. Chem.* **1995**, *34*, 1595–1598.

[141] Kunwar, A. C.; Turner, G. L.; Oldfield, E. *J. Magn. Reson.* **1986**, *69*, 124–127.

[142] Vosegaard, T.; Andersen, U.; Jakobsen, H. J. *J. Am. Chem. Soc.* **1999**, *121*, 1970–1971.

[143] Lipton, A. S.; Smith, M. D.; Adams, R. D.; Ellis, P. D. *J. Am. Chem. Soc.* **2002**, *124*, 410–414.

[144] Zhang, Y.; Mukherjee, S.; Oldfield, E. *J. Am. Chem. Soc.* **2005**, *127*, 2370–2371.

[145] Ishioka, T.; Murata, A.; Kitagawa, Y.; Nakamura, K. T. *Acta Crystallogr., Sect. C: Cryst. Struct. Commun.* **1997**, *53*, 1029–1031.

[146] Lipton, A. S.; Sears, J. A.; Ellis, P. D. *J. Magn. Reson.* **2001**, *151*, 48–59.

[147] Bear, C. A.; Duggan, K. A.; Freeman, H. C. *Acta Crystallogr., Sect. B: Struct. Sci.* **1975**, *31*, 2713–2715.

[148] Vega, R.; López-Castro, A.; Márquez, R. *Acta Crystallogr., Sect. B: Struct. Sci.* **1978**, *34*, 2297–2299.

[149] Lipton, A. S.; Heck, R. W.; Sears, J. A.; Ellis, P. D. *J. Magn. Reson.* **2004**, *168*, 66–74.

[150] Smith, G. D.; Ciszak, E.; Magrum, L. A.; Pangborn, W. A.; Blessing, R. H. *Acta Crystallogr., Sect. D: Biol. Crystallogr.* **2000**, *56*, 1541–1548.

[151] Derewenda, U.; Derewenda, Z.; Dodson, E. J.; Dodson, G. G.; Reynolds, C. D.; Smith, G. D.; Sparks, C.; Swenson, D. *Nature* **1989**, *338*, 594–596.

[152] Ciszak, E.; Smith, G. D. *Biochemistry* **1994**, *33*, 1512–1517.

[153] Holland, D. R.; Hausrath, A. C.; Juers, D.; Matthews, B. W. *Protein Sci.* **1995**, *4*, 1955–1965.

[154] Lundberg, B. K. S. *Acta Crystallogr.* **1966**, *21*, 901–909.

[155] Dalosto, S. D.; Ferreyra, M. G.; Calvo, R.; Piro, O. E.; Castellano, E. E. *J. Inorg. Biochem.* **1999**, *73*, 151–155.

[156] Kistenmacher, T. J. *Acta Crystallogr., Sect. B: Struct. Sci.* **1972**, *28*, 1302–1304.

[157] Bell, P.; Sheldrick, W. S. *Z. Naturforsch., Teil b* **1984**, *39*, 1732–1737.

[158] Newman, J. M.; Bear, C. A.; Hambley, T. W.; Freeman, H. C. *Acta Crystallogr., Sect. C: Cryst. Struct. Commun.* **1990**, *46*, 44–48.

[159] Musie, G. T.; Li, X.; Powell, D. R. *Acta Crystallogr., Sect. E: Struct. Rep. Online* **2004**, *60*, m471–m472.

[160] Démaret, A.; Mercier, D. *J. Appl. Crystallogr.* **1983**, *16*, 279–281.

[161] Berezina, L. P.; Pozigun, A. I.; Misyurenko, V. L. *Russ. J. Inorg. Chem.* **1970**, *15*, 1244–1245.

[162] Shindo, H.; Brown, T. L. *J. Am. Chem. Soc.* **1965**, *87*, 1904–1909.

[163] *SAINT, version 4*; Siemens Analytical X-ray Instruments Inc.: Madison, WI, 1995.

[164] Sheldrick, G. M. *SHELXTL, version 5.12*; Siemens Analytical X-Ray Systems: Madison, WI, 1995.

[165] Bennett, A. E.; Rienstra, C. M.; Auger, M.; Lakshmi, K. V.; Griffin, R. G. *J. Chem. Phys.* **1995**, *103*, 6951–6958.

[166] Gor'kov, P. L.; Chekmenev, E. Y.; Li, C.; Cotten, M.; Buffy, J. J.; Traaseth, N. J.; Veglia, G.; Brey, W. W. *J. Magn. Reson.* **2007**, *185*, 77–93.

[167] Available from http://anorganik.uni-tuebingen.de/klaus/soft/index.php.

[168] This work was made possible by the facilities of the Shared Hierarchical Academic Research Computing Network (SHARCNET: www.sharcnet.ca).

[169] Becke, A. D. *J. Chem. Phys.* **1993**, *98*, 5648–5652.

[170] Lee, C.; Yang, W.; Parr, R. G. *Phys. Rev. B* **1988**, *37*, 785–789.

[171] Jameson, C. J. In *Multinuclear NMR*; Mason, J., Ed.; Plenum Press: New York, 1987; Chapter 3, p 56.

[172] Jameson, C. J. In *Encyclopedia of Nuclear Magnetic Resonance*; Grant, D. M., Harris, R. K., Eds.; Wiley: Chichester, UK, 1996; Vol. 2, pp 1273–1281.

[173] Weil, J. A.; Buch, T.; Clapp, J. E. *Adv. Magn. Reson.* **1973**, *6*, 183–257.

[174] Ashbrook, S. E.; Smith, M. E. *Chem. Soc. Rev.* **2006**, *35*, 718–735.

[175] Kentgens, A. P. M. *Geoderma* **1997**, *80*, 271–306.

[176] Raulin, J. *Ann. Sci. Bot. Biol. Veg.* **1869**, *11*, 93.

[177] Vallee, B. L.; Auld, D. S. *Biochemistry* **1993**, *32*, 6493–6500.

[178] Auld, D. S. *BioMetals* **2001**, *14*, 271–313.

[179] Auld, D. S. *BioMetals* **2009**, *22*, 141–148.

[180] Coleman, J. E.; Vallee, B. L. *J. Biol. Chem.* **1961**, *236*, 2244–2249.

[181] Coleman, J. E.; Vallee, B. L. *J. Biol. Chem.* **1963**, *238*, 945–951.

[182] Latt, S. A.; Auld, D. S.; Vallee, B. L. *Proc. Natl. Acad. Sci. U.S.A.* **1970**, *67*, 1383–1389.

[183] Armitage, I. M.; Pajer, R. T.; Schoot Uiterkamp, A. J. M.; Chlebowski, J. F.; Coleman, J. E. *J. Am. Chem. Soc.* **1976**, *98*, 5710–5712.

[184] Kennedy, M. A.; Ellis, P. D. *J. Am. Chem. Soc.* **1989**, *111*, 3195–3203.

[185] McAteer, K.; Lipton, A. S.; Kennedy, M. A.; Ellis, P. D. *Solid State Nucl. Magn. Reson.* **1996**, *7*, 229–238.

[186] Lipton, A. S.; Mason, S. S.; Myers, S. M.; Reger, D. L.; Ellis, P. D. *Inorg. Chem.* **1996**, *35*, 7111–7117.

[187] Adams, M. J.; Blundell, T. L.; Dodson, E. J.; Dodson, G. G.; Vijayan, M.; Baker, E. N.; Harding, M. M.; Hodgkin, D. C.; Rimmer, B.; Sheat, S. *Nature* **1969**, *224*, 491–495.

[188] Bentley, G.; Dodson, E.; Dodson, G.; Hodgkin, D.; Mercola, D. *Nature* **1976**, *261*, 166–168.

[189] Smith, G. D.; Swenson, D. C.; Dodson, E. J.; Dodson, G. G.; Reynolds, C. D. *Proc. Natl. Acad. Sci. U.S.A* **1984**, *81*, 7093–7097.

[190] Baker, E. N.; Blundell, T. L.; Cutfield, J. F.; Cutfield, S. M.; Dodson, E. J.; Dodson, G. G.; Hodgkin, D. M. C.; Hubbard, R. E.; Isaacs, N. W.; Reynolds, C. D.; Sakabe, K.; Sakabe, N.; Vijayan, N. M. *Philos. Trans. R. Soc. London Ser. B* **1988**, *319*, 369–456.

[191] Smith, G. D.; Dodson, G. G. *Biopolymers* **1992**, *32*, 441–445.

[192] Whittingham, J. L.; Chaudhuri, S.; Dodson, E. J.; Moody, P. C. E.; Dodson, G. G. *Biochemistry* **1995**, *34*, 15553–15563.

[193] Smith, G. D.; Pangborn, W. A.; Blessing, R. *Acta Crystallogr., Sect. D: Biol. Crystallogr.* **2003**, *59*, 474–482.

[194] Kaarsholm, N. C.; Ko, H.; Dunn, M. F. *Biochemistry* **1989**, *28*, 4427–4435.

[195] Krüger, P.; Gilge, G.; Çabuk, Y.; Wollmer, A. *Biol. Chem. Hoppe-Seyler* **1990**, *371*, 669–673.

[196] Brzovic, P. S.; Choi, W. E.; Borchardt, D.; Kaarsholm, N. C.; Dunn, M. F. *Biochemistry* **1994**, *33*, 13057–13069.

[197] Bloom, C. R.; Choi, W. E.; Brzovic, P. S.; Ha Sheng-Tung Huang, J. J.; Kaarsholm, N. C.; Dunn, M. F. *J. Mol. Biol.* **1995**, *245*, 324–330.

[198] Schlichtkrull, J. *Insulin Crystals*; Munksgaard: Copenhagen, 1958.

[199] Thomas, A. L. *Phthalocyanine Research and Applications*; CRC Press: Boston, 1990.

[200] *The Porphyrin Handbook*; Kadish, K. M., Smith, K. M., Guilard, R., Eds.; Academic Press: San Diego, 2003; Vol. 17–19.

[201] *Phthalocyanines: Properties and Applications*; Leznoff, C. C., Lever, A. B. P., Eds.; VCH Publishers: New York, 1996; Vol. 1–4.

[202] Berezin, B. D. *Coordination Compounds of Porphyrins and Phthalocyanines*; John Wiley & Sons: New York, 1981.

[203] McKeown, N. B. *Phthalocyanine Materials: Synthesis, Structure and Function*; Cambridge University Press: Cambridge, 1998.

[204] Jiang, J.; Kasuga, K.; Arnold, D. P. In *Supramolecular Photosensitive and Electroactive Materials*; Nalwa, H. S., Ed.; Academic Press: New York, 2001; pp 113–210.

[205] Schultz, H.; Lehmann, H.; Rein, M.; Hanack, M. *Structure and Bonding* **1991**, *74*, 41–146.

[206] De la Torre, G.; Claessens, C. G.; Torres, T. *Chem. Commun.* **2007**, 2000–2015.

[207] *The Porphyrin Handbook*; Kadish, K. M., Smith, K. M., Guilard, R., Eds.; Academic Press: San Diego, 2003; Vol. 5.

[208] *Phthalocyanines: Properties and Applications*; Leznoff, C. C., Lever, A. B. P., Eds.; VCH Publishers: New York, 1993; Vol. 2.

[209] Medek, A.; Frydman, V.; Frydman, L. *J. Phys. Chem. A* **1999**, *103*, 4830–4835.

[210] Tang, J. A.; ODell, L. A.; Aguiar, P. M.; Lucier, B. E. G.; Sakellariou, D.; Schurko, R. W. *Chem. Phys. Lett.* **2008**, *466*, 227–234.

[211] MacKenzie, K. J. D.; Smith, M. E. *Multinuclear Solid-State NMR of Inorganic Materials*; Pergamon Press: Oxford, UK, 2002.

[212] Akitt, J. W. *Prog. Nucl. Magn. Reson. Spectrosc.* **1989**, *21*, 1–149.

[213] Baugher, J. F.; Taylor, P. C.; Oja, T.; Bray, P. J. *J. Chem. Phys.* **1969**, *50*, 4914–4925.

[214] Cheng, J. T.; Edwards, J. C.; Ellis, P. D. *J. Phys. Chem.* **1990**, *94*, 553–561.

[215] Lee, S. K.; Stebbins, J. F. *J. Phys. Chem. B* **2000**, *104*, 4091–4100.

[216] Züchner, L.; Chan, J. C. C.; Müller-Warmuth, W.; Eckert, H. *J. Phys. Chem. B* **1998**, *102*, 4495–4506.

[217] Chan, J. C. C.; Bertmer, M.; Eckert, H. *J. Am. Chem. Soc* **1999**, *121*, 5238–5248.

[218] van Bokhoven, J. A.; Koningsberger, D. C.; Kunkeler, P.; van Bekkum, H.; Kentgens, A. P. M. *J. Am. Chem. Soc.* **2000**, *122*, 12842–15847.

[219] Lentz, P.; Carvalho, A. P.; Delevoye, L.; Fernandez, C.; Amoureux, J. P.; Nagy, L. B. *Magn. Reson. Chem.* **1999**, *37*, S55–S62.

[220] Chen, T. H.; Wouters, B. H.; Grobet, P. J. *J. Phys. Chem. B* **1999**, *103*, 6179–6184.

[221] Kentgens, A. P. M.; Iuga, D.; Kalwei, M.; Koller, H. *J. Am. Chem. Soc.* **2001**, *123*, 2925–2926.

[222] Bodart, P. R.; Amoureux, J. P.; Pruski, M.; Bailly, A.; Fernandez, C. *Magn. Reson. Chem.* **1999**, *37*, S69–S74.

[223] Ashbrook, S. E.; Whittle, K. R.; Le Pollès, L.; Farnan, I. *J. Am. Ceram. Soc.* **2005**, *88*, 1575–1583.

[224] Ashbrook, S. E.; MacKenzie, K. J. D.; Wimperis, S. *Solid State Nucl. Magn. Reson.* **2001**, *20*, 87–99.

[225] Alemany, L. B.; Steuernagel, S.; Amoureux, J. P.; Callender, R. L.; Barron, A. R. *Solid State Nucl. Magn. Reson.* **1999**, *14*, 1–18.

[226] Alemany, L. B.; Callender, R. L.; Barron, A. R.; Steuernagel, S.; Iuga, D.; Kentgens, A. P. M. *J. Phys. Chem. B* **2000**, *104*, 11612–11616.

[227] Rocha, J. *J. Phys. Chem. B* **1999**, *103*, 9801–9804.

[228] Rocha, J.; Morais, C. M.; Fernandez, C. *Clay Miner.* **2003**, *38*, 259–278.

[229] Smith, M. E. *Appl. Magn. Reson.* **1993**, *4*, 1–64.

[230] Kemp, T. F.; Smith, M. E. *Solid State Nucl. Magn. Reson.* **2009**, *35*, 243–252.

[231] Neuville, D. R.; Cormier, L.; Montouillout, V.; Florian, P.; Millot, F.; Rifflet, J. C.; Massiot, D. *Am. Mineral.* **2008**, *93*, 1721–1731.

[232] Neuville, D. R.; Cormier, L.; Massiot, D. *Geochim. Cosmochim. Acta* **2004**, *68*, 5071–5079.

[233] Schurko, R. W.; Wasylishen, R. E.; Foerster, H. *J. Phys. Chem. A* **1998**, *102*, 9750–9760.

[234] Ashenhurst, J.; Wu, G.; Wang, S. *J. Am. Chem. Soc.* **2000**, *122*, 2541–2547.

[235] Ashenhurst, J.; Wang, S.; Wu, G. *J. Am. Chem. Soc.* **2000**, *122*, 3528–3529.

[236] Utz, M.; Nandagopal, M.; Mathai, M.; Papadimitrakopoulos, F. *Appl. Phys. Lett.* **2003**, *83*, 4023–4025.

[237] Nishiyama, Y.; Fukushima, T.; Takami, K.; Kusaka, Y.; Yamazaki, T.; Kaji, H. *Chem. Phys. Lett.* **2009**, *471*, 80–84.

[238] Schurko, R. W.; Hung, I.; Macdonald, C. L. B.; Cowley, A. H. *J. Am. Chem. Soc* **2002**, *124*, 13204–13214.

[239] Tang, J. A.; Masuda, J. D.; Boyle, T. J.; Schurko, R. W. *ChemPhysChem* **2006**, *7*, 117–130.

[240] Amoureux, J. P.; Fernandez, C.; Steuernagel, S. *J. Magn. Reson., Ser. A* **1996**, *123*, 116–118.

[241] Massiot, D.; Fayon, F.; Capron, M.; King, I.; Le Calvé, S.; Alonso, B.; Durand, J.-O.; Bujoli, B.; Gan, Z.; Hoatson, G. *Magn. Reson. Chem.* **2002**, *40*, 70–76.

[242] Hasegawa, M.; Sato, N. *Mol. Cryst. Liq. Cryst.* **1997**, *296*, 409–426.

[243] Engel, M. K. In *The Porphyrin Handbook*; Kadish, K. M., Smith, K. M., Guillard, R., Eds.; Academic Press: San Diego, 2003; Vol. 20, p 223.

[244] Harris, R. K.; Becker, E. D.; Cabral de Menezes, S. M.; Granger, P.; Hoffman, R. E.; Zilm, K. W. *Pure Appl. Chem.* **2008**, *80*, 59–84.

[245] Arfken, G. *Mathematical Methods for Physicists*, 3rd ed.; Academic Press: New York, 1985.

[246] Fernandez, C.; Amoureux, J. P.; Chezeau, J. M.; Delmotte, L.; Kessler, H. *Microporous Mater.* **1996**, *6*, 331–340.

[247] Fyfe, C. A.; zu Altenschildesche, H. M.; Wong-Moon, K. C.; Grondey, H.; Chazeau, J. M. *Solid State Nucl. Magn. Reson.* **1997**, *9*, 97–106.

[248] Jansen, S. R.; Hintzen, H. T.; Metselaar, R.; de Haan, J. W.; van de Ven, L. J. M.; Kentgens, A. P. M.; Nachtegaal, G. H. *J. Phys. Chem. B* **1998**, *102*, 5969–5976.

[249] Schmücker, M.; Schneider, H. *J. Sol-Gel Sci. Technol.* **1999**, *15*, 191–199.

[250] Bryant, P. L.; Harwell, C. R.; Wu, K.; Fronczek, F. R.; Hall, R. W.; Butler, L. G. *J. Phys. Chem. A* **1999**, *103*, 5246–5252.

[251] Sykes, D.; Kubicki, J. D.; Farrar, T. C. *J. Phys. Chem. A* **1997**, *101*, 2715–2722.

[252] Amoureux, J. P.; Huguenard, C.; Engelke, F.; Taulelle, F. *Chem. Phys. Lett.* **2002**, *356*, 497–504.

[253] Viles, J. H.; Patel, S. U.; Mitchell, J. B. O.; Moody, C. M.; Justice, D. E.; Uppenbrink, J.; Doyle, P. M.; Harris, C.; Sadler, P. J.; Thornton, J. M. *J. Mol. Biol.* **1998**, *279*, 973–986.

[254] Marmorstein, R.; Carey, M.; Ptashne, M.; Harrison, S. C. *Nature* **1992**, *356*, 408–414.